Université de Paris

École Doctorale 564
Physique en Île-de-France

Laboratoire
Matériaux et Phénomènes Quantiques

AlGaAs quantum photonics: From device engineering to quantum information protocols

Par

Félicien APPAS

Thèse de doctorat de Physique

Dirigée par **Sara DUCCI**

Présentée et soutenue publiquement le 10/01/2022,
devant la commission d'examen composée de :

Maria Amanti	Maître de conf.	Université de Paris	Co-encadrante de thèse
Fabien Boitier	Docteur	Nokia Bell Labs	Invité
Alberto Bramati	Professeur	Sorbonne Université	Examinateur
Eleni Diamanti	Dir. de recherche	CNRS - Sorbonne Université	Invitée
Sara Ducci	Professeure	Université de Paris	Directrice de thèse
Arnaud Grisard	Ingénieur TRT	Thales Research & Technology	Examinateur
Valerio Pruneri	Professeur	ICFO	Rapporteur
Isabelle Zaquine	Professeure	Telecom ParisTech	Rapporteure

Abstract

Integrated quantum photonics is one of the main routes towards the realization of scalable quantum information processing with applications ranging from quantum computation and simulation to secure communications. In this work, we address some of the current challenges in integrated quantum photonics using the AlGaAs platform. Thanks to its second order optical nonlinearity, high refractive index and large electro-optic coefficient, this material is particularly well suited for the on-chip generation and manipulation of entangled photons pairs at room temperature and telecom wavelengths. This dissertation is divided in two parallel research directions: on the one hand the integration of novel functionalities on a monolithic AlGaAs quantum photonic chip and on the other hand the application of AlGaAs sources of entangled photons to quantum communications. In the first project, we successfully demonstrate the monolithic integration of an AlGaAs source with, on the one hand, an electro-optic delay line and, on the other hand, a broadband polarizing mode splitter of 50 nm bandwidth. In the second project, we take advantage of the high-quality and spectrally broadband polarization-entangled state generated by the source to build a reconfigurable multi-user quantum communication network. We implement entanglement-based quantum key distribution between up to 8 users with flexible bandwidth management in a fully-connected topology including long-distance fiber links supporting positive finite-key rates for up to 75 km. These results show the potential of the AlGaAs platform for future scalable photonic quantum information processing.

Keywords: quantum optics, integrated photonics, quantum communications

Résumé

La photonique quantique intégrée est l'une des principales approches pour la réalisation de technologies quantiques polyvalentes et flexibles. Les applications les plus notables vont du calcul quantique et la simulation quantiques aux communications sécurisées. Dans cette thèse, nous relevons certains des défis actuels de la photonique quantique intégrée avec l'aide de la plate-forme AlGaAs. Grâce à sa non-linéarite optique du second ordre, son haut indice de réfraction et son important coefficient électro-optique, ce matériau est particulièrement adapté à la génération et la manipulation sur puce de paires de photons intriqués à température ambiante et aux longueurs d'onde télécom. Ce travail de thèse est divisé en deux axes de recherches parallèles : d'une part l'intégration monolithique de nouvelles fonctionnalités sur une puce photonique quantique AlGaAs et d'autre part l'application des sources AlGaAs de photons intriqués aux communications quantiques. Dans le premier projet nous démontrons l'intégration monolithique d'une source AlGaAs avec, d'une part, une ligne à retard electro-optique et, d'autre part, un séparateur de faisceau polarisant doté d'une bande passante de 50 nm. Dans le second projet, nous tirons parti du haut taux d'intrication et de la large bande de l'état quantique émis par notre source pour construire un réseau de communication quantique multi-utilisateur reconfigurable. Nous implémentons un protocole de distribution de clé quantique exploitant l'intrication dans un réseau comprenant jusqu'à 8 utilisateurs avec une gestion flexible de la bande passante et à des distances allant jusqu'à 75 km en tenant compte des effets de clés finies. Ces résultats montrent le potentiel de la plateforme AlGaAs dans le contexte de l'information et des technologies quantiques.

Mots-clé: optique quantique, photonique intégrée, communications quantiques

Résumé

La photonique quantique intégrée est l'une des principales approches pour la réalisation de technologies quantiques polyvalentes et flexibles. Au cours des deux dernière décennies, le domaine des technologies quantiques a reçu une attention grandissante de la part de la communauté scientifique. Les applications les plus notables vont du calcul quantique et la simulation quantiques aux communications sécurisées et à la métrologie. Les premières démonstrations d'avantage quantique dans des tâches de calcul quantique, telles que le *boson sampling*, ou de métrologie, comme la détection d'ondes gravitationnelles, ont vu le jour très récemment, dans les cinq dernières années. Ces découvertes de premier plan sont soutenues par des programmes de financement à grande échelle, tant au niveau européen, avec le *Quantum Flagship*, que national, comme par exemple le Plan quantique français. Différentes plateformes physiques peuvent être utilisées pour l'implémentation des technologies quantiques, chacune présentant des avantages pour certains types de tâches. Les qubits supraconducteurs, les atomes froids ou les spins à l'état solide sont particulièrement adaptés au calcul quantique. Les photons, quant à eux, se prêtent naturellement à la propagation sur de longues distance ainsi qu'à la miniaturisation sur puce photonique, ce qui en fait un système polyvalent avec un haut potentiel dans les communications quantiques, la métrologie mais également le calcul ou la simulation quantique. Ces applications reposent sur les propriétés quantiques de la lumière ayant été mises en évidence dans les expériences pionnières des années 1980 et 1990 telles que l'interférence à un et deux photons ou la génération d'états comprimés ainsi que d'états intriqués. Au cours des deux dernières décennies, la réalisation de protocoles d'information quantique sur des plateformes photoniques intégrées s'est imposée comme une direction de recherche majeure pour les technologies quantiques. En effet, il est possible de réaliser des puces miniatures où la lumière se propage dans des guides d'ondes micrométriques et où son état est manipulé à l'aide de composants optiques intégrés (lames séparatrices, lignes à retard, lames d'onde). Cette approche ouvre la voie vers une mise à l'échelle des preuves de principe dans les domaines du calcul et des communications quantiques en combinant la stabilité intrinsèque des circuits photoniques intégrés et leur haute densité de composants.

Dans cette thèse, nous relevons certains des défis actuels de la photonique quantique intégrée avec l'aide de la plate-forme AlGaAs. Grâce à sa non-linéarité optique du second ordre, son haut indice de réfraction et son important coefficient électro-optique, ce matériau est particulièrement adapté à la génération et la manipulation sur puce de paires de photons intriqués à température ambiante et aux longueurs d'onde télécom. Ce travail de thèse est divisé en deux axes de recherches parallèles : d'une part l'intégration monolithique de nouvelles fonctionnalités sur une puce photonique quantique AlGaAs et d'autre part l'application des sources AlGaAs de photons intriqués aux communications quantiques.

Les source intégrées AlGaAs de paires de photons sont réalisées sous la forme de guides d'onde ruban composé d'un empilement de couches épitaxiales formant un coeur entouré de deux miroirs de Bragg. Le dispositif, dont la largeur est d'environ 5 µm et la longueur de 2 mm, est fabriqué soit par lithographie UV puis gravure chimique soit par lithographique électronique et gravure sèche ICP. Le guide d'onde supporte des modes guidés dans le proche infrarouge (775 nm) et aux longueurs d'onde télécom (1550 nm). La structure épitaxiale est conçue de façon à obtenir des conditions d'accord de phase (*phase-matching*) optimales permettant réaliser des processus optiques non-linéaires d'ordre deux. Parmi eux, la fluorescence paramétrique (SPDC), où un photon dans le proche infrarouge est spontanément converti en deux photons télécom, peut être utilisée pour la génération

de paires de photons uniques. En exploitant l'accord de phase de Type II, le processus de SPDC permet d'émettre des photons télécom intriqués en polarisation directement à la sortie du guide d'onde. Les propriétés des sources AlGaAs sont mesurées d'abord dans le régime classique. L'estimation des pertes de propagation par mesure de la transmission du guide d'onde permet d'évaluer la qualité de la fabrication. Ensuite, la valeur de la longueur d'onde de dégénérescence du processus de fluorescence paramétrique est déduite des spectres de seconde harmonique. Enfin les performances de la sources sont quantifiées dans le régime de comptage de photons. Le taux de génération interne (PGR) et le rapport signal sur bruit (CAR) sont obtenus par la mesure d'histogrammes de corrélations temporelles entre les détections des deux photons. Pour réaliser cette mesure, les photons générés par la source AlGaAs sont séparés à l'aide d'un séparateur de faisceau fibré et détectés sur des détecteurs de photons uniques à fil supraconducteur. Les corrélations temporelles sont effectuées à l'aide d'une électronique de comptage (TDC). Nous mesurons des performances de : PGR $= 6.9 \times 10^6\,\mathrm{s}^{-1}$, CAR $= 80$. Un troisième indicateur de performance de notre source est la largeur de bande d'émission des photons. Celle-ci est mesurée par effet Hong-Ou-Mandel (HOM). Dans cette expérience, après avoir séparé les photons, l'un d'entre eux est retardé à l'aide d'une ligne à retard en espace libre avant d'interférer avec le premier photon sur une lame séparatrice fibrée 50/50. En mesurant le nombre de coïncidences par unité de temps en fonction du retard temporel τ appliqué, on constant une décroissance autour de $\tau = 0$. En mesurant la largeur à mi-hauteur, on remonte à la largeur spectrale de la source, ici 60 nm. Le caractère large-bande de la source est un atout pour la réalisation de communications quantiques multi-utilisateurs ainsi que pour l'exploration de protocoles fondés sur des états de haute dimension.

Après avoir exposé le fonctionnement et les performances de la source intégrée AlGaAs de photons intriqués, nous nous attachons à montrer l'intégration monolithique d'une ligne à retard électro-optique avec une source AlGaAs. L'arsenure de galllium (GaAs) disposant d'un coefficient electro-optique de second ordre non nul, la valeur de l'indice de réfraction du matériau peut être modifiée par application d'un champ électrique statique. En exploitant cet effet dans un guide d'onde AlGaAs, il est possible de contrôler l'indice de propagation du mode fondamental TE et ainsi d'appliquer un retard de phase à ce mode. Ce mécanisme permet d'obtenir une ligne à retard intégrée dont le déphasage est déterminé par la valeur du champ electrique. Celle-ci est réalisée par dépôt métallique sur le guide d'onde d'électrodes d'or grâce auxquelles le champ statique est imposé. La caractérisation du dispositif est effectué par des mesures de transmission du guide d'onde pour différentes valeurs de tension appliquée. La ligne à retard présente une tension $\pi/2$ de 9 V, ce qui permet de contrôler l'état des photons directement sur la puce en utilisant des composants électroniques standards.

En outre, nous sommes parvenus à intégrer un séparateur de polarisation large-bande avec une source AlGaAs de Type II sur une même puce monolithique. Le séparateur de polarisation est un coupleur directionnel dans lequel la biréfringence intrisèque des guides d'onde introduit une différence entre les longueurs de couplage TE et TM. A l'aide de simulations numériques, nous identifions une région dans l'espace des paramètres (largeur des guides et espacement entre les guides) pour laquelle la lumière se propageant dans les modes TE et TM quitte le coupleur par des ports opposés. Nous avons fabriqué ce dispositif par lithographie électronique et gravure sèche ICP puis nous avons effectué une caractérisation dans le régime classique (pertes de propagation, taux de séparation de polarisation, seconde harmonique). Nous avons ainsi mesuré un taux de séparation excédant les 90 % sur une bande spectrale de 50 nm. En régime quantique, nous avons pu démontrer l'émission de paires de photons dans la structure et leur séparation sur le

séparateur de polarisation intégré. Enfin, nous avons caractérisé l'indiscernabilité spectrale des photons à la sortie de la puce en réalisant une interférométrie Hong-Ou-Mandel. Nous avons mesuré une visibilité de 80 %, intrinsèquement limitée par la biréfringence de la source, ce qui montre que nous parvenons à séparer de manière quasi-déterministe les paires de photons directement sur puce sans altérer leur état quantique. Dans un futur projet, ces deux dispositifs (ligne à retard et séparateur de polarisation) peuvent être combinés sur une même puce pour réaliser un interféromètre de Mach-Zender intégré. Cette architecture permettrait de réaliser la génération et le contrôle sur puce d'états intriqués dans différents degrés de liberté tels que la polarisation, le mode spatial ou la fréquence.

Dans la dernière partie de ce manuscrit nous exploitons la haute qualité d'intrication en polarisation et la large bande spectrale de l'état généré par notre source SPDC AlGaAs pour construire un réseau de communication quantique reconfigurable. L'intrication est une ressource centrale pour le domaine de la cryptographie quantique car elle permet de garantir la sécurité d'un protocole de distribution de clé dans des liens longue distance et dans des réseaux multi-utilisateurs sans avoir recours à des nœuds fiables. Pour montrer le potentiel des sources intégrées AlGaAs dans ce contexte, nous avons commencé par mesurer la bande spectrale de l'état à deux photons généré par la source. Pour cela, nous avons séparé les photons sur une lame séparatrice fibrée 50/50 puis nous avons inséré un filtre accordable dans l'un des bras de sortie. En mesurant le nombre de coïncidences en fonction de la position centrale du filtre, nous pouvons obtenir une estimation de la bande passante de l'état. Ici, nous mesurons une largeur spectral de 60 nm autour d'une longueur d'onde centrale de 1555.6 nm dans la bande télécom C+L. Ce resultat est cohérent avec la mesure d'effet Hong-Ou-Mandel décrite dans la première partie du manuscrit. Les 60 nm de bande passante de la source correspondent à 76 canaux ITU standards de 100 GHz. Nous avons ensuite montré la haute qualité de l'intrication en polarisation en mesurant une fidélité à un état de Bell de plus de 95 % sur une bande spectrale de 26 nm. Nous avons ensuite utilisé un filtre multiport programmable (WSS), très répandu dans l'industrie des télécommunications classiques, afin de réaliser la distribution d'intrication dans un réseau reconfigurable. En effet, le WSS permet de diviser l'état quantique des deux photons en canaux dont la longueur d'onde centrale et la largeur peuvent être définies librement puis de les distribuer entre différents ports de sortie fibrés correspondant aux différents utilisateurs du réseau. Ainsi il est possible d'augmenter la capacité du réseau en diminuant la largeur des canaux sans avoir à modifier le dispositif expérimental. Nous démontrons ainsi la distribution d'intrication entre 4, 5 et 8 utilisateurs sur des canaux respectivement de 200 GHz, 100 GHz et 50 GHz. Nous appliquons ensuite notre architecture à la distribution de clé quantique par le protocole BBM92 en montrant un faible taux d'erreurs ($< 2\,\%$) et un haut taux de clé secrète (30-40 bps) sur un ensemble de 13 canaux fréquentiels standards ITU de 100 GHz. Nous avons reproduit ces mesures en ajoutant des liens fibrés longue distance et des atténuateurs variables entre les utilisateurs. Ainsi nous avons pu obtenir un taux de clé positive en incluant les effets de taille finie jusqu'à une distance de 75 km. Enfin, nous illustrons la flexibilité de notre architecture réseau en adaptant l'allocation de bande passante à certaines contraintes structurelles telles que le déséquilibre entre les distances des liens inter-utilistateurs. L'ensemble de ces résultats montre le potentiel de la plateforme AlGaAs pour l'implémentation de technologies quantiques polyvalentes ainsi que leur intégration dans les futurs réseaux quantiques à grande échelle. Dans la continuité de ce projet, l'un des objectif à moyen terme sera d'augmenter la capacité du réseau dans des expériences en laboratoire ainsi que d'utiliser une source AlGaAs pour effectuer une démonstration réaliste de distribution de clé sur un lien fibré déployé en région parisienne.

Contents

List of acronyms **11**

Introduction **13**

I Theoretical background **21**

1 Introduction to nonlinear optics **23**
1.1 Second order parametric processes 23
1.2 The nonlinear dielectric polarization 24
1.3 Simple physical picture of three-wave mixing 25
1.4 Nonlinear optics in crystals 26
1.5 Phase-matching conditions 27

2 Spontaneous Parametric Downconversion (SPDC) **31**
2.1 Quantization of the electromagnetic field 31
2.2 Photons and field operators 32
2.3 Simple quantum model for SPDC 33

3 Quantum Entanglement **35**
3.1 From first debates to applications 35
3.2 Formal definition and measures of entanglement 36
3.3 Entanglement and local realism, Bell's inequalities 37
3.4 Polarization entanglement 39
3.5 Energy-time entanglement 40
3.6 Frequency-bin entanglement 42

II AlGaAs photon-pair source: design, fabrication and characterization **45**

4 Non-linear optics in AlGaAs waveguides **47**
4.1 Optical waveguides for nonlinear optics 47
4.2 AlGaAs Waveguide design 50
4.3 Cleanroom fabrication 56
4.4 Measurement of the optical losses of the guided modes 60
4.5 Characterization of the frequency conversion by Second Harmonic Generation 61

5 SPDC in AlGaAs waveguides: generated quantum state 65
5.1 Quantum theory of colinear SPDC . . . 65
5.2 Properties of the JSA . . . 68
5.3 Numerical simulation of the JSA . . . 70
5.4 Polarization entanglement . . . 73

6 Experimental characterization of the biphoton state 77
6.1 Pair generation rate and CAR . . . 77
6.2 Spectral indistinguishability and biphoton bandwidth: Hong-Ou-Mandel (HOM) effect . . . 82
6.3 Joint spectral intensity (JSI) reconstruction by stimulated emission tomography . . . 90
6.4 HOM and BFC state symmetry . . . 91

III AlGaAs electro-optic devices 95

7 On-chip integration of nonlinear AlGaAs waveguides and EO delay lines 97
7.1 State of the art and motivation . . . 97
7.2 Electro-Optic Effect in AlGaAs waveguides . . . 98
7.3 Design and fabrication of doped samples . . . 104
7.4 Design and fabrication of undoped samples . . . 107
7.5 Measurement of the electro-optic phase-shift . . . 109

IV Monolithic integration of an AlGaAs type II photon pair source and a broadband polarization splitter 117

8 Working principle and device design 119
8.1 State of the art and motivation . . . 119
8.2 Evanescent coupling of two waveguides . . . 120
8.3 Device design . . . 124
8.4 Realization of a test sample . . . 128

9 Experimental demonstration 131
9.1 Chip layout . . . 131
9.2 Classical characterization: propagation losses, phase-matching, splitting ratio 132
9.3 Photon-pair generation and on-chip polarization splitting . . . 136
9.4 Hong-Ou-Mandel interference at the chip output . . . 136

V Flexible entanglement-distribution network with an AlGaAs chip for secure communications 145

10 Entanglement-based quantum key distribution 147
10.1 State of the art and motivation . . . 147
10.2 Basic principle of the BBM92 protocol . . . 150
10.3 Security analysis: general considerations . . . 151
10.4 Asymptotic regime . . . 152
10.5 Finite-key regime . . . 153

11 Generation of broadband polarization entanglement with an AlGaAs source **155**
11.1 Experimental setup and calibration of the polarization analysis module . . . 155
11.2 Demultiplexing schemes . . . 157
11.3 Characterization of the broadband polarization-entangled state . . . 161

12 Flexible multi-user entanglement-based quantum key distribution network **167**
12.1 QKD performance before the distribution stage . . . 167
12.2 Long-distance entanglement-based QKD . . . 169
12.3 Comparison between WSS and passive thin-film DWDM for polarization entanglement distribution . . . 174
12.4 A reconfigurable fully-connected multi-user entanglement-distribution network . . . 175
12.5 Elastic quantum network with flexible bandwidth allocation . . . 178
12.6 Towards new topologies . . . 178

Conclusion and perspectives **181**

Appendix **187**

List of publications and conferences **187**

Software Credits **189**

Growth sheets **191**

Bibliography **205**

List of acronyms

BFC Biphoton Frequency Comb

BS Beam Splitter

CAR Coincidence-to-Accidental Ratio

CMOS Complementary Metal-Oxide-Semiconductor

CV Continuous Variables

CW Continuous Wave

CWDM Coarse Wavelength Division Multiplexing

DFG Difference Frequency Generation

DV Discrete Variables

DWDM Dense Wavelength Division Multiplexing

EDFA Erbium-Doped Fiber Amplifier

EME Eigenmodes Expansion

EO Electro-Optic

FBMS Fixed Beam Moving Stage

FPBS Fiber Polarizing Beam Splitter

FDTD Finite Difference Time Domain

FPC Fiber Polarization Controller

FTIR Fourier Transform Infrared Spectroscopy

FWHM Full Width at Half Maximum

HOM Hong-Ou-Mandel

ICP Inductively Coupled Plasma etching

IR Infrared

JSA Joint Spectral Amplitude

JSI Joint Spectral Intensity

MBE Molecular Beam Epitaxy

NA Numerical Aperture

NIR Near Infrared

OAM Orbital Angular Momentum

OPA Optical Parametric Amplification

OSA Optical Spectrum Analyzer

PBS Polarizing Beam Splitter

PECVD Plasma Enhanced Chemical Vapor Deposition

PGR Pair Generation Rate

PID Proportional-Integral-Derivative

PM Phase Matching

ppLN Periodically Poled Lithium Niobate

QBER Quantum Bit Error Rate

QI Quantum Information

QKD Quantum Key Distribution

RIE Reactive Ion Etching

SEM Scanning Electron Microscope

SET Stimulated Emission Tomography

SFG Sum Frequency Generation

SFWM Spontaneous Four-Wave Mixing

SHG Second Harmonic Generation

SNSPD Single Photon Superconducting Nanowire detector

SOI Silicon-On-Insulator

SPDC Spontaneous parametric downconversion

TDC Time-to-Digital Converter

TE Transverse Electric

TF Tunable Filter

TM Transverse Magnetic

WDM Wavelength Division Mulitplexing

WSS Wavelength Selective Switch

Introduction

Scientific context: Quantum technologies

Quantum information (QI) is a research domain at the forefront of 21st century science. It has emerged over the last three decades as a very diverse field at the crossroads between basic science and applications.

At the heart of this burgeoning field is quantum mechanics, one of the most fascinating scientific revolution of the last century. QI uses the peculiar features of quantum systems as a resource to perform tasks that are classically impossible or very hard to accomplish. Highly sought-after long-term applications include unconditionally secure communications, the speedup of computationally intensive algorithms or the efficient simulation of complex solid-state and molecular systems. The quantum phenomena at play range from the superposition principle and non-cloning theorem to wave-particle duality and entanglement.

Many significant milestones have been recently achieved such as the first demonstration of quantum advantage for computing tasks [1, 2], the deployment of quantum communication schemes on satellite infrastructure [3], gravitational wave detection using squeezed light [4] or loophole-free tests of quantum non-locality [5, 6, 7]. On the political side, the last couple of years have seen the creation of international and national funding plans such as the European Quantum Flagship or the french *"Plan quantique"*. Now that many applications seem at reach, the term **"Quantum technologies"** is gaining momentum as a avatar for QI. In the literature, the possible applications of quantum technologies are usually divided into the following branches: quantum computing, quantum communication, quantum metrology and sensing and quantum simulation.

The current state of the field of quantum technologies is often referred to as the"Second quantum revolution". When it was formulated at the beginning of the 20th century, quantum mechanics aimed at explaining unsolved problems of classical physics such as the stability of electronic orbits in atoms or the black-body radiation spectrum. Building on the newly established quantum theory, physicists in the 1960's were able to predict some of the electronic and optical properties of materials. This led to major technological applications that are now part of our everyday life such as lasers and transistors. This turnover was later coined "First quantum revolution". In the "Second quantum revolution" which, began in the late 1990's and early 2000's with the emergence of QI, the counter-intuitive features of quantum mechanics are used directly as a resource. This has been made possible partly thanks to recent advances in nanofabrication techniques, cryogenics or single photon sources and detectors which enabled the demonstration of increasingly complex and sensitive quantum phenomena.

We can list several families of physical platforms that are currently used for the implementation of quantum technologies. A first example is **atomic systems**. These include for instance ultracold atoms or trapped ions. The inherent quantum nature, high sensitivity

and spectacular degree of control that has been achieved over these systems put atoms at the heart of many applications in quantum computing and quantum simulation [8, 9, 10]. **Solid-state** quantum systems form another distinct class of physical platform for QI. Indeed, many advanced applications in quantum computing have been realized using the spin of single electrons or defect vacancies in crystals [11, 12, 13]. **Superconducting circuits** emerged in the last decades as yet another test bed for QI. They quickly became the most advanced platform in the race for building quantum computers [14, 15]. Lastly, another approach is to use **photons**, elementary particles of light, as carriers of information. It is the historical physical system that was studied by the pioneers of QI in the 1980's. Owing to their high speed and immunity to decoherence, photons are suited for quantum communications as well many applications in quantum computing and simulation [16].

Quantum information experiments with photons: landmarks

The present work deals with photon-based quantum technologies which rely on the multiple attractive properties of this physical system. In this section we give a brief historical overview of this field following the introduction of [17]

Photonic quantum information takes its root in the early developments of quantum optics. In the second half of the 20^{th} century, the very first experimental evidences of non-classical states of light were discovered. In 1956, the famous Hanbury Brown and Twiss experiment [18] on intensity interferometry with light collected from stars yielded results that could only be explained later on using the quantum theory of photodetection developed by Roy Glauber in the 1960's. A first experimental signature of photon antibuching was then observed by Kimble, Dagenais and Mandel in 1977 [19] followed eight years later by the demonstration of emission of squeezed light by Slusher and coworkers [20]. Finally, the first experiments on single and two-photon interference, probing the wave-particle duality of light, came to light at the end of the 1980's [21, 22].

One of the first milestone of quantum information is the experimental violation of Bell's inequality by Aspect, Grangier and Roger in 1981. The team of physicists used polarization-entangled photons to prove a very general result: the experimental signature of non-local correlation in the measurement of entangled states [23, 24]. This showed that the bizarre features of quantum mechanics were not mere theoretical artifacts but actual experimentally accessible resources. From this starting point, Bennett and Brassard proposed in 1984 the first major protocol for quantum cryptography (BB84) that is still widely used today [25]. In this scheme, the security of a cryptographic key is guaranteed by the combination of wave-particle duality and the non-cloning theorem. This was followed by two other proposals in which the security of the key stems from the entanglement between pairs of particles [26, 27]. All those schemes were experimentally demonstrated throughout the 1990's [28, 29, 30, 31]. Another historical landmark in quantum information with photons is the experimental teleportation of photons in 1997 by Bouwmeester and coworkers in Innsbruck [32] .

Over the course of the 1990's many experimental efforts were also devoted to the demonstration of entanglement in new degrees of freedom of photons, among which energy-time [33, 34] or orbital angular momentum [35]. This decade also saw the development of new sources of single photons and entangled photons such as quantum dots [36] or parametric photon-pair sources [37].

This opened the way to the major breakthroughs of the 2000's, which brought the proof-of-concept experiments of the previous decade into the realm of practical applications. Quantum communications emerged as a major field of research with the develop-

ment increasingly secure and device-independent protocols on the one hand, and large scale field tests on the other hand [38]. The quest for a quantum repeater, which could overcome photon loss in long-distance propagation while preserving the quantum properties of light, is also a long-standing goal of the community. Interfaces between solid-state or atomic system and photons, eventually moving towards the first operational quantum networks are also developing very fast [39, 40, 41]. Quantum computing with photons has also been a very active topic from the first demonstration of CNOT gates [42] and Shor's algorithms [43, 44] to boson sampling [45] and finally the recent achievement of quantum advantage in a photonic implementation of boson sampling [2]. Impressive results have been achieved as well in photonic quantum simulation such as complex quantum walks [46] or the simulation of molecular dynamics [47]. Another field that received growing attention in the previous decade is metrology and sensing using photons. Landmark experiments include the detection of gravitational waves using squeezed light [4] or more recently the first demonstrations of distributed quantum sensing [48, 49]. Lastly, the photonic platform is also the cornerstone of many experimental works on fundamental tests of quantum mechanics such as the first loophole-free tests of quantum non-locality mentioned in the previous section or experiments aimed at closing more advanced loopholes using basis settings from random human choices [50] or light collected from distant quasar [51].

Integrated quantum photonics

All of these applications rely on recent advances at the basic science level ranging from fundamental quantum optics to the development of new materials. Integrated quantum photonics is an example where the study of quantum phenomena is pushed forward by engineering challenges.

Many of the seminal experiments of photonic quantum information were performed using bulk optical components such as non-linear crystals and free-space interferometers. Even though this approach has the advantage of a great control over the setup and high photon detection count rates, it offers limited scalability. Indeed, protocols involving a large number of photons or high-dimensional Hilbert spaces often require the stabilization of complex and space-consuming interferometric setups.

Integrated photonics offers an alternative route for the realization of scalable quantum information processing with light. The main idea is to integrate optical functionalities directly on a single miniature chip. Indeed, light can be tightly confined at the micrometer scale and routed in nanofabricated waveguides. In addition, quantum gates can be performed on several degrees of freedom using simple building blocks such as electro-optic or thermal phase shifters and directional couplers, all of which are well-known in classical optics. Moreover, sources of single and entangled photons as well as single photon detectors can be integrated onto photonic chips. Hence, over the last 15 years, the integration of an increasingly complex combination of photonic components and the on-chip realization of intricate quantum information tasks have been demonstrated. Those recent advances are summarized in Refs. [16, 52, 53].

Here, we give an overview of the different physical platforms for the implementation of on-chip quantum information processing and briefly compare their strengths and weaknesses.

Silicon-based technologies This family of materials is one of the most widely used for quantum photonics. Their common denominator are their cheap fabrication, mature technology transfer from the complementary metal-oxide-semiconductor (CMOS) industry and third order optical non-linearity. Entangled photon pairs and

squeezed light can be generated through spontaneous four-wave mixing (SFWM). The two main Silicon-based platforms are Silicon-on-Insulator (SOI) and Silicon nitride (Si_3N_4).

The SOI platform is currently the main candidate for the race to an all-optical quantum processor. Its high refractive index allows light confinement at sub-micron scale waveguides hence a resulting small footprint. Programmable phase shifters are implemented by locally changing the refractive index of the waveguide using thermo-optic effects. The SOI platform has been proven to support the integration of multiple sources and reconfigurable quantum gates on a single chip, with applications to quantum computing [54] and quantum communications [55, 56]. Finally, the SOI platform is compatible with the integration of superconducting nanowire single photon detectors (SNSPDs) [57]. The main disadvantage of SOI for quantum photonics is its high losses at telecom wavelengths ($3\,\mathrm{dB\,cm^{-1}}$) [54].

Silicon nitride (Si_3N_4) is another common Silicon-based platform for quantum photonics that benefits from ultra-low propagation losses ($0.2\,\mathrm{dB\,cm^{-1}}$) [58]. It has been used to generate high-dimensional entangled states using SFWM [59] as well as universal gates [58, 60]. The integration of on-chip superconducting detectors and microelectromechanical systems have been also been successfully implemented in [61].

Silica-based materials Silica on Silicon (SoS) was historically the first platform to be used for the realization of on-chip quantum gates thanks to its ultra low losses ($0.05\,\mathrm{dB\,cm^{-1}}$) [62]. It has a weak third order susceptibility that can be used to generate photon pairs through SFWM [63]. Just like in Silicon, programmable gates can be implemented using thermo-optic phase-shifters [64]. The main drawback of this platform is the low refractive index contrast between the core of the waveguide and the substrate which results low integration density.

Other glass materials such as borosilicate glass can be used for photonic circuits using femtosecond laser writing (typical propagation losses of $0.8\,\mathrm{dB\,cm^{-1}}$) [65]. This technique provides easy fabrication of complex waveguide circuits that can be arranged in a 2D [46] or 3D architecture [66]. This is the platform of choice for on-chip boson sampling [45] and quantum walks [67]. Thermo-optic phase-shifters are also used to perform programmable gates [68] however the lack of optical non-linearity in the fabricated waveguides prevents the on-chip integration of parametric photon sources.

Lithium Niobate ($LiNbO_3$) Thanks to its large $\chi^{(2)}$ non-linearity and low losses at telecom wavelengths ($0.1\,\mathrm{dB\,cm^{-1}}$ [69]), $LiNbO_3$ was one of the first integrated platform for the generation of entangled-photon pairs on a photonic chip using spontaneous parametric downconversion (SPDC) [70]. Periodical poling of a $LiNbO_3$ waveguide (ppLN) is used to achieve quasi phase-matching condition for efficient photon-pair generation. Phase shifters can be realized by taking advantage of the large electro-optic effect of the material. Hence reconfigurable quantum circuits and on-chip two photon interference have been demonstrated using this platform [71, 69]. ppLN has also been used as a source in several entanglement-based quantum communications experiments [72, 73] or for on-chip generation of squeezing [74]. In addition, $LiNbO_3$ can be bonded on Silicon wafers which enables the hybrid integration of $LiNbO_3$ sources and Si-based quantum photonic circuits [75].

III-V materials Semiconductor III-V materials such as AlGaAs and InAs are ubiquitous

in classical and quantum photonics. They typically have a high refractive index allowing for tight light confinement in micrometer scale waveguides. Sources of non-classical light can be integrated on III-V chips using quantum dots that serve as bright single photon sources [76]. In AlGaAs the inherently high second and third order optical non-linearities makes it possible to engineer bright parametric sources of entangled photon pairs that have been demonstrated using SPDC in non-linear Bragg reflector waveguides [77, 78] or, more recently, SFWM in AlGaAs-on-insulator (AlGaAsOI) microring resonators [79]. The propagation losses in Bragg reflector waveguide are of the same order as in SOI, typically $2\,\mathrm{dB\,cm^{-1}}$. This is not an intrinsic limitation of the material and it could be improved with an optimized epitaxial growth process. As an example, in AlGaAsOI the losses can be lowered down to around $0.4\,\mathrm{dB\,cm^{-1}}$ which compares with ultra-low loss platforms such as Si_3N_4. Like $LiNbO_3$, AlGaAs features a strong electro-optic coefficient that can be used to engineer delay lines [80]. The fabrication of on-chip SNSPDs on top of GaAs waveguide has also been demonstrated in Ref. [81].

One of the most appealing features of III-V materials is their compliance with electrical injection, which stems from their direct electronic bandgap. This opens the possibility to drastically reduce the device footprint by integrating the pump laser directly on chip, as was demonstrated in Refs. [82, 83]. Last but not least, III-V active components can also be integrated onto Silicon chips [84]. This promising approach brings together the best of both worlds: the mature technology and cheap fabrication of Silicon waveguide circuits on the one hand and the electrical injection and second order non-linearity of III-V on the other hand.

III-V quantum photonic chips have been recently used in lab and deployed quantum communications experiments [85, 86] as well as for quantum computing application such as the generation of grid states [87, 88] or cluster states [89] and for the quantum simulation of exotic particle exchange statistics [90, 91].

Encoding quantum information in photons

Light represents one of the most versatile system for quantum information processing. There are two main approaches for encoding information in quantum states of the electromagnetic field. The first one, which is referred to as the continuous variable approach (CV), exploits the state of the quadratures of a many-photon field using squeezed light and homodyne detection [92]. CV photonic quantum information is one of the main candidates for the implementation of one-way quantum computing [93] and has also been used to build resource-efficient quantum key distribution architectures [94].

The other branch of photonic quantum information processing, which is the one that is studied in this manuscript, is the so-called discrete variable approach (DV). In this framework, information is encoded in the degrees of freedom of single photons [16]. In what follows, we give a brief overview of the main DV encoding schemes.

Polarization This degree of freedom is perhaps the most widely used for DV quantum information thanks to its convenient manipulation and the possibility to easily generate photon pairs in polarization-entangled states using parametric sources [37, 95] or single emitters [96]. The polarization state of single photons provides a natural implementation of a quantum two-level system ("qubit") which has been used in various fields of quantum information from the first violation of Bell's inequality [24] to quantum communications [97], as in the work presented in this manuscript.

Time-bin In this scheme a quantum bit is encoded in the arrival time of a single photon at a detector. The manipulation of the quantum state is implemented with the help of an unbalanced Mach-Zender interferometer, with a tunable time-delay that is much larger than the photon coherence time. This apparatus is used to perform arbitrary rotations on the state of a time-bin qubit [98]. Thanks to its robustness to noise and to dispersion in optical fibers, this encoding is commonly used in long-distance quantum key distribution [99]. Moreover, this degree of freedom can be extended to dimensions greater than two, which has been proposed as a way to increase the capacity and robustness to noise of quantum communication protocols [100, 101].

Path encoding This approach uses the occupation of a spatial mode of the electromagnetic field by a single photon as a mean to encode information. In this picture, each spatial mode is associated to a qubit where the 1 state corresponds to the mode being occupied and the 0 state to the mode being unoccupied. This scheme can be easily implemented in integrated waveguide circuits using directional couplers and phase shifters to connect the different spatial modes of an interferometer and to manipulate the path-encoded quantum states of photons [102, 54]. This approach, being suited to high-dimensional encoding, has been used to perform generation and manipulation of high-dimensional bipartite entangled states [103], simulation of quantum walks in disordered lattices [67] as well as molecular dynamics of a four-atom molecule [47] or boson sampling [45, 104].

Frequency encoding In this framework, the spectrum of single photons is used to encode information. For instance, the spectrum of a photon can be divided into distinct spectral bins that define the basis of a frequency-bin qubit. At telecom wavelengths, the quantum state of a frequency-bin qubit is easily manipulated using off-the-shelf components such as phase modulators and pulse shapers [105, 59, 106]. This approach represents the frequency analogue of time-bin encoding and lends itself to a natural extension to high-dimensionality. Indeed, photon pairs that are frequency-entangled over a large Hilbert space can be conveniently generated in integrated photonic chips using SFWM in microring resonators [107] or SPDC in III-V ridge waveguides [87].

Orbital angular momentum (OAM) This type of encoding relies on the transverse mode profile of single photons featuring twisted wavefronts. In this scheme, the quantum states are labeled by the number of wavefront twists per wavelength experienced by light along the propagation direction. This number is an integer that can, in principle, assume an infinite number of value, meaning OAM is also suited to to high-dimensional quantum information protocols [108]. Notable applications of OAM encoding include quantum key distribution with enhanced channel capacity [109] and high-dimensional Bell inequalities violation [110]

Current challenges and research directions

The future prospects and challenges for integrated quantum photonics are manifold. Many efforts are currently being devoted to developing and integrating an increasing number of functionalities on a single chip. This includes the monolithic integration of multiples sources of non-classical light, reconfigurable interferometers and on-chip detectors as well as hybrid chips combining devices from different platforms. Coupling photonic chips to

other physical systems such as ions or mechanical resonators also offer great promises for the integration of on-chip quantum memories [111, 112].

Another direction is going to high-dimensional quantum systems. This includes for instance the increasing of the number of spatial modes in integrated waveguide circuits that are used for quantum simulation or boson sampling as well as investigating inherently high-dimensional degrees of freedom such as frequency for example. The recent results on integrated quantum frequency combs offer great promises for the development of scalable frequency-based quantum computing and communication [107]. More exotic states involving multiple degrees of freedom, such as hyper-entangled states which can be generated and manipulated on-chip are also a promising resource for future quantum information protocols [113, 114].

Finally, the integration of quantum photonic chips in quantum network architectures is another major research prospect that is being currently pushed forward. Indeed the robustness of integrated photonic components make them ideal candidates for low-cost sources and detection units for quantum communication both in fiber networks [55, 85] and free-space links [115] as well as potential on-board components for satellites-based networks [116].

Scope of this work and outline of the manuscript

In this dissertation, we address some of the current challenges in integrated quantum photonics using the AlGaAs platform, both on the device engineering side and on the quantum network side. To this end, two main projects were conducted in parallel: on the one hand the integration of novel functionalities on AlGaAs quantum photonic chips and on the other hand the application of AlGaAs parametric sources of entangled photons to quantum communication.

In the first project, we successfully demonstrated the monolithic integration of an AlGaAs source with, on the one hand, an electro-optic delay line and, on the other hand, a broadband polarizing mode splitter of 50 nm bandwidth. In the second project, carried out in collaboration with Eleni Diamanti at Sorbonne Université and Fabien Boitier at Nokia Bell Labs, we took advantage of the high-quality and spectrally broadband polarization-entangled state generated by the source to build a reconfigurable multi-user quantum communication network. We demonstrated entanglement-based quantum key distribution between up to 8 users with flexible bandwidth management in a fully-connected topology including long-distance fiber links supporting positive finite-key rates for up to 75 km.

The manuscript is organized as follows. In Part I we review the main theoretical tools of classical and quantum optics that are relevant to our work before describing in Part II the working principle, design and characterization of the AlGaAs entangled photon pair source used in our experiments. Part III and Part IV are dedicated respectively to the realization of an integrated electro-optic delay line and a broadband polarization mode splitter on an AlGaAs quantum photonic chip. In Part V we report on our demonstration of an AlGaAs-chip-based reconfigurable multi-user quantum communication network. Finally, we summarize the results presented in this dissertation and outline some perspectives for future works.

Part I

Theoretical background

Chapter 1

Introduction to nonlinear optics

Contents

1.1 Second order parametric processes 23
1.2 The nonlinear dielectric polarization 24
1.3 Simple physical picture of three-wave mixing 25
1.4 Nonlinear optics in crystals 26
1.5 Phase-matching conditions 27

In this chapter, we give a brief overview of nonlinear optics. We describe qualitatively the different second order processes that will be encountered in this work then give a classical mathematical description in the framework of Maxwell's equations. We introduce the concept of phase-matching which plays a central role in the design of our AlGaAs photon-pair sources.

1.1 Second order parametric processes

Nonlinear optics is a branch of physics studying phenomena which arise when intense electromagnetic fields interact with matter. The basic physical picture behind nonlinear optics is that when an optical medium is subject to an electromagnetic of sufficiently high magnitude the response of this medium becomes nonlinear, implying that new fields are created at a frequency that is different from the excitation frequency. Nonlinear optical processes are of paramount importance in quantum optics as they are routinely used to generate quantum states of light, such as in the present work. They admit a natural

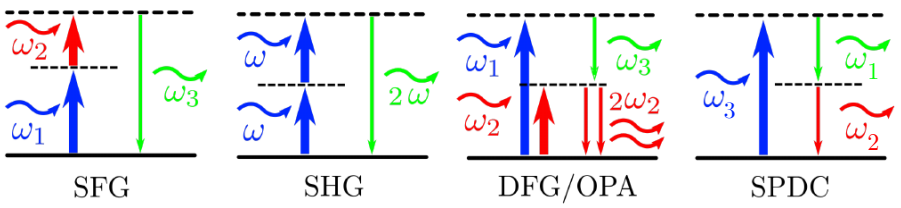

Figure 1.1: Sketch of the four main second order non-linear processes that are encountered in this manuscript. SFG: Sum Frequency Generation, SHG: Second Harmonic Generation, DFG: Difference Frequency Generation, OPA: Optical Parametric Amplification and SPDC: Spontaneous Parametric Downconversion.

interpretation in terms of photons, the elementary quanta of light. Indeed, nonlinear phenomena can be seen as an exchange of photons between different frequency modes. In this dissertation, we are dealing with second order processes, or three-wave mixing, where only three distinct frequencies are involved in the conversion process.

A sketch of the different possible three-wave mixing processes is presented in Fig. 1.1. In sum frequency generation (SFG), two incident photons at frequencies ω_1, ω_2 create a third photon at frequency ω_3. Second harmonic generation (SHG) is a special case of SFG for which the incident frequencies are identical. Hence a field at frequency ω is used to create a frequency-doubled field at 2ω. In difference frequency generation (DFG), the interaction of incident photons at frequencies ω_1, ω_2 lead to the creation of a photon at $\omega_3 = \omega_1 - \omega_2$ and two photons at ω_2. In addition to frequency conversion, DFG results in an amplification of the seed field ω_2 which is referred to as optical parametric amplification (OPA). Finally, in spontaneous parametric downconversion (SPDC), an incident photon ω_3 is downconverted into two lower energy photons of frequencies ω_1, ω_2, also called signal and idler. By convention, signal refers to the photon with the highest energy.

In a frequency conversion process the total energy of the photons of the interacting modes has to be conserved. Since the energy of a photon at frequency ω is given by $\hbar\omega$ with $\hbar$ the reduced Planck constant, in all of the listed processes, energy conservation imposes:

$$\hbar\omega_1 + \hbar\omega_2 = \hbar\omega_3. \tag{1.1}$$

SPDC stands out among the rest of the second order processes as it is the only one which cannot be described in fully classical terms. It can be seen as the quantum limit of DFG where, instead of using a classical seed field at ω_2 to trigger the nonlinear process, it is the quantum fluctuation of vacuum which couple to the pump at ω_1 to ignite the downconversion process. Thanks to its intrinsic quantum nature, SPDC is one of the most common and convenient way of generating quantum states of light such as squeezed states or entangled photon-pairs. A description of SPDC using the formalism of quantum optics will be given in Chapter 2.

Finally, third order nonlinear processes, which involve four interacting fields are also widely used in classical and quantum optics. In particular spontaneous four wave mixing (SFWM) is a way of generating entangled photons in materials that lack second order optical nonlinearity, such as Silicon.

1.2 The nonlinear dielectric polarization

In the following three sections, we give a classical description of nonlinear optical processes from Maxwell's equation following Ref. [117]. We start by introducing the nonlinear dielectric polarization vector and show how its behavior can explain frequency conversion phenomena.

Let us recall Maxwell's equations in a non-magnetic dielectric material in the absence of charges and currents:

$$\nabla \times \mathbf{E} + \frac{\partial \mathbf{B}}{\partial t} = 0, \tag{1.2}$$

$$\nabla \times \mathbf{B} - \mu_0 \frac{\partial \mathbf{D}}{\partial t} = 0, \tag{1.3}$$

where $\mathbf{E}$ is the electric field, $\mathbf{D}$ the electric displacement field, $\mathbf{B}$ the magnetic induction and μ_0 the vacuum magnetic permeability. The response of an optical medium to an external electromagnetic field can be described by the dielectric polarization $\mathbf{P}$. When

subject to an electric field, the electronic cloud of the atoms constituting the medium gets polarized in the direction of this external field. The dielectric polarization $\mathbf{P}$ is essentially proportional to the induced electric field resulting from the displacement of electronic charges in the material. This quantity relates to $\mathbf{E}$ and $\mathbf{D}$ as

$$\mathbf{D} = \epsilon_0 \mathbf{E} + \mathbf{P}. \tag{1.4}$$

where ϵ_0 is the permittivity of vacuum. At low electric fields $\mathbf{P}$ is linear in $\mathbf{E}$ but, as the magnitude increases, a higher order response can be observed. Mathematically, we assume that $\mathbf{P}$ can be expanded as [117]:

$$\mathbf{P} = \underbrace{\epsilon_0 \chi^{(1)} \mathbf{E}}_{\mathbf{P}^{\mathrm{L}}} + \underbrace{\epsilon_0 \chi^{(2)} \mathbf{E}\mathbf{E} + \epsilon_0 \chi^{(3)} \mathbf{E}\mathbf{E}\mathbf{E}}_{\mathbf{P}^{\mathrm{NL}}} + ... \tag{1.5}$$

In this expression $\chi(1)$,$\chi(2)$ and $\chi(3)$, are respectively second, third and fourth order tensors the tensor product is implicit. The first term is simply the linear response of the medium, which by definition is proportional to the applied electric field. $\chi^{(1)}$ is called the first order dielectric susceptibility. The second term is the second order nonlinear response, which is quadratic in the applied field and will be responsible for three-wave mixing. $\chi^{(2)}$ is called the second order dielectric susceptibility. Similarly, the third term models the third order non-linear response of the medium that gives rise to four-wave mixing processes.

In what follows, we are only concerned with second order processes and we only retain the second order term:

$$\mathbf{P}^{\mathrm{NL}} = \chi^{(2)} \mathbf{E}\mathbf{E} \tag{1.6}$$

The vector $\mathbf{P}^{\mathrm{NL}}$ has a very direct physical interpretation according to Maxwell's equations. By taking the curl of (1.2) and plugging it in (1.3), we obtain the following inhomogeneous wave equation describing the propagation of electromagnetic waves through the medium:

$$\nabla^2 \mathbf{E} - \frac{n^2}{c^2} \frac{\partial^2 \mathbf{E}}{\partial t^2} = \mu_0 \frac{\partial^2 \mathbf{P}^{\mathrm{NL}}}{\partial t^2}, \tag{1.7}$$

with c the speed of light in vacuum, μ_0 the magnetic permeability and n the refractive index of the medium. We see that the time derivative of $\mathbf{P}^{\mathrm{NL}}$ acts as a source term in the wave equation. This shows us that, thanks to the nonlinear response of the materials, fields at different frequencies are being created which can be, in principle, of different frequency that the driving field.

1.3 Simple physical picture of three-wave mixing

To see this more explicitly, we show from a simple example how the different classical processes described in Fig. 1.1 emerge naturally from the mathematical form of the nonlinear polarization vector. We take the simplest case of a homogeneous and isotropic medium under applied field $E(t)$. The nonlinear dielectric polarization given in equation Eq. (1.6) reduces to a simple scalar quantity

$$P^{\mathrm{NL}} = \epsilon_0 \chi^{(2)} E^2(t), \tag{1.8}$$

where $\chi^{(2)}$, in this case, is a scalar. We assume that the incident field $E(t)$ is the sum of two independent monochromatic fields at frequencies $\omega_1 > \omega_2$:

$$\begin{aligned} E(t) &= E_1(t) + E_2(t), \\ E_i(t) &= E_i e^{i\omega_i t} + \text{c.c.}, \quad i = 1, 2. \end{aligned} \tag{1.9}$$

The nonlinear dielectric polarization becomes:

$$P^{\mathrm{NL}} = \epsilon_0 \chi^{(2)} \left[E_1^2(t) + E_2^2(t) + 2E_1(t)E_2(t) \right]. \tag{1.10}$$

When expanding the individual terms of the sum we obtain:

$$E_1^2(t) = |E_1|^2 + E_1^2 e^{i2\omega_1 t} + \text{c.c.}, \tag{1.11}$$

$$E_2^2(t) = |E_2|^2 + E_2^2 e^{i2\omega_2 t} + \text{c.c.}, \tag{1.12}$$

$$E_1(t)E_2(t) = E_1 E_2 e^{i(\omega_1+\omega_2)t} + \text{c.c.} \tag{1.13}$$

$$+ E_1^* E_2 e^{i(\omega_1-\omega_2)t} + \text{c.c.}. \tag{1.14}$$

In Eqs. (1.11) and (1.12), we see that the two incident fields at ω_1, ω_2 have been frequency doubled to $2\omega_1, 2\omega_2$ which describes second harmonic generation (SHG). SFG appears in Eq. (1.13) where we notice that that the phase factor depends on the sum of the two frequencies $\omega_1 + \omega_2$. Finally the last term, Eq. (1.14), models DFG since it features an oscillation at the difference frequency $\omega_1 - \omega_2$.

1.4 Nonlinear optics in crystals

Most optical media used for non-linear optics are crystals. In this kind of material the above description where $\chi^{(2)}$ and E are scalars is too simplistic. Indeed, crystals can be birefringent, meaning the induced dielectric polarization vector can depend on the direction of the applied electric field. Hence, in this case, $\chi^{(2)}$ is a third rank tensor whose symmetries reflects the atomic structure of the unit cell of the crystal. This tensor will couple the different components of the electric field through non-linear processes.

We derive the expression for the nonlinear dielectric polarization in a general anisotropic medium. Again, we consider the case of three interacting fields at frequencies $\{\omega_\ell\}_{\ell=1,2,3}$ fulfilling energy conservation $\omega_3 = \omega_1 + \omega_2$. Since we are interested in describing the propagation of waves, we include the spatial dependence of the electric field in the equations. The electric field and nonlinear dielectric polarization inside the medium consists of the sum of terms at different frequencies that can be written :

$$\mathbf{E}(\mathbf{r}, t) = \frac{1}{2} \sum_{\ell=1}^{3} \left[\mathbf{E}_\ell(\mathbf{r}, t) + \text{c.c.} \right], \tag{1.15}$$

$$\mathbf{P}^{\mathrm{NL}}(\mathbf{r}, t) = \frac{1}{2} \sum_{\ell=1}^{3} \left[\mathbf{P}_\ell^{\mathrm{NL}}(\mathbf{r}, t) + \text{c.c.} \right], \tag{1.16}$$

where we assume that the interacting fields are monochromatic waves:

$$\mathbf{E}_\ell(\mathbf{r}, t) = \mathbf{A}_\ell(\mathbf{r}) e^{-i(\omega_\ell t - \mathbf{k}_\ell \cdot \mathbf{r})}, \quad \ell = 1, 2, 3. \tag{1.17}$$

The variable $\mathbf{k}_\ell$ denotes the wave-vector of the field at frequency ω_ℓ. Thanks to the linearity of Eq. (1.7) we obtain a inhomogeneous wave equation for each frequency component ℓ:

$$\nabla^2 \mathbf{E}_\ell - \frac{n^2}{c^2} \frac{\partial^2 \mathbf{E}_\ell}{\partial t^2} = \mu_0 \frac{\partial^2 \mathbf{P}_\ell^{\mathrm{NL}}}{\partial t^2}, \quad \ell = 1, 2, 3. \tag{1.18}$$

Here we do not seek a general solution to this system of coupled equations. A more comprehensive approach can be found for example in Ref. [117]. In what follows we are simply interested in isolating the different terms corresponding to the non-linear processes

of interest. For each value of ℓ, the source term has to be evaluated separately by keeping the terms in $\mathbf{P}^{\mathrm{NL}}$ which satisfy energy conservation. In the case we are considering ($\omega_3 = \omega_1 + \omega_2$) only three terms are relevant to describe the possible nonlinear processes:

$$P^{\mathrm{NL}}_{3,i}(\mathbf{r},t) = \epsilon_0 \sum_{jk} \chi^{(2)}_{ijk} E_{1,j}(\mathbf{r},t) E_{2,k}(\mathbf{r},t), \quad \text{[SFG]} \tag{1.19}$$

$$P^{\mathrm{NL}}_{1,i}(\mathbf{r},t) = \epsilon_0 \sum_{jk} \chi^{(2)}_{ijk} E_{3,j}(\mathbf{r},t) E^*_{2,k}(\mathbf{r},t), \quad \text{[DFG]} \tag{1.20}$$

$$P^{\mathrm{NL}}_{2,i}(\mathbf{r},t) = \epsilon_0 \sum_{jk} \chi^{(2)}_{ijk} E_{3,j}(\mathbf{r},t) E^*_{1,k}(\mathbf{r},t), \quad \text{[DFG]}. \tag{1.21}$$

where the subscripts i, j, k span the three spatial directions $i, j, k \in \{x, y, z\}$ and the star denotes complex conjugation. These equations assume a general form for the dielectric susceptibility tensor $\chi^{(2)}$. However in a crystal the exact form of $\chi^{(2)}$ can be inferred from the symmetries of its crystalline unit cell. The structure of this tensor will dictate which components of the electric field can be coupled together through three-wave mixing. For each nonzero matrix element of $\chi^{(2)}$, there is a corresponding allowed non-linear process. We will detail the case of GaAs in Section 4.2.2.

Note that so far we have assumed that $\chi^{(2)}$ does not depend on the frequencies. This assumption, which is referred to as Kleinmann's symmetry, is valid provided the frequencies involved in the non-linear interaction are much smaller than the natural resonance frequency of the medium which is typically the case in the dielectric materials we are considering.

1.5 Phase-matching conditions

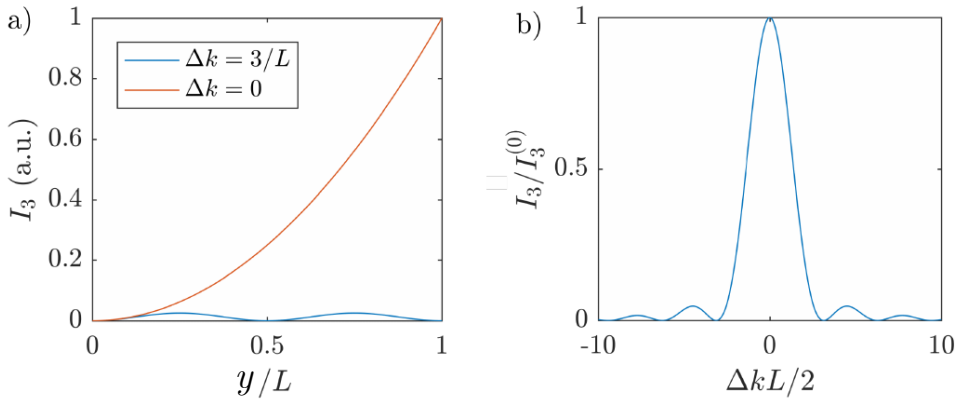

Figure 1.2: (a) SFG intensity as a function of normalized distance in the direction of propagation in the case of perfect phase-matching $\Delta k = 0$ (red curve) and in the presence of a nonzero wave-vector mismatch (blue curve). (b) SFG intensity at a given point of the nonlinear medium as a function of wave-vector mismatch Δk exhibiting characteristic squared cardinal sine dependence.

Now that we have a general expression for the nonlinear dielectric polarization, we can derive the spatial evolution of the field amplitudes as the interacting fields propagate through the optical medium. This will allow us to compute the power that is transferred from one frequency to another in the nonlinear process. For the sake of example, we

focus on SFG but the extension of this analysis to DFG and SHG is straightforward. We study the case of two pump fields at frequencies ω_1, ω_2 traveling through a homogeneous non-linear medium of length L and producing a SFG field at frequency $\omega_3 = \omega_1 + \omega_2$.

To simplify our analysis, we make a few additional assumptions. First we consider only one specific interaction where the electromagnetic plane waves at frequencies $\omega_1, \omega_2, \omega_3$ are linearly polarized. Then, we consider that the three interacting fields are propagating along a common direction y such that $\mathbf{k}_\ell = (1/c)n_\ell(\omega_\ell)\omega_\ell \mathbf{e}_y$ where $\mathbf{e}_y$ is a unit vector oriented along the y-axis and $n_\ell(\omega)$ is the index of refraction seen by mode $\ell = 1, 2, 3$. This assumption is justified in our case since the present work deals with parametric sources in waveguides where the interacting fields are guided along the same direction. Under these two assumptions, the electric fields of the three modes reduce to:

$$\mathbf{E}_\ell(\mathbf{r}, t) = \mathbf{e}_\ell E_\ell(y, t) = \mathbf{e}_\ell A_\ell(y) e^{-i(\omega_\ell t - k_\ell y)}, \quad \ell = 1, 2, 3, \tag{1.22}$$

with $\mathbf{e}_\ell$ a unit vector oriented along the direction of the electric field of mode ℓ. We see that thanks to these approximations we can again obtain scalar equations for the spatio-temporal evolution of the fields. By introducing the tensor d which, as a matter of historical conventions, is commonly encountered in the literature:

$$d_{ijk} = \frac{1}{2}\chi^{(2)}_{ijk}, \tag{1.23}$$

we get the following the expression for the nonlinear dielectric polarization associated to the SFG process:

$$P_3^{\mathrm{NL}}(\mathbf{r}, t) = \epsilon_0 d_{\mathrm{eff}} E_1(y, t) E_2(y, t), \tag{1.24}$$

where we dropped the subscript denoting the vector component from Eq. (1.19) since we are focusing on fields at fixed polarization. d_{eff} is the specific matrix element of the tensor d which couples fields with these given polarization directions. In addition, we also assume that the variation of the field amplitude in the direction of propagation is small compared to the wavelength. This is often referred to as the slowly varying envelope approximation and can be mathematically formulated as:

$$\left| \frac{\mathrm{d}A_3}{\mathrm{d}y} k_3 \right| \gg \left| \frac{\mathrm{d}^2 A_3}{\mathrm{d}y^2} \right|. \tag{1.25}$$

To finally compute the spatial evolution of the SFG field, we plug the expression for the non-linear polarization Eq. (1.24) into the inhomogeneous wave equation Eq. (1.18). With the help of Eq. (1.22) and Eq. (1.25) we obtain the following relation:

$$\frac{\mathrm{d}A_3}{\mathrm{d}y} = \frac{2id_{\mathrm{eff}}\omega_3}{n_3 c} A_1 A_2 e^{i\Delta k y}, \tag{1.26}$$

where we introduced the wavevector mismatch:

$$\Delta k = k_3 - k_2 - k_1. \tag{1.27}$$

We integrate equation Eq. (1.26) between $y = 0$ and $y = L$ by further assuming that the pump fields at ω_1, ω_2 are sufficiently intense to be treated as undepleted, meaning the portion of their electromagnetic power that will be exchanged in the frequency conversion process is small. Then their amplitudes A_1, A_2 can be treated as constant over the whole interaction region. From the obtained expression for $A_3(y)$ we evaluate the Poynting vector of the field $E_3(y, t)$ at $y = L$ and finally get the intensity of the SFG field at the output of the interaction region:

$$I_3(L) = I_3^{(0)} \mathrm{sinc}^2\left(\Delta k L/2\right). \tag{1.28}$$

The value of the maximum SFG intensity that can be generated in a propagation length L is given by the prefactor

$$I_3^{(0)} = \frac{2d_{\text{eff}}^2\omega_3^2 I_1 I_2 L^2}{n_1 n_2 n_3 \epsilon_0 c^3}. \tag{1.29}$$

In Fig. 1.2 (a), we plot the value of the intensity $I_3(L)$ as a function of the interaction length L for different values of the wave-vector mismatch. We see that this parameter is crucial for the efficiency of the frequency conversion process. Indeed, when it is exactly zero, a situation that we refer to as **phase-matching**, the intensity of the SFG field grows quadratically with the distance, eventually reaching its maximum value $I_3^{(0)}$ at $y = L$. However, for non-zero mismatch, the intensity oscillates with y which hinders the efficient generation of a field at ω_3.

We see that, in order for the conversion process to be efficient, phase-matching conditions must be fulfilled. Note that phase-matching can be thought of in terms of conservation of momentum. Indeed, a photon of wave-vector $\mathbf{k}$ carries a momentum $\hbar\mathbf{k}$ and phase-matching conditions are simply equivalent to the conservation of momentum of the interacting photons. We see that we finally have a very simple physical picture for nonlinear optical processes, which are governed by two conservation rules for energy and momentum:

$$\hbar\omega_1 + \hbar\omega_2 = \hbar\omega_3, \tag{1.30}$$

$$\hbar\mathbf{k}_1 + \hbar\mathbf{k}_2 = \hbar\mathbf{k}_3. \tag{1.31}$$

Chapter 2

Spontaneous Parametric Downconversion (SPDC)

Contents

2.1 Quantization of the electromagnetic field 31
2.2 Photons and field operators 32
2.3 Simple quantum model for SPDC 33

In this chapter, we give a mathematical description of the SPDC process and show how it can be used to generate photon pairs. We start by recalling the basics of quantum optics then we study a simple model which displays the basic physical picture behind photon pair generation through SPDC.

2.1 Quantization of the electromagnetic field

To begin with, we briefly recall the formalism of quantized modes of the electromagnetic field that will be used to write down the quantum state of light generated by SPDC. The quantization of the electromagnetic field can be formulated using Lagrangian or Hamiltonian formalism. In the latter, the basic idea is to map Maxwell's equations onto equivalent Hamilton equations of motion. By doing so, one defines a classical Hamiltonian $H(\{q_\ell\},\{p_\ell\})$ which is equal to the total energy contained in the electromagnetic field. This function depends on new physical quantities $\{q_\ell\},\{p_\ell\}$ that are the quasi position and momentum associated with the different modes ℓ of the electromagnetic field. The goal is to find a proper set of variables for which the Hamilton equations of motion hold:

$$\begin{aligned}\frac{\partial q_\ell}{\partial t} &= \frac{\partial H}{\partial p_\ell},\\ \frac{\partial p_\ell}{\partial t} &= -\frac{\partial H}{\partial q_\ell}.\end{aligned} \tag{2.1}$$

Details about the derivation of H and $\{q_\ell\},\{p_\ell\}$ can be found in most quantum optics textbooks such as Ref.[118]

To get a quantum model of the electromagnetic field we simply associate to the classical Hamiltonian H a quantum-mechanical Hamiltonian operator $\hat{H}$. This is done by defining a quantum-mechanical observable for the quasi-position and momentum of each mode. We impose that these pairs of newly defined operators $\{\hat{q}_\ell\}$ and $\{\hat{p}_\ell\}$ have to satisfy the

canonical commutation relation $[\hat{q}_\ell, \hat{p}_{\ell'}] = i\hbar\delta_{\ell\ell'}$ with $\delta_{\ell\ell'}$ the Kronecher symbol. Then the quantum Hamiltonian operator can be simply obtained by replacing the classical variables by their quantum-mechanical counterparts:

$$\hat{H} = H(\{\hat{q}_\ell\}, \{\hat{p}_\ell\}). \tag{2.2}$$

One can show that, in the case of free radiation in vacuum, the Hamiltonian of the quantized field takes the form:

$$\hat{H}_R = \sum_\ell \hbar\omega_\ell \left(\hat{a}_\ell^\dagger \hat{a}_\ell + \frac{1}{2}\right), \tag{2.3}$$

where, for each mode ℓ, we defined the ladder operators:

$$\begin{aligned} \hat{a}_\ell &= \frac{1}{\sqrt{2\hbar}} \left(\hat{q}_\ell + i\hat{p}_\ell\right), \\ \hat{a}_\ell^\dagger &= \frac{1}{\sqrt{2\hbar}} \left(\hat{q}_\ell - i\hat{p}_\ell\right). \end{aligned} \tag{2.4}$$

In this picture, all the modes ℓ of the electromagnetic field are decoupled and can be described independently by a Hamiltonian $\hat{h}_\ell = \hbar\omega_\ell \left(\hat{a}_\ell^\dagger \hat{a}_\ell + 1/2\right)$ and a pair of observables $\hat{q}_\ell, \hat{p}_\ell$.

2.2 Photons and field operators

These operators are identical to those describing a quantum harmonic oscillator having a discrete energy spectrum divided in quanta of energy $\hbar\omega_\ell$. In the case of modes of the electromagnetic field, these elementary excitations are what we call **photons**.

The non-hermitian operators $\hat{a}_\ell$ and $\hat{a}_\ell^\dagger$ are simply the operators associated to the annihilation or creation of one photon in mode ℓ. They satisfy the commutation relations

$$[\hat{a}_\ell, \hat{a}_{\ell'}] = 0, \quad \left[\hat{a}_\ell, \hat{a}_{\ell'}^\dagger\right] = \delta_{\ell\ell'}. \tag{2.5}$$

When a mode is in a state where it contains only one quantum of energy, we say that it is populated by one photon. Such a state can be mathematically written:

$$|1_\ell\rangle = \hat{a}_\ell^\dagger |\text{vac}\rangle. \tag{2.6}$$

where $|\text{vac}\rangle$ denotes the state of vacuum. It is an eigenstate of the number operator $\hat{N}_\ell = \hat{a}_\ell^\dagger \hat{a}_\ell$ with eigenvalue 1. Here the mode ℓ can label any degree of freedom of light such as spatial mode, frequency, momentum, polarization and so on.

By building on our analogy between classical fields and quantum operator, we can define an observable associated to the electric field. We adopt the Schrödinger picture, where operators are time-independent and the dynamics of the system is described by the state vector. In this framework, the electric field operator reads:

$$\hat{\mathbf{E}}(\mathbf{r}) = i\sum_\ell \mathbf{A}_\ell(\mathbf{r}) \left(e^{i\mathbf{k}_\ell\cdot\mathbf{r}}\hat{a}_\ell - e^{-i\mathbf{k}_\ell\cdot\mathbf{r}}\hat{a}_\ell^\dagger\right) = \hat{\mathbf{E}}^+(\mathbf{r}) + \hat{\mathbf{E}}^-(\mathbf{r}), \tag{2.7}$$

where the terms $\hat{\mathbf{E}}^\pm(\mathbf{r})$ containing all annihilation (resp. creation) operators are called the positive (resp. negative) frequency term. The prefactor $\mathbf{A}_\ell(\mathbf{r})$ is simply the classical field amplitude that has already been defined in Eq. (1.17). Note that, as expected, although the mathematical form is very close to a classical expression for the electric field of an

electromagnetic wave, these operators in the Schrödinger picture do not carry explicit time-dependence. In the Heisenberg picture, which is not discussed here, the operators have a time evolution which follows closely that of the classical fields.

In this dissertation, the modes of the photons will be determined by their frequency and polarization. Hence we replace the symbolic labels ℓ of the modes by two variables $\omega \in \mathbb{R}^+$ and $\mu \in \{H, V\}$ where H, V denote horizontal and vertical polarization modes. Frequency being a continuous variable, the ladder operators obey a continuous version of the commutations relations of Eq. (2.5):

$$\left[\hat{a}_\mu(\omega), \hat{a}_{\mu'}(\omega')\right] = 0, \quad \left[\hat{a}_\mu(\omega), \hat{a}^\dagger_{\mu'}(\omega')\right] = \delta_{\mu\mu'}\delta(\omega - \omega'), \tag{2.8}$$

with $\delta(\omega - \omega')$ the Dirac distribution. Consequently, the hamiltonian for free radiation in this notation can be written:

$$\hat{H}_R = \sum_\mu \iint \mathrm{d}\omega \left[\hat{a}^\dagger_\mu(\omega)\hat{a}_\mu(\omega) + \frac{1}{2}\right], \tag{2.9}$$

and the electric field operator is:

$$\hat{\mathbf{E}}(\mathbf{r}) = i\sum_\mu \iint \mathrm{d}\omega \mathbf{A}_{\mu,\omega}(\mathbf{r}) \left(e^{i\mathbf{k}_\mu(\omega)\cdot\mathbf{r}}\hat{a}_\mu(\omega) - e^{-i\mathbf{k}_\mu(\omega)\cdot\mathbf{r}}\hat{a}^\dagger_\mu(\omega)\right) = \hat{\mathbf{E}}^+(\mathbf{r}) + \hat{\mathbf{E}}^-(\mathbf{r}) \tag{2.10}$$

2.3 Simple quantum model for SPDC

This mathematical expression for the field operators will be very useful later on to derive the exact mathematical form of the quantum state emitted by our source. For now, we only give a physical picture behind the quantum treatment of SPDC using a simple model for the nonlinear interactions following the derivation in Ref. [119].

To this end, we need to add to the Hamiltonian for free radiation a term $\hat{H}_I$ which describes the interaction between the fields:

$$\hat{H} = \hat{H}_R + \hat{H}_I. \tag{2.11}$$

SPDC being a weak nonlinear process, the bright pump field at frequency ω_3 can again be considered undepleted. Therefore, we treat it as a classical field which will not be described by quantum-mechanical operators but will rather play the role of a constant parameter of the model. We write down a toy-model Hamiltonian that describes second order nonlinear processes:

$$\hat{H}_I = i\hbar\chi\hat{a}^\dagger(\omega_1)\hat{a}^\dagger(\omega_2) + \text{H.c.}, \tag{2.12}$$

with χ a parameter proportional to the amplitude of the pump field and ω_1, ω_2 the signal and idler frequencies.

We start at $t = 0$ from the vacuum state $|\Psi(0)\rangle = |\text{vac}\rangle$ and derive the time-evolution of the state vector. We do this in the framework of the interaction picture which is particularly well-suited for these kind of problems [120]. Indeed, this formalism allows to decouple the dynamics of the interaction term and of the free radiation term. The time evolution of the observables will be dictated by the term $\hat{H}_R$ while the state vector will evolve under the effect of $\hat{H}_I$. Hence, in this picture, the time evolution of the quantum state is governed by the following evolution operator:

$$\hat{U}(t) = \exp\Big(-i\hat{H}_I t/hbar\Big) = \exp\left(\eta\hat{a}^\dagger(\omega_1)\hat{a}^\dagger(\omega_2) - \text{H.c.}\right), \tag{2.13}$$

with $\eta = \chi t$. After the three fields have interacted for a time t, the state of the electromagnetic field becomes

$$|\Psi(t)\rangle = \hat{U}(t)\,|\Psi(0)\rangle\,. \tag{2.14}$$

We expand the exponential term as a power series and only retain the terms up to second order, an approximation which is reasonable in the low pump power regime $\eta \ll 1$. This is indeed the situation we would like to describe as it is the regime in which SPDC can produce pairs of single photons. The state of the system at time t is given by:

$$\begin{aligned} |\Psi(t)\rangle &\approx \Big[1 + (\eta \hat{a}^\dagger(\omega_1)\hat{a}^\dagger(\omega_2) - \text{H.c.}) + ...\Big]\,|\text{vac}\rangle \\ &= |\text{vac}\rangle + \eta \hat{a}^\dagger(\omega_1)\hat{a}^\dagger(\omega_2)\,|\text{vac}\rangle + ... \end{aligned} \tag{2.15}$$

The first term in the expansion is the vacuum contribution. The second term represents the creation of a photon pair. Higher order terms in the series expansion would model multi-pair emission that can arise at high pump powers. Those higher order terms enter in the description of squeezed states, which can be observed when the SPDC source is operated at high pump power.

By only post-selecting the second term, we successfully obtain a genuine two-photon state:

$$|\Psi\rangle_{\text{two-photon}} = \hat{a}^\dagger(\omega_1)\hat{a}^\dagger(\omega_2)\,|\text{vac}\rangle\,. \tag{2.16}$$

We see that if we only consider an interaction involving two modes of the electromagnetic field $\ell = 1, 2$, as it is the case here, we obtain a quantum state that is separable. Indeed, it can be rewritten as the tensor product of states of the two modes $(\hat{a}^\dagger(\omega_1)\,|\text{vac}\rangle) \otimes (\hat{a}^\dagger(\omega_2)\,|\text{vac}\rangle)$.

Non-separable states can also be generated by SPDC provided photons can be emitted in more than two modes. For instance, we study the case where the generated photons, just like previously, can have different frequencies ω_1 or ω_2 but can also be emitted in two distinct modes μ, ν of the electromagnetic field. These modes could be for example spatial modes, orbital angular momentum or, such as in the work described in this manuscript, polarization. We end up with a total of four modes $\{\omega_2, \mu\}, \{\omega_3, \mu\}, \{\omega_2, \nu\}, \{\omega_3, \nu\}$. We adapt the interaction Hamiltonian of Eq. (2.12) to this four-mode case and assume it takes the following form :

$$\hat{H}_I = i\hbar\chi_1 \hat{a}^\dagger_\mu(\omega_1)\hat{a}^\dagger_\nu(\omega_2) + i\hbar\chi_2 \hat{a}^\dagger_\nu(\omega_1)\hat{a}^\dagger_\mu(\omega_2) - \text{H.c.} \tag{2.17}$$

After the interaction, the state of the electromagnetic field features a two-photon term of the form:

$$|\Psi\rangle_{\text{two-photon}} = \Big(\eta_1 \hat{a}^\dagger_\mu(\omega_1)\hat{a}^\dagger_\nu(\omega_2) + \eta_2 \hat{a}^\dagger_\nu(\omega_1)\hat{a}^\dagger_\mu(\omega_2)\Big)\,|\text{vac}\rangle\,. \tag{2.18}$$

We see that this state is indeed non-separable as it cannot be factored into a tensor product of the state of two independent modes of the electromagnetic field. This kind of state is referred to as an **entangled state**, which will be the topic of the next section.

Chapter 3

Quantum Entanglement

Contents

3.1 From first debates to applications 35
3.2 Formal definition and measures of entanglement 36
3.3 Entanglement and local realism, Bell's inequalities 37
3.4 Polarization entanglement 39
3.5 Energy-time entanglement 40
3.6 Frequency-bin entanglement 42

In this chapter, we cover the basic formalism and physical intuition behind quantum entanglement. After a brief historical outlook of this concept, we give a few definitions relating to entanglement and its characterization. Then we explain the link between entanglement and local realism before describing in detail entanglement in the degrees of freedom that are going to be encountered in this manuscript namely polarization and energy-time.

3.1 From first debates to applications

Entangled states are one of the most singular feature of quantum mechanics. This type of system was studied since the early days of quantum theory in famous thought experiments which predicted astonishing counter-intuitive phenomena. In their key 1935 paper, Einstein, Podolsky and Rosen shed light on an apparent paradox in the prediction of quantum mechanics [121]. They study the case of two particles that have interacted and which end up in a non-separable state. The main conclusion of this pioneer work is that if quantum mechanics is correct then the measurement of this entangled states can only be interpreted in terms of nonlocal phenomena, or "Spooky action at distance" as they were later coined by Einstein. Essentially, measuring the state of one particle would instantaneously project the other particle in a well-defined state, a phenomenon that cannot be explained by local physical variables.

Although they have been the source of great debate in the community, these ideas remained in the realm of theoretical speculation for several decades. It was not until the 1960's that proposals were made to solve this paradox experimentally. In his pioneering work, Irish theoretical physicist John Bell provided the first quantitative experimental criterion that could be used to lift the uncertainty on the nonlocal nature of quantum mechanics [122]. This result, often referred to as Bell's theorem or Bell's inequalities, opened the way to the seminal experiments of the 70's and 80's aiming at testing quantum

nonlocality in the laboratory. The work on experimental violation of Bell's inequalities of Freedman an Clauser in 1972 then Aspect, Grangier and Roger in 1981-1982 confirmed experimentally the non-local character of quantum mechanics [123, 23, 24]. Since then, increasingly refined experiments have been carried out in order to test quantum mechanics against experimental loopholes that could hinder the unambiguous evidence of true physical non-locality. Very recently, as stated in the introduction of this dissertation, most crucial loopholes were closed and non-locality is now widely accepted as experimentally sound [5].

In addition to being an intense research topic in itself, entanglement is a major resource in the field of quantum information. It is at the root of many quantum communication protocols such as entanglement-based quantum key distribution [27] or quantum teleportation [32]. Entanglement is also at the core of quantum computing since the universal set of gates needed to perform a computation on a quantum computer includes the CNOT gate which creates entanglement between two qubits. Therefore, to perform quantum algorithms, quantum computers rely on massively entangled states of their multi-qubit register.

3.2 Formal definition and measures of entanglement

In our analysis, we only consider the case of bipartite entanglement meaning entanglement between two subsystems. Let $\mathcal{H}$ be a Hilbert space and $|\Psi\rangle$ the state vector of the system we want to describe. We assume this system is in a pure state and can be divided into two subsystems A and B. Mathematically, it means that $\mathcal{H} = \mathcal{H}_A \otimes \mathcal{H}_B$ where $\mathcal{H}_A, \mathcal{H}_B$ are the Hilbert space for the individual subsystems. The state of the system is said to be entangled if it cannot be written in a separable form:

$$|\Psi\rangle = |\phi\rangle_A \otimes |\xi\rangle_B \tag{3.1}$$

with $|\phi\rangle_A \in \mathcal{H}_A$ and $|\xi\rangle_B \in \mathcal{H}_B$.

Several degrees of freedom of single photons can carry entanglement : discrete variables that take integer values such as polarization [95], time-bin [98] or orbital angular momentum [124], or variables that have a continuous spectrum, such as momentum or energy-time [34, 59] [1].

All entangled state do not carry the same level of entanglement. There are several indicators, called entanglement monotones, which can be used to quantify the amount of entanglement in a quantum system.

Entanglement entropy This is one of the fundamental way of quantifying entanglement and has a natural interpretation in analogy with classical information theory [125]. For a quantum state described by the density matrix ρ, the Von Neumann entropy is given by:

$$\mathcal{S}(\rho) = -\operatorname{tr}(\rho \ln_2 \rho). \tag{3.2}$$

We see that it has an analogous form to the classical information entropy which quantifies the degree of uncertainty of a random variable. When applied to a quantum system, $\mathcal{S}$ quantifies the mixedness of the state, with a maximum value of $\mathcal{S} = \ln 2$ for a totally mixed state and $\mathcal{S} = 0$ for a pure state. In the case of a bipartite state,

[1] Note that, in this work, we are not dealing with what is commonly called "continuous variables" in the the quantum information literature, the latter referring to the the state of the quadratures of a many-photon field.

the Von Neumann entropy has to be computed over the reduced density matrix of of one of the subsystems:

$$\rho_{A(B)} = \mathrm{tr}_{B(A)}(\rho), \tag{3.3}$$

where $\mathrm{tr}_{A(B)}$ denotes the partial trace over the state of subsystem $A(B)$. The so-called entanglement entropy of the two-particle state is then defined as:

$$\mathcal{S} = \mathcal{S}(\rho_A) = \mathcal{S}(\rho_B). \tag{3.4}$$

In an entangled state, there are strong correlations between the states of the two individual particles. Hence tracing out the state of particle A will add some uncertainty about the state of particle B. When the entanglement between the particles is maximum, the state of particle B will be left in a fully mixed state and we get a maximum entanglement entropy of $\mathcal{S} = \ln 2$. On the contrary, if the two-particle system is in a separable state, then ignoring the state of particle A will leave no uncertainty on the state of particle B which will remain in a pure state and hence the entropy is minimum $\mathcal{S} = 0$. As a consequence, a bipartite state is said to be **maximally entangled** when its density matrix saturates the entanglement entropy.

Fidelity to a maximally entangled state Another way to quantify the entanglement of a given state ρ is to calculate its distance to a maximally entangled state σ. In this work, we use the fidelity, which is defined as:

$$F = \left(\mathrm{tr}\sqrt{\sqrt{\rho}\sigma\sqrt{\rho}}\right)^2, \tag{3.5}$$

and which will be equal to 1 when the two states are identical and to 0 if they are orthogonal.

Concurrence and tangle Several other measures of entanglement are commonly used in the literature, such as the concurrence C or tangle $T = C^2$ [126]. Unlike the fidelity, these quantities are independent of a target state and can be computed directly from the density matrix. Hence, just like the entanglement entropy, they reflect the intrinsic entanglement contained in the quantum state.

3.3 Entanglement and local realism, Bell's inequalities

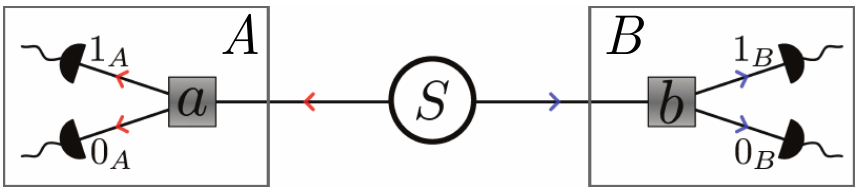

Figure 3.1: Sketch of a Bell-type experiment. A source $\mathcal{S}$ emits pairs of correlated particles that are sent to two parties A and B. The particles enter measurement devices controlled by A and B producing binary outcomes 0 or 1.

The connection between entanglement and nonlocality can be understood from the simple thought experiment sketched in Fig. 3.1. Suppose two parties A and B receive pairs of particles emitted simultaneously by a source $\mathcal{S}$ in an entangled state of the form:

$$|\Psi\rangle = \frac{1}{\sqrt{2}}\left(|0\rangle_A |1\rangle_B + |1\rangle_A |0\rangle_B\right). \tag{3.6}$$

Here we suppose that the Hilbert spaces of the two subsystems $\mathcal{H}_A = \mathcal{H}_B = \mathbb{C}^2$ are of dimension 2 and that the kets $\{|0\rangle, |1\rangle\}$ form an orthogonal basis of these two spaces. Those kets typically describe the orthogonal values that can be taken by the spin of a massive particle or the polarization of a photon. If A measures the state of its photon and finds a result $|0\rangle_A$, then this instantaneously projects the state of the photon received by B onto $|1\rangle_B$ and vice versa. It seems as if the measurement of one party had instantaneous action at distance on the other subsystem.

To verify that this is a genuine non-local effect, A and B need to carry out a violation of Bell's inequalities, also called Bell test. To do so, the two parties A and B are equipped with a measurement apparatus that is used to perform a projection of the state of their particle. For now, we do not assume anything about the nature of the apparatus itself and treat it a a black box. We simply postulate that when a particle enters the device, the latter records a binary outcome 0 or 1 that will depend on the setting a, b, which can be tuned by the user. By repeating the experiment many times for a given setting a, b the parties can measure an estimate of a correlation function of the form:

$$E(a,b) = P(1,1|a,b) + P(0,0|a,b) - P(0,1|a,b) - P(1,0|a,b), \tag{3.7}$$

where $P(i,j|a,b)$ is the probability of obtaining an outcome $i,j \in \{0,1\}$ given the measurement devices were set to a, b. In his derivation [122], Bell considered the case of local hidden variable models. In this kind of physical theory, all phenomena can be explained by variables that are local in the sense that they take a definite value for any point in space-time. Bell's theorem implies that, under this assumption, for any set of measurement settings a, b, a', b', the following inequality holds:

$$S = |E(a,b) - E(a,b') + E(a',b) + E(a',b')| \leq 2. \tag{3.8}$$

This equation is the Clauser-Horne-Shimony-Holt (CHSH) formulation of Bell's theorem [127]. It is equivalent to the original equality that was derived by Bell, and is today the most commonly used criterion for experimental proofs of non-locality.

Now we show that in the case of a entangled state this inequality can be violated, hence proving the non-local character of quantum mechanics. We suppose that the measurement apparatus simply measures a projection of the input state onto a target state $|\theta\rangle = \cos\theta\,|0\rangle + \sin\theta\,|1\rangle$ where the parameter θ can be chosen at will. In the case of photons emitted in a polarization-entangled state, this projection is achieved with a polarizer set at angle θ and a single-photon detector. Using simple algebra, one can show that for the entangled state given in Eq. (3.6) the conditional probabilities appearing in Eq. (3.7) become:

$$P(i,i|a,b) = \frac{1}{2}\cos^2\left(\frac{\theta_a - \theta_b}{2}\right), \quad i = 0,1, \tag{3.9}$$

$$P(i,j|a,b) = \frac{1}{2}\sin^2\left(\frac{\theta_a - \theta_b}{2}\right), \quad i \neq j. \tag{3.10}$$

$$\tag{3.11}$$

By carefully choosing the settings $\theta_a, \theta_b, \theta_{a'}, \theta_{b'}$ it is possible to make the quantity S in Eq. (3.8) larger that 2. Maximum violation of the CHSH inequality is obtained with $\theta_a = 0, \theta_b = \pi/2, \theta_{a'} = \pi/4, \theta_{b'} = -\pi/4$ for which quantum mechanics predicts:

$$S = 2\sqrt{2}. \tag{3.12}$$

As we can observe, by measuring experimentally the value of S with sufficient statistical significance, one can unambiguously show that the measurement of an entangled state features non-local correlations.

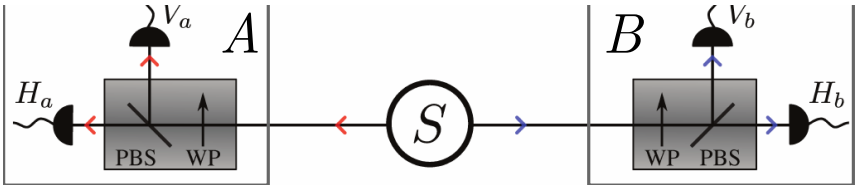

Figure 3.2: Sketch of an experiment for the measurement of polarization-entanglement. S: source of photon pairs. WP: $\lambda/2$ and $\lambda/4$ waveplates. PBS: polarizing beam splitter.

3.4 Polarization entanglement

The first experiments on violation of Bell's inequalities were performed on polarization-entangled photon pairs and polarization-entanglement is still widely used nowadays in many quantum optics and quantum communication experiments. We also point out that the AlGaAs photon pair source described in this manuscript is designed to emit polarization-entangled states as will be shown in Section 5.4. Here, we give a mathematical description of two-photon polarization-entangled states which can be straightforwardly transposed to the other discrete degrees of freedom of light, such as spatial modes or time-bin.

Like in the previous example, polarization states of the quantized electromagnetic field belong to a Hilbert space $\mathcal{H}_A = \mathcal{H}_B = \mathbb{C}^2$ of dimension 2. As a convention, we label $|H\rangle, |V\rangle$ the basis vectors corresponding to a photon being in a horizontally or vertically polarized state. Polarization is widely used in quantum information because it provides a natural implementation of quantum bits, or qubits, quantum systems of dimension 2 which are the quantum analogs to classical bits. In its most general form, the polarization state of a single photon can be written:

$$|\phi\rangle = \alpha\,|H\rangle + e^{i\varphi}\beta\,|V\rangle \tag{3.13}$$

where $|H\rangle = \hat{a}_H^\dagger\,|\text{vac}\rangle$, $|V\rangle = \hat{a}_V^\dagger\,|\text{vac}\rangle$ and α, β, φ are real coefficients satisfying $\alpha^2+\beta^2 = 1$. With this formulation, the quantum state of a polarization qubit can be seen as an analog of the Jones vector for the polarization of classical electromagnetic fields. Hence the states $|D\rangle, |A\rangle, |L\rangle, |R\rangle$ corresponding respectively to ± 45 deg linear and left/right-handed circular polarization states can be defined in a similar way:

$$\begin{aligned} |D\rangle &= \frac{1}{\sqrt{2}}\left(|H\rangle + |V\rangle\right), \;\; |L\rangle = \frac{1}{\sqrt{2}}\left(|H\rangle + i\,|V\rangle\right), \\ |A\rangle &= \frac{1}{\sqrt{2}}\left(|H\rangle - |V\rangle\right), \;\; |R\rangle = \frac{1}{\sqrt{2}}\left(|H\rangle - i\,|V\rangle\right), \end{aligned} \tag{3.14}$$

In the case of a pair of photons, the polarization state of the system $|\Psi\rangle \in \mathcal{H}_A \otimes \mathcal{H}_B$ can be written:

$$|\Psi\rangle = c_1\,|H\rangle_A\,|H\rangle_B + c_2\,|H\rangle_A\,|V\rangle_B + c_3\,|V\rangle_A\,|H\rangle_B + c_4\,|V\rangle_A\,|V\rangle_B \tag{3.15}$$

with $\{c_i\}_{i=1,\ldots,4}$ a set of complex coefficients normalized to 1. The tensor product symbol has been omitted for lighter notations. We stress that, of course, this state is generally not separable as in Eq. (3.1).

An example of non-separable two-photon states that is of particular interest for quan-

tum information is the set of so-called Bell states:

$$\begin{aligned} \left|\Psi^{\pm}\right\rangle &= \frac{1}{\sqrt{2}}\left(\left|H\right\rangle_A \left|V\right\rangle_B \pm \left|V\right\rangle_A \left|H\right\rangle_B\right), \\ \left|\Phi^{\pm}\right\rangle &= \frac{1}{\sqrt{2}}\left(\left|H\right\rangle_A \left|H\right\rangle_B \pm \left|V\right\rangle_A \left|V\right\rangle_B\right). \end{aligned} \tag{3.16}$$

They are a set of four orthogonal maximally entangled states forming a basis for the 4-dimensional Hilbert space of the two-photon polarization states.

A typical setup for measuring polarization-entangled pairs is displayed in Fig. 3.2. A source emits pairs of polarization-entangled photons which are traveling towards polarization analysis modules, composed of waveplates ($\lambda/2$ and $\lambda/4$) and a polarizing beam splitter (PBS), followed by single photon detectors. The waveplates and PBS are used to project the state of the photons on the different basis states listed in Eq. (3.14). This can be used to perform a Bell inequality violation or a tomography of the quantum state [128]. The latter permits the experimental reconstruction of the full density matrix of the two-photon state which can be used to compute all the properties of the system, including the measures of entanglement described in the previous sections.

3.5 Energy-time entanglement

Energy-time entanglement is a characteristic feature of parametric sources of photon pairs. It stems from the correlations that exist in the frequencies ω_1, ω_2 and arrival times at a detector t_1, t_2 of the two photons of the pair. As will be shown in a later chapter (Section 5.1), the quantum state of light generated by a SPDC source can be written:

$$\left|\Psi\right\rangle = \iint \mathrm{d}\omega_1\omega_2 \mathcal{C}(\omega_1,\omega_2)\hat{a}^\dagger(\omega_1)\hat{a}^\dagger(\omega_2)\left|\mathrm{vac}\right\rangle, \tag{3.17}$$

with $\hat{a}^\dagger(\omega)$ the operator associated to the creation of a photon at frequency ω and $\mathcal{C}(\omega_1,\omega_2)$ a complex function called the Joint Spectral Amplitude (JSA) that is determined by energy conservation and phase-matching conditions in the SPDC source. We see that the state in Eq. (3.17) is separable when the JSA can be written in a factored form $\mathrm{JSA}(\omega_1,\omega_2) = \phi(\omega_1)\xi(\omega_2)$ with $\phi(\omega), \xi(\omega)$ two complex functions. It can be shown that for a separable state the following inequality holds [129]:

$$\Delta(\omega_1+\omega_2)\Delta(t_1-t_2) \geq 1, \tag{3.18}$$

However, in SPDC sources pumped by a narrowband laser, such as in this thesis, the quantum state presents strong frequency anti-correlations arising from energy conservation $\omega_1+\omega_2=\omega_p$. As a consequence, in this configuration, we can have simultaneously a very small uncertainty on both $\omega_1+\omega_2$ and t_1-t_2 and a violation of Eq. (3.18) can be measured. This violation reveals that the two photons are in a so-called energy-time entangled state.

In practice, the accurate measurement of t_1-t_2 requires advanced ultrafast detection schemes since most commercially available single photon detectors and coincidence electronics have a timing jitter much larger than the typical spread of t_1-t_2. As a consequence, the direct measurement of energy-time entanglement through Eq. (3.18) remained out of reach experimentally until the work presented in Ref. [129]. In all previous experiments, energy-time entanglement is demonstrated indirectly using an interferometric setup referred to as a Franson scheme, allowing for the violation of a Bell-type inequality for time and frequency [33, 130, 34]. The experimental setup is sketched in Fig. 3.3 (a). A source $\mathcal{S}$

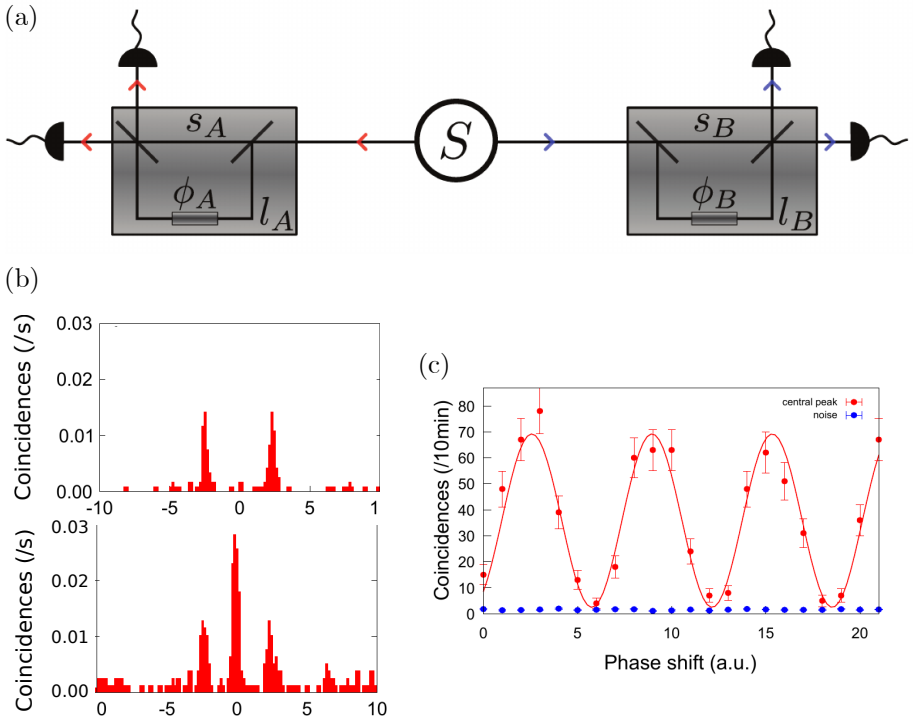

Figure 3.3: Measurement of energy-time entanglement using a Franson scheme. (a) Sketch of the experiment, see text for details. (b) Measured time-correlation histograms featuring three peaks corresponding to the different trajectories of the two photons inside the interferometers. (c) Total number of counts in the central peak as function of applied delay showing interference fringes that are characteristic of energy-time entanglement. Data from Ref. [78].

emits energy-time entangled photons that are directed to two unbalanced interferometers A and B each one consisting of two 50/50 beam splitters separated by a long arm l and a short arm s. A tunable delay line is introduced in the long arm of each interferometer inducing a phase shift of ϕ_A and ϕ_B respectively for A and B. When traveling through these interferometers, the photons can take either the long path l or the short path s before being detected with single photon detectors. This setup leads to three possible combinations of arrival times for the photons depending on which path has been taken : sl, ls and ss/ll. This can be seen from the time-correlations histograms in Fig. 3.3 (b) which features three peaks corresponding to those three possibilities. By measuring the pairs detected in the central peak, the following state is post-selected:

$$|\Psi\rangle = |s\rangle_A |s\rangle_B + e^{i\phi} |l\rangle_A |l\rangle_B \tag{3.19}$$

where the relative phase difference between the two interferometers is $\phi = \phi_A - \phi_B$ and the kets $|s\rangle, |l\rangle$ denote the state of a photon which has traveled through the short or long path respectively. When recording the number of coincidence counts as a function of ϕ, interference fringes are observed, as shown in Fig. 3.3 (c). Experimentally, this effect can only be observed if the temporal delay τ introduced by the unbalanced interferometers is much larger than the photon coherence time to ensure that we do not measure a single photon interference. In addition, τ also has to be smaller than the pump coherence time otherwise the phase coherence between the two temporal bins s, l will be lost and no interference can be seen. It can be shown that the visibility of the interference fringes in a Franson experiment performed with a separable state cannot exceed 50 % [130]. As a consequence, the measurement of a visibility exceeding this bound, such as in the data presented in Fig. 3.3, is sufficient to certify energy-time entanglement.

3.6 Frequency-bin entanglement

As stated in the introduction of the manuscript, frequency can also be used as a degree of freedom for the implementation of quantum information tasks. Frequency entanglement arises naturally in the quantum state of a SPDC source pumped by a narrowband laser. Indeed, in this regime, as will be shown in Section 5.4, the state in Eq. (3.17) is not separable and can be written as a frequency-entangled state:

$$|\Psi\rangle = \int_{-\infty}^{+\infty} \mathrm{d}\Omega \Phi(\Omega) \hat{a}^\dagger(\omega_p/2 + \Omega) \hat{a}^\dagger(\omega_p/2 - \Omega) |\mathrm{vac}\rangle , \tag{3.20}$$

where $\Phi(\Omega)$ is the complex-valued JSA defined by the phase-matching conditions and Ω the detuning to the biphoton degeneracy frequency $\omega_p/2$. Frequency can be converted into a discrete variable by carving spectral bins within the spectrum of the downconverted photons using filters, an approach that was pioneered by Olislager and coworkers [105]. The state of frequency-bin qubits can be manipulated using standard telecommunication components such as electro-optic modulators and pulse shapers [106]. Frequency-bin entanglement has been demonstrated using a scheme equivalent to a Franson-type experiment where the time-shifts performed by unbalanced interferometers are replaced by frequency-shifts induced by electro-optic modulators. This configuration was employed to study nonlocal effects manifested through the violation of a Bell type inequality for frequency [105, 131] or to perform quantum state tomography of frequency-bin entangled photons [59]. The main advantages of this degree of freedom are its robustness to noise, its intrinsic stability ruling out the need for interferometric stabilization and its compatibility with standard off-the-shelf telecommunication components. As a consequence,

frequency-bin encoding has been used in entanglement-based quantum key distribution protocols [132] as well as for the realization of gates for frequency-based quantum computing [133].

Frequency-bin encoding lends itself to a natural extension to high-dimensionality. Indeed, by embedding the SPDC source within an optical cavity, one can generate high-dimensional frequency-entangled photon pairs, as demonstrated in Refs. [134, 59, 87]. In this configuration, the photon pairs can only be emitted in the cavity modes which define a discrete frequency spectrum consisting of resonances separated by the free-spectral range of the cavity. The generated quantum state can be written approximately as:

$$|\Psi\rangle = \sum_{k=1}^{d} a_k \left|-k\right\rangle_s \left|k\right\rangle_i \tag{3.21}$$

where a_k is a complex coefficients and $|k\rangle = \hat{a}^\dagger(\omega_p/2 + k\bar{\omega})\,|\text{vac}\rangle$ with $\bar{\omega}$ the cavity free spectral range. The integer d represents the number of cavity resonances spanning the biphoton bandwidth of the emitted state. This type of state is often referred to in the literature as a biphoton frequency comb (BFC) or an entangled frequency qudit state. As already mentioned, the different frequency bins of this high-dimensional entangled state can be addressed using electro-optic modulators and pulse shapers [134, 59]. Frequency qudits are at the core of experimental demonstrations of high-dimensional optical quantum logic [135] or two-photon measurement-based quantum computing [114].

Part II

AlGaAs photon-pair source: design, fabrication and characterization

Chapter 4

Non-linear optics in AlGaAs waveguides

Contents

4.1 Optical waveguides for nonlinear optics 47
4.2 AlGaAs Waveguide design 50
4.3 Cleanroom fabrication 56
4.4 Measurement of the optical losses of the guided modes 60
4.5 Characterization of the frequency conversion by Second Harmonic Generation 61

In this chapter, we describe the mechanisms of third-order nonlinear optical processes in AlGaAs waveguides. We introduce optical waveguides and show how they can be used in the context of frequency conversion. Then we detail the phase-matching strategy that is adopted in the devices described in this manuscript before covering the fabrication process of the nonlinear waveguides. We finally present the experimental characterization of losses and second order nonlinear frequency conversion in the fabricated devices.

4.1 Optical waveguides for nonlinear optics

4.1.1 Guided modes and effective mode index

Integrated photonics relies on the capability of light to be confined inside optical waveguides. Waveguides are structures made of a core of high refractive index n_{core} surrounded by a cladding of lower refractive index n_{clad}. Consequently, there exists stationary solutions to the wave equation for which the intensity of the wave is concentrated inside the high-refractive index region. This can be seen as the total internal reflection of light at the interface between core and cladding, such as in optical fibers. According to the material that is used and to the specific application, several geometries can be adopted, as sketched in Fig. 4.1. For instance, buried channel waveguides can be encountered in the SOI platform as well as in III-V materials or femtosecond laser writing in borosilicate glasses. In rib and ridge waveguides, which are also frequently used in III-V materials, the optical confinement is provided by the refractive index contrast between the core and both the air and the substrate.

Guided modes propagate along the structure at a phase velocity that is different from the velocity of light in the bulk material of the core. Indeed, these modes will have an

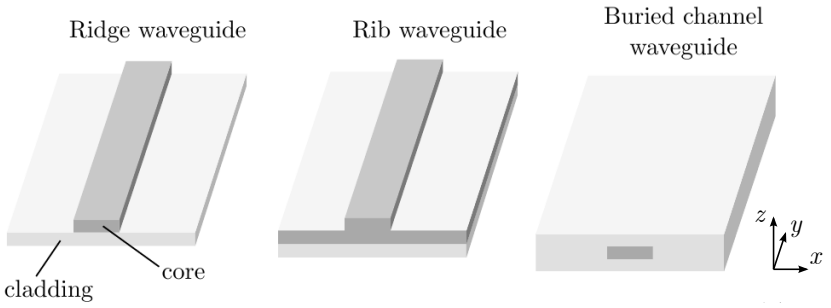

Figure 4.1: Example of the most commonly used waveguide geometries in integrated photonics. The dark grey regions indicate high-refractive index material. The axes are labeled following the orientation of the electric field for TE and TM modes of the structures.

effective refractive index n_{eff}, also called effective mode index, that is determined by the geometry of the waveguide and the optical properties of the constituting materials. The dispersion of these effective mode indices play a crucial role for achieving phase-matching conditions in a waveguide, as will be shown later.

If we assume that the waveguide structure is invariant along the y direction, as depicted in Fig. 4.1, then the electric field of a wave of frequency ω propagating in a guided mode takes the form:

$$\mathbf{E}(\mathbf{r}, t) = \mathbf{e}A(x, z)e^{-i(\omega t - ky)}, \tag{4.1}$$

where $A(x, z)$ is the spatial amplitude profile of the mode, $\mathbf{e}$ is the unit vector defining the polarization of the mode, and

$$k = \frac{\omega}{c} n_{\text{eff}} \tag{4.2}$$

is the effective wavenumber. Assuming there are no source of currents or charge in the waveguide region, an expression for $A(x, z)$ and n_{eff} can be obtained by solving the wave equation:

$$\left[\frac{\partial^2}{\partial x^2} + \frac{\partial^2}{\partial x^2}\right] A(x, z) + \left[\frac{\omega}{c} n(x, z) - k\right] A(x, z) = 0, \tag{4.3}$$

with $n(x, z)$ the refractive index profile of the waveguide cross-section. This expression is analogous to the Schrödinger equation for a particle in a two-dimensional square potential, which admits an integer number of eigenfunctions of quantized energy. Likewise here the waveguide structure will support discrete guided modes characterized by their spatial profile and mode index. The equation needs to be solved in the different regions of the waveguides then the solutions are matched at the interfaces. More details on the solutions of Eq. (4.3) can be found in [136].

Depending whether the factor $(\omega/c)n - k$ in Eq. (4.3) has a positive or negative sign respectively, the field of the wave will vary sinusoidally or exponentially. In a guided mode, the amplitude decreases exponentially in the cladding and reaches a maximum in the core. This is verified provided the effective wavenumber of the mode satisfies the inequality [136]:

$$\frac{\omega}{c} n_{\text{clad}} < k < \frac{\omega}{c} n_{\text{core}}. \tag{4.4}$$

The solutions to the wave equation corresponding to guided modes can be divided into transverse electric (**TE**) and transverse magnetic (**TM**). In a TE mode, the electric field is perpendicular to the yz plane and only the components E_x, H_z, H_y of the electromagnetic field are nonzero. The TM modes have their electric field perpendicular to the xy plane with nonzero components H_x, E_z, E_y.

In practice, analytical solutions to Eq. (4.3) can be found only in simple geometries. In this work, we calculated numerically the guided modes profiles and effective indices of our waveguides using commercial electromagnetic simulation software suites, such as COMSOL or Lumerical, which rely on finite element methods.

4.1.2 Conversion efficiency

Waveguides are widely used in nonlinear optics. Frequency conversion in a waveguide benefits from the fact that all fields are colinear, making light injection and collection easier by avoiding walk-off effects that affect nonliner conversion in bulk crystals. For example, nonlinear waveguides can be fiber-pigtailed removing any need for optical alignment. In addition to this, the nonlinear interaction can be made more efficient thanks to the tight confinement of the fields inside the structure.

The efficiency of frequency conversion in a waveguide depends strongly on the properties of the guided modes. By taking once again the example of SFG: $\omega_1 + \omega_2 \rightarrow \omega_3$, we define the time-averaged optical power of the generated sum-frequency field as

$$\mathcal{P}_3 = \iint_{\mathcal{A}} \mathrm{d}x\mathrm{d}z I_3, \tag{4.5}$$

where the integral is taken over the area $\mathcal{A}$ of the waveguide cross-section. With the help of Eq. (1.28) and Eq. (1.29) we obtain:

$$\mathcal{P}_3 = \frac{2\omega_3^2 L^2}{n_1 n_2 n_3 \epsilon_0 c^3} |\Gamma|^2 \mathcal{P}_1 \mathcal{P}_2 \mathrm{sinc}^2(\Delta k L/2). \tag{4.6}$$

The nonlinear overlap Γ is defined as:

$$\Gamma = \iint_{\mathcal{A}} \mathrm{d}x\mathrm{d}z d_{\mathrm{eff}}(x,z) \tilde{A}_1(x,z) \tilde{A}_2(x,z) \tilde{A}_3(x,z), \tag{4.7}$$

where the tilde denotes the normalized field amplitudes $\iint_{\mathcal{A}} \mathrm{d}x\mathrm{d}z |\tilde{A}_i(x,z)|^2 = 1$. We finally obtain the conversion efficiency as the ratio:

$$\eta_{\mathrm{SFG}} = \frac{\mathcal{P}_3}{\mathcal{P}_1 \mathcal{P}_2} = \frac{2\omega_3^2 L^2}{n_1 n_2 n_3 \epsilon_0 c^3} |\Gamma|^2 \mathrm{sinc}^2(\Delta k L/2). \tag{4.8}$$

This equations indicates the parameters that have to be optimized when designing a waveguide for nonlinear optics:

- The nonlinear overlap Γ, which is controlled by the nonlinear properties of the materials that are used and the geometry of the waveguide cross-section.
- The wave-vector mismatch Δk which needs to be made the closest possible to zero (phase-matching). This is done through the engineering of the dispersion of the guided modes.
- The length L of the waveguide. According to Eq. (4.8), in a lossless medium the efficiency increases monotonically with L. However, when taking into account the inevitable optical losses of the material, there is a trade-off between conversion efficiency and loss which dictates the optimal waveguide length.

In addition, it can be shown that, in a semi-classical approximation, since SFG and SPDC are reverse processes, the SPDC conversion efficiency, defined as the number of generated pairs per pump photon, is proportional to the SFG efficiency [137]:

$$\eta_{\mathrm{SPDC}} = \eta_{\mathrm{SFG}} \frac{\hbar\omega_1\omega_2}{\omega_3} \frac{\Delta\omega}{2\pi}, \tag{4.9}$$

where ω_3 is the frequency of the pump field, ω_1, ω_2 the frequencies of the signal and idler photons and $\Delta\omega$ the spectral bandwidth of the emitted state, which can be derived from the phase-matching conditions.

4.1.3 Phase-matching

In a waveguide, the perfect phase-matching condition $\Delta k = 0$ reduces to a simple relation between the frequency and effective index of the different interacting modes:

$$\omega_3 n_3(\omega_3) - \omega_1 n_1(\omega_1) - \omega_2 n_2(\omega_2) = 0. \tag{4.10}$$

It is obvious that, if we consider that the three photons occupy the same guided mode, in other words: $n_i(\omega) = n(\omega),\ i = 1, 2, 3$, then phase-matching could only occur if this mode is perfectly non-dispersive: $n(2\omega) = n(\omega)$, a condition that is never reached in practice. Therefore, several strategies can be adopted to fulfill phase-matching in waveguides:

Birefringence A dielectric material is said to be birefringent if the refractive index of an electromagnetic wave traveling through the medium depends on its polarization. Hence phase-matching can occur between modes of different polarization μ, ν if the birefringence is sufficient to obtain $n_\nu(2\omega) = n_\mu(\omega)$. In many materials, including AlGaAs, the intrinsic birefringence is not strong enough to meet this requirement. However, it is possible to design waveguides with artificial form birefringence to obtain perfect phase-matching, as explained, for instance, in Ref. [138].

Quasi phase-matching In this scheme, the waveguide is divided into several regions along the propagation direction. The length of these regions is chosen to match the period of the oscillations of the intensity of the generated field when there is a nonzero wave-vector mismatch, as shown in Fig. 1.2. To achieve quasi phase-matching, the $\chi^{(2)}$ coefficient in the different regions needs to changes sign at each interface. Then, instead of oscillating along the waveguide, the optical power will ramp up at each interface, thanks to the inversion of the $\chi^{(2)}$ coefficient. Examples of quasi-phase matching include ppKTP, ppLN and ppGaAs crystals or waveguides [139].

Modal phase-matching This is the phase-matching strategy used in this work. The principle is to use a multimode waveguide whose guided modes have different chromatic dispersion. By suitably engineering the waveguide structure, it is possible to obtain guided modes that are compatible with perfect phase-matching. In the case of SPDC, this amounts to using a pump mode that has the same mode index at frequency 2ω than the down-converted modes at frequency ω.

4.2 AlGaAs Waveguide design

4.2.1 Epitaxial structure and guided modes

The elementary working principle of the nonlinear AlGAs waveguides studied in this thesis is depicted in Fig. 4.2 (a). We perform SPDC by sending near infrared (NIR) photons

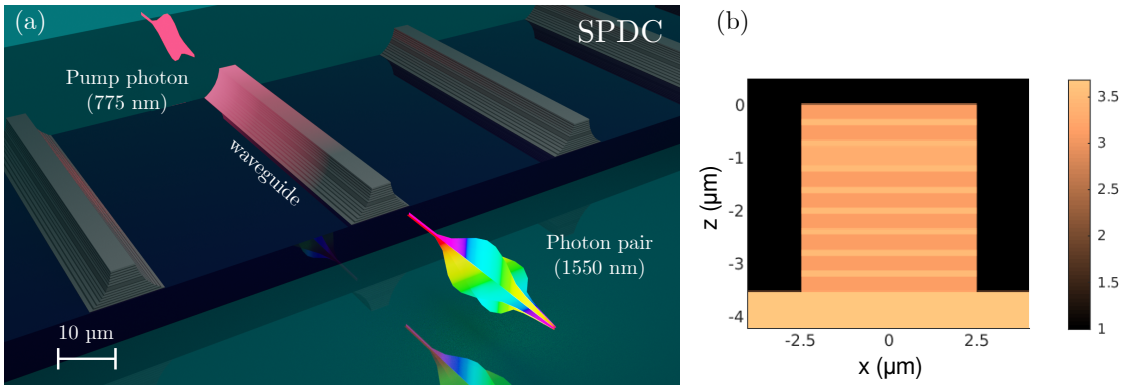

Figure 4.2: (a) Artist view of an AlGaAs ridge waveguide used as a source of entangled photon pairs. The pump photon in the NIR is represented on the upper left corner and the generated telecom photons are depicted in the bottom right corner. This drawing represents a Type II interaction since the photons are depicted as cross-polarized. (b) Refractive index profile in a 2/6-Bragg mirrors ridge waveguide.

Layer	**Cycles**	**Δz (nm)**	**x (%)**	**$n_{770.5nm}$**	**n_{1541nm}**
Cap	1	5	0	3.692	3.378
Top Bragg	2 or 6	280	80	3.122	2.978
		116	25	3.487	3.239
Core	1	351	45	3.336	3.142
Bottom Bragg	6	116	25	3.487	3.239
		280	80	3.122	2.978
Substrate	1	-	0	3.692	3.378

Table 4.1: Epitaxial structure of the AlGaAs nonlinear waveguides. Two configurations were used in this dissertation: either with 2 or 6 upper periods for the Bragg reflectors. The growth sheets for the different wafers used in this thesis are reported in Appendix 12.6.

at around 775 nm inside the waveguide which, thanks to the strong $\chi^{(2)}$ of AlGaAs, are downconverted into pairs of telecom photons around 1550 nm. In this spectral region GaAs typically has a refractive index of 3.7 at 775 nm and 3.4 at 1550 nm at room temperature ensuring tight confinement of guided mode at the micrometer scale. The nonlinear coefficient d_{41} of GaAs has a typical value of 119 pm V^{-1}. In AlGaAs, this value strongly depends on the concentration of Al and can be determined using the Ohashi model [140, 141].

The devices are fabricated by etching ridge waveguides into an AlGaAs wafer consisting of a stacking of different layers of $Al_xGa_{1-x}As$ with a varying Al concentration x. The layers are epitaxially grown on a [001] GaAs substrate. As depicted in Fig. 4.2 (b) an $Al_{0.45}Ga_{0.55}As$ core is sandwiched between two Bragg mirrors that are made of alternating 116 nm thick layers of high refractive index $Al_{0.25}Ga_{0.75}As$ and 280 nm-thick layers of low refractive index $Al_{0.2}Ga_{0.8}As$. The epitaxial structure is given in Table 4.1. Those Bragg mirrors have been engineered to provide a photonic bandgap around 775 nm such that specific guided modes can propagate by total internal reflection. Details on the design of the Bragg reflectors can be found in Ref. [142, 143, 137]. The waveguides that we fabricate are typically 2 mm-long with a ridge width ranging from about 1.5 µm to 5 µm and etching depth between 0.8 µm and 4 µm. The influence of the geometric parameters

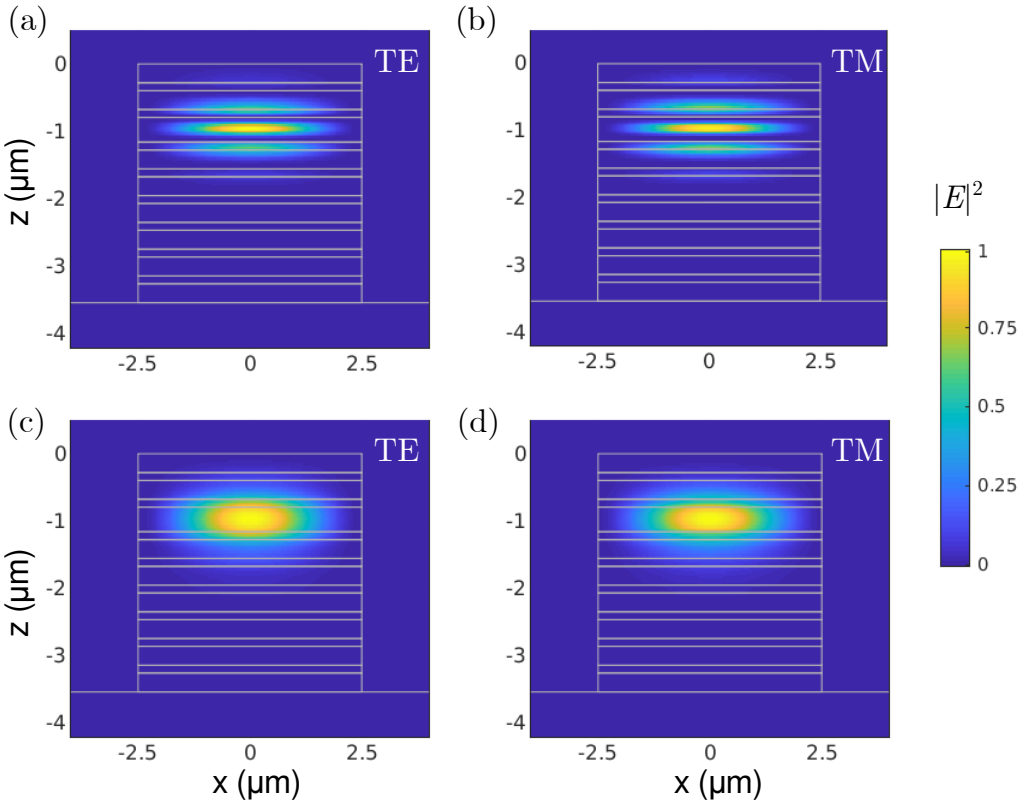

Figure 4.3: Square modulus of the electric field of the (a) TE Bragg mode at $\lambda_p = 775\,\text{nm}$, (b) TM Bragg mode at $\lambda_p = 775\,\text{nm}$, (c) TE fundamental mode at $\lambda = 1550\,\text{nm}$ and (d) TM fundamental mode at $\lambda = 1550\,\text{nm}$.

of the waveguide on the nonlinear processes is discussed below.

The different modes that are involved in three-wave mixing are the following :

- The NIR photons propagate in the so-called Bragg mode that is confined in the core of the waveguide thanks to the photonic bandgap provided by the two Bragg mirrors. As shown in Fig. 4.3 (a-b), its spatial profile features a bright central lobe, located in the core, and peripheral lobes spreading in the surrounding layers. The Bragg mode exists as a TE or TM mode of the waveguide.

- In the telecom range, the refractive index contrast between the core and the surrounding layers of the Bragg mirrors provide tight confinement for guided modes within the core. The guided modes at $\lambda = 1550\,\text{nm}$ involved in the downconversion process are the fundamental TE and TM modes of the waveguide which are displayed in Fig. 4.3 (c-d).

Another important feature of AlGaAs waveguides is the modal reflectivity of the facets. Indeed, due to the refractive index contrast between AlGaAs and air, light propagating in a guided mode will undergo Fresnel reflection at the waveguide facet. The modal reflectivity depends on the mode and wavelength and can be estimated numerically using finite difference time domain methods. We give typical simulated values for the modal reflectivity of the four guided modes described in Fig. 4.3:

$$\begin{aligned} R_{\text{Bragg,TE}} &= 0.86, \quad R_{\text{Fund,TE}} = 0.29, \\ R_{\text{Bragg,TM}} &= 0.85, \quad R_{\text{Fund,TM}} = 0.27. \end{aligned} \tag{4.11}$$

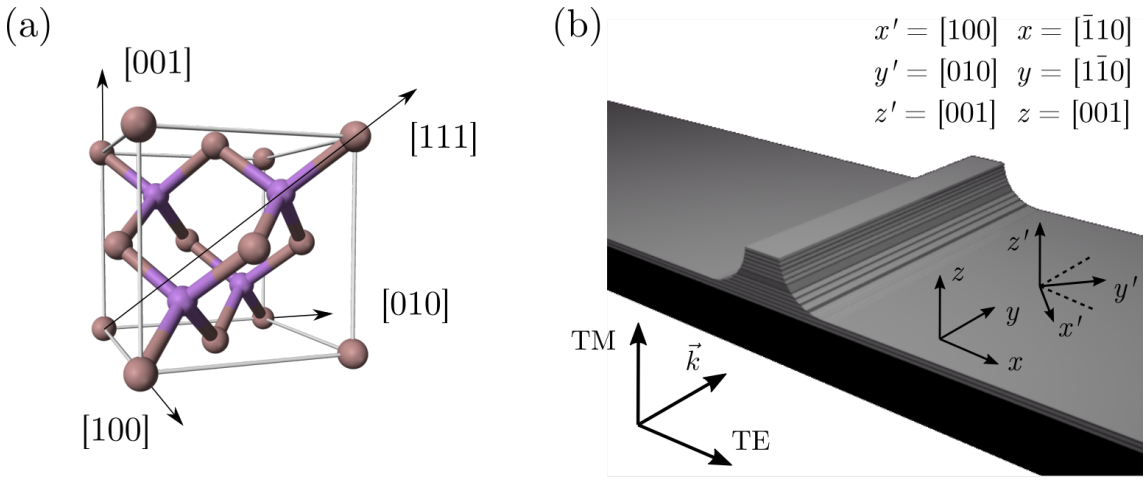

Figure 4.4: (a) Sketch of the GaAs unit cell with principal crystallographic directions. (b) Waveguide layout with corresponding crystallographic axes.

In this dissertation, we used two different epitaxial structures. In the majority of the previous works from our group, structures having six upper and six lower Bragg periods have been used. However, in most of the designs of this work we chose to use structures consisting of two upper Bragg periods and six lower Bragg periods. This choice was motivated by practical concerns. Indeed the thickness of AlGaAs layers that has to be etched to obtain a ridge waveguide is smaller for structures with only two top Bragg mirrors than with six top Bragg mirrors (0.8 µm versus 2.4 µm), which simplifies the fabrication process of the device. In addition, we did not notice a degradation of the performance of the device when going from six to two periods. Hence if not otherwise mentioned, all simulations and experimental results presented in the manuscript were obtained using epitaxial structures with two upper periods (wafers `G5X038` and `K7AD118`).

4.2.2 Allowed parametric processes in AlGaAs

Depending on the polarization of the interacting fields, several nonlinear interactions are possible in AlGaAs which are determined by the crystal symmetries of the material. Indeed, as mentioned in Section 1.4, those symmetries are reflected in the second order dielectric susceptibility tensor d_{ijk} defined in Eq. (1.23) which governs non-linear optical processes in the medium. The crystal unit cell of GaAs, sketched in Fig. 4.4 (a), obeys a $\bar{4}3m$ group symmetry. Based on these symmetry considerations, only three matrix element of d_{ijk} are nonzero, as shown in [136]. By contracting the last two indices of $\chi^{(2)}$ with the convention:

jk	11	22	33	23/32	13/31	12/21
ℓ	1	2	3	4	5	6

(4.12)

we obtain the reduced tensor :

$$d = \begin{pmatrix} 0 & 0 & 0 & d_{41} & 0 & 0 \\ 0 & 0 & 0 & 0 & d_{41} & 0 \\ 0 & 0 & 0 & 0 & 0 & d_{41} \end{pmatrix}. \tag{4.13}$$

The basis in which we wrote down this expression for the matrix coincides with the crystallographic axes of GaAs: $x' = [100], y' = [010], z' = [001]$. However we fabricate waveguides whose facets are cleaved at a 45 degree angle with respect to the crystallographic axes : $x = [\bar{1}10], y = [\bar{1}10], z = [001]$, as depicted in Fig. 4.4 (b). With the help

of Eqs. (1.19) and (4.13), we write down the nonlinear dielectric polarization vector for frequency $\omega_3 = \omega_1 + \omega_2$ in the crystal reference frame:

$$\begin{pmatrix} P^{\mathrm{NL}}_{3,x'} \\ P^{\mathrm{NL}}_{3,y'} \\ P^{\mathrm{NL}}_{3,z'} \end{pmatrix} = 2\epsilon_0 d_{41} \begin{pmatrix} E_{1,y'}E_{2,z'} + E_{1,z'}E_{2,y'} \\ E_{1,x'}E_{2,z'} + E_{1,z'}E_{2,x'} \\ E_{1,x'}E_{2,y'} + E_{1,y'}E_{2,x'} \end{pmatrix}, \tag{4.14}$$

where the frequency is implicitly indicated by the subscripts $1, 2, 3$ and the spatio-temporal dependence of the fields is omitted for clarity. We rewrite the three components of the vector in the laboratory frame by rotating the xy axes counterclockwise around the z axis by an angle $\pi/4$. This is done by applying to Eq. (4.14) the $R_z(-\pi/4)$ rotation matrix

$$R_z(-\pi/4) = \frac{1}{\sqrt{2}} \begin{pmatrix} 1 & 1 & 0 \\ -1 & 1 & 0 \\ 0 & 0 & 1 \end{pmatrix}. \tag{4.15}$$

After applying this transform, the non-linear polarization vector in the laboratory frame reads:

$$\begin{pmatrix} P^{\mathrm{NL}}_{3,x} \\ P^{\mathrm{NL}}_{3,y} \\ P^{\mathrm{NL}}_{3,z} \end{pmatrix} = 2\epsilon_0 d_{41} \begin{pmatrix} E_{1,z}E_{2,x} + E_{1,x}E_{2,z} \\ -E_{1,z}E_{2,y} - E_{1,y}E_{2,z} \\ E_{1,x}E_{2,x} - E_{1,y}E_{2,y} \end{pmatrix} \tag{4.16}$$

By inspecting Eq. (4.16) we conclude that three processes are allowed:

1. **Type II** : TE + TM $\leftrightarrow$ TE, $P^{\mathrm{NL}}_{3,x} = E_{1,z}E_{2,x} + E_{1,x}E_{2,z}$
2. **Type I** : TE + TE $\leftrightarrow$ TM, $P^{\mathrm{NL}}_{3,z} = E_{1,x}E_{2,x}$
3. **Type 0** : TM + TM $\leftrightarrow$ TM, $P^{\mathrm{NL}}_{3,z} = -E_{1,y}E_{2,y}$

Note that the Type 0 process is made possible by the nonzero electric field component of the TM mode along the propagation direction y [144].

4.2.3 Modal phase-matching

As already stated above, the SPDC process in AlGaAs nonlinear waveguides involves a pump photon in a Bragg mode, either TE or TM, and two downconverted photons in the fundamental TE and TM modes of the waveguide. In Fig. 4.5, we show the value of the numerically calculated effective mode index of the four modes of interest as a function of wavelength. Those simulations were performed with the Lumerical software. For clarity, we plotted the dispersion curves of the NIR mode as function of half the wavelength of the telecom modes. As we can see, there is a region around which the values of the effective mode indices become close. Around this region, the phase mismatch Δk is minimal and frequency conversion between the NIR and telecom modes is possible. For each of the three possible interactions, we indicate on the plot the point for which $n(2\omega_{\mathrm{PM}}) = \frac{1}{2}\left(n_\mu(\omega_{\mathrm{PM}}) + n_\nu(\omega_{\mathrm{PM}})\right)$ with $\mu, \nu \in \{\mathrm{TE}, \mathrm{TM}\}$, where ω_{PM} is called the phase-matching frequency. The phase matching conditions for the three possible interactions can be summarized as:

1. **Type II** : TE + TM $\leftrightarrow$ TE, $\omega_3 n_{\mathrm{Bragg,TE}}(\omega_3) = \omega_1 n_{\mathrm{fund,\ TE}}(\omega_1) + \omega_2 n_{\mathrm{fund,TM}}(\omega_2)$
2. **Type I** : TE + TE $\leftrightarrow$ TM, $\omega_3 n_{\mathrm{Bragg,TE}}(\omega_3) = \omega_1 n_{\mathrm{fund,\ TM}}(\omega_1) + \omega_2 n_{\mathrm{fund,TM}}(\omega_2)$
3. **Type 0** : TM + TM $\leftrightarrow$ TM, $\omega_3 n_{\mathrm{Bragg,TM}}(\omega_3) = \omega_1 n_{\mathrm{fund,\ TM}}(\omega_1) + \omega_2 n_{\mathrm{fund,TM}}(\omega_2)$

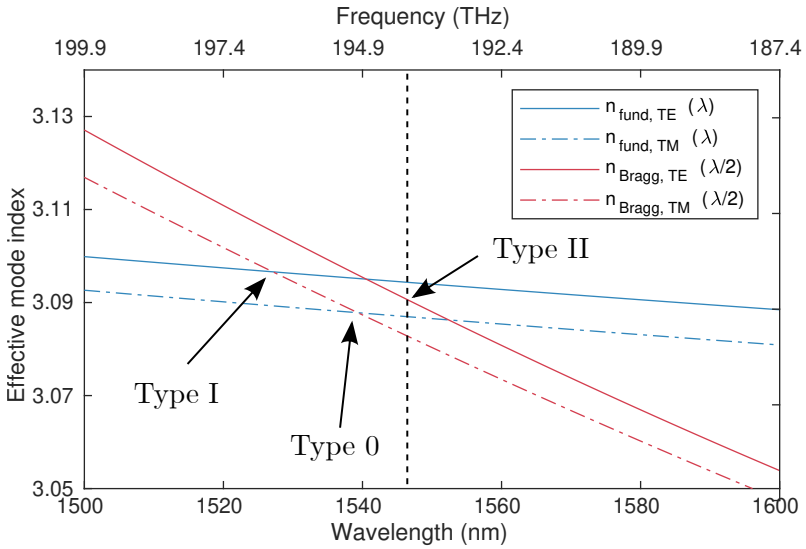

Figure 4.5: (a) Simulated dispersion of effective mode indices for Bragg mode around 775 nm , and fundamental TE and TM modes around 1550 nm.

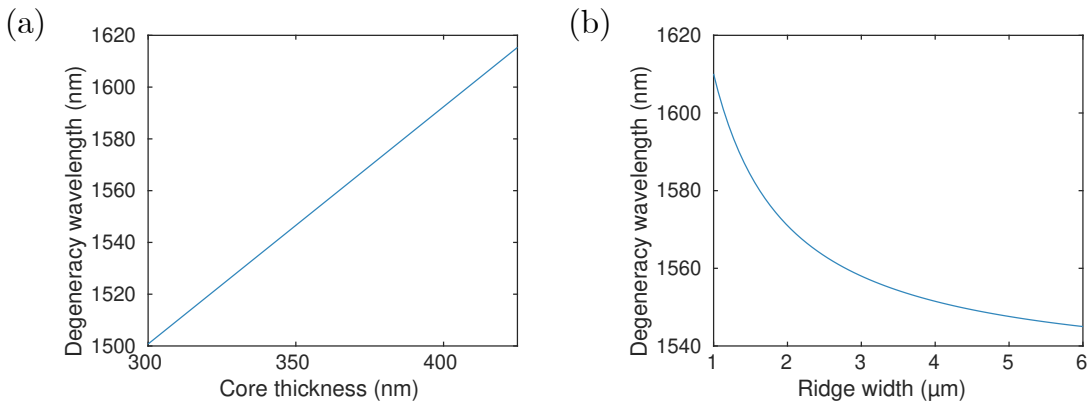

Figure 4.6: Numerically simulated phase-matching wavelength for the Type II interaction as a function of (a) core thickness for a ridge width of 5 µm (b) ridge width for a core thickness of 351 nm.

In the work presented in this manuscript, we will mostly focus on Type II SPDC interaction as it is the process that is used to produce polarization-entangled photon pairs. Indeed, in a Type II process for a given value of the frequencies $\omega_1, \omega_2, \omega_3$ two equivalent processes can occur: $\mathrm{TE}(\omega_3) \rightarrow \mathrm{TE}(\omega_1) + \mathrm{TM}(\omega_2)$ and $\mathrm{TE}(\omega_3) \rightarrow \mathrm{TE}(\omega_2) + \mathrm{TM}(\omega_1)$. Those processes being indistinguishable, the generated photons are emitted in a polarization entangled state directly at the waveguide output. Type 0 and Type I SPDC can be used to produce energy-time entangled photon pairs, since the two photons have the same polarization. However, by inserting the source in a Sagnac interferometer, it is also possible to create polarization-entangled photon pairs from a Type 0 or Type I process, at the cost of increasing the setup complexity [145].

4.2.4 Tuning of the phase-matching wavelength

As we can see from Fig. 4.5, phase-matching occurs for signal and idler frequencies ω_1, ω_2 in the vicinity of the phase-matching frequency ω_{PM}. When generating photon pairs through

SPDC, the frequency of the pump will be adjusted to this phase-matching frequency and therefore the generated photons will be distributed within a certain bandwidth $\Delta\omega$ around a central degeneracy frequency $\omega_d = \omega_p/2 = \omega_{\mathrm{PM}}$. Hence ω_{PM} is a parameter of the source that has to be well controlled as defines the spectral region where the pairs are being emitted. For instance, in the quantum communication experiment described in Part V, the source had to be optimized to generate photon pairs in the telecom C-Band between 1535 nm to 1575 nm in order to be compatible with off-the-shelf optical components.

The value of ω_{PM} strongly depends on the dispersion of the modes and hence on the waveguide design. We can use two main parameters to tune the phase-matching: ridge width and core thickness. The numerically simulated value of the phase-matching wavelength as a function of these quantities for a Type II interaction is reported in Fig. 4.6. We observe from Fig. 4.6 (a) that λ_{PM} is proportional to the core thickness. Hence by carefully adjusting the epitaxial structure, one can get a coarse tuning of the value of λ_{PM}. In addition to this, we see in Fig. 4.6 that λ_{PM} is also inversely proportional to the ridge width. This way of controlling the phase-matching is less constraining since the ridge width can be chosen at the fabrication stage when etching the waveguide. On the contrary, changing the epitaxial structure requires growing a brand new sample, which is a sensitive process. What is more, numerical simulations show that, in these structures, the etching depth has a negligible impact on the phase-matching wavelegth and therefore cannot be used as an extra control parameter.

Finally, to get a fine tuning of the phase-matching, one can also change the temperature of the waveguide. Indeed, the Gerschitz model [146] predicts the variation of the AlGaAs refractive index as a function of the fraction x of Al and the temperature T. By using this model in our simulations, we find a linear temperature dependence of about $0.1\,\mathrm{nm\,°C^{-1}}$ that is consistent with previous experimental results from our group [147]. As we can see, the dependence on temperature is much weaker but can be still be useful for setting the value of λ_{PM} to a precise wavelength.

4.3 Cleanroom fabrication

4.3.1 Epitaxial growth

To fabricate AlGaAs waveguides, we start from 1" wafers where the the nominal structure presented in Section 4.2.1 has been grown on an undoped GaAs substrate. The wafers are grown by molecular beam epitaxy (MBE) at C2N lab in Palaiseau (France) by Aristide Lemaître and Martina Morassi. We cleave small rectangular portions of this wafer, whose edges are oriented along the $[1\bar{1}0]$ and $[\bar{1}10]$ crystallographic axis of AlGaAs, and fabricate our devices out of these individual pieces of wafer.

During the MBE process, the GaAs substrate is set on a rotating plate and the different atomic species entering in the composition of AlGaAs are sputtered across the surface of the substrate. By controlling tightly the gas flow, the MBE machine can deposit AlGaAs of variable Al concentration atomic layer by atomic layer. The rotating sample holder is used to ensure that the deposition is uniform across the wafer and hence that the epitaxial structure will be constant over the whole sample.

In some cases, however, we might want the core thickness to have a gradient in order to be able to fabricate samples with different phase-matching wavelengths out of a single growth, depending on the target application. Indeed, since this value is directly proportional to the core thickness, as shown in Fig. 4.6, this give us the freedom to tune the phase matching by simply choosing the region of the wafer that is used to etch the waveg-

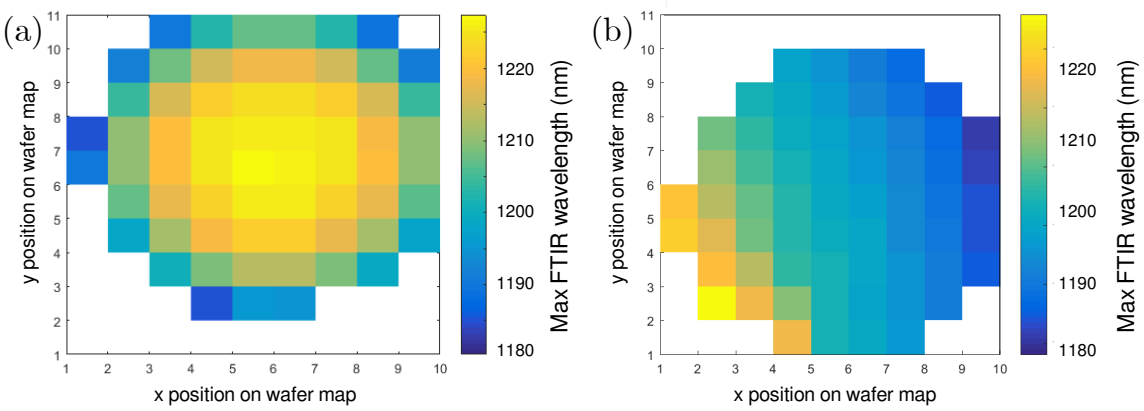

Figure 4.7: Spatial map of the maximum FTIR reflectivity wavelength for wafers (a) `L5AF052`, without a core thickness gradient, and (b) `K7AD118`, with a linear core thickness gradient.

uide. To this end it is possible to stop the rotation of the substrate during the growth of the waveguide core. Consequently, the deposition of the $Al_{0.45}Ga_{0.55}As$ layer will not be uniform across the substrate and will feature a linear gradient.

After each new growth, the epitaxy team perform a complete Fourier transform infrared reflection (FTIR) spatial map of the wafer. For 110 locations on the surface of the sample a FTIR spectrum is acquired. We can compare this data to numerical simulations[1] to verify that the sample that has been grown corresponds to the nominal structure. In Fig. 4.7 we show the spatial map of the wavelength at which the FTIR spectrum takes its maximum value for two different wafers, one with a core thickness gradient (`K7AD118`) and one without gradient (`L5AF052`). From simulations, we observe that the maximum FTIR spectrum wavelength gives the trend for the value of the core thickness: when the thickness of the core increases, the maximum of the FITR spectrum is redshifted. We see that the linear gradient in the core thickness is clearly visible in the second plot. On the contrary, when the rotating plate is on during all of the growth process, we observe that the FTIR spatial map is relatively homogeneous across the surface of the sample, with a slight radial gradient.

Those spatial FTIR maps are an interesting characterization tool as they give us a trend for the value of the phase-matching wavelength across the wafer. Indeed, numerical simulations show that when the core thickness increases, so does the maximum FTIR wavelength. Therefore, by measuring experimentally from a fabricated sample a reference for the phase-matching wavelength at one location of the growth, one can obtain a relative estimate of its value across the whole wafer from the spatial FTIR map.

4.3.2 Cleanroom process #1 : photolithography and chemical etching

In the two following sections, we describe the fabrication process of the AlGaAs ridge waveguide. We first focus on the easiest and quickest method : photolithography and wet chemical etching:

1. Cleaning of the piece of AlGaAs wafer with acetone, isopropanol and water then additional surface cleaning with a light O_2 plasma.

[1] We used either the *stack* function in the Lumerical FDTD software or a home-brewed solver to simulate FTIR curves.

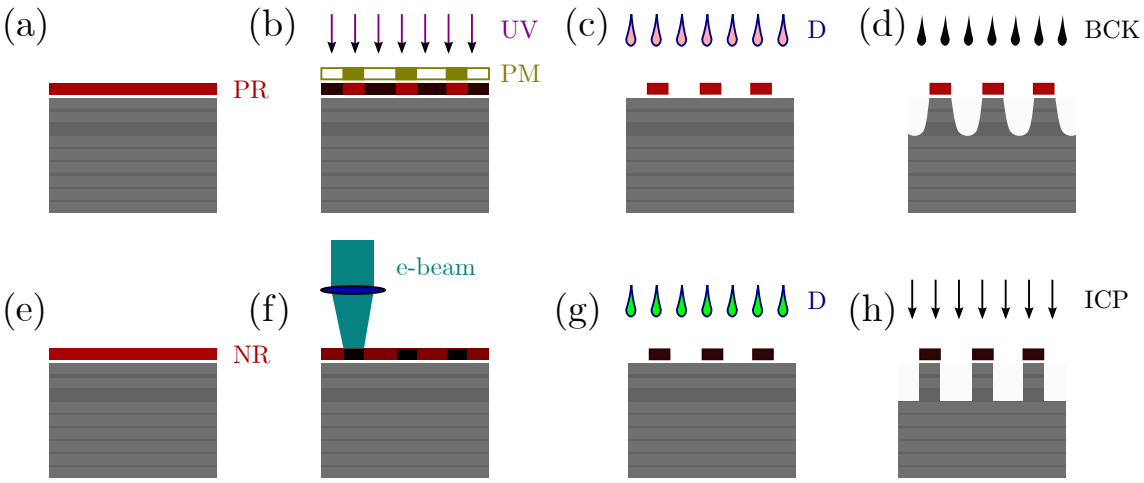

Figure 4.8: Fabrication steps for (a-d) wet etched waveguides and (e-h) dry etched waveguides. PR: Positive resist, NR: Negative resist, PM: Photomask, UV: Ultraviolet beam, D: Developer, BCK: Chemical etching solution, ICP: Inductively coupled plasma etching

2. Spincoating of the positive photoresist S1805 (nominal thickness of 500 nm) using adhesion promoter HMDS (Fig. 4.8 (a)). Both the resist and the promoter are spun at 5000 rpm for 30 s. After spincoating, the resist is baked at 110 °C for 1 min.

3. UV lithography of waveguides using a custom Cr photomask from the company Delta Mask (Fig. 4.8 (b)).

4. Resist development using a MF-319 developer (Fig. 4.8 (c)). The development time is 15 s.

5. Chemical etching using a BCK solution composed of acetic acid, potassium dichromate ($K_2Cr_2O_2$) and hydrobromic acid (HBr) in stoechiometric proportions (Fig. 4.8 (d)).

6. Resist removal using acetone.

Due to the isotropic nature of chemical etching the resulting fabricated waveguides have smooth curvy sidewalls as shown in Fig. 4.9 (a). However the resolution we can achieve in the lithography is limited by the wavelength of the UV light that is used to irradiate the sample and the roughness of the metallic mask.

4.3.3 Cleanroom process #2 : e-beam lithography and inductively coupled plasma (ICP) etching

A second way of fabricating the waveguides involves electron-beam (e-beam) lithography followed by dry inductively coupled plasma (ICP) etching. This method has a much higher spatial resolution since the wavelength of electrons is much smaller than the wavelength of UV light. The fabrication steps are as follows :

1. Cleaning of the sample (same as above).

2. Plasma enhanced chemical vapor deposition (PECVD) of a 5 nm layer of SiO that promotes the adhesion of the resist.

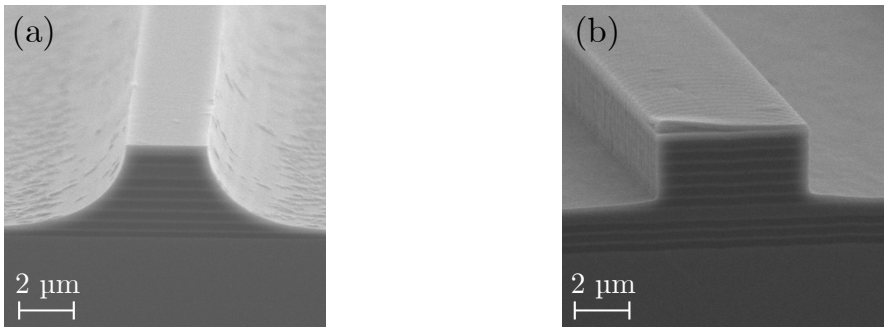

Figure 4.9: Scanning electron microscope (SEM) images of the facet of AlGaAs ridge waveguides fabricated by (a) wet etching and (b) dry etching.

3. Spin coating of HSQ negative e-beam resist (Fig. 4.8 (e)). The solution that is used has a 6 % concentration in HSQ. The resist is spun at 3000 rpm for 30 s and then baked at 80 degrees for 4 minutes. The final resist thickness is around 90 nm.

4. E-beam lithography using a Raith Pioneer scanning electron microscope (SEM) with a fixed beam moving stage (FBMS) module (Fig. 4.8 (f)). Thanks to this particular writing mode, long waveguides can be patterned much faster than with conventional e-beam lithography, where the stage remains fixed while the electron beam is moved to draw the patterns. However, in FBMS mode, the SEM can only draw paths of fixed width, but not polygons, as it would in conventional e-beam lithography. Later in this manuscript, in Chapter 9, we use a simple hack to be able to draw polygons in FBMS: we simply define the contour of the polygon using a first FBMS path then we filled the polygon using other path of various width. We use an electron beam of 20 kV and an aperture of 30 µm resulting in an electronic current of 300 pA that is used to irradiate the resist by an electron dose of 800 $\mu C\,cm^{-1}$.

5. Development of the resist with the AZ400K developer (Fig. 4.8 (g)).

6. Removal of the 5 nm-thick SiO layer using reactive ion etching (RIE). We did this in order to avoid having to etch out the SiO in addition to the AlGaAs layers in the next step.

7. Waveguide etching using ICP based on Ar and $SiCl_4$ (Fig. 4.8 (h)). This etching method is strongly directional, resulting in vertical sidewalls, as can be seen from Fig. 4.9. It is however weakly chemically selective, and the HSQ resist also gets etched away by the plasma. SiO having a very low etch rate, if we ommitted the previous step, the HSQ photoresist would have been completely removed during the etching process before we even reached the first AlGaAs layer under the SiO. What is more, with our ICP recipe AlGaAs itself has a low etch rate of 11 $nm\,min^{-1}$. Because of this slow etching process, we chose to use exclusively an epitaxial structure with only 2 upper Bragg mirror periods to avoid exposing the sample to ICP for too long before etching the waveguide down to the core.

An important step when designing FBMS masks (and e-beam masks in general) is to minimize the number of distinct paths or polygons that make up a single pattern to ensure there is no risk of having mismatches or gaps at the interface between polygons. For instance, a waveguide with S-bends should be done in a single FBMS path and not several paths stuck end-to-end. By doing this, one ensures that the waveguide will be

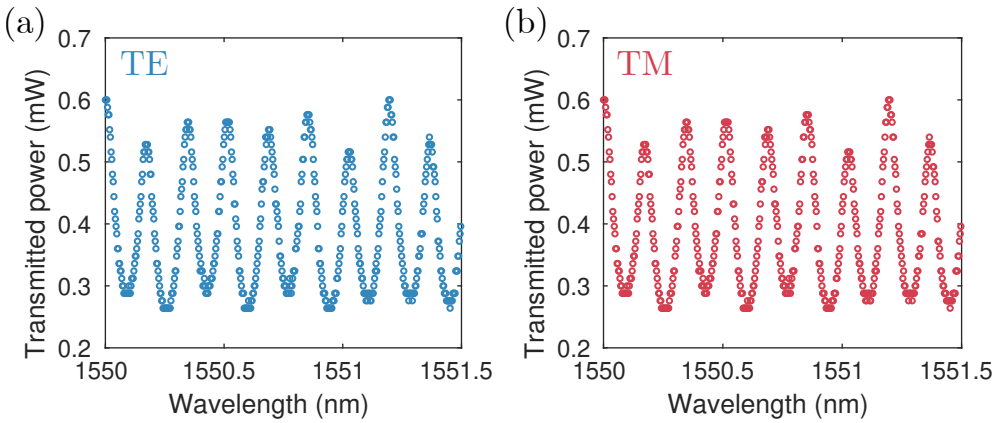

Figure 4.10: Data from a transmission measurement on a wet etched waveguide of ridge width 4 µm (`K7AD118`) for (a) TE polarization and (b) TM polarization. We see Fabry-Perot fringes arising from the effective cavity formed by the waveguide facet

perfectly smooth, without any discontinuity caused by the interface between the paths When multiple polygons or paths are unavoidable, one can make the adjacent objects overlap by about 50 nm to 100 nm to avoid any gaps.

4.4 Measurement of the optical losses of the guided modes

To check the quality of the fabricated device, we characterize the propagation losses of the telecom modes inside the waveguide by using a method described in [148]. We measure the transmission of the waveguide as a function of frequency, which will feature a series of Fabry-Perot resonances arising from the reflectivity of the waveguide facets, as explained in Section 4.2.1. For a given guided mode, the transmission of the waveguide is expressed as:

$$T(\omega) = \frac{(1-R)^2 e^{-\alpha L}}{(1-Re^{-\alpha L})^2 + 4R^2 e^{-\alpha L}\sin^2[\phi(\omega)]}, \tag{4.17}$$

where ω is the frequency, α the propagation losses, R the modal reflectivity and L the length of the waveguide. The phase factor $\phi(\omega)$ is given by:

$$\phi(\omega) = Ln(\omega)\omega/c. \tag{4.18}$$

By measuring the contrast K of the Fabry-Perot fringes $K = (T_{\max} - T_{\min})/(T_{\max} + T_{\min})$ with $T_{\max/\min}$ the maximum and minimum of Eq. (4.17), it is possible to obtain the combined loss-reflectivity coefficient

$$\tilde{R} = Re^{-\alpha L} = \frac{1}{K}(1 - \sqrt{1-K^2}). \tag{4.19}$$

Using the numerically computed value for the modal reflectivity R, an estimate of the propagation losses can be found as:

$$\alpha = \ln\left(R/\tilde{R}\right)/L. \tag{4.20}$$

To measure $T(\omega)$ experimentally, a telecom laser beam is focussed on the input facet of the waveguide using a NA=0.65 microscope objective. Light at the output facet of the device is collected using a NA=0.95 objective then directed to an infrared (IR) powermeter.

The transmitted power is recorded while scanning the input laser wavelength λ. The transmissivity T is obtained by taking the ratio between the transmitted power and the input power of the laser. The result of a transmission measurement on a wet-etched waveguide of width 4 µm (wafer `K7AD118`) is shown in Fig. 4.10. We observe characteristic Fabry-Perot fringes with a free-spectral range of 22 GHz (0.17 nm), which is compatible with the length of the device, about 2 mm in this case, and the value of the effective mode indices of TE and TM fundamental modes, around 3.1. From the fringe contrast, we extract a value of 1.3 cm^{-1} and 2.5 cm^{-1} for the TE and TM losses respectively.

Ridge width (µm)	Losses TE (cm^{-1})	Losses TM (cm^{-1})
2	6.6	6.0
3	2.6	3.2
4	1.3	2.5

Table 4.2: Measured propagation losses of the fundamental telecom modes around 1550 nm for waveguides of different ridge width fabricated by wet etching in wafer `K7AD118`.

In Table 4.2 we display the measured values for propagation losses in waveguides of increasing width that were fabricated on the same chip. The general trend is that the losses decrease in broader waveguides. Moreover, we observe that for narrow waveguides losses are higher for the TE than for the TM mode. This is what we would expect intuitively since the TM mode has its E field polarized parallel to the waveguide sidewalls and hence is less affected by a reduced ridge width.

The fact that losses increase significantly in narrow waveguides introduces a trade-off in the tunability of the phase-matching resonance with ridge width presented in Fig. 4.6 (a). Indeed, the price to pay when attempting to reach higher values for λ_{PM} by reducing the waveguide width is to have a lower conversion efficiency due to the losses. This is why the thickness gradient in the epitaxial structure is a crucial tuning parameter since, despite being harder to control, it allows to change the PM wavelength without introducing losses.

4.5 Characterization of the frequency conversion by Second Harmonic Generation

4.5.1 Principle of the experiment

The second step in the characterization of a device is the measurement of second harmonic generation. Since it is the reverse classical process of SPDC, it can be used to measure the phase-matching wavelength λ_{PM} of the different SPDC interactions.

The setup used for this experiment is depicted in Fig. 4.11. We couple a telecom laser beam at frequency ω in and out of the waveguide using the same microscope objectives as in the previous section. The beam exiting the waveguide will contain the undepleted strong pump field at frequency ω and a weak frequency-doubled field at 2ω that has been created by SHG. The beam exiting the waveguide is filtered using a dichroic mirror with cutoff wavelength 1000 nm. The reflected part, which contains the SHG field, is sent to an InGaAs photodiode, whose analog electrical output is amplified by a factor of 1×10^7 to 1×10^8 then fed into a SRS830 lockin amplifier. We add a beam chopper just before the input microscope objective to modulate the input beam at a frequency of about 220 Hz. The reference signal from the chopper is sent to the lockin amplifier which will amplify the measured SHG signal at the frequency of the chopper and measure the amplitude and

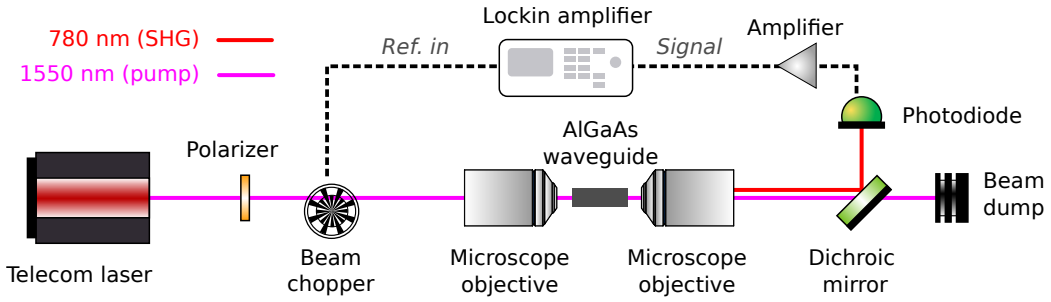

Figure 4.11: Sketch of the experimental setup for a SHG experiment. An optional polarizer (not shown) can be added before the photodiode to project the SHG field on different polarizations.

phase of the field. To monitor and keep the waveguide temperature constant, we use a thermistor and a Peltier cooler, connected to a PID controller (not shown).

By recording the amplitude of the generated beam at 2ω as a function of input frequency ω, we obtain a spectrum where the phase-matching resonances will appear as maxima of the recorded SHG power. As explained in Section 4.2.2, several interaction involving modes of different polarizations can occur in the device. Those processes can be probed separately by adjusting the polarization of the telecom pump beam. There are two possibilities :

- An input beam with a linear polarization at 45 deg with respect to the vertical direction, which corresponds to a linear superposition of the TE and TM modes, will excite all three possible interactions:
  - Type II : $\mathrm{TE} + \mathrm{TM} \rightarrow \mathrm{TE}$
  - Type I : $\mathrm{TM} + \mathrm{TM} \rightarrow \mathrm{TE}$
  - Type 0 : $\mathrm{TM} + \mathrm{TM} \rightarrow \mathrm{TM}$
- An input beam with a linear polarization at 0 deg with respect to the vertical direction, corresponding to the TM mode will only trigger the two interactions:
  - Type I : $\mathrm{TM} + \mathrm{TM} \rightarrow \mathrm{TE}$
  - Type 0 : $\mathrm{TM} + \mathrm{TM} \rightarrow \mathrm{TM}$

Eventually, the only way to discriminate Type I from Type 0 is to project the polarization of the generated SHG field by using a polarizer. Type II is usually the brightest since the epitaxial structure has been optimized favor Type II over the other processes.

4.5.2 Results

The result of a SHG measurement performed using a linearly polarized beam at 45 deg is displayed in Fig. 4.12 (a). We observe Type II and Type 0 resonances, as expected. For each interaction, the value of the phase-matching wavelength λ_{PM} is given by the wavelength for which the SHG signal is maximum. For instance, we see that Type 0 phase matching occurs at lower wavelength than Type II, as expected from the simulations of Fig. 4.5. Note that the Type 0 peak is smaller than Type II. This comes from the fact that a 45 deg polarized pump is not optimal for generating Type 0, which would require a 0 deg polarization. However, we did not repeat the measurement in this other setting

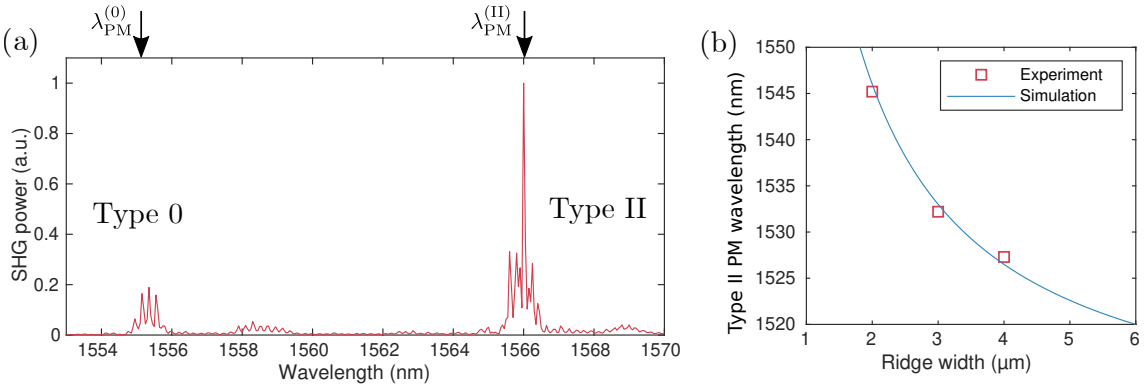

Figure 4.12: (a) Measured SHG spectrum in a wet etched waveguide from wafer `L5AF052` using a a 45 deg polarized telecom pump laser. The spectrum exhibits two interactions: Type II and Type 0. The satellite peaks on the right of each resonance correspond to SHG emission in the second order transverse spatial mode. (b) Experimental and simulated values for phase-matching wavelength as a function of ridge width in wet-etched waveguides fabricated in wafer `K7AD118`.

since we were only interested in finding the position of the resonances and not comparing the conversion efficiencies of the two processes.

Furthermore, for a given interaction, according to our simulations in Fig. 4.6 (b), the phase-matching wavelength depends on the waveguide width. To verify this, we fabricated a sample with groups of neighboring waveguides of increasing width, 2 µm, 3 µm and 4 µm, using photolithography and wet chemical etching (wafer `K7AD118`). By acquiring the SHG spectrum in all waveguides, we can observe its dependence on ridge width and compare it to the numerical simulations. The results are shown in Fig. 4.12 (b). Since the absolute values of the phase-matching wavelength are hard to predict numerically we obtained an offset of 25 nm between simulations and experiments. However, when removing this offset, which has been done in the plot Fig. 4.12 (b), we see that the trend of the simulated curve follows closely experimental observations.

Therefore, we confirm that the ridge width, which is easy to set on the lithography mask, can provide a useful tuning parameter to control the biphoton degeneracy wavelength.

Chapter 5

SPDC in AlGaAs waveguides: generated quantum state

Contents

5.1 Quantum theory of colinear SPDC 65
5.2 Properties of the JSA 68
5.3 Numerical simulation of the JSA 70
5.4 Polarization entanglement 73

In this chapter, we describe the quantum state generated by our AlGaAs SPDC source. We give a detailed derivation of the mathematical form of the state from first principles before showing simulations on the joint spectral amplitude (JSA). Then we describe polarization entanglement for a Type II interaction.

5.1 Quantum theory of colinear SPDC

To calculate the quantum state of the electromagnetic field at the output of the photon-pair source, we will need to make a generalization of the simple model of Section 2.3 when considering a continuum of possible interacting modes, which corresponds to the different polarization and frequencies that are allowed by the phase-matching conditions.

As in the previous model, the quantum Hamiltonian of the system is the sum of the Hamiltonian for free radiation $\hat{H}_R$ and an interaction Hamiltonian $\hat{H}_I$ which will depend on the non-linear dielectric susceptibility tensor. The Hamiltonian for free radiation reads:

$$\hat{H}_R = \int \mathrm{d}\omega_p \hat{a}_p^\dagger(\omega_p)\hat{a}_p(\omega_p) + \int \mathrm{d}\omega_1 \hat{a}_\mu^\dagger(\omega_1)\hat{a}_\mu(\omega_1) + \int \mathrm{d}\omega_2 \hat{a}_\nu^\dagger(\omega_2)\hat{a}_\nu(\omega_2). \tag{5.1}$$

By considering a SPDC process where the pump p will generate twin photons of polarizations $\mu, \nu \in \{H, V\}$, the interaction term can be written classically as [119]:

$$\begin{aligned} H_I &= \frac{1}{8\pi}\int_V \mathrm{d}\mathbf{r}^3 \mathbf{P}^{\mathrm{NL}} \cdot \mathbf{E} \\ &= \frac{\epsilon_0}{16\pi}\int_V \mathrm{d}\mathbf{r}^3 d_{\mathrm{eff}}(\mathbf{r}) E_p(\mathbf{r},t) E_\mu(\mathbf{r},t) E_\nu(\mathbf{r},t). \end{aligned} \tag{5.2}$$

When going to the quantum mechanical Hamiltonian, we replace the classical fields of the three photons by their quantum mechanical operators, given in Eq. (2.10). We only keep

the terms satisfying energy conservation and get the following expression:

$$\hat{H}_I = \int_V \mathrm{d}^3\mathbf{r} d_{\mathrm{eff}}(\mathbf{r}) \hat{E}_p^{(+)}(\mathbf{r}) \hat{E}_\mu^{(-)}(\mathbf{r}) \hat{E}_\nu^{(-)}(\mathbf{r}) + \mathrm{H.c.} \tag{5.3}$$

Since we are dealing with guided modes in a waveguide oriented along the y axis, we assume that the propagation of the three fields is in the y direction: $\mathbf{k}_p = k_p \mathbf{e}_y, \mathbf{k}_\mu = k_\mu \mathbf{e}_y, \mathbf{k}_\nu = k_\nu \mathbf{e}_y$. We can therefore simplify the expression for the positive and negative frequency components of the field operators:

$$\begin{aligned}
\hat{E}_p^{(+)} &= \frac{i}{c} \int \mathrm{d}\omega_p E_p(x,z) e^{-ik_p(\omega_p)y} \hat{a}_p(\omega_p), \\
\hat{E}_\mu^{(-)} &= \frac{i}{c} \int \mathrm{d}\omega_1 E_\mu(x,z) e^{ik_\mu(\omega_1)y} \hat{a}_\mu^\dagger(\omega_1), \\
\hat{E}_\nu^{(-)} &= \frac{i}{c} \int \mathrm{d}\omega_2 E_\nu(x,z) e^{ik_\nu(\omega_2)y} \hat{a}_\nu^\dagger(\omega_2).
\end{aligned} \tag{5.4}$$

In these expressions, we introduced the spatial mode profiles $E_i(x,z)$ of the three interacting fields. The expression for the interaction hamiltonian can be expanded as:

$$\begin{aligned}
\hat{H}_I = i\hbar \Bigg[\iint \mathrm{d}x\mathrm{d}z d_{\mathrm{eff}}(x,z) E_p(x,z) E_\mu(x,z) E_\nu(x,z) \Bigg] \\
\Bigg[\iiint \mathrm{d}\omega_p \mathrm{d}\omega_1 \mathrm{d}\omega_2 \int \mathrm{d}y e^{-i(k_p(\omega_p) - k_\mu(\omega_1) - k_\nu(\omega_2))y} \\
\hat{a}_p(\omega_p) \hat{a}_\mu^\dagger(\omega_1)\ \hat{a}_\nu^\dagger(\omega_2) \Bigg] + \mathrm{H.c.}.
\end{aligned} \tag{5.5}$$

The first term in (5.5) is the nonlinear overlap integral between the three interacting modes, that has already been introduced in Section 4.1.2:

$$\Gamma = \iint \mathrm{d}x\mathrm{d}z d_{\mathrm{eff}}(x,z) E_p(x,z) E_\mu(x,z) E_\nu(x,z). \tag{5.6}$$

Note that since TE and TM mode have slightly different spatial profiles, Γ will vary for all three interaction. The integral over y in Eq. (5.5) controls the phase-matching and can be rewritten:

$$\Phi_{\mathrm{PM}}(\omega_p, \omega_1, \omega_2) = \int \mathrm{d}y e^{-i(k_p(\omega_p) - k_\mu(\omega_1) - k_\nu(\omega_2))y} = e^{-i\Delta k L/2} \mathrm{sinc}(\Delta k L/2) \tag{5.7}$$

where $\Delta k = k_p(\omega_p) - k_\mu(\omega_1) - k_\nu(\omega_2)$ is the wave-vector mismatch and L the interaction length of the medium. Again, we obtain a familiar sinc^2 dependence on the wave-vector mismatch, which is reminiscent of the conversion efficiency for a classical nonlinear process.

To compute the steady state of the system, we want to decouple the dynamics induced by $\hat{H}_R$ and $\hat{H}_I$ by going to the interaction picture [120]. We obtain a time-dependent Hamiltonian:

$$\hat{H}^{(I)}(t) = e^{-i\hat{H}_R t/\hbar} \hat{H} e^{i\hat{H}_R t/\hbar}. \tag{5.8}$$

We denote by the superscript (I) the operators and state vector in the interaction picture. The effect of this transform is to introduce phase factors to the creation and annihilation operators present in the expression of $\hat{H}$. Indeed, under the effect of the unitary

transformation of Eq. (5.8), the ladder operations evolve as [1]:

$$\begin{aligned}\hat{a}_p(\omega_p) &\to \hat{a}_p(\omega_p)e^{-i\omega_p t}\\ \hat{a}^\dagger_\mu(\omega_1) &\to \hat{a}^\dagger_\mu(\omega_1)e^{i\omega_1 t}\\ \hat{a}^\dagger_\nu(\omega_2) &\to \hat{a}^\dagger_\nu(\omega_2)e^{i\omega_2 t}\end{aligned} \tag{5.9}$$

The free radiation part is unchanged in the interaction picture $\hat{H}_R^{(I)}(t) = \hat{H}_R$. The interaction part can be rewritten with the help of equations (5.7), (5.6) and (5.9):

$$\begin{aligned}\hat{H}_I^{(I)}(t) = i\hbar\Gamma \iiint \mathrm{d}\omega_p \mathrm{d}\omega_1 \mathrm{d}\omega_2 \Big[&\Phi_{\mathrm{PM}}(\omega_p,\omega_1,\omega_2)e^{-i(\omega_p-\omega_1-\omega_2)t}\\ &\hat{a}_p(\omega_p)\hat{a}^\dagger_\mu(\omega_1)\hat{a}^\dagger_\nu(\omega_2)\Big] + \mathrm{H.c.}\end{aligned} \tag{5.10}$$

The state of the electromagnetic field is obtained by applying the corresponding time-evolution operator $\hat{U}^{(I)}(t,t')$ in the interaction picture:

$$\begin{aligned}|\Psi\rangle_{\text{steady-state}} &= \hat{U}^{(I)}(-\infty,+\infty)\left|\Psi^{(I)}(0)\right\rangle\\ &= \exp\left[-\frac{i}{\hbar}\int_{-\infty}^{+\infty}\mathrm{d}\tau \hat{H}_I^{(I)}(\tau)\right]\left|\Psi^{(I)}(0)\right\rangle\end{aligned} \tag{5.11}$$

The integral is carried out between $\pm\infty$ as we are assuming the system has interacted for a very long time and has reached its steady state. The intial state in the Schrödinger picture is $|\Psi(0)\rangle = |\alpha(\omega_p)\rangle_p \otimes |\mathrm{vac}\rangle_\mu \otimes |\mathrm{vac}\rangle_\nu$, where we assumed the pump field is in a coherent state $\alpha(\omega_p)$, which is a good description for a classical laser beam. On the contrary, the modes of the generated twin photons are initially in a vacuum state, since SPDC is a spontaneous process. By definition, a coherent state verifies: $\hat{a}_p(\omega_p)\,|\alpha(\omega_p)\rangle_p = \alpha(\omega_p)\,|\alpha(\omega_p)\rangle_p$, hence

$$\hat{a}_p(\omega_p)\,|\Psi(0)\rangle = \alpha(\omega_p)\,|\Psi(0)\rangle\,. \tag{5.12}$$

This implies that $|\Psi(0)\rangle$ is an eigenstate of the free Hamiltonian (5.1) with eigenvalue $\alpha(\omega_p)$. The function $\alpha(\omega_p)$ can simply be interpreted as the spectrum of the pump field. Consequently, the initial state in the interaction picture remains unchanged:

$$\left|\Psi^{(I)}(0)\right\rangle = e^{i\hat{H}_I t/\hbar}\,|\Psi(0)\rangle = |\alpha(\omega_p)\rangle_p \otimes |\mathrm{vac}\rangle_\mu \otimes |\mathrm{vac}\rangle_\nu\,, \tag{5.13}$$

where we omitted the global phase factor in the last equality.

We are only interested in the vacuum and two-photon contribution of $|\Psi\rangle_{\text{steady-state}}$. Thus we expand the exponential in (5.11) as a Taylor series and only keep the first two terms:

$$\begin{aligned}|\Psi\rangle_{\text{steady-state}} &\approx \left[1 - \frac{i}{\hbar}\int_{-\infty}^{+\infty}\mathrm{d}\tau \hat{H}_I^{(I)}(\tau)\right]|\Psi(0)\rangle\\ &= \left\{1 + \left[\Gamma\iiint \mathrm{d}\omega_p\mathrm{d}\omega_1\mathrm{d}\omega_2\left(\int_{-\infty}^{+\infty}\mathrm{d}\tau e^{-i(\omega_p-\omega_1-\omega_2)\tau}\right)\right.\right.\\ &\quad \left.\left.\Phi_{\mathrm{PM}}(\omega_p,\omega_1,\omega_2)\hat{a}_p(\omega_p)\hat{a}^\dagger_\mu(\omega_1)\hat{a}^\dagger_\nu(\omega_2) - \mathrm{H.c.}\right]\right\}|\Psi(0)\rangle\end{aligned} \tag{5.14}$$

[1] The proof is straightforward. Using the Baker-Campbell-Hausdorff formula : $e^{\hat{X}}\hat{Y}e^{-\hat{X}} = Y + [X,Y] + \frac{1}{2!}[X,[X,Y]] + \frac{1}{3!}[X,[X,[X,Y]]] + ...$, one can show that for any ladder operators $\hat{a},\hat{a}^\dagger$ satisfying $[\hat{a},\hat{a}^\dagger] = 1$ and κ a scalar, one gets $e^{\kappa\hat{a}\hat{a}}\hat{a}e^{-\kappa\hat{a}\hat{a}} = e^{-\kappa}\hat{a}$ and $e^{\kappa\hat{a}\hat{a}}\hat{a}^\dagger e^{-\kappa\hat{a}\hat{a}} = e^{\kappa}\hat{a}^\dagger$.

By using equation (5.12) along with the identity

$$\int_{-\infty}^{+\infty} \mathrm{d}\tau e^{-i(\omega_p-\omega_1-\omega_2)\tau} = \delta(\omega_p-\omega_1-\omega_2), \tag{5.15}$$

we further simplify the expression to:

$$\begin{aligned} |\Psi\rangle_{\text{steady-state}} = \Big\{1 + \Big[\Gamma \iint \mathrm{d}\omega_p \mathrm{d}\omega_1 \mathrm{d}\omega_2 \delta(\omega_p-\omega_1-\omega_2) \\ \Phi_{\text{PM}}(\omega_p,\omega_1,\omega_2)\alpha(\omega_p)\hat{a}^\dagger_\mu(\omega_1)\hat{a}^\dagger_\nu(\omega_2) - \text{H.c.}\Big]\Big\}|\Psi(0)\rangle\,. \end{aligned} \tag{5.16}$$

Finally, by carrying out the integral on ω_p and dropping the vacuum contribution, the state generated by the SPDC process can be written:

$$|\Psi\rangle_{\text{SPDC}} = \iint \mathrm{d}\omega_1 \mathrm{d}\omega_2 \mathcal{C}(\omega_1,\omega_2)\hat{a}^\dagger_\mu(\omega_1)\hat{a}^\dagger_\nu(\omega_2)\,|\text{vac}\rangle\,. \tag{5.17}$$

The complex function $\mathcal{C}(\omega_1,\omega_2)$ is called the joint spectral amplitude (JSA) and can be expressed as:

$$\mathcal{C}(\omega_1,\omega_2) = \alpha(\omega_1+\omega_2)\Phi_{PM}(\omega_p,\omega_1,\omega_2)\big|_{\omega_p=\omega_1+\omega_2}. \tag{5.18}$$

The JSA is normalized to unity $\iint \mathrm{d}\omega_1 \mathrm{d}\omega_2 |\mathcal{C}(\omega_1,\omega_2)|^2 = 1$ and it admits a simple physical interpretation: the probability of generating a photon pair at frequency (ω_1,ω_2) is given by the modulus square of the JSA $|\mathcal{C}(\omega_1,\omega_2)|^2$. This quantity, is also referred to as the joint spectral intensity (JSI). In practice, the JSA contains all the information on the generated two-photon state, including spectral correlations between the photons and polarization entanglement.

5.2 Properties of the JSA

5.2.1 Pump spectrum

In all the experiments presented in this dissertation, the AlGaAs SPDC source was pumped using a narrowband continuous-wave laser (CW) with a linewidth $\Delta\nu_p = 100\,\text{kHz}$. The laser spectrum has a Lorentzian lineshape which is expressed as:

$$\alpha(\omega) = \frac{1}{\pi\Delta\omega_p}\left[\frac{\Delta\omega_p^2}{(\omega-\omega_p)^2+\Delta\omega_p^2}\right], \tag{5.19}$$

with $\Delta\omega_p = 2\pi\Delta\nu_p$. Since the FWHM of the laser line is very narrow compared to the bandwidth of the emitted photons, the pump spectrum will essentially be nonzero only along the anti-diagonal: $\omega_1+\omega_2 = \omega_p$. The resulting quantum state will therefore be strongly anti-correlated. To a good approximation, we can assume that the lineshape of the laser is described by a Dirac delta distribution:

$$\alpha(\omega) \approx \delta(\omega-\omega_p). \tag{5.20}$$

5.2.2 JSA in the rotated (ω_+,ω_-) basis

In this regime, it can be useful to express the JSA in the rotated basis:

$$\begin{aligned} \omega_+ &= \omega_1+\omega_2, \\ \omega_- &= \omega_1-\omega_2. \end{aligned} \tag{5.21}$$

Using these new coordinates, the JSA can be rewritten as [149]:

$$\mathcal{C}(\omega_+, \omega_-) = f_+(\omega_+) f_-(\omega_-), \tag{5.22}$$

where f_+, f_- can be determined by identifying term by term this expression to Eq. (5.18). Note that the transformation in Eq. (5.21) is not strictly speaking a rotation since it does not preserve the norm. However, this basis is the most natural for expressing the JSA since the coordinate ω_+ reflects directly the energy conservation condition.

Essentially, the expression of $f_+(\omega_+)$ will be dictated by the pump spectrum while $f_-(\omega_-)$ will depend on the phase-matching function. If we use the narrow pump approximation of Eq. (5.20), then we simply obtain:

$$f_+(\omega_+) = \delta(\omega_+ - \omega_p). \tag{5.23}$$

In this case, the quantum state becomes:

$$|\Psi\rangle = \int \mathrm{d}\omega_- f_-(\omega_-) \hat{a}_\mu(\omega_p + \omega_-) \hat{a}_\nu(\omega_p - \omega_-) \left|\mathrm{vac}\right\rangle . \tag{5.24}$$

We see that, under these assumptions, the JSA is fully determined by $f_-(\omega_-)$. This function is given by taking a cut of the phase-matching function $\Phi_{\mathrm{PM}}(\omega_+, \omega_-)$ along the line defined by $\omega_+ = \omega_p$.

5.2.3 Approximate expression for the wave-vector mismatch Δk

To have a physical intuition on how phase-matching conditions influence the shape of the JSA, it can be useful to derive an approximate analytical expression for the wave-vector mismatch Δk entering in the formula for the phase-matching function. More details on this derivation can be found in Ref. [150].

We consider the case of Type II SPDC since it will be the process that will be used in the experiments described in this manuscript. The wave-vector mismatch reads:

$$\begin{aligned} \Delta k &= k_p - k_H - k_V \\ &= \frac{1}{c} \left[\omega_p n_p(\omega_p) - \omega_H n_H(\omega_1) - \omega_V n_V(\omega_2) \right], \end{aligned} \tag{5.25}$$

where n_p, n_H, n_V are respectively the effective mode indices of the pump Bragg TE, fundamental TE and fundamental TM modes of the waveguide. To simplify this expression, we make several assumptions:

- The effective mode indices for the fundamental TE and TM modes have a linear dispersion in the spectral region of interest. Hence for a small variation of frequency $\delta\omega$ we have:

  $$n_i(\omega + \delta\omega) = n_i(\omega) + \delta\omega \frac{\mathrm{d}n_i}{\mathrm{d}\omega}, \tag{5.26}$$

  with $i = H, V$. This assumption is justified when inspecting the simulated modal dispersion curves in Fig. 4.5, which indeed can be considered linear in a good approximation. A corollary is that the fundamental mode birefringence, given by the difference in effective mode index between the TE and TM fundamental modes, is a constant:

  $$n_H(\omega) - n_V(\omega) \equiv \Delta n. \tag{5.27}$$

- The fundamental TE and TM modes have the same modal dispersion, meaning that:

$$\frac{\mathrm{d}n_H}{\mathrm{d}\omega} = \frac{\mathrm{d}n_V}{\mathrm{d}\omega} \equiv \frac{\mathrm{d}n}{\mathrm{d}\omega}. \tag{5.28}$$

  Again, Fig. 4.5 shows that the two lines corresponding to n_H and n_V are nearly parallel, which corroborates this assumption.

Using the two approximations given in Eqs. (5.26) and (5.28), we can split the expression for Δk into three terms:

$$\Delta k = \Delta k_{\mathrm{modal}}(\omega_+) + \Delta k_{\mathrm{birefringence}}(\omega_-) + \Delta k_{\mathrm{dispersion}}(\omega_-). \tag{5.29}$$

The expression of those terms is given by:

$$\Delta k_{\mathrm{modal}}(\omega_+) = \frac{\omega_+}{c}\Delta n_{\mathrm{modal}}(\omega_+) = \frac{\omega_+}{c}\left[n_p(\omega_+) - \frac{n_H(\omega_+/2) + n_V(\omega_+/2)}{2}\right], \tag{5.30}$$

$$\Delta k_{\mathrm{birefringence}}(\omega_-) = -\frac{\omega_-}{2c}\Delta n = -\frac{\omega_-}{2c}\left[n_H(\omega_+/2) - n_V(\omega_+/2)\right], \tag{5.31}$$

$$\Delta k_{\mathrm{dispersion}} = -\frac{\omega_-^2}{2c}\frac{\mathrm{d}n}{\mathrm{d}\omega}. \tag{5.32}$$

The term $\Delta k_{\mathrm{modal}}$ is proportional to the mismatch between the pump mode index and the average of the fundamental TE and TM mode indices. $\Delta k_{\mathrm{birefringence}}$ arises from the birefringence between the TE and TM telecom modes. Finally, $\Delta k_{\mathrm{dispersion}}$ represents the wavevector mismatch coming from the chromatic dispersion of the modes. We combine all of those terms in a single expression in the (ω_+, ω_-) basis:

$$\Delta k = \frac{\omega_+}{c}\Delta n_{\mathrm{modal}}(\omega_+) - \frac{\omega_-}{2c}\Delta n - \frac{\omega_-^2}{2c}. \tag{5.33}$$

We see that the wave-vector mismatch has a polynomial dependence on ω_-. Hence the region of (ω_+, ω_-) space for which perfect phase matching $\Delta k = 0$ is verified will have the shape of a parabola. In addition, we notice that the birefringence term introduces an asymmetry of the phase-matching function with respect to $\omega_- = 0$. Indeed, Δn enters in the first order term in ω_- and it is clear that if $\Delta n = 0$ then $\Delta k \propto \omega_-^2$. In that case, the phase matching function and hence the JSA become symmetric in ω_-. As we will see, the presence of birefringence results in an asymmetry of the JSA.

5.3 Numerical simulation of the JSA

5.3.1 Without cavity effects

We simulate the JSA for a Type II SPDC process using the numerically calculated effective indices of the interacting modes. In Fig. 5.1 (a), we plot the simulated JSI for an AlGaAs waveguide in the narrow pump regime. We see that we have a strongly anti-correlated state, which stems from the narrow bandwidth of the pump, with a degeneracy frequency, for which $\omega_- = 0$, of $\omega_d = \omega_p/2 = 198 \times 2\pi\mathrm{THz}$.

In Fig. 5.1 (b-d), we detail the different ingredients defining the structure of the JSA. A simulation of the phase matching function Φ_{PM} is shown in Fig. 5.1 (b). We observe that the phase-matching function has indeed the characteristic parabolic shape that was predicted from Eq. (5.33). The simulated pump spectrum and corresponding JSA are shown in in Fig. 5.1 (c-d). The bandwidth of the two-photon state is $\Delta\omega = 8\,\mathrm{THz}$

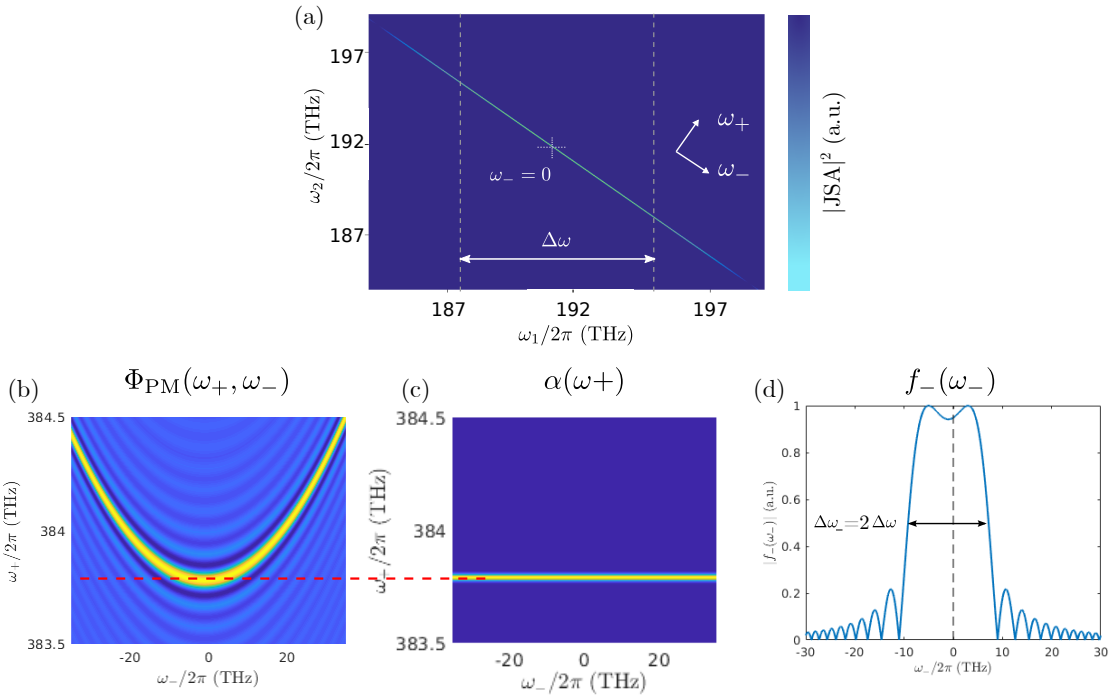

Figure 5.1: (a) Simulated joint spectral intensity in the (ω_1, ω_2) basis for a source in the narrow pump regime. For the sake of clarity, the pump bandwidth value has been taken much larger that what it should be (10 GHz instead of 100 kHz) to be able to visualize the totality of the JSI on a single plot. (b) Simulated phase-matching function Φ_{PM} in the (ω_+, ω_-) basis. (c) Simulated pump spectrum for $\omega_p/2\pi = 383.8$ THz. Again, here the value of the pump bandwidth is not to scale. (d) Corresponding antidiagonal profile $f_-(\omega_-)$ of the joint spectral amplitude.

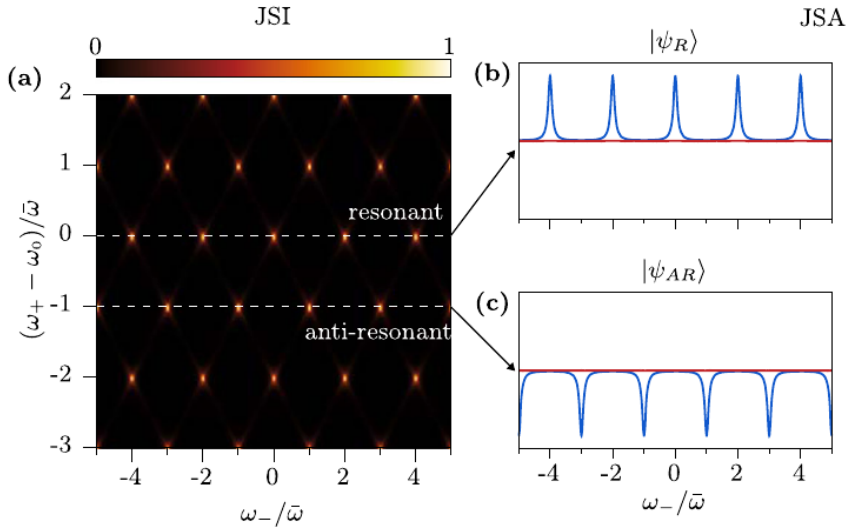

Figure 5.2: (a) Frequency grid resulting from the product of the cavity transmission functions for the two photons present in the expression of the JSA in Eq. (5.34). Dashed lines indicate two possible values of the pump frequency used to generate a resonant or anti-resonant BFC. (b) JSA of a resonant BFC. (c) JSA of an anti-resonant BFC (blue line: real part, red line: imaginary part. Figure from Ref.[87]).

corresponding to $\Delta\lambda = 60\,\text{nm}$. An important feature of the JSA generated by our source is that it is slightly asymmetric with respect to $\omega_- = 0$. This can be seen from the plots of $f_-(\omega_-)$, where the $\omega_- = 0$ axis has been indicated with a black dashed line. This asymmetry is a direct consequence of the waveguide birefringence as explained in the previous section.

5.3.2 With cavity effects

In this paragraph, we give a more accurate description of the JSA by taking into account the fact that the two end facets of the waveguide act like the two mirrors of a cavity. When photons are emitted by SPDC within an optical cavity, they bounce back and forth between the mirrors before exiting the system, like light in a Fabry-Perot resonator. Another way picture this is to consider that the cavity presents discrete resonances and that the SPDC photons can only be generated in the cavity modes corresponding to those resonances. Hence we expect that the resonances of the cavity will appear in the joint spectrum of the emitted photon-pairs.

To describe this situation, we add an additional factor to the expression of the JSA given in Eq. (5.18). The JSA $\tilde{\mathcal{C}}(\omega_1, \omega_2)$ in the presence of a cavity can be expressed as:

$$\tilde{\mathcal{C}}(\omega_1, \omega_2) = t_H(\omega_1) t_V(\omega_2) \alpha(\omega_1 + \omega_2) \Phi_{PM}(\omega_p, \omega_1, \omega_2)\big|_{\omega_p = \omega_1 + \omega_2}. \tag{5.34}$$

where the functions t_H, t_V are simply the amplitude transmission coefficient of H and V polarized light after traveling through a cavity:

$$t_H(\omega) = \frac{(1 - R_H) e^{i\omega\tau_H(\omega)/2}}{1 - R_H e^{i\omega\tau_H(\omega)}}, \tag{5.35}$$

$$t_V(\omega) = \frac{(1 - R_V) e^{i\omega\tau_V(\omega)/2}}{1 - R_V e^{i\omega\tau_V(\omega)}}, \tag{5.36}$$

with the round-trip time τ_i defined as $\tau_i(\omega) = 2n_i(\omega)L/c$ where $n_i(\omega)$ is the effective index of mode $i = H, V$. The transmission function consists of a series of discrete peaks spaced by $\bar{\omega} = 2\pi/\tau$, which is the free spectral range of the cavity. Hence the product of the two cavity factors in Eq. (5.34) will result in a two-dimensional grid in frequency space. This is shown in Fig. 5.2 (a) where we plot the product of the two cavity functions in the (ω_+, ω_-) basis for values of the fundamental TE and TM mode reflectivity of $R_H = R_V = 0.8$. These values are higher than the simulated modal reflectivity for an AlGaAs waveguide given in Section 4.2 and have been chosen such as to give a clear picture of the cavity effects on the JSA. The resulting JSA is plotted in Fig. 5.2 (b-c). We see that it features a series of peaks spaced by $2\bar{\omega}$. Hence, taking into account all the terms of Eq. (5.34), the JSA is given by the product of this comb structure and the bell-shaped envelope of the phase-matching function shown in Fig. 5.1 (d).

This property of the JSA suggests that the emitted state can be seen as a biphoton frequency comb (BFC), the quantum analog of an optical frequency comb. This kind of quantum states of light has been first investigated by Ou and coworkers [151] and recently received growing attention from the integrated quantum photonics community thanks to their potential applications in quantum computing and communications [134, 114, 87]. One can generate different kinds of BFC by changing the value of the pump frequency as indicated in Fig. 5.2 (b-c). Two particular cases are highlighted here: resonant BFC, for which there is a cavity resonance at $\omega_- = 0$ and anti-resonant BFC for which there is no cavity resonance at ω_-. As will be seen later in Section 6.4, this ability to control the comb by changing the pump frequency can be used to manipulate the symmetry of the quantum-state.

5.4 Polarization entanglement

Now that we discussed in details the spectral correlation between photons generated by our source, we investigate polarization entanglement created by a Type II interaction. In this case, the quantum state reads:

$$|\Psi\rangle = \iint_{-\infty}^{+\infty} \mathrm{d}\omega_1 \mathrm{d}\omega_2 \mathcal{C}(\omega_1, \omega_2) \, |\omega_1, H\rangle \, |\omega_2, V\rangle \,, \tag{5.37}$$

where $|\omega, H\rangle = a_H^\dagger(\omega) \, |\mathrm{vac}\rangle$ and $|\omega, V\rangle = a_V^\dagger(\omega) \, |\mathrm{vac}\rangle$. In the case of a narrowband pump, the state can be rewritten in the (ω_+, ω_-) basis:

$$|\Psi\rangle = \int_{-\infty}^{+\infty} \mathrm{d}\Omega \Phi(\Omega) \, |\omega_d + \Omega, H\rangle \, |\omega_d - \Omega, V\rangle \,, \tag{5.38}$$

where we defined for convenience $\omega_d = \omega_p/2$ the degeneracy angular frequency, $\Omega = \omega_-/2$ the detuning with respect to the degeneracy and $\Phi(\Omega) = f_-(\omega_-)$. To reveal polarization entanglement, we rewrite the state as a continuous superposition of bipartite polarization-entangled states. To do so, we split the summation in Eq. (5.38) into two parts using the identity: $\int_\infty^\infty = \int_0^\infty - \int_0^{-\infty}$ then make the change of variable $\Omega \to -\Omega$ into the second term and finally recombine the two integrals to obtain:

$$\begin{aligned} |\Psi\rangle = \int_0^\infty \mathrm{d}\Omega \, [&\Phi(\Omega) \, |\omega_d + \Omega, H\rangle \, |\omega_d - \Omega, V\rangle \\ &+ \Phi(-\Omega) \, |\omega_d + \Omega, V\rangle \, |\omega_d - \Omega, H\rangle] \,. \end{aligned} \tag{5.39}$$

This expression can be seen as a continuous sum of polarization $|\Psi^+\rangle$ Bell states that are distributed over the whole two-photon spectral bandwidth. We see that the JSA, encapsulated in the function $\Phi(\Omega)$, plays a crucial role in the structure of the polarization-entangled state emitted by our device. In particular we see that the state is maximally entangled over the whole bandwidth only if the JSA is perfectly symmetric: $\Phi(\Omega) = \Phi(-\Omega)$. However, we have seen that a slight asymmetry in the JSA arises from the birefringence of our device, which is detrimental to the quality of polarization entanglement.

To assess the quality of the entangled state generated by our source, we calculate the fidelity F to a $|\Psi^+\rangle$ Bell state and the concurrence C, defined in Section 3.2. Since the state is spectrally broadband, we want to obtain a value for these measures of entanglement as a function of the signal and idler frequency. To this end, we define a grid of energy-conjugate bins of fixed width Δ and central frequency $\omega_d \pm \Omega_0$ spanning the spectral range of the quantum state, and compute F and C over all these different bins. For a given value of Ω_0, we label by A the signal photons within the frequency window $[\omega_d + (\Omega_0 - \Delta/2), \omega_d + (\Omega_0 + \Delta/2)]$ and by B the idler photons within the frequency window $[\omega_d - (\Omega_0 + \Delta/2), \omega_d - (\Omega_0 - \Delta/2)]$. The resulting post-selected quantum state takes the form:

$$\begin{aligned}\left|\Psi'\right\rangle = \int_0^\infty \mathrm{d}\Omega f(\Omega) \left[\Phi(\Omega) \left|\omega_d + \Omega, H\right\rangle_A \left|\omega_d - \Omega, V\right\rangle_B \right. \\ \left. + \Phi(-\Omega) \left|\omega_d + \Omega, V\right\rangle_A \left|\omega_d - \Omega, H\right\rangle_B\right],\end{aligned} \tag{5.40}$$

with $f(\Omega)$ a rectangular distribution:

$$f(\Omega) = \begin{cases} 1, & \text{for } \Omega \in [\Omega_0 - \Delta/2, \Omega_0 + \Delta/2], \\ 0, & \text{elsewhere.} \end{cases} \tag{5.41}$$

The corresponding density operator is $\tilde{\rho} = |\Psi'\rangle \langle\Psi'|$. Following the approach of Ref. [152], we compute the reduced polarization density matrix ρ by tracing out the frequency part of the density operator:

$$\rho = \frac{1}{\mathcal{N}} \iint \mathrm{d}\omega' \mathrm{d}\omega''_A \left\langle\omega'\right|_B \left\langle\omega''\right| \tilde{\rho} \left|\omega''\right\rangle_B \left|\omega'\right\rangle_A, \tag{5.42}$$

with $\mathcal{N}$ a normalization constant. After some straightforward algebra, one obtains:

$$\begin{aligned}\rho = \alpha \left|HV\right\rangle_{ABAB} \left\langle HV\right| + \mathcal{D} \left|HV\right\rangle_{ABAB} \left\langle VH\right| \\ + \mathcal{D}^* \left|VH\right\rangle_{ABAB} \left\langle HV\right| + \beta \left|VH\right\rangle_{ABAB} \left\langle VH\right|,\end{aligned} \tag{5.43}$$

where the 4 non-zero matrix elements are:

$$\alpha = \frac{1}{\mathcal{N}} \int_0^\infty \mathrm{d}\Omega f(\Omega) |\Phi(\Omega)|^2, \tag{5.44}$$

$$\beta = \frac{1}{\mathcal{N}} \int_0^\infty \mathrm{d}\Omega f(\Omega) |\Phi(-\Omega)|^2, \tag{5.45}$$

$$\mathcal{D} = \frac{1}{\mathcal{N}} \int_0^\infty \mathrm{d}\Omega f(\Omega) \Phi(\Omega) \Phi^*(-\Omega), \tag{5.46}$$

and the normalization constant is set to $\mathcal{N} = \int_0^\infty \mathrm{d}\Omega f(\Omega) \left[|\Phi(\Omega)|^2 + |\Phi(-\Omega)|^2\right]$ such that $\mathrm{Tr}\,\rho = 1$.

In Fig. 5.3, we display simulations of the fidelity F and concurrence C as a function of detuning Ω to biphoton degeneracy in the presence and in the absence of cavity effects. We computed the values over a frequency grid with of bin width $\Delta = 100\,\mathrm{GHz}$. We

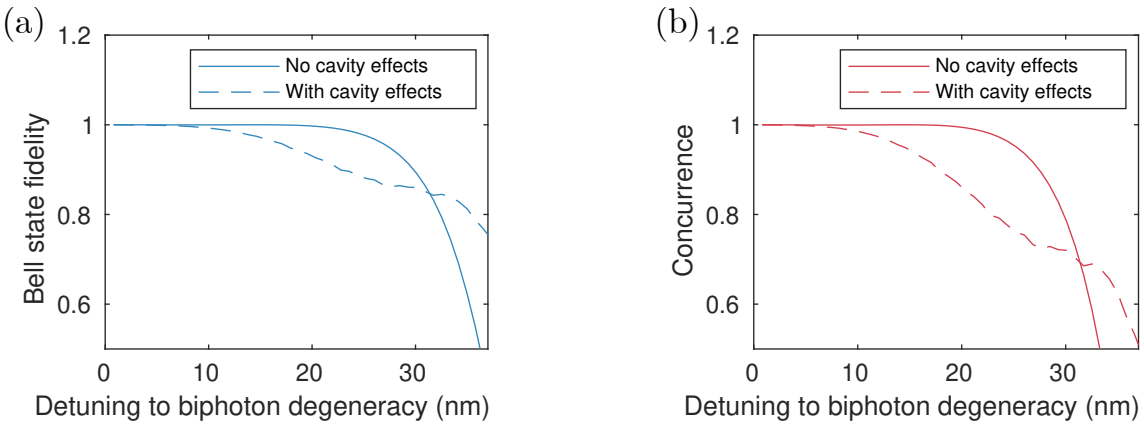

Figure 5.3: (a) Simulated fidelity F to a $|\Psi^+\rangle$ Bell state and (b) Concurrence as a function of detuning to biphoton degeneracy for the two-photon state emitted by the AlGaAs source.

see that both quantities remain very close to 1 in a broad region around the biphoton degeneracy before dropping sharply for a detuning value of around 30 nm detuning. As stated earlier, this drop is the result of the asymmetry of the JSA induced by waveguide birefringence. We see from the dashed lines in Fig. 5.3 (a-b) that cavity effects result in a faster decrease of the entanglement with detuning. This can be understood intuitively by considering that, due to birefringence and chromatic dispersion, the resonances of the cavity for TE and TM photons are not perfectly lined up with the antidiagonal defined by energy conservation, resulting in extra asymmetries in specific regions of the JSA.

The entanglement bandwidth can be increased in several ways. To get rid of cavity effects, our group has been developing anti-reflection coatings based on SiO that can be deposited on the facets of the waveguide. In addition, an optimization of the device structure could be carried out in order to reduce the birefringence and broaden the phase-matching bandwidth.

Chapter 6

Experimental characterization of the biphoton state

Contents

6.1 Pair generation rate and CAR 77
6.2 Spectral indistinguishability and biphoton bandwidth: Hong-Ou-Mandel (HOM) effect 82
6.3 Joint spectral intensity (JSI) reconstruction by stimulated emission tomography 90
6.4 HOM and BFC state symmetry 91

In this chapter, we present the techniques that were used to experimentally characterize the photon pairs generated by the AlGaAs source. We first describe our setup and data processing method for photon-counting experiments before highlighting the performance of our device in terms of brightness and coincidence to accidental ratio (CAR). Then we introduce Hong-Ou-Mandel (HOM) interferometry and show how the biphoton bandwidth and indistinguishability can be assessed using this effect. Finally, we present our results on experimental reconstruction of the JSI using stimulated emission tomography before turning to measurements of HOM revivals and their physical interpretation in terms of biphoton frequency combs.

6.1 Pair generation rate and CAR

6.1.1 Experimental setup

We start by describing the basic setup that is used to measure time correlations between the photons emitted by SPDC. The experiment is sketched in Fig. 6.1. An AlGaAs waveguide is pumped with a tunable CW diode laser (TOPTICA TM Photonics DL pro 780) which is coupled into the waveguide through a microscope objective (NA = 0.95, 63×). In order to generate pairs through SPDC, the frequency of the pump laser is set to the phase-matching resonance of the device. Light emerging from the end facet of the waveguide is collected with a second microscope objective (NA = 0.65) and sent to a fiber coupler, after filtering out the pump wavelength with a high pass filter. Just like in the SHG experiment, temperature is kept constant using a Peltier cell and a thermistor in a PID loop. In the case of Type II SPDC, the photon pairs are then split deterministically into two separate fibers using a fibered polarization controller (FPC) followed by a fibered polarizing beam

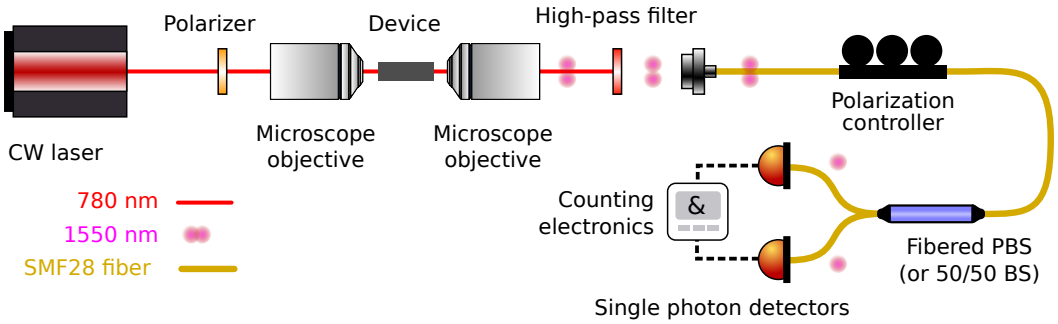

Figure 6.1: Sketch of the experimental setup for the measurement of temporal correlations in a SPDC process. Generated photon pairs are depicted as pink dots.

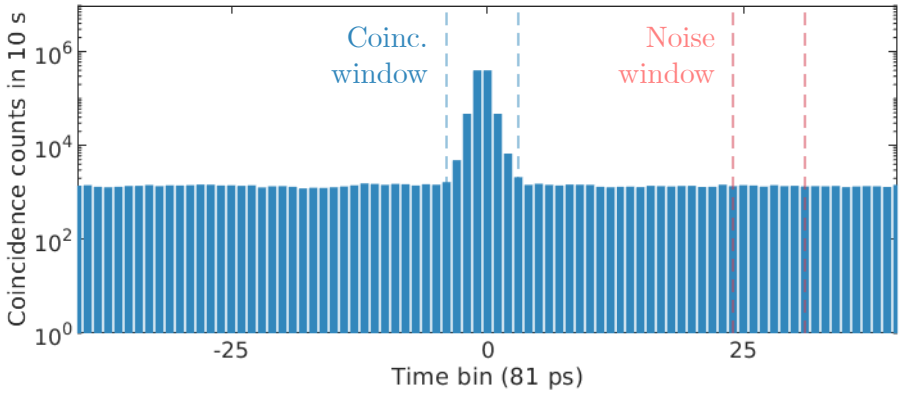

Figure 6.2: Time-correlation histogram acquired from sample `K7AD118`. The blue and red dashed lines delimit the post-processed coincidence and noise windows respectively.

splitter (FPBS). For Type I or 0 processes where photons have the same polarization, a conventional fibered 50/50 splitter is used (consequently dividing the coincidence rate by half). The photons are finally detected with superconducting nanowire single photon detectors (SNSPD, Quantum Opus) featuring a 85 % detection efficiency and $10\,\mathrm{s}^{-1}$ dark count rate.

The FPC is used to compensate polarization rotation in the fiber and ensure that the orthogonal polarization of the generated Type II photons matches the optical axes of the FPBS, reaching an optimal splitting. The FPC can be adjusted using several techniques. One can simply put a H or V polarizer before the collimator and adjust the FPC such that the single counts from SPDC are minimum at one output arm and maximum at the opposite arm. If the SPDC coincidence signal is strong enough, another possibility is to plug a fibered 50/50 BS to one of the output arms of the FPBS and adjust the FPC such as to minimize coincidence counts, making sure that photon pairs never end up in the same output arm of the FPBS.

6.1.2 Photon counting and data processing

The electrical pulses generated by the detectors upon detecting a photon are sent to a counting electronics unit, which will compute on-the-fly time-correlations between the clicks from both detectors. We used a time-to-digital converter (TDC, quTau) which counts the "start-stop" events within a fixed time buffer of about 4 µs with a temporal resolution of 81 ps. In some experiments, we also used a more advanced device called

time-tagger (Swabian Instruments). The latter has the ability to record the absolute time of the detection events with respect to a common reference. In our case, this can be interesting for experiments involving correlations between events that are separated by a very long time interval. Indeed, if this interval exceeds the size of the buffer of the TDC, we cannot record any time-correlations. On the other hand, the time-tagger record the absolute time-tags and sends it to the computer for correlation analysis thus getting rid of time buffer problem.

We collect data under the form of time-correlation histograms such as the one displayed in Fig. 6.2. To do so, we let the detectors and TDC acquire data during a fixed acquisition time τ. For each time bin of its buffer, the TDC will count the number of "start-stop" events that have occurred. When recording time correlation from photon pairs with perfectly correlated emission time, we expect all the coincidence events to occur within the same temporal bin. However, because of the combined timing jitter of the detectors and counting electronics, the coincidence peak in the histogram will span several time bins, typically between 5 and 10.

The number of recorded raw signal counts S will be defined as the total number of start-stop event within a user-defined coincidence window spanning Δ_s time bins around the coincidence peak, as shown in Fig. 6.2. Similarly, we define the number of noise counts N as the total number of start-stop events within a separate window spanning Δ_n time bins that is shifted away in time from the coincidence peak. By doing so, the noise counts will simply be a measure of the average number of background counts that are recorded, while the signal counts will be the number of coincidence counts that we attribute to true raw photon pair-detection events. Note that all this procedure is done at the post-processing stage. The raw coincidence rate is then obtained as:

$$R_{\text{raw}} = \frac{S}{\tau}. \tag{6.1}$$

The coincidence-to-accidental ratio is defined as the average number of signal counts per signal bin over the average number of noise counts per signal bin :

$$\text{CAR} = \frac{S}{N}\frac{\Delta_n}{\Delta_s}. \tag{6.2}$$

Finally, we can define a net coincidence rate which corresponds to the raw signal counts per unit time from which we subtracted the background noise counts :

$$R_{\text{net}} = \frac{1}{\tau}\left(S - N\frac{\Delta_s}{\Delta_n}\right) = S\left(1 - \frac{1}{\text{CAR}}\right). \tag{6.3}$$

6.1.3 Source performance

In Fig. 6.3, we show the measured coincidence counts and CAR as a function of input pump power. As we can see the number of recorded coincidence counts grows linearly with pump power while the CAR is inversely proportional to the pump power. This is the usual behavior of SPDC sources operated in the low pump power regime, where the double pair emission events are negligible [77].

To compare the brightness of our source to different photon-pair sources in the literature, we need to measure a figure of merit, the pair generation rate (PGR), that quantifies the intrinsic number of pairs generated per unit time regardless of experimental setup losses. In the literature, the PGR is usually obtained as the product between the measured coincidence rate and the transmission of the setup, including the coupling between

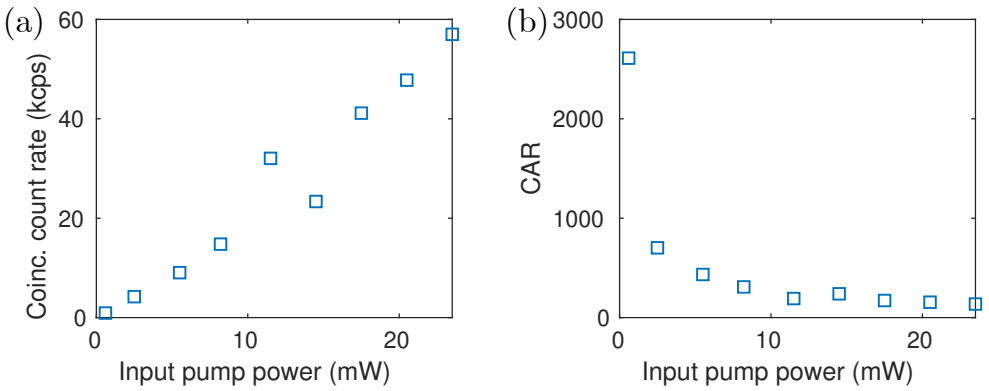

Figure 6.3: (a) Raw coincidence counts and (b) CAR as a function of input pump power for sample K7AD118 (kcps: kilo counts per second).

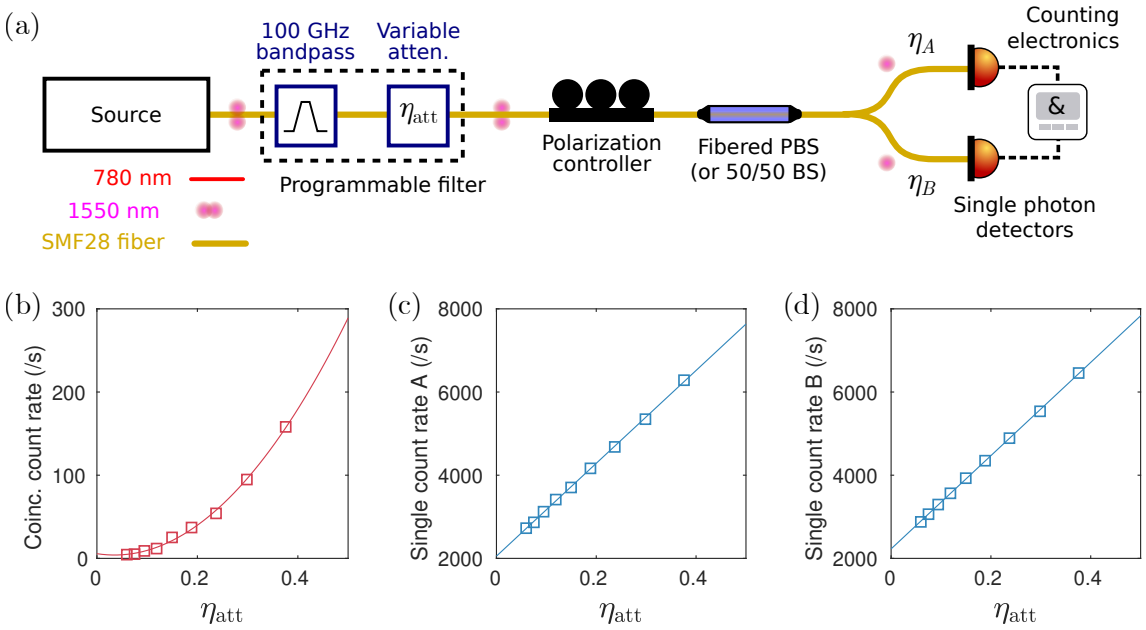

Figure 6.4: (a) Experimental setup for the measuremenf of the PGR. The bandpass filter and attenuation η_{att} are both implemented by a single programmable filter with controllable attenuation (Finisar Waveshaper 4000s). (b) Coincidence counts and (c-d) single counts as a function of applied attenuation η_{att} (sample `K7AD118`).

the waveguide facet and microscope objective, the propagation through optical components and the detector efficiency. However, the exact value of the coupling losses between the device and the objective that is used to collect the photons is hard to characterize.

Here we present a method, representing an extension of the model of Ref. [70], which only relies on coincidence measurements and which enables a more direct estimation of the PGR. The experimental setup is sketched in Fig. 6.4 (a). We send the photons from our source into a programmable filter with controllabed attenuation η_{att} (Finisar Waveshaper 4000s). The two photons are filtered in a 100 GHz window around the biphoton degeneracy before being separated using a FPBS and detected with SNSPDs. The photons in each arm, A or B, of the FPBS will experience different optical losses η_A, η_B. These coefficient take into account both propagation loss and detection efficiency. The PGR is obtained as:

$$\text{PGR} = \frac{R_{\text{net}}}{\eta_A \eta_B}. \tag{6.4}$$

We see that the estimation of the PGR relies on the knowledge of η_A, η_B. To measure those quantities, we record the number of coincidences and single counts at the output of the PBS as a function of applied attenuation η_{att}. If we denote by M the number of generated pairs per unit time, then the number of recorded coincidences and single counts is given by:

$$C = \eta_{\text{att}}^2 \eta_A \eta_B M, \tag{6.5}$$

$$S_A = \eta_{\text{att}} \eta_A M + d_A, \tag{6.6}$$

$$S_B = \eta_{\text{att}} \eta_B M + d_A. \tag{6.7}$$

where d_A, d_B are the dark count rates of the two detectors. By fitting our data to these formulas, we can obtain a value for η_A, η_B that will be used to estimate the PGR according to Eq. (6.4). Note that η_A and η_B are measured in a 100 GHz channel and not for the totality of the state emitted by the source. However, we can assume that η_A, η_B do not depend on the wavelength and that their value will be the same over the full two-photon state.

We experimentally measure $\eta_A = 11.8\,\%$ and $\eta_B = 11.7\,\%$. For a pump power of 20 mW we measure a maximum net coincidence rate of $R_{\text{net}} = 9.55 \times 10^4\,\text{s}^{-1}$ which corresponds to a pair generation rate and CAR of:

$$\begin{aligned} &\text{PGR} = 6.9 \times 10^6\,\text{s}^{-1}, \\ &\text{CAR} = 80. \end{aligned} \tag{6.8}$$

In principle, since the number of coincidences is proportional to the pump power, the PGR could be further increased at higher pump powers. However, when going to high powers, the strong intensity of the pump mode results in a heating of the waveguide, which will modify the phase-matching conditions and subsequently deteriorate the coincidence rate. In addition, there is a risk of damaging the waveguide when the pump power per unit area that is focussed on the facet is too large. Hence, the optimal value for the pump power in our case is around 20 mW and the values in Eq. (6.8) represent the peak performance of our source.

We can also quantify the performance of the source using the brightness, which is commonly used in the literature, given by the number of generated pairs per mW of internal pump power and per nm of bandwidth. In the measurements of Fig. 6.3 we displayed the pump power before the injection objective. Based on consideration on the transmission of the microscope objective and the waveguide facet, we estimate the internal

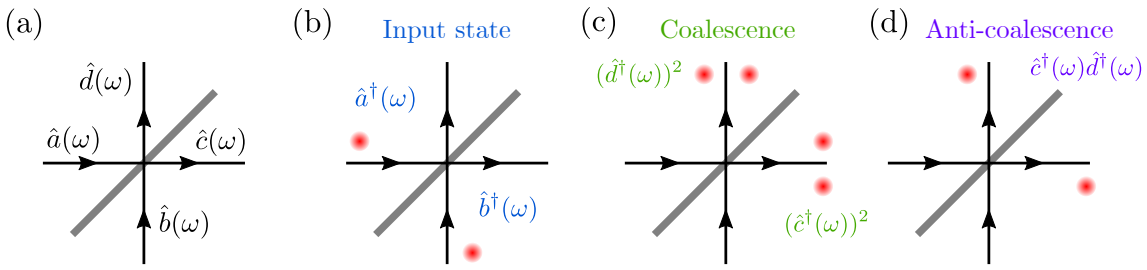

Figure 6.5: Sketch of the Hong-Ou-Mandel effect. (a) Spatial input and output modes on a beam splitter with associated annihilation operators. (b) Input state for the Hong-Ou-Mandel effect: two indistinguishable photons are incident on the beam splitter. (c) Photon coalescence (bunching): the two photons are exiting the beam-splitter by the same port. (d) Photon anti-coalescence (anti-bunching): the two photons are exiting the beam-splitter on opposite ports.

pump power to be around 600 µW for an input pump power of 20 mW [78]. From our simulations we know that the bandwidth of our state is 60 nm which gives us a brightness of about:

$$\text{Brightness} = 0.2 \times 10^6\,\text{s}^{-1}\,\text{mW}^{-1}\,\text{nm}^{-1}. \tag{6.9}$$

As a comparison, the brightest ppLN waveguide $\chi^{(2)}$ sources have a brightness of $250 \times 10^6\,\text{s}^{-1}\,\text{mW}^{-1}\,\text{nm}^{-1}$ for a total device length of 3 cm to 4 cm and SFWM sources in microring resonators using Si-based materials can reach up to $640 \times 10^6\,\text{s}^{-1}\,\text{mW}^{-1}\,\text{nm}^{-1}$ thanks to the enhancement provided by the resonator [53]. Note that this figure of merit tends to be disadvantageous for sources like AlGaAs waveguides exhibiting a broad bandwidth, which can be, nevertheless, an asset for certain applications. In Ref. [153] the authors develop an ultra-broadband source based on ppLN waveguides and use as an alternative indicator of performance the product PGR × CAR which in their case reaches a value of $8.0 \times 10^8\,\text{s}^{-1}$ for a bandwidth of 100 THz. As a comparison, our source operates at PGR × CAR $= 5.4 \times 10^8\,\text{s}^{-1}$, which is of the same order of magnitude but for a smaller bandwidth of 7 THz (60 nm).

6.2 Spectral indistinguishability and biphoton bandwidth: Hong-Ou-Mandel (HOM) effect

6.2.1 Derivation of the HOM coincidence probability

A quantum-mechanical effect that we extensively used to characterize the spectral properties of the emitted state is Hong-Ou-Mandel (HOM) interference. More specifically, HOM give us direct access to the bandwidth of the emitted photons and to their degree of spectral indistinguishability

Th basic idea of HOM is to split the photon of the pair into distinct spatial modes and recombine them on a beam splitter after adding a temporal delay τ to one of them. At the beam splitter output ports, one measures the probability of a coincidence event as a function of the applied delay. When this time delay is zero, and if they are perfectly indistinguishable, the probability of a coincidence event at the output of the beam splitter drops to zero. It means that the two photons always exit the beam splitter from the same output port. However, when the photons are not perfectly indistinguishable, the probability of coincidence is not exactly zero. It can be shown that as long as it remains

under 0.5 the effect cannot be explained by interference of classical fields. Hence, the value of the visibility in a HOM setup is at the same time a criterion for the non-classicality of two-photon state and a figure of merit for indistinguishability.

Let us now mathematically derive, following Refs. [154, 155], the HOM coincidence probability for a SPDC state with a JSA $\mathcal{C}(\omega_1, \omega_2)$ where the two photons occupy distinct spatial modes a, b with associated annihilation operators $\hat{a}(\omega), \hat{b}(\omega)$ as sketched in Fig. 6.5 (a-b). The initial quantum state reads:

$$|\Psi\rangle = \iint \mathrm{d}\omega_1 \mathrm{d}\omega_2 \mathcal{C}(\omega_1, \omega_2) \hat{a}^\dagger(\omega_1) \hat{b}^\dagger(\omega_2) |\mathrm{vac}\rangle . \tag{6.10}$$

An optical delay τ is applied to the photon in spatial mode a and the state becomes:

$$|\Psi\rangle = \iint \mathrm{d}\omega_1 \mathrm{d}\omega_2 \mathcal{C}(\omega_1, \omega_2) \hat{a}^\dagger(\omega_1) \hat{b}^\dagger(\omega_2) e^{-i\omega_1 \tau} |\mathrm{vac}\rangle , \tag{6.11}$$

where the phase factor accounts for the temporal delay in mode a. The photons then hit the beam splitter. As sketched in Fig. 6.5 (a-b), the input spatial modes of the beam splitter can be expanded onto the output modes c, d using the following transform :

$$\begin{aligned} \hat{a}(\omega) &= \frac{1}{\sqrt{2}} \left(\hat{c}(\omega) + \hat{d}(\omega) \right) , \\ \hat{b}(\omega) &= \frac{1}{\sqrt{2}} \left(\hat{c}(\omega) - \hat{d}(\omega) \right) . \end{aligned} \tag{6.12}$$

Using these relations, we can rewrite the state as:

$$\begin{aligned} |\Psi\rangle = \iint \mathrm{d}\omega_1 \mathrm{d}\omega_2 \mathcal{C}(\omega_1, \omega_2) e^{-i\omega_1 \tau} \frac{1}{2} \Big[& c^\dagger(\omega_1) c^\dagger(\omega_2) - d^\dagger(\omega_1) d^\dagger(\omega_2) \\ & - c^\dagger(\omega_1) d^\dagger(\omega_2) + d^\dagger(\omega_1) c^\dagger(\omega_2) \Big] |\mathrm{vac}\rangle . \end{aligned} \tag{6.13}$$

Since we are interested only in the coincidence events, we discard the first two terms, corresponding to photons ending up in the same output mode c or d. By splitting the summation using $\iint \mathrm{d}\omega_1 \mathrm{d}\omega_2 = \iint_{\omega_1 < \omega_2} \mathrm{d}\omega_1 \mathrm{d}\omega_2 + \iint_{\omega_1 > \omega_2} \mathrm{d}\omega_1 \mathrm{d}\omega_2 + \iint_{\omega_1 = \omega_2} \mathrm{d}\omega_1 \mathrm{d}\omega_2$ and inverting the variables ω_1, ω_2 in the second term, we obtain the following expression:

$$\begin{aligned} \left| \Psi' \right\rangle = \frac{1}{2} \iint_{\omega_1 < \omega_2} \mathrm{d}\omega_1 \mathrm{d}\omega_2 & \left[\mathcal{C}(\omega_1, \omega_2) e^{-i\omega_1 \tau} - \mathcal{C}(\omega_2, \omega_1) e^{-i\omega_2 \tau} \right] \\ & \left(c^\dagger(\omega_1) d^\dagger(\omega_2) - d^\dagger(\omega_1) c^\dagger(\omega_2) \right) |\mathrm{vac}\rangle . \end{aligned} \tag{6.14}$$

To calculate the coincidence probability, we define the projection operators [155]:

$$\hat{p}_c = \int \mathrm{d}\omega \hat{c}^\dagger(\omega) |\mathrm{vac}\rangle \langle \mathrm{vac}| \hat{c}(\omega), \tag{6.15}$$

$$\hat{p}_d = \int \mathrm{d}\omega \hat{d}^\dagger(\omega) |\mathrm{vac}\rangle \langle \mathrm{vac}| \hat{d}(\omega), \tag{6.16}$$

and the coincidence probability, in the case of a pure state, is given by:

$$P_c = \left\langle \Psi' \right| \hat{p}_c \otimes \hat{p}_d \left| \Psi' \right\rangle . \tag{6.17}$$

After some algebra, the total probability of finding the system in the post-selected state Eq. (6.14) is simply:

$$P_c = \frac{1}{4} \iint \mathrm{d}\omega_1 \mathrm{d}\omega_2 \left| \mathcal{C}(\omega_1, \omega_2) e^{-i\omega_1 \tau} - \mathcal{C}(\omega_2, \omega_1) e^{-i\omega_2 \tau} \right|^2 , \tag{6.18}$$

where we used the symmetry of $\left|\mathcal{C}(\omega_1,\omega_2)e^{-i\omega_1\tau}-\mathcal{C}(\omega_2,\omega_1)e^{-i\omega_2\tau}\right|^2$ with respect to subscript permutation to go back to an integral over the whole frequency domain. This equation can be rewritten:

$$P_c=\frac{1}{2}\left[1-\mathrm{Re}\iint \mathrm{d}\omega_1\mathrm{d}\omega_2\mathcal{C}^\star(\omega_1,\omega_2)\mathcal{C}(\omega_2,\omega_1)e^{-i(\omega_1-\omega_2)\tau}\right]. \tag{6.19}$$

If we assume that the single photon detectors have a flat frequency response and that their temporal resolution is much larger than the single photon coherence time, the coincidence rate between the two detectors at the output of the 50/50 beam splitter will be directly proportional to P_c

6.2.2 Physical interpretation of a HOM interferogram

HOM visibility and indistinguishability

The figure of merit for HOM interference is the visibility of the HOM dip, which is defined as:

$$V=\frac{P_c(\infty)-P_c(\tau=0)}{P_c(\infty)}=1-2P_c(\tau=0). \tag{6.20}$$

assuming $P_c(\infty)=1/2$. If we plug expression Eq. (6.19) evaluated at $\tau=0$ into this definition, we obtain:

$$V=2\mathrm{Re}\iint \mathrm{d}\omega_1\mathrm{d}\omega_2\mathcal{C}^\star(\omega_1,\omega_2)\mathcal{C}(\omega_2,\omega_1). \tag{6.21}$$

This integral can be seen as an overlap integral between the JSA and its transpose. When the JSA is perfectly symmetric with respect to the degeneracy frequency, this overlap integral is maximum. Hence, we clearly see that the HOM visibility is a direct way to quantify the indistinguishability of the generated two-photon wavepacket.

Coalescence and anti-coalescence

Furthermore at zero time delay $\tau=0$, the coincidence probability can exhibit several distinct behaviors depending on the symmetry of the JSA. Two special cases are represented schematically in Fig. 6.5 (c-d):

1. For $\mathcal{C}(\omega_1,\omega_2)=\mathcal{C}(\omega_2,\omega_1)$ we have $P_c=0$ (Photon coalescence or bunching)
2. For $\mathcal{C}(\omega_1,\omega_2)=-\mathcal{C}(\omega_2,\omega_1)$ we have $P_c=1$ (Photon anti-coalescence or anti-bunching)

The difference between the two regimes only comes from the JSA's phase. The phase has to change sign at $\omega_-=0$ to fulfill perfect anti-coalescence, while it is required to be flat for coalescence. In both cases, however, the overlap integral that comes up in the expression for the visibility given in Eq. (6.21) is maximum, and hence we obtain a 100 % visibility for either coalescence or anti-coalescence.

HOM and biphoton bandwidth

In addition, a HOM measurement allows to estimate the biphoton bandwidth of the emitted state. To illustrate this, we take the example of a symmetric anticorrelated gaussian JSA:

$$\mathcal{C}(\omega_+,\omega_-)=\delta(\omega_+-\omega_p)\exp\left(-2\omega_-^2/(2\Delta\omega_-)^2\right) \tag{6.22}$$

where $\Delta\omega_- = 2\Delta\omega$ with $\Delta\omega$ is the biphoton bandwidth. Then according to Eq. (6.19), the HOM coincidence probability becomes:

$$P_c(\tau) = \frac{1}{2}\left[1 - \exp\left(-\frac{1}{2}\tau^2\Delta\omega_-^2\right)\right]. \tag{6.23}$$

By inspecting Eq. (6.23), we see that the full width at half maximum $\Delta\tau$ of the HOM dip relates directly to the biphoton bandwidth:

$$\Delta\tau = \frac{1}{\sqrt{2}\Delta\omega_-}. \tag{6.24}$$

We see that HOM interferometry, in addition to being an elegant signature of two-photon interference, can be a powerful characterization tool, since a single HOM measurement allows us obtain directly the bandwidth of the two-photon state.

Examples

In Fig. 6.6, we show the calculated HOM coincidence probability for selected examples:

Perfectly symmetric JSA This is the kind of state that is described in the simple example of Eq. (6.22). Since the JSA is symmetric with respect to ω_- the two photons are spectrally indistinguishable. As a consequence P_c goes to zero, according to Eq. (6.19), and the dip visibility is 100 %. As shown in Eq. (6.24), the width of the dip is proportional to the inverse of the spectral bandwidth over which the photons are emitted. The simulations for this case are shown in Fig. 6.6 (a-b).

Perfectly antisymmetric JSA This case is similar to the first one, the only difference being the phase flip at ω_- responsible for anti-coalescence. Since the amplitude of the JSA is remains symmetric with respect to ω_-, we observe perfect anti-coalescence with unit visibility as can be seen from Fig. 6.6 (c-d).

Asymmetric JSA In this last example, we consider a state that is slightly asymmetric with respect to $\omega_- = 0$. As we have seen from the simulations in Fig. 5.1, this is the case for the JSA of the state emitted by our source. Since the JSA is asymmetric the two photon are slightly spectrally distinguishable. As a result, at $\tau = 0$, the coincidence probability does not reach zero and the dip visibility is less than 100 %. For a Type-II SPDC source, this asymmetry in the JSA is caused by birefringence as discussed in the previous chapter.

6.2.3 Measurement of HOM interference

Experimental setup and alignment procedure

In a HOM measurement, as sketched in Fig. 6.7, we use a similar setup as for SPDC except that the output fibers of the FPBS are sent into a fibered Mach-Zender interferometer. A free-space delay line is used to balance the optical path between the two arms. It consists of two collimators separated by a free space distance of around 1.5 m, one of which is mounted on a linear translation stage controlled by a stepper motor (Thorlabs). Translating the collimator by a distance z creates a temporal delay z/c. The smallest increment of our motor is 0.1 µm which corresponds to a temporal resolution of about 30 fs. After the delay line, the two fibers are recombined on a fibered 50/50 BS. The output of this second BS is finally sent to single photon detectors and counting electronics. Additional FPCs, labeled

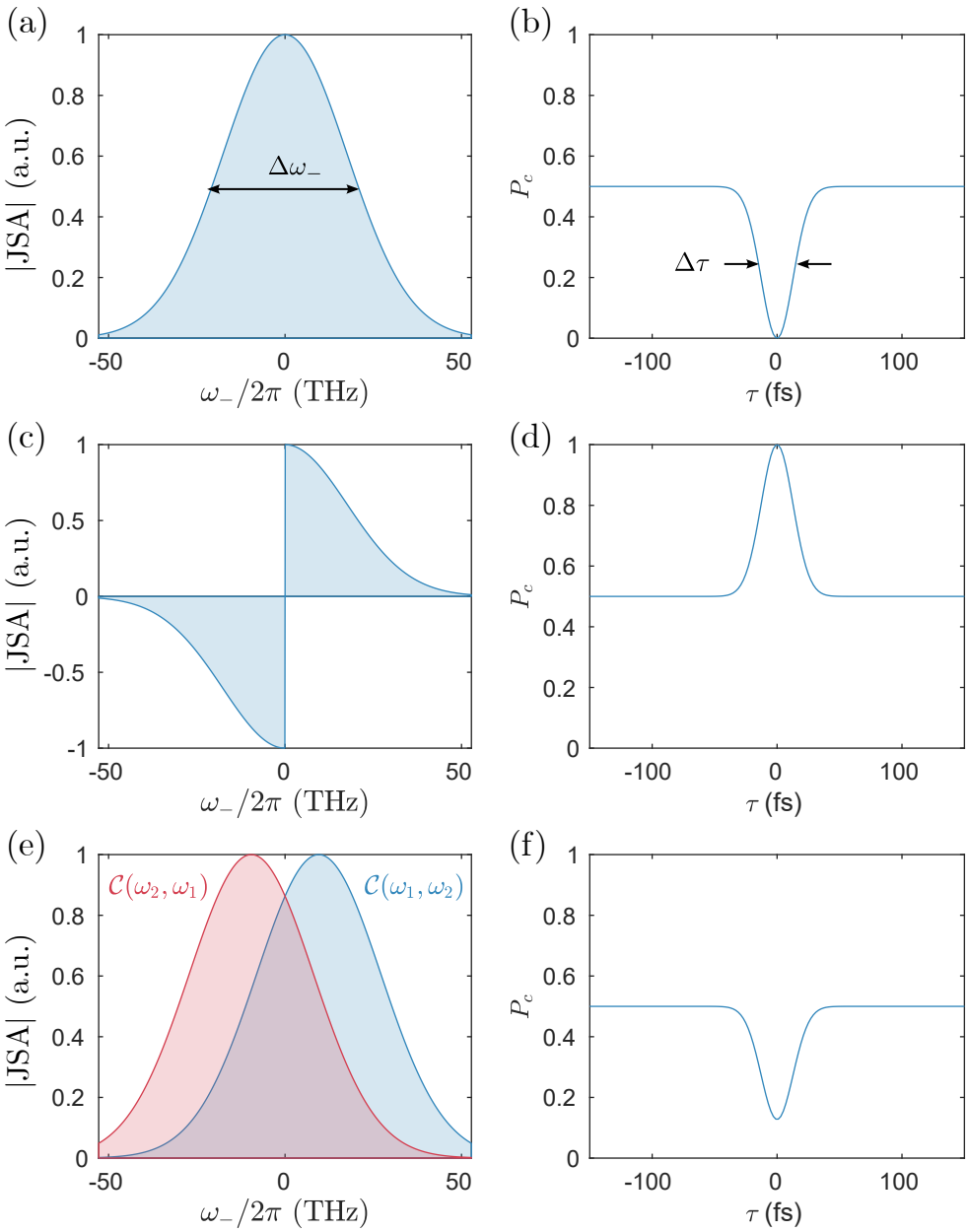

Figure 6.6: Examples of simulated gaussian JSA and HOM interferograms for (a-b) Perfectly symmetric anticorrelated state, exhibiting perfect HOM coalescence with 100 % visibility. (b-c) Perfectly anti-symmetric anticorrelated state, exhibiting perfect HOM anti-coalescence with 100 % visibility. (c-d) Asymmetric anticorrelated state, which exhibits HOM coalescence with reduced visibility. In (e) we plotted the JSA and its transpose to clearly show the asymmetry with respect to $\omega_- = 0$.

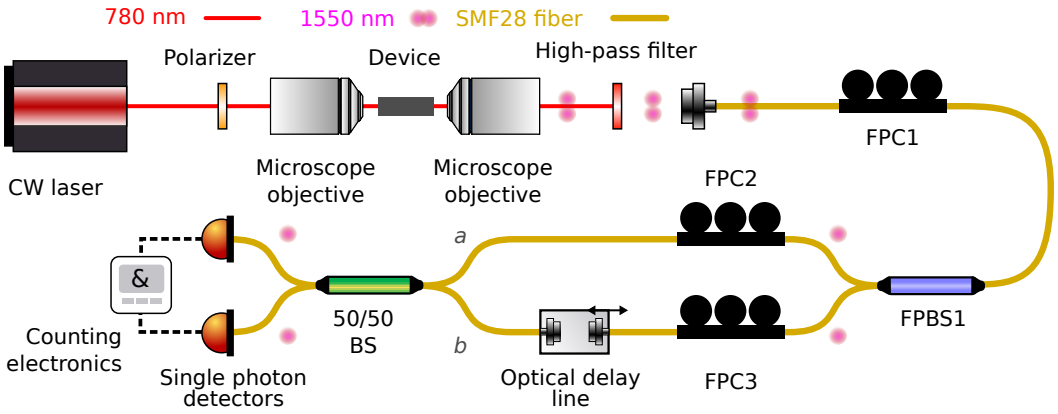

Figure 6.7: Sketch of the experimental setup for a HOM experiment.

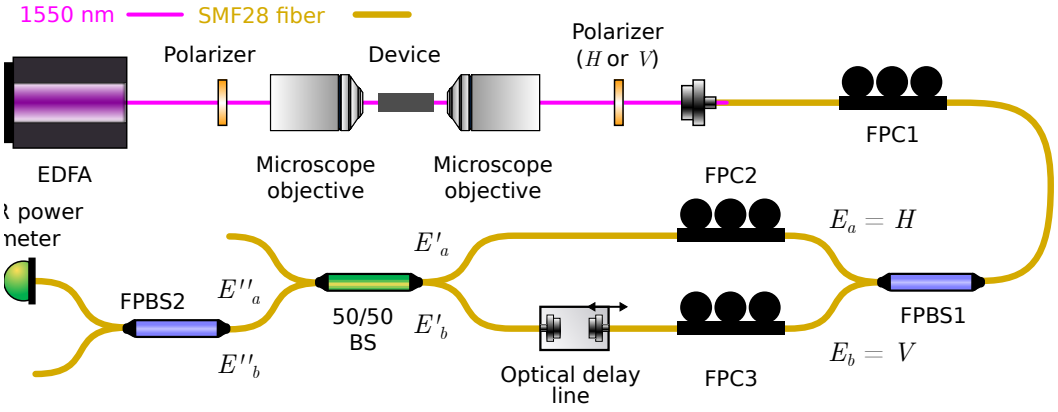

Figure 6.8: Sketch of the alignment procedure setup for a HOM experiment. We send the output of an EDFA successively in both arms of the HOM interferometer and adjust the FPCs 2 and 3 to minimize the recorded power at the output of one arm of FPBS2. By doing so, we ensure that the polarization of incoming photons are identical through the interferometer (see text for details).

FPC2 and FPC3 in Fig. 6.7, are inserted in the arms of the interferometer to ensure the photons have identical polarization.

A careful procedure is needed to align the FPCs in order to maximize the indistinguishability and thus the HOM visibility. The alignment protocol we use is schematically depicted in Fig. 6.8. We couple the output of an EDFA into the waveguide instead of the pump laser. At the output of the waveguide, the transmitted light is then either H or V polarized using a free-space polarizer then sent to FPBS1 before entering the interferometer through either arm a or b depending on the polarization that has been set by the polarizer. An extra FPBS, labeled FPBS2, is plugged onto one of the output arms of the 50/50 BS and one of its output fiber is sent to an infrared powermeter. When the light from the EDFA is H polarized, it goes through arm a and FPC2 is adjusted such as to minimize the measured power at the output of the BS + FPBS2 chain. Similarly, when reversing the polarization of the input light from the EDFA, light enters through arm b and FPC3 is adjusted such as to minimize the measured power. By doing so, one ensures that the polarization of photons entering both path a and b are exactly the same at the 50/50 BS. Indeed, using the Jones notation, if the input polarization state is linearly H polarized: $E_a = (1, 0)$, then at the 50/50 BS, the state has been rotated and becomes $E'_a = U_a E_a$. After the BS and FPBS, we end up with a polarization state $E''_a = U_c U_a E_a$. Similarly, for light entering through arm b the linearly-polarized input polarization state $E_b = (0, 1)$ is transformed into $E''_b = U_c U_b E_b$. By minimizing the transmitted power at the IR power meter, we make sure that $E''_a = E''_b$ and hence, by applying the inverse unitary U_c^{-1}, that $E'_a = E'_b$. As a result, the polarization states of the input fields are exactly the same at the 50/50 BS.

Experimental results

In Fig. 6.9 (a-b) we show the measured HOM coincidence probability at the output of the 50/50 BS that was obtained using the AlGaAs waveguide source and a pump power of 25 mW. The raw visibility is 86 % and the FWHM is 83 fs corresponding to a state bandwidth of about 80 nm. In our simulations, the only free parameter is the pump wavelength, which was adjusted to obtain the best agreement with the experimental data. Therefore, for both simulated curves in Fig. 6.9 (b) and (d), the pump wavelength was chosen to be 781.13 nm. As already explained, the limitation to the visibility is the inherent birefringence of the waveguide, which makes the JSA slightly asymmetric with respect to degeneracy.

In Fig. 6.9 (c-d), we show the result of the same experiment but with a 20 nm tunable square spectral filter (Finisar Waveshaper 4000s) centered on the biphoton degeneracy wavelength inserted before the FPBS. As a result, the observed dip width is larger, 267 fs corresponding to a biphoton bandwidth of about 20 nm, as expected. The visibility has increased up to 94 %. This can be explained by the fact that the JSA asymmetry is negligible close to degeneracy $\omega_- = 0$. Hence when filtering the JSA around degeneracy with a square filter, we sweep away the spectral distinguishability between the two photons resulting in a higher HOM visibility.

We see that filtering is indeed a way to increase indistinguishability, at the cost of a reduction both in biphoton bandwidth and measured coincidence rates. In Fig. 6.9 (e), we compare our experimental data with a simulation of HOM visibility as a function of filter width. By decreasing the filter bandwidth down to 10 nm one can reach visibilities above 98 %. We also notice that, as expected, when increasing the filter width above 70 nm the visibility finally reaches the asymptotic value that was experimentally measured on the full biphoton state.

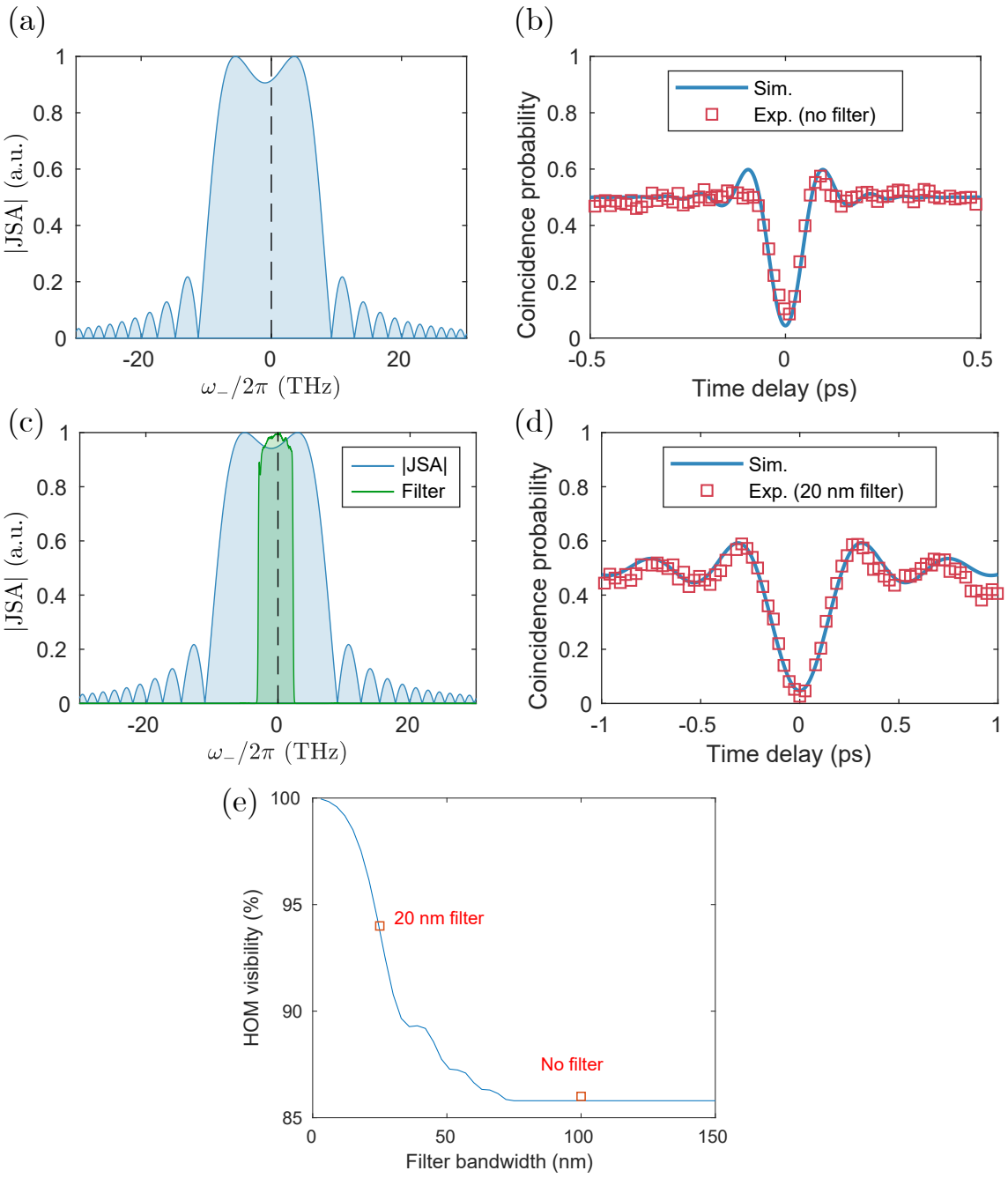

Figure 6.9: Simulated JSI and corresponding measured HOM interferogram acquired from sample `G5X038` in the case of (a-b) no filtering, showing a visibility of 86 % and (c-d) a 20 nm bandwidth filter at the waveguide output, with a resulting visibility of 94 %. (e) Simulated HOM visibility as a function of filter bandwidth. The red squares correspond to the two measurements.

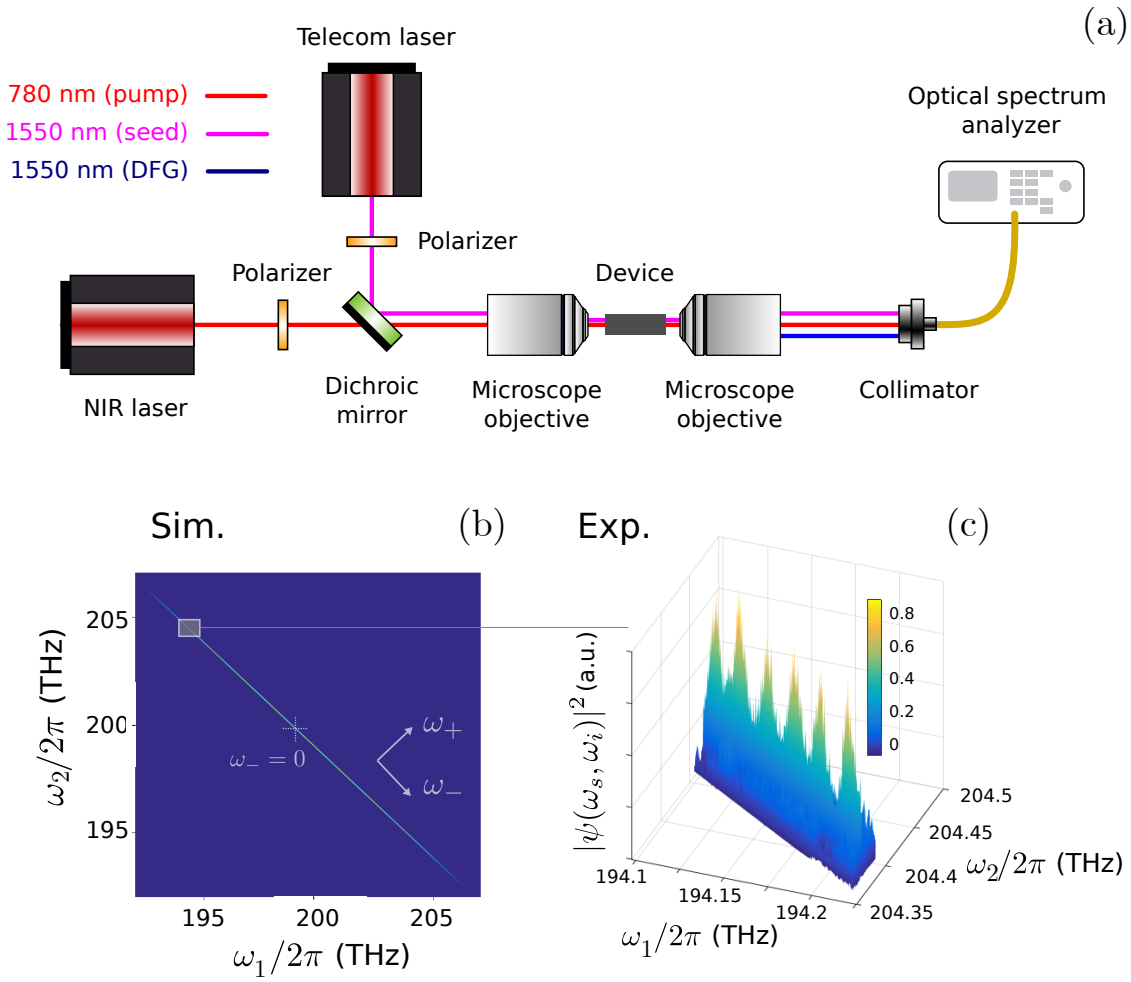

Figure 6.10: (a) Experimental setup for the SET reconstruction of the JSI. (b) Simulated JSI (sample `ABQ71`). (c) Reconstructed portion of the JSI using the stimulated emission tomography technique.

6.3 Joint spectral intensity (JSI) reconstruction by stimulated emission tomography

When characterizing the quantum state of the AlGaAs photon-pair source, another goal is to directly measure the joint spectral amplitude. The JSI can be reconstructed from classical DFG measurements in the framework of stimulated emission tomography (SET) as proposed and demonstrated in [156, 157]. SET relies on the correspondence between SPDC and DFG processes which are the quantum and classical equivalent of each other. In [156], it is shown that the measured DFG power as a function of seed and idler frequencies is proportional to the generated number of SPDC photon pairs at the same given frequencies, which is simply given by the JSI $= |\mathcal{C}(\omega_1, \omega_2)|^2$.

The experimental setup for this experiment is sketched in Fig. 6.10 (a). We simultaneously couple into the device a pump laser beam of frequency ω_p, around 775 nm and a seed telecom beam ω_1 from a telecom laser (Tunics) of output power 3 mW that was amplified by an erbium doped fiber amplifier (EDFA, Keopsys) to about 20 mW. The pump field was produced by a TOPTICA DL 780 laser with a power of 24 mW at $\lambda_p = 764.6$ nm. The interacting fields in the non-linear waveguide will create a field at $\omega_2 = \omega_p - \omega_1$ by DFG.

We collect the outgoing light using a second microscope objective and couple it into a SMF28 fiber directed towards an optical spectrum analyzer (OSA, Yokogawa AQ6370C). We scan the seed frequency ω_1 and for each value we record the DFG spectrum on the OSA. To give an order of magnitude, the peak DFG power that was recorded by the OSA was about 247 pW. By juxtaposing all the DFG spectra for different values of ω_1, ω_2, we reconstruct a full map of the JSI. Note that the input polarization of both pump and seed fields has to be carefully adjusted to match one of the allowed non-linear processes.

A typical SET measurement and the corresponding simulated JSI are shown in Fig. 6.10 (b-c). This measurement was performed on a 4 mm-long waveguide with a 6-upper-periods epitaxial structure (`ABQ71`) whose phase-matching wavelength was 1529.2 nm. The discrete peaks in Fig. 6.10 (c) are a clear signature of cavity effects on the JSA. We measure a spacing of 6.5 GHz between adjacent peaks, which matches the free spectral range of the effective cavity formed by the two facets of the waveguide used in the experiment.

One of the shortcomings of the current setup comes from the fact that we needed to amplify our seed laser with an EDFA. The issue is that the amplifier has a broadband emission spectrum and, in the vicinity of the degeneracy $\omega_1 = \omega_2 = \omega_p/2$, the generated DFG field will have its frequency within the amplifier spectrum. As a result, the strong amplifier emission will superimpose to the weak DFG signal which then cannot be detected. Hence the tomography cannot be performed over the whole spectral range in our current setup and we could not reconstruct the totality of the JSI that is presented in the simulation of Fig. 6.10 (c). This limitation can be overcome by replacing the laser and EDFA by a more powerful tunable laser, avoiding the unwanted background radiation from the amplifier. To reconstruct the JSI near the degeneracy, the pump laser could be filtered out using a narrowband tunable filter.

Finally, we note that this method allows for the measurement of the amplitude of the JSA but not its phase. A full tomography of the JSA, including intensity and phase, is a much more involved process. Several scheme have been demonstrated to achieve this result, such as in Refs. [158, 159, 160].

6.4 HOM and BFC state symmetry

As explained in Section 5.3.2 thanks to the cavity effects induced by the reflectivity of the waveguide facets, the state emitted by our source can be seen as a biphoton frequency comb (BFC). A signature of this comb-like structure of the JSA can be obtained from Hong-Ou-Mandel interference under the form of revivals of the HOM dip at integer multiple of half the round trip time τ_{RT} of the cavity. We can see this revival effect from simulations, as shown in Fig. 6.11. Since τ_{RT} is inversely proportional to the free-spectral range of the cavity, the spacing between the revivals increases when decreasing the cavity length. In our waveguides, whose length is typically 2 mm, we have a free spectral range of around 22 GHz corresponding to $\tau_{\mathrm{RT}} = 45$ ps. Note that the temporal width of the HOM revivals is the same as for the central dip. We also observe from the simulations that the visibility of the revivals decreases when increasing the time delay. This trend is controlled by the finesse of the cavity: a cavity having a higher finesse will produce HOM revivals with a higher visibility [161]. Hence we see that to observe a revival with appreciable visibility, one needs to use a cavity with mirrors of high reflectivity. However, because of the chromatic dispersion and birefringence in our structure, the HOM visibility will decrease if the cavity finesse is too high. Indeed, the combination of these three phenomenon can lead to a situation where the narrow cavity resonances of the TE and TM photons are not

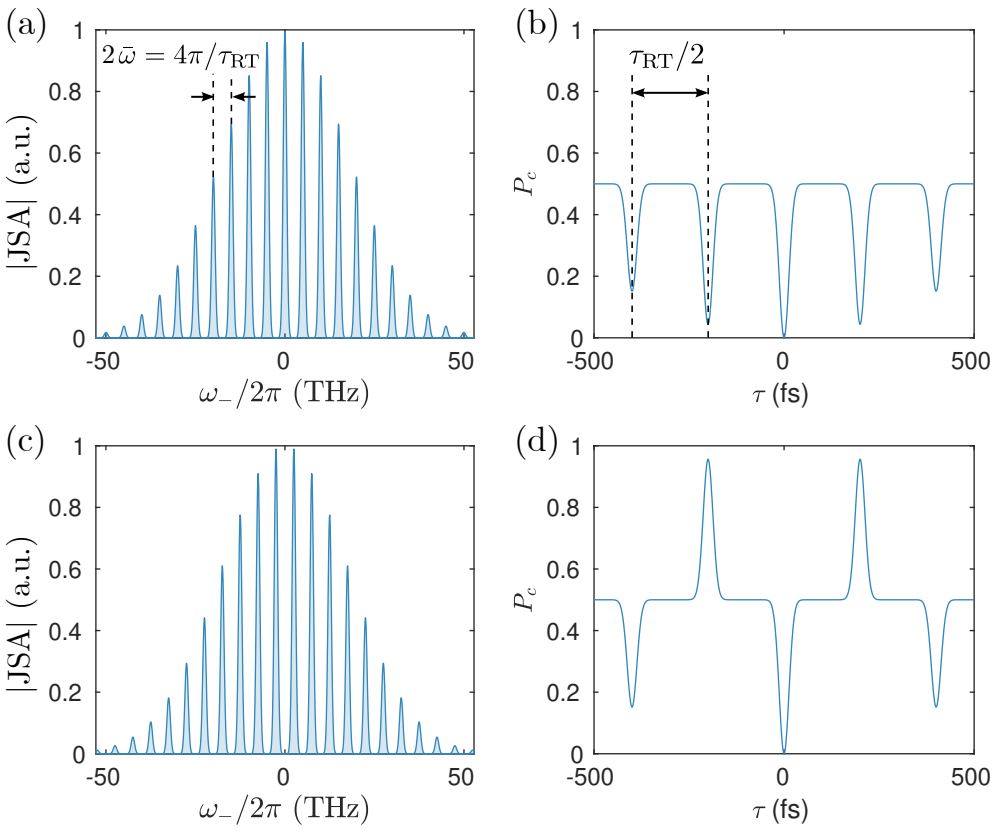

Figure 6.11: Simulated JSA an corresponding HOM interferogram for a (a) resonant and (b) anti-resonant biphoton frequency comb.

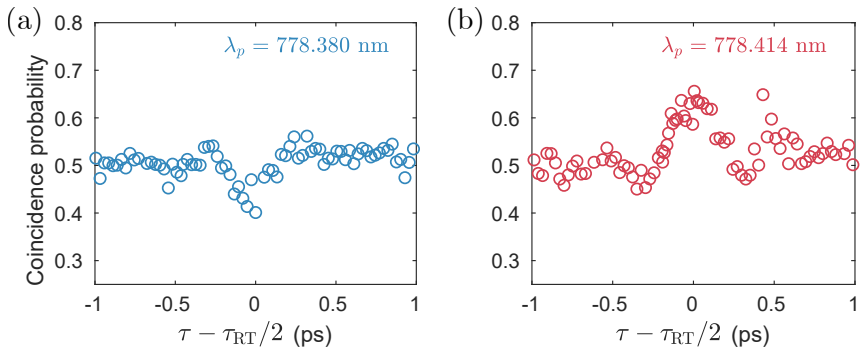

Figure 6.12: Measured HOM revival interferogram around $\tau = \tau_{RT}/2$ with a pump wavelength corresponding to a (a) resonant biphoton frequency comb and (b) antiresonant biphoton frequency comb.

overlapping in some parts of the biphoton spectrum, therefore increasing the asymmetry of the JSA [150]. For this reason a compromise has to be found. As an example, for a facet reflectivity of 50 % and a biphoton bandwidth limited to 25 nm a HOM revival visibility of 70 % could be obtained [87].

Finally, we see that the HOM interferogram varies between the case of a resonant or anti-resonant BFC. Indeed, as demonstrated in Fig. 6.11 (c-d) for an anti-resonant BFC the odd HOM revivals will feature anti-coalescence, manifested in a peak in coincidence probability. This anti-coalescence means that that when tuning the pump frequency to an anti-resonant state and setting the time delay at $\tau = \tau_{RT}/2$, one successfully generated a antisymmetric BFC. In other words, under applied delay $\tau = \tau_{RT}/2$ changing the pump frequency has the effect of switching the state symmetry from symmetric (coalescence) to antisymmetric (anti-coalescence). A comprehensive theoretical analysis of this phenomenon can be found in Ref. [150].

We demonstrate this effect in our waveguide by performing HOM interference around $\tau = \tau_{RT}/2$. To obtain a better visibility, we perform this experiment with the 20 nm filter on. In the measurement shown in Fig. 6.12 (a), we observe a revival HOM dip of visibility 20 % and FWHM of 250 fs. The reduced visibility compared to the central dip can be explained by the poor facet reflectivity and residual JSA asymmetry. Furthermore, we observe that, when detuning the pump wavelength, the shape of the recorded HOM interferogram changes from a dip to a peak of visibility 28 % hence proving the symmetry inversion of the quantum state.

This phenomenon can also be interpreted in terms of two-photon statistics. Coalescence and anti-coalescence being the hallmark of bosonic and fermionic statistics respectively, by changing the pump frequency we artificially modify the statistics of the photons incident on a beam-splitter from bosonic to fermionic. This phenomenon has also been investigated by our group with a different approach based on a counterpropagating geometry, enabling the demonstration of exotic two-photon fermionic and anyonic statistics [91, 90].

Part III

AlGaAs electro-optic devices

Chapter 7

On-chip integration of nonlinear AlGaAs waveguides and EO delay lines

Contents

7.1 State of the art and motivation 97
7.2 Electro-Optic Effect in AlGaAs waveguides 98
7.3 Design and fabrication of doped samples 104
7.4 Design and fabrication of undoped samples 107
7.5 Measurement of the electro-optic phase-shift 109

This chapter is dedicated to the demonstration of monolithic integration of an AlGaAs parametric photon-pair source and an electro-optic phase-shifter. We start by a brief review of the state of the art in integrated delay lines for quantum photonics before giving a theoretical description of electro-optic effect in AlGaAs waveguides. Then, we describe the design and fabrication of electro-optic delay lines in both doped and undoped AlGaAs waveguides. Finally, we present our experimental results, showing the ability of our device to apply electro-optically induced optical phase-shifts.

7.1 State of the art and motivation

Generating entangled photons and manipulating their state on a single photonic chip is a major requirement for applications such as photonic quantum computing, quantum simulation and quantum communications [16, 52]. The control of the quantum state can be achieved using simple building blocks such as integrated beam-splitters and phase-shifters. As stated in the introduction of this thesis, several strategies exist for the realization of on-chip phase-shifters depending on the physical platform. In Silicon-based materials and femtosecond-laser-written waveguides in glass, the refractive index can be changed locally by thermo-optic effect [102, 68]. Compact integrated delay lines can be fabricated onto waveguides by depositing metallic electrodes that will be heated by thermal dissipation of electrical current. The thermally-induced local change of refractive index in the waveguide will create a phase-shift that can be tuned by changing the current flowing through the electrode. Despite being implemented in ultra-low loss photonic platforms, this kind of phase shifter cannot achieve fast phase modulation since thermal effects remain intrinsi-

cally slow. Moreover, with this kind of device, the spatial distribution of heat flow and hence the exact local variation of refractive index is hard to control.

These drawbacks can be avoided in materials exhibiting non-zero electro-optic coefficient, such as $LiNbO_3$ and AlGaAs, by exploiting the electro-optic (EO) effect. Indeed, when applying an electric field to a waveguide using metallic electrodes, one can change the local refractive index of the material and hence obtain a tunable phase-shifter. The spatial distribution of the applied field inducing the change in refractive index can be precisely controlled by suitable engineering of the contacts. In addition, the electric field can be modulated at high speeds which is not the case of the heat dissipation in thermo-optic phase-shifters. In classical photonics, the EO effect has been exploited for the realization of integrated high-frequency phase modulators [162, 163] and polarization rotators [164].

Recently, electro-optic phase shifters have been used for the demonstration of two-photon state manipulation on photonic chips. On-chip generation, control and interference of two-photon states using integrated parametric sources, beam splitters and EO phase-shifters on a monolithic chip have been demonstrated in the ppLN platform, albeit with relatively important footprint since the chips are typically several centimeters long [71, 69]. This approach has also been developed in the AlGaAs platform. In Ref. [80], the authors generate photon pairs using an off-chip source then recombine them on a GaAs chip composed of a phase-shifter and a 50/50 coupler to demonstrate Hong-Ou-Mandel effect. However, up to now the full integration of SPDC sources, beam splitters and electro-optic phase-shifters on a monolithic chip is lacking in the AlGaAs platform. This achievement could serve several purposes such as the generation of high-dimensional entangled states on a reconfigurable photonic chip or the demonstration of fully-integrated HOM interference, a scheme that has been recently realized experimentally in the ppLn platform [69]. In AlGaAs sources are well mastered and their monolithic integration with on-chip beam splitters and detectors has already been demonstrated in Refs. [165, 166]. One of the goals of this thesis has been to fill in the gaps by demonstrating the integration of a SPDC source and an electro-optic phase-shifter on a monolithic chip. We emphasize that none of the applications demonstrated in previous works require fast phase-modulation. Nevertheless, the capability of integrating high-speed phase modulators with parametric sources opens the way towards on-chip manipulation of the frequency state of photon pairs [59].

7.2 Electro-Optic Effect in AlGaAs waveguides

7.2.1 Propagation of electromagnetic waves in crystals

In this section, we start by reviewing briefly the theory of electromagnetic waves in crystals and electro-optic effect following Ref. [167]. Our goal is to describe how the application of a static electric field to an AlGaAs ridge waveguide affects the propagation of light in its guided modes. We start from Maxwell's equations, linking the spatio-temporal evolution of the electric displacement field $\mathbf{D}$ and electric field $\mathbf{E}$ to that of the magnetic field $\mathbf{B}$. We consider the case of a non-magnetic dielectric medium in the absence of charges and currents:

$$\nabla \times \mathbf{E} + \frac{\partial \mathbf{B}}{\partial t} = 0, \tag{7.1}$$

$$\nabla \times \mathbf{B} - \mu_0 \frac{\partial \mathbf{D}}{\partial t} = 0, \tag{7.2}$$

where μ_0 is the vacuum magnetic permeability. The constituting equation that relates the displacement field to the electric field is :

$$\mathbf{D} = \varepsilon \mathbf{E} \tag{7.3}$$

where ε is the dielctric permittivity. It encodes the response of a dielectric material to an electric field, such as that of an electromagnetic wave traveling through the material.

In crystals, such as lithium niobate ($LiNbO_3$), calcite (CaC_{03}) or quartz (SiO_2) the propagation of light is anistotropic. In other words, the phase velocity of the electromagnetic wave can depend on the direction of propagation and the polarization with respect to the crystal axis. This anisotropy arises from the atomic structure of the unit cell of the crystal. Formally, this means that ε will be a tensor and not a scalar, as it would be the case for an isotropic optical medium such as glass or crystals including GaAs. The symmetry group of the unit cell dictates the form of this tensor and hence determines whether the crystal is optically isotropic or anisotropic. In what follows we calculate the refractive index n of a wave as a function of its propagation direction $\mathbf{s}$ and its polarization.

In a lossless medium, ε is a third rank real symmetric tensor. It is always possible to find a set of axes of the three-dimensional euclidean space, called the principal coordinate system, where ε takes a diagonal form :

$$\varepsilon = \begin{pmatrix} \varepsilon_x & 0 & 0 \\ 0 & \varepsilon_y & 0 \\ 0 & 0 & \varepsilon_z \end{pmatrix} = \varepsilon_0 \begin{pmatrix} n_x^2 & 0 & 0 \\ 0 & n_y^2 & 0 \\ 0 & 0 & n_z^2 \end{pmatrix}. \tag{7.4}$$

ε_0 is the vacuum permittivity and n_x, n_y, n_z are the refractive indices of a wave polarized along the x, y, or z axis.

We consider the propagation of a monochromatic plane wave of frequency ω, whose electric and magnetic field can be written :

$$\mathbf{E}(\mathbf{r}, t) = \mathbf{E} e^{\mathbf{k}\cdot\mathbf{r} - \omega t} \tag{7.5}$$

$$\mathbf{B}(\mathbf{r}, t) = \mathbf{B} e^{\mathbf{k}\cdot\mathbf{r} - \omega t} \tag{7.6}$$

where $\mathbf{k}$ denotes the wavevector $\mathbf{k} = k\mathbf{s} = (\omega/c)n\mathbf{s}$ with c the speed of light in vacuum, n the refractive index that we want to solve for and $\mathbf{s}$ the propagation direction of the wave. To evaluate n for a wave propagating along a given direction, we inject equations (7.5) and (7.6) into (7.2) and (7.1) and, with the help of (7.3), we get the following relations :

$$\mathbf{k} \times \mathbf{E} = \omega \mathbf{B} \tag{7.7}$$

$$\mathbf{k} \times \mathbf{B} = -\mu_0 \omega \mathbf{D} \tag{7.8}$$

By feeding the first equation into the second one, we obtain the wave equation for plane waves :

$$\mathbf{k}(\mathbf{k} \times \mathbf{E}) + \frac{\omega^2}{\varepsilon_0 c^2} \varepsilon \mathbf{E} = 0. \tag{7.9}$$

In the principal coordinate system, this equation reads :

$$\begin{pmatrix} \frac{\omega^2}{\varepsilon_0 c^2}\varepsilon_x - k_y^2 - k_z^2 & k_x k_y & k_x k_z \\ k_y k_x & \frac{\omega^2}{\varepsilon_0 c^2}\varepsilon_y - k_x^2 - k_z^2 & k_y k_z \\ k_z k_x & k_z k_y & \frac{\omega^2}{\varepsilon_0 c^2}\varepsilon_z - k_x^2 - k_y^2 \end{pmatrix} \begin{pmatrix} E_x \\ E_y \\ E_z \end{pmatrix} = 0. \tag{7.10}$$

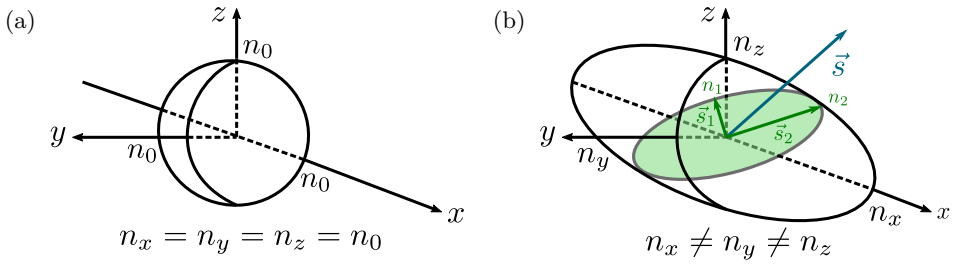

Figure 7.1: (a) Index ellipsoid for an isotropic medium. (b) Index ellipsoid for an anisotropic medium. The geometric procedure for finding the normal modes of propagation and associated refractive indices is schematically represented.

Since this system of equation has to admit non-trivial solutions, the determinant of the matrix has to be 0 :

$$\begin{vmatrix} \frac{\omega^2}{\varepsilon_0 c^2}\varepsilon_x - k_y^2 - k_z^2 & k_x k_y & k_x k_z \\ k_y k_x & \frac{\omega^2}{\varepsilon_0 c^2}\varepsilon_y - k_x^2 - k_z^2 & k_y k_z \\ k_z k_x & k_z k_y & \frac{\omega^2}{\varepsilon_0 c^2}\varepsilon_z - k_x^2 - k_y^2 \end{vmatrix} = 0. \tag{7.11}$$

It can be shown that the matrix is of rank 2 therefore (7.11) will be a second order polynomial in k^2. Thus we get two solutions k_1^2 and k_2^2, corresponding to two refractive indices n_1, n_2. Replacing these values in (7.10), one can then solve for the electric field vector and obtain two solutions $\mathbf{E}_1$ and $\mathbf{E}_2$. Those two solutions are called the normal modes of propagation. Their electric field is oriented along the directions :

$$\mathbf{s}_1 = \begin{pmatrix} \frac{s_x}{n_1^2 - n_x} \\ \frac{s_y}{n_1^2 - n_y} \\ \frac{s_z}{n_1^2 - n_z} \end{pmatrix}, \quad \mathbf{s}_2 = \begin{pmatrix} \frac{s_x}{n_2^2 - n_x} \\ \frac{s_y}{n_2^2 - n_y} \\ \frac{s_z}{n_2^2 - n_z} \end{pmatrix} \tag{7.12}$$

which are orthogonal to the propagation direction $\mathbf{s}$. n_1 and n_2 are the refractive indices associated with the normal modes of propagation. In other words, for a given propagation direction we have two solutions for the E field, $\mathbf{E}_1$ and $\mathbf{E}_2$, with two different phase velocities c/n_1 and c/n_2.

An elegant way of finding geometrically $n_1, n_2, \mathbf{s}_1, \mathbf{s}_2$ from the expression of the dielectric tensor ε, without resorting directly to equation (7.10), is the so-called index ellipsoid method. A proof for this approach can be found in ref [136]. We construct the index ellipsoid from the following equation :

$$\frac{x^2}{n_x^2} + \frac{x^y}{n_y^2} + \frac{z^2}{n_z^2} = 1. \tag{7.13}$$

The set of points (x, y, z) form an ellipsoid in euclidean space (see Fig. 7.1). Its principal axis coincide with the principal axes of the dielectric tensor ε. Their length is equal to $2n_x$, $2n_y$ and $2n_z$ respectively. The rule for finding the normal modes of propagation and their refractive index is the following : i) Draw the propagation direction vector $\mathbf{s}$. ii) Draw the plane that is normal to $\mathbf{s}$ and which contains the origin. iii) Draw the ellipse that constitutes the intersection between this plane and the index ellipsoid iv) The direction of

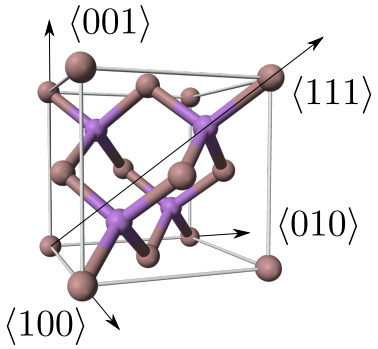

Figure 7.2: Unit cell of a GaAs crystal.

the principal axes of this ellipse are $\mathbf{s}_1$ and $\mathbf{s}_2$. Their length is equal respectively to $2n_1$ and $2n_2$.

As shown schematically in Fig. 7.1, isotropic optical media have $n_x = n_y = n_z = n_0$ and their index ellipsoid is a sphere. Whatever the value of $\mathbf{s}$, any polarization direction is a normal mode with unique refractive index n_0. The phase velocity is independent of the direction and the polarization. In anisotropic media n_x, n_y and n_z are not equal. The ellipsoid index has an elliptical shape and according to the above procedure, the normal mode of propagation and associated refractive indices will depend on $\mathbf{s}$.

7.2.2 Electro-optic effect in GaAs

Now that we understand how electromagnetic waves propagate in an anisotropic medium, we turn to the case of GaAs. GaAs has a Zinc Blend structure of symmetry group $\bar{4}3m$ (Fig. 7.2). It has a threefold symmetry along the $\langle 111 \rangle$ axis and a fourfold mirror symmetry along the edge of the unit cell. Bulk GaAs is an isotropic optical medium of refractive index $n_0 = 3.1$. Its permittivity tensor can be written :

$$\varepsilon = \varepsilon_0 \begin{pmatrix} n_0^2 & 0 & 0 \\ 0 & n_0^2 & 0 \\ 0 & 0 & n_0^2 \end{pmatrix} \tag{7.14}$$

However under strong electric fields, the charge distribution of the electronic cloud surrounding the atoms of the crystal is deformed. This induces a change in ε making GaAs artificially anisotropic. This effect is called the electro-optic effect.

In the following, we derive the mathematical expressions for the principal axis of GaAs under applied electric field and their associated refractive indices following Ref [167]. The convention for labeling the crystallographic axis of GaAs is the following : $x' = \langle 100 \rangle, y' = \langle 010 \rangle, z' = \langle 001 \rangle$. Historically, the electro-optic tensor r, which quantify the effect of an electric field field on the dielectric properties of a crystal, is defined relative to the impermeability tensor η which is proportional to the inverse of ε : $\eta = \varepsilon_0 \varepsilon^{-1}$. Under an electric field $\mathbf{E}$, the impermeability tensor becomes to the first order in $\mathbf{E}$:

$$\eta_{ij} = \eta_{0,ij}(0) + \sum_k r_{ijk} E_k \tag{7.15}$$

with η_0 the impermeability tensor in the absence of an electric field :

$$\eta_0 = \begin{pmatrix} 1/n_0^2 & 0 & 0 \\ 0 & 1/n_0^2 & 0 \\ 0 & 0 & 1/n_0^2 \end{pmatrix}. \tag{7.16}$$

Equation (7.15) describes the so-called linear electro-optic effect, where the change in η is proportional to $\mathbf{E}$. There also exists a quadratic electro-optic effect, scaling as the square of $\mathbf{E}$, which is negligible at the field magnitudes we are considering. r is a third rank tensor that depends on the symmetry group and the atomic properties of the material. Only crystals lacking inversion symmetry like GaAs have a nonvanishing r tensor [136]. ε, and therefore η, being symmetric, r is invariant under the permutation of indices i and j, according to equation (7.15). In other words $r_{ijk} = r_{jik}$ and we can contract the first two indices, using the notation $1 = x'x', 2 = y'y', 3 = z'z', 4 = y'z' = z'y', 5 = x'z' = z'x', 6 = x'y' = y'x'$. This procedure is identical to the derivation of the nonlinear susceptibility tensor in GaAs in Section 4.2.2. Thanks to the $4\bar{3}m$ group symmetry of the GaAs unit cell, only three matrix elements of r are non-zero :

$$r = \begin{pmatrix} 0 & 0 & 0 \\ 0 & 0 & 0 \\ 0 & 0 & 0 \\ r_{41} & 0 & 0 \\ 0 & r_{41} & 0 \\ 0 & 0 & r_{41} \end{pmatrix}. \tag{7.17}$$

We note that, due to the symmetry of the unit cell, the structure of r is similar to the nonlinear susceptibility tensor d given in Eq. (4.13). For GaAs, the numerical value for the electro-optic tensor element at a wavelength $\lambda = 1550\,\mathrm{nm}$ is $r_{41} = 1.5\,\mathrm{pm\,V^{-1}}$[168]. As a comparison, the largest electro-optic coefficients of $LiNbO_3$ in the telecom range is $r_{22} = 5.3\,\mathrm{pm\,V^{-1}}$. Plugging (7.17) into (7.15), we get the expression for η under a field $\mathbf{E}$:

$$\eta = \begin{pmatrix} 1/n_0^2 & r_{41}E_{z'} & r_{41}E_{y'} \\ r_{41}E_{z'} & 1/n_0^2 & r_{41}E_{x'} \\ r_{41}E_{y'} & r_{41}E_{x'} & 1/n_0^2 \end{pmatrix} \tag{7.18}$$

η, and consequently ε, are no longer proportional to the identity matrix as in (7.16). GaAs has become anisotropic.

7.2.3 Electro-optic delay line in a guided geometry

In this section, we apply this formalism to AlGaAs nonlinear waveguides. As was already stated in Chapter 4, AlGaAs wafers are grown along the $\langle 001 \rangle$ axis (z direction). A piece of this wafer can be cleaved off along one of the weak crystallographic axes $\langle 110 \rangle$ and $\langle 1\bar{1}0 \rangle$ corresponding to $x = (x' + y')/\sqrt{2}$ and $y = (x' - y')/\sqrt{2}$. As shown in Fig. 7.3 the top surface of our samples will be the crystallographic plane (001) (normal to the growth axis $\langle 001 \rangle$) and the sidewalls will consist of planes (110) and $(1\bar{1}0)$ (normal to the $\langle 110 \rangle$ and $\langle 1\bar{1}0 \rangle$ axis respectively).

We consider the case of an electric field oriented along z' : $\mathbf{E} = (0, 0, E)$. According to (7.18) the impermeability tensor reads:

$$\eta = \begin{pmatrix} 1/n_0^2 & r_{41}E & 0 \\ r_{41}E & 1/n_0^2 & 0 \\ 0 & 0 & 1/n_0^2 \end{pmatrix}, \tag{7.19}$$

We look for the principal axes by diagonalizing η. We find the new principal coordinate

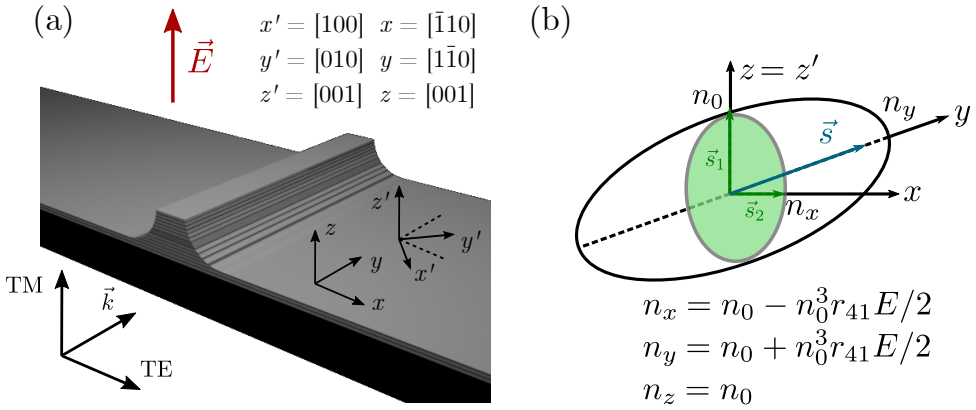

Figure 7.3: (a) Scheme of an AlGaAs waveguide indicating the crystallographic planes corresponding to the top surface and sidewalls, as well as the direction of a TE and TM polarized mode and the propagation direction $\mathbf{k}$. (b) Corresponding index ellipsoid under applied field $\mathbf{E} = (0, 0, E_z)$.

system to be :

$$\begin{cases} x &= \dfrac{x' + y'}{\sqrt{2}} \\ y &= \dfrac{x' - y'}{\sqrt{2}} \\ z &= z'. \end{cases} \tag{7.20}$$

The z' axis is left unchanged while the x' and y' axes are rotated by a 45 degrees angle around z'. Note that the principal axes coincide with the growth direction z of our wafer and the direction of the TE and TM modes of the waveguide as indicated in Fig. 7.3. In this basis, the impermeability tensor reads :

$$\eta = \begin{pmatrix} 1/n_x^2 & 0 & 0 \\ 0 & 1/n_y^2 & 0 \\ 0 & 0 & 1/n_z^2 \end{pmatrix} \tag{7.21}$$

The refractive indices associated with x, y, z are derived from the eigenvalues of η :

$$\begin{cases} n_x &= n_0 - n_0^3 r_{41} E/2 \\ n_y &= n_0 + n_0^3 r_{41} E/2 \\ n_z &= n_0 \end{cases} \tag{7.22}$$

We see from Fig. 7.3 that both TE and TM modes of the waveguides have their $\mathbf{E}$ field along one of the principal axes : x for TE and z for TM. We deduce from equation (7.22) that applying an electric field of magnitude E along z will decrease the TE mode index by the quantity $n_0^3 r_{41} E_z/2$, leaving the TM mode index unchanged. Hence by tuning the magnitude E_z of the field, we can control the phase of a TE polarized photon traveling through the waveguide.

If we instead apply an horizontal E field, oriented along x, the new normal modes of propagation would be along the $(x \pm y)/\sqrt{2}$ axes, which do not coincide with TE and TM directions. Hence, in this configuration, instead of shifting the phase of a TE photon, the electro-optic effect would rotate its polarization.

7.2.4 Figure of merit: Pi-shift voltage

Our final goal being to implement an on-chip interferometer, we use as figure of merit for the electro optic device the pi-shift voltage V_π, which corresponds to the voltage difference that has to be applied across the structure to induce a phase shift of π to the light propagating in a guided mode after a single pass in the waveguide. As we have seen earlier, the fields of the guided modes are confined to the core of the waveguide, which has a thickness h_{core}. The potential drop across the core, will be $V_{\text{core}} = Eh_{\text{core}}$. According to (7.22) the relative phase picked up by a TE polarized beam of wavelength λ_0 while traveling through a ridge waveguide of length l under a field of magnitude E is then :

$$\Gamma = \frac{2\pi}{\lambda_0}\frac{n_0^3 r_{41} E}{2} l = \frac{2\pi}{\lambda_0}\frac{n_0^3 r_{41}}{2}\frac{V_{\text{core}}}{h_{\text{core}}} l. \tag{7.23}$$

To get $\Gamma = \pi$, the voltage applied to the core has to be equal to :

$$V_{\text{core},\pi} = \frac{\lambda_0}{n_0^3 r_{41}}\frac{h_{\text{core}}}{l}. \tag{7.24}$$

For a typical ridge waveguide of length $l = 3\,\text{mm}$ and core thickness $h_{\text{core}} = 426\,\text{nm}$, we expect $V_{\text{core},\pi} = 5\,\text{V}$. As we will see below, since our devices are made out of semiconductor and not perfectly conducting metal, the effective voltage V_π that has to be applied to the structure will be larger than $V_{\text{core},\pi}$.

To apply a z-oriented electric field to our waveguides, we design a structure where gold contact are deposited on top of the waveguide then connected to a voltage source, as sketched in Figure 7.4. Undoped or p-i-n doped samples can be used, each one having its strengths and drawbacks. Undoped samples have the lowest losses, both in the near infrared and at telecom wavelengths, but, since the structure has no mobile charges, measuring electro-optic effect requires applying high voltages across the waveguide. P-i-n doped samples are fabricated from the same wafers as the electrically injected photon pair sources of Refs. [82, 83]. We observe that these samples have higher optical losses caused by the presence of free carriers introduced by the doping. However, the doping profile is designed such that the voltage drop occurs across the core of the waveguide where the optical mode are confined. As a result, the observation of the electro-optic effect requires the application of much lower voltages than in an undoped sample.

7.3 Design and fabrication of doped samples

7.3.1 Electrostatic behavior : p-i-n junction under reverse bias

In doped samples, the upper and lower Bragg mirrors are p-doped and n-doped respectively, while the core is undoped (intrinsic), forming a p-i-n junction. The substrate is located in the n-side of the junction and is also n-doped. The carrier concentration is equal to $10 \times 10^{19}\,\text{cm}^{-2}$ in the substrate and is gradually decreased to $10 \times 10^{17}\,\text{cm}^{-2}$ towards the core region (see full growth sheet in Table 12.4). The same doping profile is applied symmetrically to the p-side. To apply a static field to the core of the waveguide, where guided modes are confined, without inducing any electrical current, we operate the junction in the reverse bias regime.

We recall the basic working principle of a p-i-n junction. The p side has excess holes and the n sides has excess electrons. Near the interface between the two sides, free electrons of the n side, attracted by the holes on the other side, diffuse to the p-doped region. Conversely, holes near the intrinsic core region diffuse to the n side. The positively charged

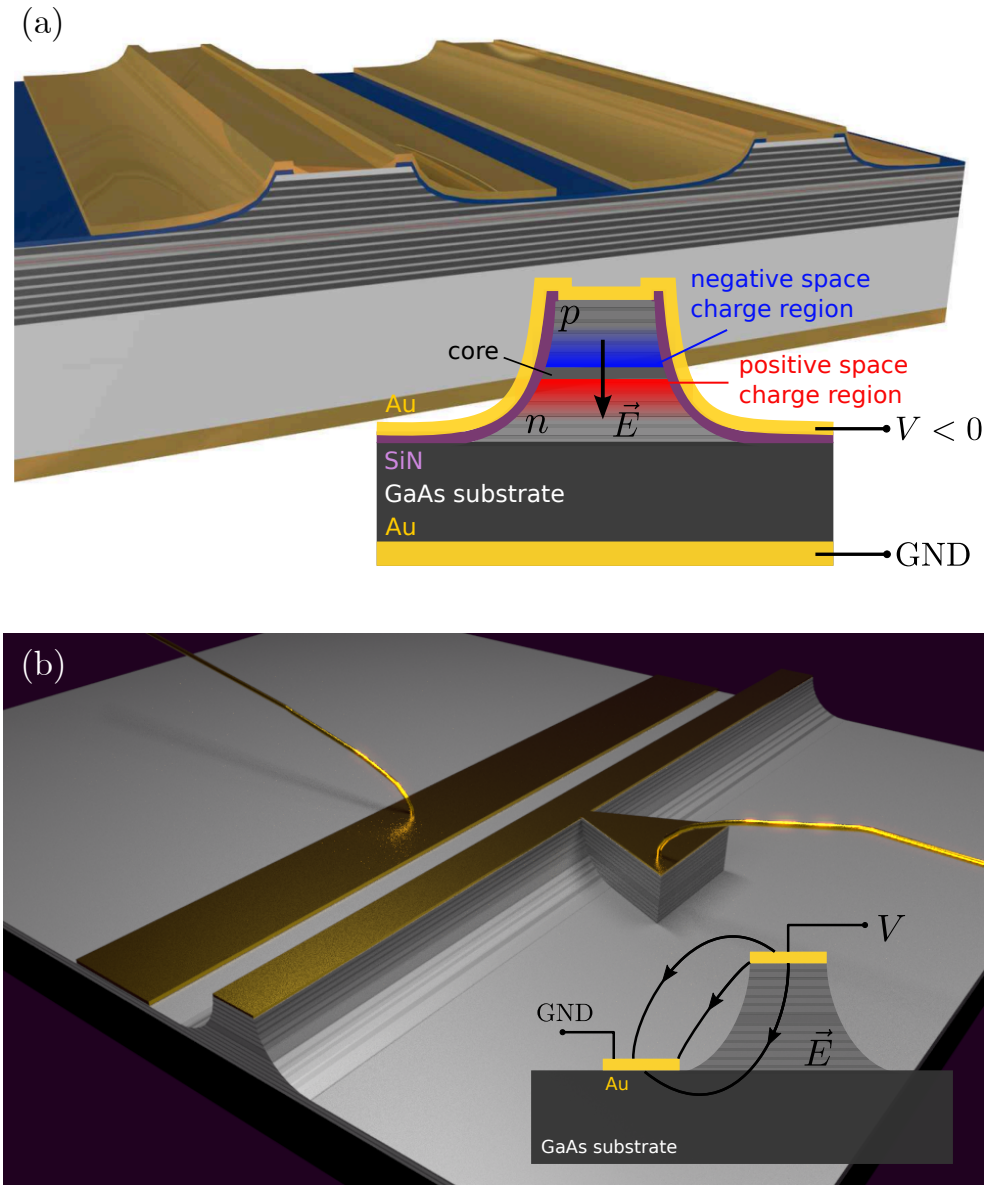

Figure 7.4: (a) Artist view of a p-i-n doped single ridge waveguide electro-optic modulator. Inset : View of the waveguide facet under reverse bias ($V < 0$) with negative and positive space-charge regions regions highlighted in blue and red respectively. The p-side and n-sides of the junction are respectively on top and at the bottom of the core. (b) Artist view of an undoped single ridge waveguide electro-optic modulator. Inset : View of the waveguide facet under applied voltage featuring some electric field lines.

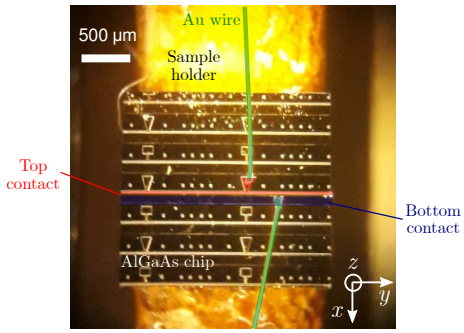

Figure 7.5: Top view image of a mounted sample. The bottom and top contact are highlighted in blue and red respectively while the soldered gold wires are highlighted in green.

dopant atoms on the n side and the negatively charged acceptor atoms on the p side cannot move. As a result, a positively charged region will form on the n-side near the interface and a negatively charged region will form on the p-side near the interface. The resulting electric field opposes electron and hole diffusion. This charged region is called the space charge region and can be seen as the two charged plates of a capacitor.

When connecting the junction to a voltage source, two behaviors can occur depending on the sign of the voltage that is applied. **Forward bias** $V > 0$: In this case, the p-side is connected to the + terminal of the voltage supply. The electrons and holes on the n-side and p-side are pushed towards each other, reducing the width of the space charge region. When a sufficiently high voltage is reached, electron and holes diffusion cannot be balanced by the electric field of the space charge region and a macroscopic current starts to flow. **Reverse bias** $V < 0$: In this case, electrons are removed from the p region and holes are removed from the n region. As a consequence, the width of the space charge region gets larger, increasing the voltage difference between the two sides, as sketched in the inset of Fig. 7.4. The intrinsic core acts as a potential barrier that cannot be crossed by electrons and holes. The junction is then insulating : no current will flow and a voltage drop V_{core} occurs across the intrinsic core region, just like in a parallel plate capacitor.

7.3.2 Contact Geometry

The application of a voltage across the device is done via two gold contacts, as shown in Fig. 7.4 (a): one on top of the waveguide and the other under the substrate. To ensure that the top electrode is connected to the p-side only, we deposit an insulating SiN layer between the waveguide and the top contact. We leave an opening in this SiN layer on top of the waveguide, where the Au electrode will be in contact with the p-doped AlGaAs. This opening is located on top of the waveguide to make sure the applied field is vertical, which would not have been the case if the Au layers were in contact with the sidewalls of the waveguide. In addition, to ensure good electronic conduction between the bottom electrode and the n-doped AlGaAs layers, the GaAs substrate itself is n-doped, as we mentioned earlier.

The voltage can be applied to the structure by soldering a gold microwire onto the top contact and connecting it to a DC voltage supply. The bottom contact will be soldered with an indium paste onto the copper sample holder we use in our test bench, the latter being connected to the ground. An image of a mounted sample showing the gold contacts and soldered microwires is shown in Fig. 7.5.

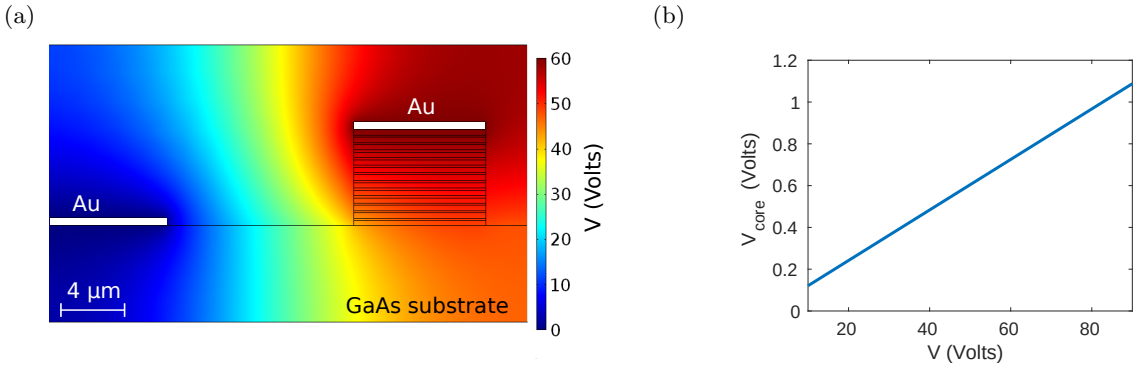

Figure 7.6: (a) Finite element numerical simulation with the COMSOL software suite of the electrostatic potential distribution in an undoped structure for $V = 60\,\mathrm{V}$. (b) Simulated potential drop across the core region V_{core} as a function of V.

7.3.3 Cleanroom Fabrication

The fabrication steps are the same as for the device from ref. [82].

- Ridge waveguide fabrication : Ridge waveguides are fabricated by optical lithography using a S1828 positive photoresist with HMDS adhesion promoter and etched with a BCK solution (acetic acid + $K_2Cr_2O_7$ + HBr in stoechiometric proportions). The procedure is identical to the one described in Section 4.3[1].

- SiN layer deposition and opening : A uniform 400 nm thick SiN layer is then deposited at the surface of the sample by plasma enhanced chemical vapor deposition (PECVD) at 280 °C. This will form an insulating layer between the gold contact and the ridge waveguide. This insulating layer is then opened at the top of the ridges (see Fig. 7.4). To do this, we make a second optical lithography, with the same resist as before. After development, we etch out the SiN layer using reactive ion etching (RIE).

- Top gold contact deposition : A third optical lithography is performed with a negative resist to draw the shape of each ridge waveguide's contact. The resist is spun, then insulated and finally baked, in order to invert it. A 10nm Ti / 400 nm Au metallic layer is subsequently deposited by metallic evaporation. The resist lift-off is done with acetone.

- Bottom gold contact deposition : Finally, the bottom contact is deposited on the bottom side of the substrate by the same technique. No lithography is needed because the gold layer will cover the whole surface of the bottom of the sample. We simply put the sample upside down in the evaporating machine

7.4 Design and fabrication of undoped samples

7.4.1 Contact Geometry

Undoped waveguides require a slightly different contact geometry. If we were to apply a voltage between the top of the waveguide and the bottom of the substrate, like in the

[1]The photomask that was used is "Laser Claire".

doped sample, the resulting voltage across the core would be negligible. Indeed, because the structure is undoped and has no free carriers, charges cannot be drawn out of the p and n regions and accumulate on both side of the core. As a result, for a given value of V, the voltage drop across the core V_{core} would be much smaller than in a device with p-n doping.

To circumvent this issue, we need to put the two gold contacts much closer one to another. The top contact remains on top of the waveguide while the bottom contact sits at the base of the waveguide as sketched in the right panel of Figure 7.4. We wanted to simplify the cleanroom process and avoid the deposition of a SiN layer between the waveguide and the top contact like in the doped structure. Indeed, the SiN layer opening on top of the waveguide is difficult to perform perfectly. As a consequence, we reduced the size of the top contact, which now covers only the flat portion at the top of the ridge waveguide. This narrower top contact is not connected to the bottom layers of the waveguide and hence short circuits are avoided. It is however too narrow to allow for directly soldering gold microwires on it. To this end, we added triangular electrical pads to the top contacts on which we bond the wire. Again, to avoid any short circuit and to make sure the applied electric field is as uniform as possible, we set those electrical pads on small pedestals that are connected to the waveguide. The lithographic pattern for the waveguide and the pedestals consists of a single polygon therefore the etching of the waveguides and the pedestals can be done in one step only. Morover, the merging region between the pedestal and the waveguide has been made thin enough such that the perturbation of the propagating modes is minimal.

In order to accurately calculate the voltage drop across the core for a given voltage V applied between the two contacts, finite element electromagnetic simulations of the electric potential have been performed, using the commercial COMSOL software suite. The results are presented in Figure 7.6. We see that most of the voltage drop occurs in the air between the two contacts. The simulations show a linear dependence of V_{core} on V (left panel of Fig. 7.6) with a slope of 0.012.

7.4.2 Cleanroom Fabrication

The fabrication of electro-optic phase-shifter on an undoped ridge waveguides is carried out the following way :

- Ridge waveguides and electrical pads : We perform an optical lithography of the straight waveguide with the electrical pad pedestal. The same photoresist and etching solution as above are used[2].

- Top contact deposition : Since we want the top contact to cover completely the top of the waveguide and the pedestal, we make a second optical lithography with the exact same pattern as the first one, carefully aligning the photomask onto the chip thanks to alignment marks. For this second lithography, a reversible AZ5214 negative photoresist is used. After development, a 10 nm Ti/ 400 nm Au contact is deposited by metallic evaporation. The photoresist is then removed in acetone.

- Bottom contact deposition : Finally, to fabricate the bottom contact, we repeat the last two steps (lithography, evaporation and lift-off) using a different lithographic mask with a simple rectangular pattern.

[2]We used the photomask "EO modulator Félicien 2019".

7.5 Measurement of the electro-optic phase-shift

7.5.1 Phase shift measurement from the device transmission

Principle of the experiment

We describe a first experiment that allows us, at the same time, to verify qualitatively that the TE mode index is modified by electro-optic effect and to estimate quantitatively the voltage drop V_{core} seen by the guided modes as a function of net applied voltage V. To this end, we measure the TE transmission of our waveguide as a function of laser beam frequency and applied voltage.

Since the TE effective mode index is affected by electro-optic effect, the transmission spectrum will change with V. Indeed, the modal transmission for the fundamental TE mode of an AlGaAs ridge waveguide as a function of frequency ν is that of a Fabry-Perot cavity:

$$T_{\text{TE}}(\nu) = \frac{(1-R_{\text{TE}})^2 e^{-\alpha_{\text{TE}} l}}{(1-R_{\text{TE}}e^{-\alpha_{\text{TE}} l})^2 + 4R_{\text{TE}}e^{-\alpha_{\text{TE}} l}\sin^2\left(\pi\dfrac{\nu}{\Delta\nu}\right)}, \tag{7.25}$$

where R_{TE} is the modal TE reflectivity of the waveguide facets, α_{TE} the optical loss coefficient and l the waveguide length. The free spectral range $\Delta\nu$ of the ridge waveguide depends on the value of the TE modal effective index n_{TE}:

$$\Delta\nu = \frac{c}{2n_{\text{TE}}l}. \tag{7.26}$$

We recall that according to equation (7.22), the TE mode index varies with V_{core} as

$$n_{\text{TE}}(V_{\text{core}}) = n_{\text{TE}}(0) + \frac{n_{\text{TE}}(0)^3 r_{41}}{2h_{\text{core}}} V_{\text{core}}. \tag{7.27}$$

Therefore, the application of a bias voltage to the waveguide changes the value of the free spectral range and we expect the transmission maxima to be shifted according to the value of V_{core}.

For typical values of the core voltage drop of the order of 1 V, the relative change in the free spectral range is of the order of 20 kHz, which is very small compared to typical values of $\Delta\nu$, in the GHz range. However, if we look at the n^{th} Fabry-Perot resonance with $n = \nu/\Delta\nu$, the free spectral range shift is amplified since the n^{th} Fabry-Perot resonance will be shifted by n times the variation in free spectral range. In our waveguides, working in the telecom range, we obtain $n \approx 6500$ and the Fabry-Perot resonance shift will be significant, of the order of the free spectral range.

To observe this effect, we measure $T(\nu)$ for different values of the bias voltage V set across the structure. We probe our device by coupling a continuous wave (CW) tunable telecom laser (Tunics) inside our waveguide. The beam is focused onto the waveguide facet with the help of a C-coated aspheric lens of numerical aperture 0.7 (Thorlabs C330TMD-C). Light at the waveguide output is collected using a microscope objective of NA = 0.95 (Zeiss Achroplan 63x). We record the output power with a powermeter (Coherent FieldMax II). The waveguide is kept at a constant temperature of 20 °C using a Peltier cell and a thermistor set in a P-I-D feedback loop. A DC voltage supply is used to produce the bias voltage that is applied to the waveguide. Its electrodes are connected to gold pads that are wire-bonded onto the electrical contacts of the chip.

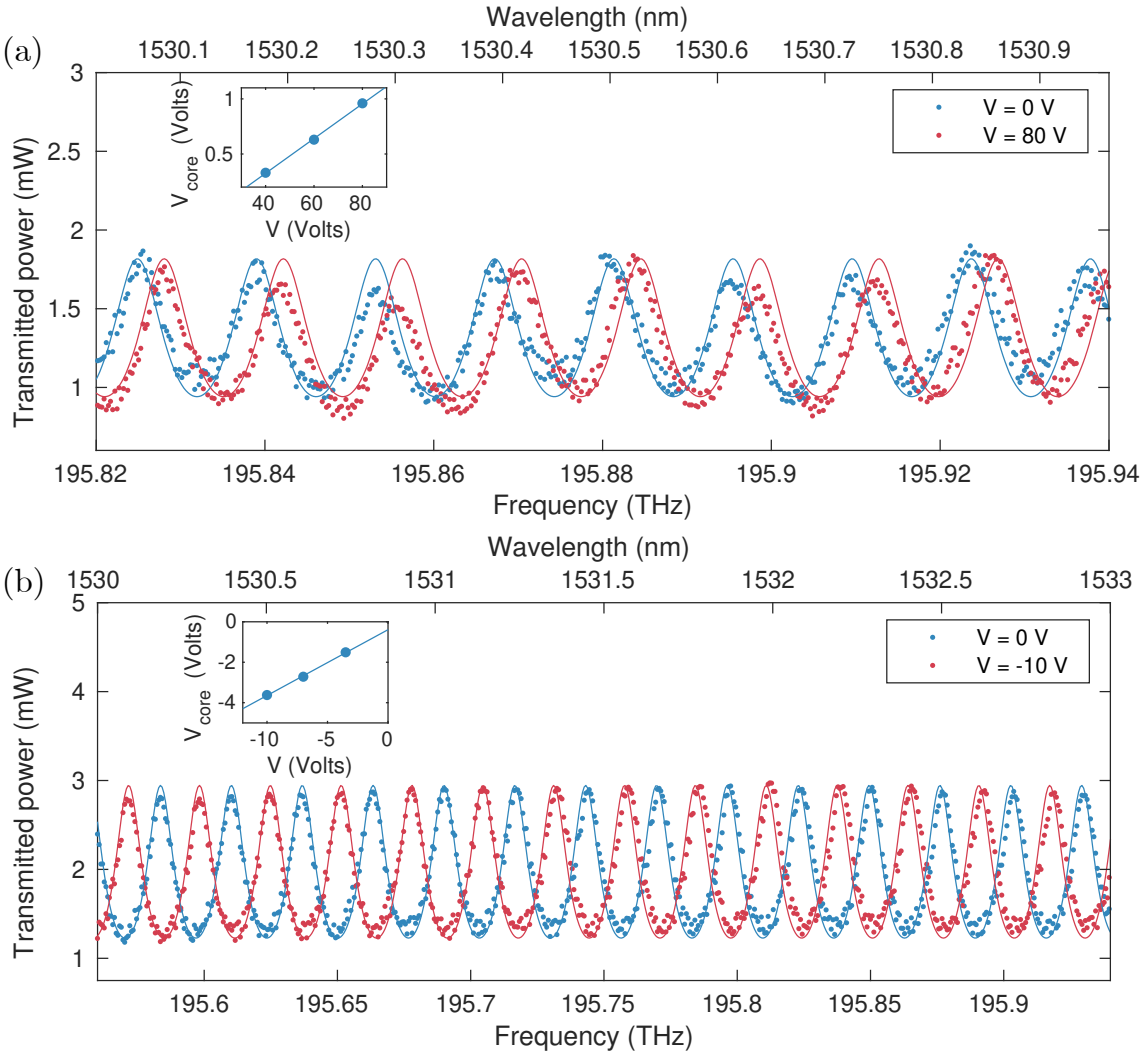

(c) Undoped sample (`EBW002`)

V (V)	V_{core} (V) direct fit	V_{core} (V) resonance shift
-40	0.35	0.33
-60	0.61	0.63
-80	0.90	0.96

(d) Active sample (`HIY021`)

V (V)	V_{core} (V) direct fit	V_{core} (V) resonance shift
-3.5	-1.25	-1.51
-7	-2.47	-2.71
-10	-3.48	-3.62

Figure 7.7: (a-b) Transmission spectrum for two different applied voltages V of an (a) undoped device (wafer: `EBW002`) and (b) doped device (wafer: `HIY021`). Points: experimental data, solid lines: fit to theoretical formula (see main text for details). Insets: Value of V_{core} extracted from the fit as a function of V. Points: experimental data, solid lines: linear fit. (c-d) Comparison of the experimental values for V_{core} obtained by direct fit of the data or by measurement of Fabry-Perot resonance shift in (c) undoped and (d) doped waveguides.

Direct fit of the data

We perform the measurement at bias voltages $V = [0\,\mathrm{V}, 40\,\mathrm{V}, 60\,\mathrm{V}, 80\,\mathrm{V}]$ in the undoped structure and $V = [0\,\mathrm{V}, -3.5\,\mathrm{V}, -7\,\mathrm{V}, -10\,\mathrm{V}]$ in the doped structure. The spectra that were obtained at maximum bias, $V = 80\,\mathrm{V}$ and $V = -10\,\mathrm{V}$ respectively, are presented in Fig. 7.7 (a-b) and compared to the zero voltage transmission. We can clearly see the Fabry-Perot resonances shifting when turning on the bias voltage, which is a clear evidence of the electro-optic effect. As expected, a much stronger voltage is required to see this effect on the undoped structure than on the doped structure. We want to underline that any thermal effect is neglected in this experiment since there is a very small current, smaller than 50 µA, flowing across the structure and the electrical power dissipated in the waveguide remains negligible.

Direct fit of the data with formula (7.25) and (7.27) yields experimental values for the core voltage drop V_{core} that are plotted in the inset of Fig. 7.7 (a-b). We see that in both structures, V_{core} evolves linearly with V. For the undoped structure $V_{\mathrm{core}} = 0.016V - 0.30$ and for the doped structure $V_{\mathrm{core}} = 0.326V - 0.39$. The experimental values for undoped waveguides are comparable to the electrostatic simulation shown in Figure 7.6, where the slope was found to be 0.012. Doped waveguides have a steepest slope thanks to the doping. Indeed, because of the presence of freee carriers the voltage drop between the Au contacts and the core is reduced and the voltage drop across the core is subsequently increased.

In undoped structures, as we can see from these measurements, the expected pi-shift voltage is very high, around 400 V for a 3 mm device. To reduce the pi-shift voltage, several strategies can be adopted such as bringing the bottom contact closer to the side of the waveguide, increasing the length of the waveguide or designing a new device in a Mach-Zender geometry with a push-pull voltage scheme. In addition, we could make the samples out of a wafer with only two upper Bragg mirror periods to reduce the length between top and bottom contacts, increasing subsequently the applied field in the waveguide core region. By combining all these improvements, we expect the pi-shift voltage to be reduced to a value in the 100 V range. In doped structures, the expected pi-shift voltage is much smaller, 15.3 V, and the elctro-optic effect can be conveniently studied in this compact geometry.

Tracking the location of the Fabry-Perot resonances

We describe an alternative method for measuring the effect of the applied voltage on the propagation of the guided fields from these data by quantitatively analyzing the shift of the location of the Fabry-Perot resonances when applying a voltage V. We track the n^{th} Fabry-Perot resonance of our waveguide for different values of V and record its central frequency ν_n. The ratio between the resonance frequency at $V = 0$ and $V \neq 0$ is :

$$\frac{\nu_n(0)}{\nu_n(V)} = \frac{n\Delta\nu(0)}{n\Delta\nu(V)} = \frac{n_{\mathrm{TE}}(V)}{n_{\mathrm{TE}}(0)} \tag{7.28}$$

where we used the expression (7.26) for the free spectral range $\Delta\nu$. Given the value of $n_{\mathrm{TE}}(V = 0)$, the change in TE mode index can be calculated as :

$$n_{\mathrm{TE}}(V) - n_{\mathrm{TE}}(0) = n_{\mathrm{TE}}(0)\left(\frac{\nu_n(0)}{\nu_n(V)} - 1\right). \tag{7.29}$$

Using equation (7.27) we can rewrite this quantity in terms of V_{core}, yielding :

$$V_{\mathrm{core}}(V) = \frac{2h_{\mathrm{core}}}{n_{\mathrm{TE}}(0)^2 r_{41}}\left(\frac{\nu_n(0)}{\nu_n(V)} - 1\right) \tag{7.30}$$

This relation shows that an experimental value for V_{core} can be obtained from the measurement of the ratio $\nu_n(0)/\nu_n(V)$. The values for V_{core} obtained with this method are displayed on the tables in Fig. 7.7 (c-d) alongside the values obtained by direct fit in the previous paragraph. We observe that the two methods are in excellent agreement.

7.5.2 Phase shift measurement from the TE/TM dephasing

Principle of the measurement

Another way of assessing the performance of our electro-optic modulator is to directly measure its pi-shift voltage. To this end, we couple a 45° linearly polarized beam to a waveguide and measure the induced dephasing between its TE and TM component after exiting the sample. By reconstructing the polarization state of the beam for different values of V, we can access the relative phase between its TE and TM components and thus infer the change in TE mode index induced by electro-optic effect. Using the Jones vector notation, in the TE/TM basis the input polarization state reads :

$$\mathbf{E}_i = \frac{1}{\sqrt{2}} \begin{pmatrix} 1 \\ 1 \end{pmatrix}. \tag{7.31}$$

At the output of the waveguide, it becomes :

$$\mathbf{E}_o = \begin{pmatrix} t_{\text{TE}}(V) \\ t_{\text{TM}} \end{pmatrix} = \begin{pmatrix} |t_{\text{TE}}(V)|e^{i\Gamma(V)} \\ |t_{\text{TM}}|e^{i\Gamma_0} \end{pmatrix} = \begin{pmatrix} |t_{\text{TE}}(V)|e^{i\Delta\Gamma} \\ |t_{\text{TM}}| \end{pmatrix}, \tag{7.32}$$

where $t_{\text{TE(TM)}}$ is the TE (TM) complex transmission coefficient of the waveguide, whose expression is given by the Airy formula :

$$\begin{cases} t_{\text{TE}}(V) & = \dfrac{(1-R_{\text{TE}})\exp\left(i\frac{2\pi l}{c}n_{\text{TE}}(V)\nu\right)\exp(-\alpha_{\text{TE}}l)}{1-R_{\text{TE}}\exp\left(i\frac{4\pi l}{c}n_{\text{TE}}(V)\nu\right)\exp(-2\alpha_{\text{TE}}l)}, \\ t_{\text{TM}} & = \dfrac{(1-R_{\text{TM}})\exp\left(i\frac{2\pi l}{c}n_{\text{TM}}\nu\right)\exp(-\alpha_{\text{TM}}l)}{1-R_{\text{TM}}\exp\left(i\frac{4\pi l}{c}n_{\text{TM}}\nu\right)\exp(-2\alpha_{\text{TM}}l)}, \end{cases} \tag{7.33}$$

with $R_{\text{TE(TM)}}$ the modal reflectivity of mode TE (TM). Note that since the TE mode index is affected by electro optic effect, its phase $\Gamma(V)$ depends on the value of V. This is not the case for the TM mode therefore Γ_0 is independent of V. The relative phase between the two components can be expressed as :

$$\begin{aligned} \Delta\Gamma(V) &= \Gamma(V) - \Gamma_0 \\ &= \arg\left[t_{\text{TE}}(V)\right] - \arg\left[t_{\text{TM}}\right] \\ &= \arg\left[t_{\text{TE}}(V)\right] - \arg\left[t_{\text{TE}}(0)\right] + \Delta\Gamma_0 \end{aligned} \tag{7.34}$$

with $\Delta\Gamma_0$ the phase difference at zero voltage.

We assume that for a given frequency ν the transmission coefficients for the TE and TM modes are equal : $|t_{\text{TE}}| = |t_{\text{TM}}|$. As shown later on, experimental data confirms that this conditions is fulfilled in our experiments. Under this assumption the output Jones vector can be written (up to a normalization factor) :

$$\mathbf{E}_o = \frac{1}{\sqrt{2}} \begin{pmatrix} e^{i\Delta\Gamma(V)} \\ 1 \end{pmatrix}. \tag{7.35}$$

When $\Delta\Gamma = 0$ the output beam is linearly polarized along the +45° axis while when $\Delta\Gamma = \pi$ (pi phase shift), it is linearly polarized along the -45° axis. In the intermediate case : $\Delta\Gamma = \pi/2$ (pi/2 phase shift) the beam is circularly polarized.

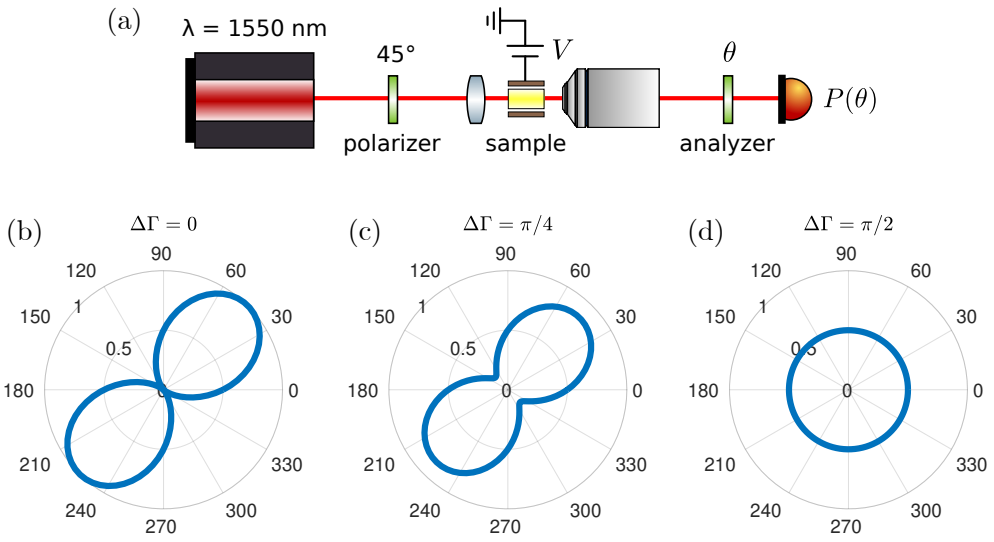

Figure 7.8: (a) Experimental setup for the reconstruction of the output polarization state. (b-d) Theoretical polar maps of $P(\theta)$, the projection of the output polarization vector on an arbitrary direction (equation (7.36)) for different values of the dephasing $\Delta\Gamma$. The radial coordinate is the value of $P(\theta)$ and the angular coordinate is the value of θ in degrees. (b) $\Delta\Gamma = 0$ (linear polarization). (c) $\Delta\Gamma = \pi/4$ (elliptical polarization). (d) $\Delta\Gamma = \pi/2$ (circular polarization).

Suppose that for $V = 0$ the output beam is circularly polarized. To measure V_π, we increase V until the beam becomes linearly polarized along the $+45°$ direction, meaning the electro-optically induced phase shift is $\pi/2$. The value of the voltage for which this occurs will be half the pi-shift voltage V_π.

Reconstruction of the output polarization state

This experiment has been performed only on the doped structure because of its lower operating voltages. The measurement setup is sketched in the top panel of Figure 7.8. The same optical elements as before are used to couple the light in and out of the waveguide. We adjust the polarization of the input laser beam to 45° using a polarizer. The working wavelength has been chosen to be $\lambda = 1570\,\text{nm}$. At this wavelength, as it is shown on the upper right panel of Figure 7.9, TE and TM transmission are comparable, and the output polarization state can be effectively described by our simple model (equation (7.35)).

To reconstruct the polarization state, we project the output beam onto several directions spanning a 360° angle. We place an analyzer followed by a powermeter at the exit of the output microscope objective and we record the normalized transmitted power P as a function of the analyzer angle θ. Formally, by using (7.35) as the mathematical expression for the output polarization vector, this quantity can be calculated as :

$$P(\theta) = |\mathbf{E}_o \cdot \mathbf{e}_\theta|^2 = \frac{1}{2}\left[1 + \cos(\Delta\Gamma)\sin(2\theta)\right] \tag{7.36}$$

where $\mathbf{e}_\theta$ is the unit vector corresponding to the direction of the analyzer axis. The measurement of this $P(\theta)$ map allow us to discriminate between several polarization states. Theoretical curves of $P(\theta)$ for different values of $\Delta\Gamma$ are plotted in Figure 7.8 (b-d).

We see that linear and circular polarizations yield polar charts with very distinct shapes. For the first case (Fig. 7.8 (b)), we observe two lobes. As expected for 45°

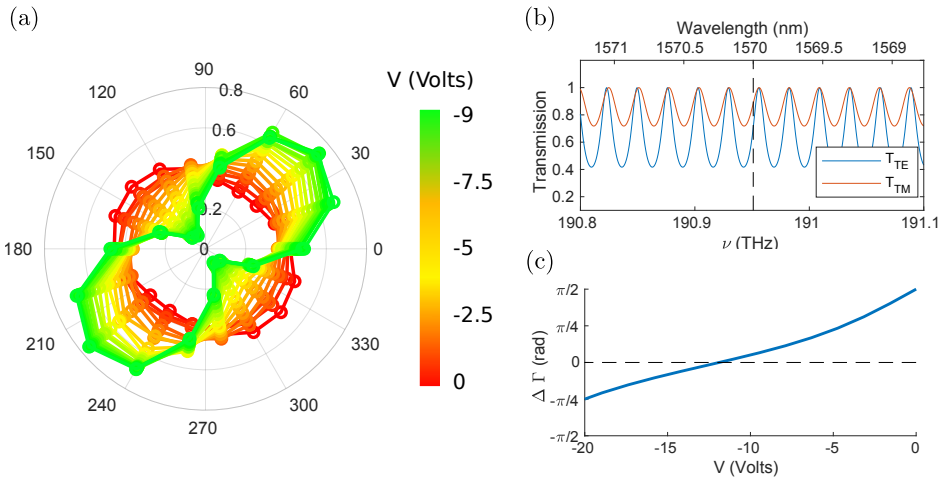

Figure 7.9: (a) Polar representation of $P(\theta)$ (in a.u.) for different values of V at $\lambda = 1570\,\text{nm}$. (b) Simulated TE and TM Fabry-Perot transmission around the working wavelength. (c) Simulated phase shift $\Delta\Gamma$ between TE and TM components as a function of V at $\lambda = 1570\,\text{nm}$ (solid line). The theoretical value of V for which $\Delta\Gamma = 0$ (dashed line) is $-8.2\,\text{V}$.

linearly polarized light, the transmitted power is maximum when the analyzer angle is set to $\theta = 45°$ and minimal when $\theta = -45°$. For circularly polarized light (Fig. 7.8 (d)), the transmitted power is the same, for all analyzer angles θ, hence a $P(\theta)$ map with a circular shape. In short, by looking at the profile of $P(\theta)$ we can tell whether the output polarization is in a linear or circular state. Note that this technique does not allow us to tell whether the light is left or right circularly polarized i.e. if the electric field vector of the wave is rotating clockwise or counterclockwise. This property is given by the sign of $\Delta\Gamma$ and we see that, indeed, equation (7.36) is left invariant when flipping the sign of $\Delta\Gamma$.

Results

The experimental $P(\theta)$ maps obtained for different values of applied voltage V are plotted in Fig. 7.9. We see that at $V = 0\,\text{V}$, we measure a circle (red curves). The output beam is therefore in a circular polarization state. At $V = -9\,\text{V}$, we measure two lobes rotated by $+45°$ (green curve). The output beam is therefore in an almost perfect $+45°$ linear polarization state. The small remaining ellipticity, resulting in nonzero transmission for $\theta = 45 \pm 90°$, can be explained by a slight misalignment between the direction of the polarizer and that of the TE and TM axes. For all intermediate bias voltages, we can see the smooth transition from circular to linear, with intermediate elliptical polarization states (orange curves with a peanut shape).

As we explained earlier, the phase shift required to switch from a circular to a linear polarization is $\pi/2$. In our doped structure, this occurs for $V = -9\,\text{V}$. From the Fabry-Perot resonance measurement, we know that this voltage corresponds to a core potential drop of $V_{\pi/2,\text{core}} = -3.46\,\text{V}$, yielding a pi-shift voltage value of $V_{\pi,\text{core}} = -6.92\,\text{V}$. This experimental value is compatible with the theoretical value of $-5\,\text{V}$ that we obtained earlier using equation (7.24).

To further support this result, we calculate the expected phase shift $\Delta\Gamma(V)$ for different values of V and compare it with the experimental data. This quantity can be straightforwardly computed using formula (7.34). From our experiment, we know that at

$V = 0$ the ouput polarization is circular, therefore the phase difference at zero voltage is $\Delta\Gamma_0 = \pi/2$. The simulation for $\Delta\Gamma(V)$ is shown on the lower right panel of Fig. 7.9. We see that the voltage for which the phase difference switches from $\pi/2$ to zero is $-9.4\,\mathrm{V}$, which is very close to the experimental value $V_{\pi/2} = -9\,\mathrm{V}$.

Part IV

Monolithic integration of an AlGaAs type II photon pair source and a broadband polarization splitter

Chapter 8

Working principle and device design

Contents

8.1 State of the art and motivation 119
8.2 Evanescent coupling of two waveguides 120
8.3 Device design 124
8.4 Realization of a test sample 128

In this chapter, we present the working principle of a monolithic device consisting of an AlGaAs Type II photon-pair source and a broadband polarization splitter. We start by a brief review of the state of the art for integrated polarization splitters and their applications to quantum photonics. Then, we give a theoretical description of evanescent coupling between waveguides before describing in details the design of the generation and polarization splitting regions. Finally, we will show some preliminary experimental results on a first generation of samples consisting only of a polarization splitter without a photon-pair generation region.

8.1 State of the art and motivation

Polarization is one of the most frequently used degree of freedom for quantum information protocols. As a consequence, on-chip manipulation of the polarization state of photons pairs is crucial for future integrated quantum photonics. This approach relies on elementary building blocks such as phase shifters and polarization rotators, that have been discussed in Part III, as well as integrated polarization mode splitters. Moreover, broadband two-photon states are an important resource for a number of applications, such as quantum communications, which requires integrated polarization handling devices to be effective over a large spectrum.

Many efforts have been made towards the realization of broadband polarizing mode splitters in various photonic platforms. Silicon-On-Insulator (SOI) devices relying on birefringent directional couplers have been reported in references [169, 170, 171]. This scheme has also been used in femtosecond laser written waveguides for the realization of integrated quantum gates on polarization qubits [65]. Another approach based on adiabatic evanescent coupling has been demonstrated in lithium niobate in Ref. [172]. To

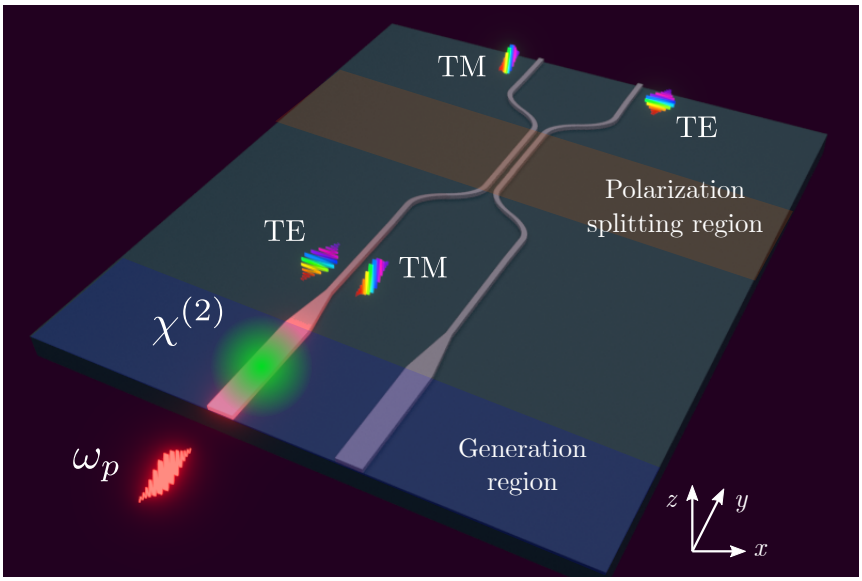

Figure 8.1: Artist view of the integrated AlGaAs SPDC source and polarizing mode splitter.

the best of our knowledge, the only successful integration of a photon-pair sources and a polarization splitter on a single photonic chip has been reported on $LiNbO_3$ in Ref. [69]. In this paper, the authors fabricate on a monolithic chip a ppLN source, a polarization splitter, an integrated polarization rotator and a 50/50 coupler to realize an on-chip HOM experiment. However, the chip demonstrated in that reference doesn't display a broadband operation since the photon pairs are filtered with a 1.2 nm-wide spectral filter.

AlGaAs nonlinear waveguides are ideal candidates for the integration of Type-II polarization entangled photon sources and broadband polarizing mode splitters on monolithic chips. In this project, we designed, fabricated and characterized an AlGaAs photonic device, depicted in Fig. 8.1, consisting of a source of entangled photon pairs followed by a broadband polarizing mode splitter. Pump photons are coupled into a a 5 µm wide waveguide section, where entangled photon pairs are generated by Type-II SPDC. The waveguide width is then tapered down to around 1.5 µm as we approach the polarization splitting region which is made of two evanescently coupled waveguides. Thanks to the waveguide birefringence, generated TE photons will be coupled into the opposite waveguide while TM photons will remain in the same waveguide. At the end of the coupling region, TE and TM photons have been split into two distinct spatially separated waveguides.

8.2 Evanescent coupling of two waveguides

8.2.1 Symmetric and Antisymmetric supermodes

To explain in more details the polarization splitting mechanism, we start by describing the propagation of light in two evanescently coupled waveguides in the framework of coupled modes theory, as described in Ref. [167]. Let us consider two ridge waveguides a and b, of corresponding widths w_a and w_b, separated by a gap g, as shown schematically in Figure 8.2. In what follows, we consider the two waveguides to be identical $w_a = w_b = w$. The propagation direction corresponds to the y-axis. Let $\mathbf{E}_a$ (resp. $\mathbf{E}_b$) denote the complex electric field amplitude for the fundamental guided mode of waveguide a (resp. b) with

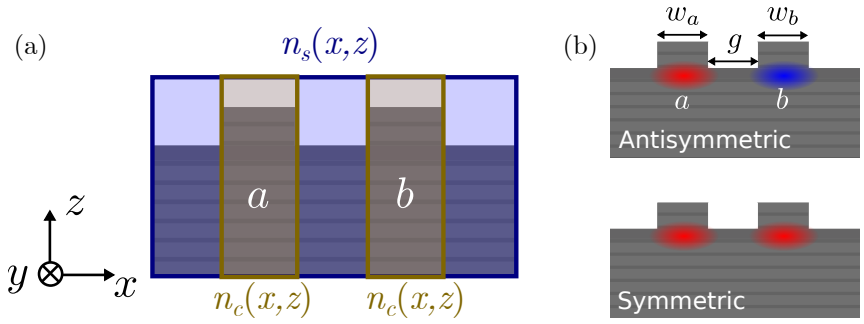

Figure 8.2: (a) Sketch of the cross-section of the two coupled waveguides indicating the refractive index profiles $n_c(x,z)$ and $n_s(x,z)$ in the different regions of the structure. (b) Symmetric and anti-symmetric supermode field profile. Red and blue colors correspond to positive and negative field amplitudes.

associated propagation constants $\beta_a = \beta_b = \beta_0$. We assume the waveguides are lossless such that $\beta_0 = (\omega/c)n_0$ where n_0 is the real-valued effective mode index of the fundamental mode, ω the frequency and c the speed of light in vacuum. When the two waveguides are far apart, $\mathbf{E}_a$ and $\mathbf{E}_b$ are independent solutions of the wave equation:

$$\Box_i \mathbf{E}_i - \beta_0^2 \mathbf{E}_i = 0, \tag{8.1}$$

where $i = a, b$ and $\Box_i$ denotes the D'Alembertian operator : $\Box_i = \partial_x^2 + \partial_z^2 + (\omega/c_0)^2 n_i^2(x,z)$. The function $n_i^2(x,z)$ stands for the refractive index profile of waveguide i. It is composed of the sum of a background term $n_s^2(x,z)$, corresponding to the index profile of the region outside the waveguides (blue area in Fig. 8.2 (a)), and a term, $\Delta n_i^2(x,z)$, that encodes the index profile in the waveguide region (brown area in Fig. 8.2 (a)) [167]:

$$n_i^2(x,z) = n_s^2(x,z) + \Delta n_i^2(x,z), \tag{8.2}$$

where we defined :

$$\Delta n_i^2(x,z) = \begin{cases} n_c^2(x,z) - n_s^2(x,z), & \text{in } i, \\ 0, & \text{elsewhere.} \end{cases} \tag{8.3}$$

The refractive index profile of the two-waveguide system is given by:

$$n^2(x,z) = n_s^2(x,z) + \Delta n_a^2(x,z) + \Delta n_b^2(x,z). \tag{8.4}$$

When we bring the two waveguide close to each other, we observe a hybridization of the two fundamental modes, creating so-called supermodes that are delocalized over the two waveguides. This phenomenon is mathematically analogous to the tunnel effect in a quantum-mechanical double well model. We look for new solutions to the wave equation corresponding to these supermodes under the form:

$$\mathbf{E} = A\mathbf{E}_a + B\mathbf{E}_b, \tag{8.5}$$

where A and B are two complex coefficients. The wave equation reads:

$$\Box \mathbf{E} - \beta^2 \mathbf{E} = 0, \tag{8.6}$$

with β the propagation constant of the supermode and $\Box = \partial_x^2 + \partial_z^2 + (\omega/c_0)^2 n^2(x,z)$. By plugging (8.5) into (8.6) and with the help of (8.1) and (8.2) we obtain the following relation:

$$A\left[\beta_0^2 + \left(\frac{\omega}{c_0}\right)^2 \Delta n_b^2(x,z) - \beta^2\right]\mathbf{E}_a + B\left[\beta_0^2 + \left(\frac{\omega}{c_0}\right)^2 \Delta n_a^2(x,z) - \beta^2\right]\mathbf{E}_b = 0. \quad (8.7)$$

We take the scalar product of this equation independently with $\mathbf{E}_a$ then $\mathbf{E}_b$ to obtain a set of two coupled equations for the variables A and B [167]. If we assume a very small overlap between the fields of the two fundamental modes : $\iint \mathrm{d}x\mathrm{d}z\mathbf{E}_a^*\mathbf{E}_b \ll 1$, this set of equations takes the form:

$$\begin{pmatrix} \beta_0^2 - \beta^2 + K & J \\ J & \beta_0^2 - \beta^2 + K \end{pmatrix}\begin{pmatrix} A \\ B \end{pmatrix} = 0, \quad (8.8)$$

with:

$$K = \left(\frac{\omega}{c_0}\right)^2 \iint \mathrm{d}x\mathrm{d}z\mathbf{E}_{a(b)}^*\Delta n_{b(a)}^2\mathbf{E}_{a(b)}, \quad (8.9)$$

$$J = \left(\frac{\omega}{c_0}\right)^2 \iint \mathrm{d}x\mathrm{d}z\mathbf{E}_{a(b)}^*\Delta n_{a(b)}^2\mathbf{E}_{b(a)}. \quad (8.10)$$

K represents the dielectric perturbation to the field of the fundamental mode of one waveguide due due to the presence of the other waveguide and J is the exchange coupling between waveguides, analogous to the tunnel amplitude in quantum mechanics.

We can now find A, B and β by solving Eq. (8.8). Since it is quadratic in β, the system of equations has two solutions. The new solutions to the wave equation for the two-waveguide system are:

$$\text{Symmetric :}\quad \mathbf{E}_S = \frac{1}{\sqrt{2}}\left(\mathbf{E}_a + \mathbf{E}_b\right),\ \beta_S^2 = \beta_0^2 + K + J, \quad (8.11)$$

$$\text{Antisymmetric :}\quad \mathbf{E}_{AS} = \frac{1}{\sqrt{2}}\left(\mathbf{E}_a - \mathbf{E}_b\right),\ \beta_{AS}^2 = \beta_0^2 + K - J. \quad (8.12)$$

The amplitude field profiles of the symmetric and anti-symmetric supermodes are schematically shown in Fig. 8.2 (b). Of course, these solutions are not unique as there exists and infinite set of solutions to (8.6). We simply limited our treatment to the subspace spanned by the two solutions with the highest mode index. This is equivalent to keeping only the low-energy solutions of a double potential well problem in quantum mechanics by only considering one bound state in each well.

8.2.2 Splitting ratio

We now study the propagation of an electromagnetic wave that is initially located in the fundamental mode of waveguide a. At $y = 0$ the state of the electromagnetic field can be written:

$$\mathbf{E}(y=0) = \mathbf{E}_a = \frac{1}{\sqrt{2}}\left(\mathbf{E}_S + \mathbf{E}_{AS}\right). \quad (8.13)$$

After traveling a distance y, the field becomes:

$$\mathbf{E}(z) = \frac{1}{\sqrt{2}}\left(\mathbf{E}_S e^{-i\beta_S y} + \mathbf{E}_{AS}e^{-i\beta_{AS}y}\right) \quad (8.14)$$

$$= \frac{1}{\sqrt{2}}\left(\mathbf{E}_S + \mathbf{E}_{AS}e^{-i(\beta_{AS}-\beta_S)y}\right)e^{-i\beta_S y}. \quad (8.15)$$

Equation (8.15) shows that a beating occurs between the fundamental modes of the two waveguides $\mathbf{E}_a$ and $\mathbf{E}_b$. Since $\mathbf{E}_b = (\mathbf{E}_S - \mathbf{E}_{AS})/\sqrt{2}$, for propagation distances that are odd multiples of the beating length

$$L_c = \frac{\pi}{\beta_S - \beta_{AS}} \tag{8.16}$$

the electromagnetic field is localized in waveguide b. Indeed, up to a global phase factor $\mathbf{E}((2q+1)L_c) = \mathbf{E}_b$, with $q \in \mathbb{N}$. Similarly, at even multiples of L_c, the electric field is localized in waveguide a : $\mathbf{E}(2qL_c) = \mathbf{E}_a$. Thus, as the wave, initially confined to waveguide a, travels through the coupled waveguide structure, it hops back and forth between the two waveguides with a periodicity given by L_c. The normalized power in waveguides a and b at the output of the device ($y = L$) is proportional to:

$$P_a(L) = \mathbf{E}(L) \cdot \mathbf{E}_a^* = \frac{1}{2}\left[1 + \cos(\pi L/L_c)\right] P_0, \tag{8.17}$$

$$P_b(L) = 1 - P_a(L) = \frac{1}{2}\left[1 - \cos(\pi L/L_c)\right] P_0, \tag{8.18}$$

where P_0 is the normalized input power. We see that by carefully choosing the length L of the coupled waveguides, one can transfer all the optical power from one waveguide to the other or split the power between the two waveguide with an arbitrary splitting ratio. A device consisting of two such coupled waveguides is called a directional coupler and is very widely used for light routing on photonic chips [167]. As we explained earlier (see Section 4.2), in our AlGaAs ridge waveguides, the effective TE and TM mode index are different due to birefringence. Therefore, S and AS supermodes will have different propagation constants for TE and TM polarized light. As a result, TM light traveling through a directional coupler will not have the same beating length as TE light. Let $L_c^{(\mathrm{TE})} = \pi/(\beta_S^{(\mathrm{TE})} - \beta_{AS}^{(\mathrm{TE})})$ and $L_c^{(\mathrm{TM})} = \pi/(\beta_S^{(\mathrm{TM})} - \beta_{AS}^{(\mathrm{TM})})$ denote the TE and TM beating lengths. We can engineer the modal birefringence and waveguide coupling by adjusting the width w of the ridges and the gap g between them to find an optimal point where:

$$\frac{L_c^{(\mathrm{TM})}}{L_c^{(\mathrm{TE})}} = \frac{p}{p+1} \tag{8.19}$$

with p is a positive integer. When this condition is met, TM light will be totally transferred to one output port after hopping p times between the waveguides, while TE light will hop $p+1$ times before exiting through the opposite port.

The figure of merit that we use to quantify the ability of the coupler to spatially separate the two orthogonal polarizations is the splitting ratio. This is defined separately for both polarization as:

$$s_{\mathrm{TE}} \equiv \frac{P_a^{(\mathrm{TE})}}{P_a^{(\mathrm{TE})} + P_b^{(\mathrm{TE})}} = \frac{1}{2}\left[1 + \cos\left(\pi \frac{L}{L_c^{(\mathrm{TE})}}\right)\right], \tag{8.20}$$

$$s_{\mathrm{TM}} \equiv \frac{P_b^{(\mathrm{TM})}}{P_a^{(\mathrm{TM})} + P_b^{(\mathrm{TM})}} = \frac{1}{2}\left[1 - \cos\left(\pi \frac{L}{L_c^{(\mathrm{TM})}}\right)\right]. \tag{8.21}$$

This definition depends on which arm, a or b, a given polarization is supposed to exit the directional coupler. Indeed, for an ideal splitting $s_{\mathrm{TE}} = s_{\mathrm{TM}} = 1$ corresponding to the case where all TE light ends up in arm a and all TM light in arm b. But the splitting is also optimal when $s_{\mathrm{TE}} = s_{\mathrm{TM}} = 0$ for which all TE and TM light exits in arm b or a respectively. Hence, when designing the device, we are willing to maximize either $s_{\mathrm{TE}}, s_{\mathrm{TM}}$ or $1 - s_{\mathrm{TE}}, 1 - s_{\mathrm{TM}}$ depending on the output port assigned to each polarization.

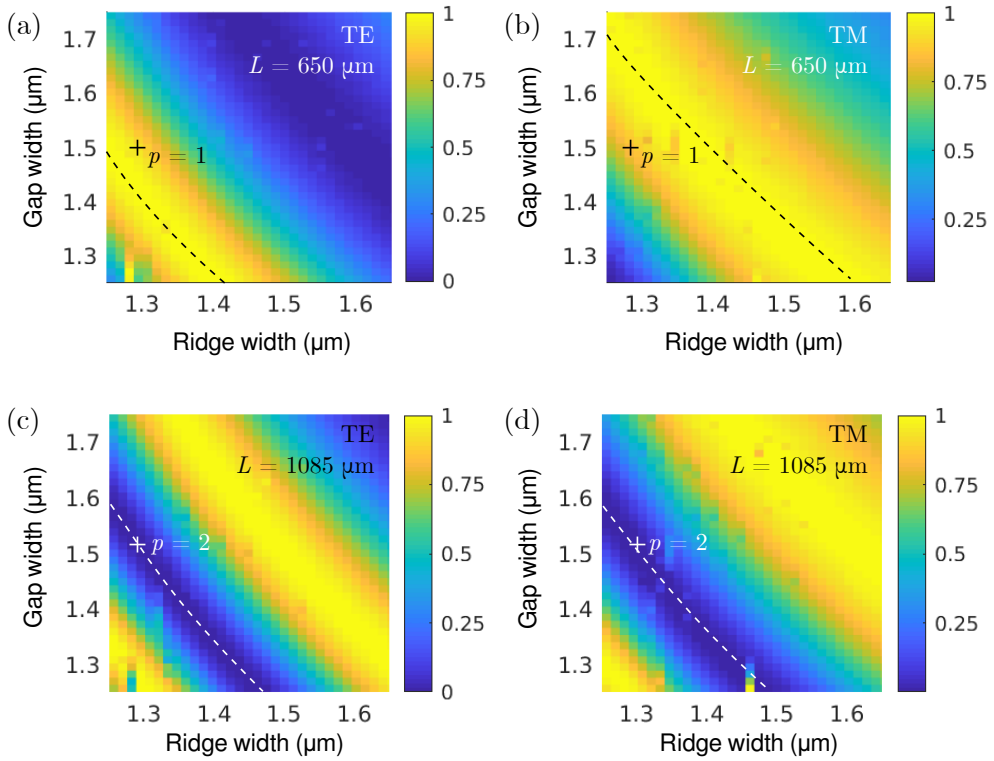

Figure 8.3: Simulated TE and TM splitting ratios for (a-b) $L = 650\,\mu\text{m}$ and (b-c) $L = 1085\,\mu\text{m}$. The regions for which s_{TE} and s_{TM} are either 0 or 1 are highlighted with dotted lines. The optimal working point of the device are indicated with crosses, corresponding to a region where Eq. (8.19) is fulfilled for $p = 1$ or $p = 2$.

8.3 Device design

8.3.1 Polarization splitting region

We performed electromagnetic mode analysis in our polarization mode splitter by solving Maxwell's equations with the COMSOL software suite to find a region in parameter space where condition (8.19) is fulfilled. For this project, we used an epitaxial structure with two upper Bragg mirrors (wafers `G5X038` and `K7AD118`). Note that in all designs, the waveguides feature a shallow etching profile, as indicated in the drawing of the waveguide cross-section of Fig. 8.2 (b). Only the first four upper layers, corresponding to two Bragg periods, are etched, leaving the core untouched. This has been done to ensure optimal coupling between the propagating modes of the waveguides. Indeed, if the core is etched, then the overlap between the spatial profile of the fundamental modes is drastically reduced, thus decreasing the coupling strength. The software solves Maxwell's equations in the coupled waveguide structure using finite element methods and extracts the spatial profile and effective index for a given number of modes at a fixed frequency. We implemented a simple algorithm to automatically detect the two S and AS supermodes from the multitude of guided modes that are calculated by COMSOL. However, this procedure can feature some errors when unphysical modes are accidentally identified instead of the supermodes of interest. As a result, we obtain some outlier points in the simulation data for certain values of w and g which have been subsequently removed.

From the simulated effective S and AS mode indices, using, Eqs. (8.17) and (8.18), we

were able to compute the transmitted power for both polarizations as a function of the waveguide width w, gap g and coupling length L and infer the splitting ratio. In Fig. 8.3, we display the simulated TE and TM splitting ratios for two selected values of L yielding the best performance. The regions for which s_{TE} and s_{TM} are either 0 or 1 are highlighted with dotted lines. In Fig. 8.3 (a-b), we observe that for $L = 650\,\mu\mathrm{m}$, the two dotted lines cannot be superimposed, meaning that the TE and TM splitting ratios cannot be simultaneously maximum. We indicate by a cross the optimal working point that has been found based on these simulations, corresponding to a situation where the condition in Eq. (8.19) for $p = 1$ is nearly fulfilled. On the contrary, for $L = 1085\,\mu\mathrm{m}$, we observe from Fig. 8.3 (c-d) that the dotted lines denoting the regions where s_{TE} and s_{TM} are the closest to zero can be almost perfectly superimposed. As a consequence, in this design, we can achieve simultaneously perfect TE and TM polarization splitting. The optimal working point, corresponding to the region where the two TE and TM dotted lines have the best overlap, is denoted by a cross. This corresponds to a situation where $p = 2$ according to Eq. (8.19).

To better understand the physical picture behind these simulations, we compute the TE and TM splitting ratios a function of coupling length for the optimal set of parameters $w = 1.29\,\mu\mathrm{m}$, $g = 1.51\,\mu\mathrm{m}$ using the S and AS mode indices computed numerically with COMSOL along with Eqs. (8.16), (8.20) and (8.21). In addition, using the Lumerical software, we simulate the eigenmode expansion (EME) propagation of a wave that is initially in waveguide a and record the spatial distribution of the intensity as it travels through the directional coupler. The results are plotted in Fig. 8.4. The two oscillating curves in Fig. 8.4 (a) correspond to the beating of the cosine terms in Eqs. (8.20) and (8.21) and the coupling length associated with the two possible designs that were indicated in Fig. 8.3 are labeled by black arrows.

In the first design, the TE polarized light does a round-trip by hopping onto the opposite waveguide before returning to the input waveguide, as shown in the simulated EME mode propagation in Fig. 8.4 (b). As for the TM mode, it only travels half a round-trip by directly hopping onto the adjacent waveguide. This is consistent with a TM/TE coupling length ratio of $p = 1$, as defined in Eq. (8.19). This design is the simplest in the sense that it involves the least possible number of round-trips while achieving reasonable polarization splitting. In addition, it only requires a relatively small coupling length of about $650\,\mu\mathrm{m}$, which can be useful to minimize losses. In this case, the TE and TM splitting ratios are both around 0.9. However, despite its simplicity, this design is not adapted to the broadband operation requirement for the integration with an AlGaAs photon-pair source. Indeed, we can see that this design corresponds to a point where the two curves $s_{\mathrm{TE}}, s_{\mathrm{TM}}$ intersect but are not at a maximum. When plotting the splitting ratios as a function of wavelength, as in Fig. 8.4 (c), we see that the two quantities are never simultaneously maximum over a broad bandwidth.

In the second design, as shown in Fig. 8.4 (d), the TE polarized light does an extra hop and ends up in the opposite waveguide while the TM polarized light is only having a single round-trip. In this configuration, which corresponds to a TM/TE beating length ratio of $p = 2$, the coupling length is longer, around $1085\,\mu\mathrm{m}$. However if offers much more robust polarization splitting. Indeed, this design corresponds to a maximum of both TE and TM splitting ratios. When looking at the wavelength dependence in Fig. 8.4 (e), we observe that $1 - s_{\mathrm{TE}}$ and $1 - s_{\mathrm{TM}}$ are above 0.9 over a 50 nm bandwidth. The only drawback to this design is its longer length which leads to higher losses in the fabricated device.

We analyze the fabrication tolerances by simulating the impact of a variation in the

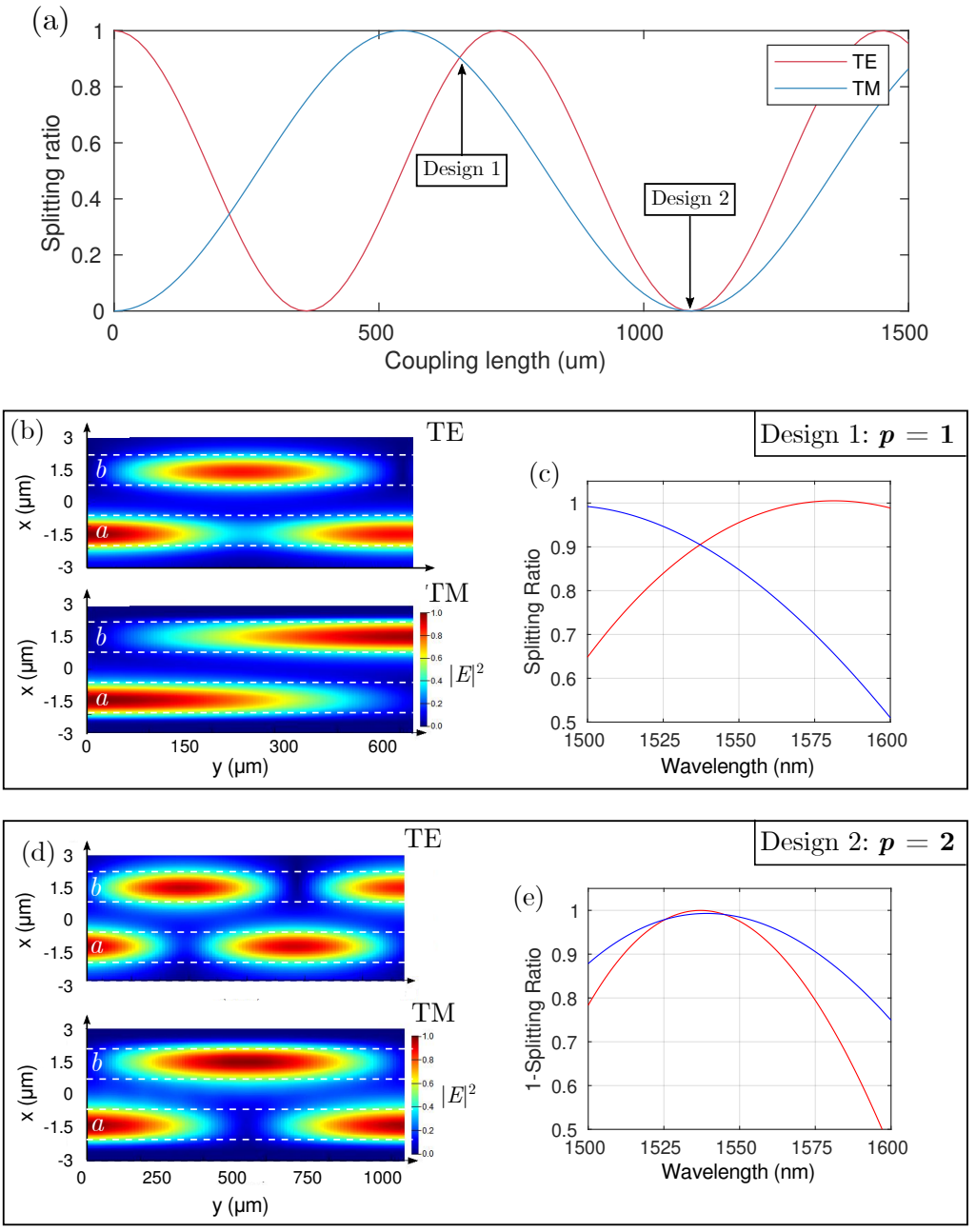

Figure 8.4: (a) Simulated splitting ratio as a function of coupling length for a directional coupler with $w = 1.29\,\mu\text{m}$, $g = 1.51\,\mu\text{m}$. The two designs that were studied in this work are highlighted. (b,d) Top-view EME simulation of the propagation of fundamental TE and TM modes for (b) Design 1 and (d) Design 2. The outlines of the two waveguides are indicated with white dashed lines. (c,e) Simulated splitting ratio as a function of wavelength for (c) Design 1 and (e) Design 2.

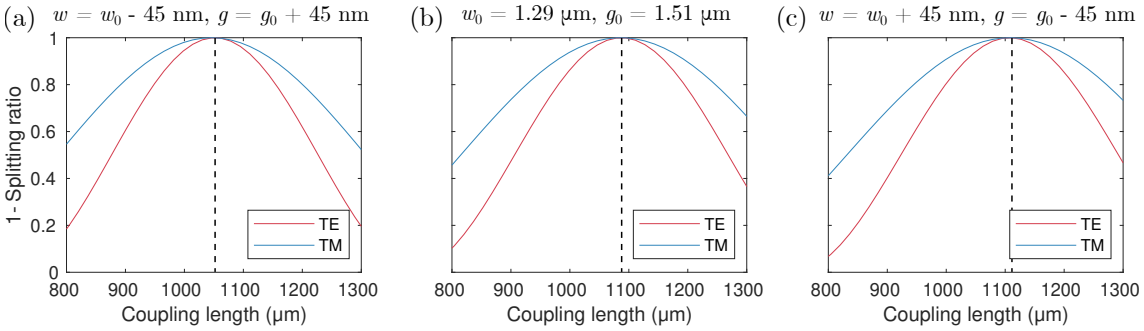

Figure 8.5: Analysis of the tolerance of the TE and TM splitting ratios with respect to a variation of $\delta = \pm 45$ nm from the nominal values of Design 2 ($p = 2$). Note that we plot here $1 - s_{\mathrm{TE}}$ and $1 - s_{\mathrm{TM}}$ for clarity. Splitting ratio as a function of coupling length for (a) $\delta = -45$ nm, (b) the nominal design and (c) $\delta = +45$ nm. The optimal coupling length in each graph is indicated by a black dashed line.

value of the ridge width w or the gap g on the splitting ratio. What usually happens in the fabrication process in our type of device is that the waveguides are either slightly broader or narrower than the nominal value but their spacing is relatively well controlled. Indeed, the width of the waveguides depend on several fabrication steps such has the resist deposition or the etching process, which inevitably feature some imperfections. On the contrary, the spatial positioning of the lithography patterns, and hence the spacing between the two waveguides, is determined by the positioning of the SEM moving stage, which has a much higher degree of reproducibility. Hence if w changes with respect to its nominal value w_0 by an amount $\pm\delta$ e.g. $w = w_0 \pm \delta$, then g deviates from its nominal value g_0 by the same amount: $g = g_0 \mp \delta$. We found out that a deviation of this kind in the waveguide width and gap according to the optimal values $w_0 = 1.29\,\mu\mathrm{m}, w_0 = 1.51\,\mu\mathrm{m}$ does not decrease the maximum achievable splitting ratio but simply shifts the optimal coupling length. In Fig. 8.5, we simulate effect on the splitting ratio of a variation of $\delta = \pm 45$ nm, which is chose to be well above the empirical uncertainty on the waveguide width that we observed in the fabrication process. We show that a variation of $\delta = +45$ nm shifts the optimal coupling length, for which $1 - s_{\mathrm{TE}}$ and $1 - s_{\mathrm{TM}}$ are maximum, by $+45\,\mu\mathrm{m}$ while a variation of $\delta = -45$ nm shifts the optimal length by -40 µm. In principle, these tolerances are larger that the achievable resolution of the electron-beam lithography and dry etching fabrication process that was used to fabricate the devices (see Section 4.3). In addition, we make sure that the tuning range of the coupling length is sufficient to make up for any variation resulting from imperfect fabrication by fabricating multiple devices on a single chip with various L in steps of 20 µm to 30 µm.

8.3.2 Photon-pair generation region

As shown in Fig. 8.1, the photon-pair generation region consists of a waveguide of width W that is tapered down to match the width w of the polarization splitting region. This design ensures that no photon pairs are generated in the polarization mode splitter. Indeed, as we have seen in Section 4.5, the phase-matching wavelength depends significantly on the ridge width. Hence, the phase-matching wavelength will not be the same for the two regions allowing to generate photon pairs only in the generation region. The engineering of the generation region is illustrated in Fig. 8.6. The simulated phase-matching wavelength for a 1.29 µm-wide ridge is equal to 780.5 nm. Consequently, we choose a generation width of $W = 5\,\mu\mathrm{m}$ corresponding to the standard ridge width that we used in most samples and

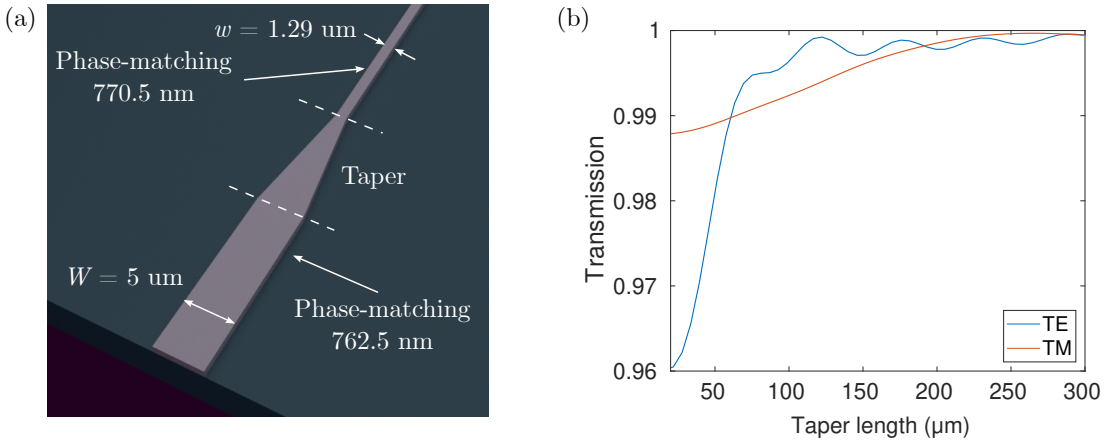

Figure 8.6: (a) Schematic of the photon-pair generation region with calculated phase-matching wavelengths. (b) Taper transmission for TE and TM fundamental mode at a wavelength of 1550 nm.

which is broad enough to allows for an easy coupling of the pump beam into the waveguide. For $W = 5\,\mu m$, phase-matching occurs at 762.5 nm, corresponding to a detuning of 8 nm with respect to the waveguides in the polarization mode splitter.

The taper is designed to have a high transmission of both polarizations while maintaining the shortest possible length. A FDTD simulation of the taper transmission as a function of taper length at a wavelength of 1550 nm is displayed in Fig. 8.6 (b). We see that TE and TM modes are transmitted with more than 99.5 % transmissivity when the taper is longer than 200 µm. Consequently, in our design, we set the taper length to 250 µm.

8.4 Realization of a test sample

To experimentally validate the polarization splitting mechanism, we fabricated a first generation of prototype devices following the first design ($p = 1$). In this chip, which was fabricated from wafer `G5X038`, there is no photon-pair generation region, only a polarization mode splitter. We chose to first implement the simpler design, with the shortest coupling region, simply to calibrate the fabrication process and adjust the simulation parameters accordingly. The nominal waveguide parameters were $w = 1.5\,\mu m, g = 1.5\,\mu m$.

The device was fabricated using electron-beam lithography and dry ICP etching, a process that has been described in Section 4.3. Since we needed to pattern long waveguides, we used the fixed beam moving stage (FBMS) mode. On this chip, we fabricated 13 directional couplers with lengths ranging from 400 µm to 640 µm in steps of 20 µm. The spacing between the output ports was set to 250 µm to be compatible with the standard pitch of commercial fiber arrays which can be used to collect light from the chip. The length of the S-bend was 450 µm resulting in a radius of curvature of 400 µm which is smooth enough to avoid losses due to the waveguide curvature [166]. In between each device, we inserted straight 1.5 µm-wide waveguides to characterize the propagation losses and phase-matching of the sample.

After fabrication, the first characterization step was to precisely measure the width w of the waveguides and the gap g in the evanescent coupling region with a SEM and compare those values to the nominal design. There was a slight asymmetry, of the order

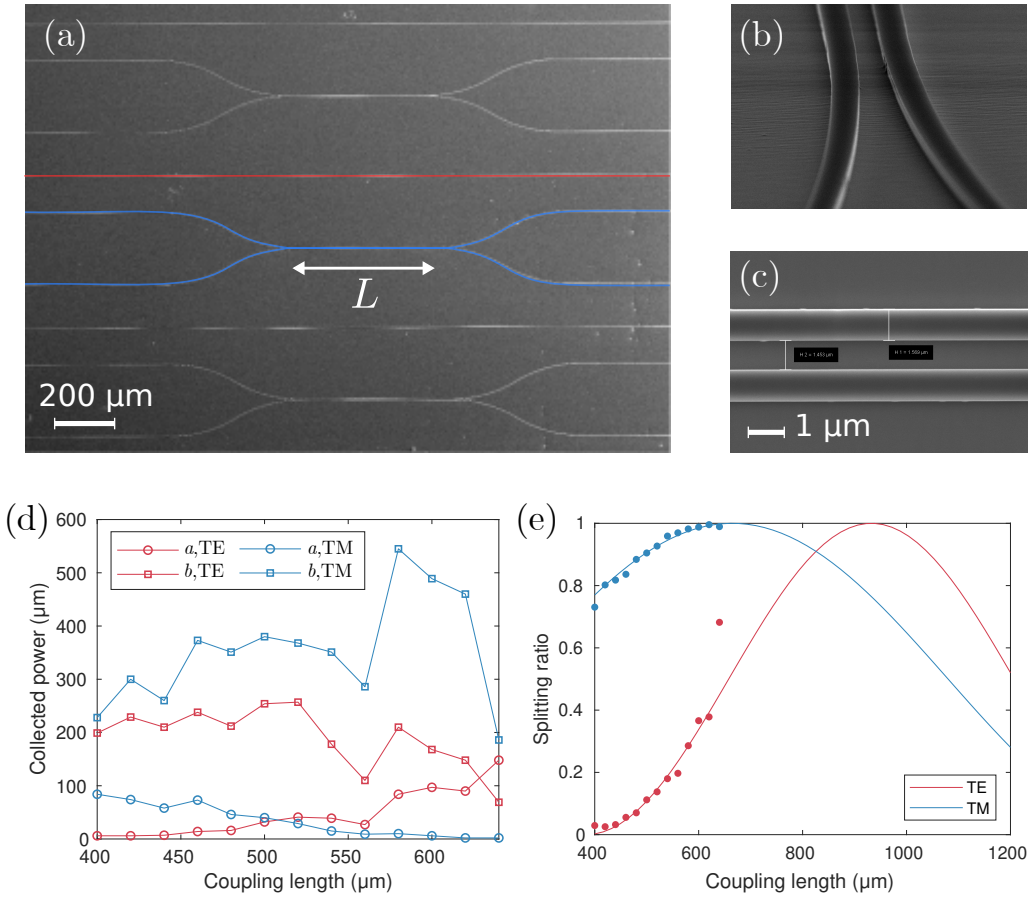

Figure 8.7: (a) False-color SEM images of the test sample fabricated from wafer `G5X038`. The blue lines highlight the polarization splitter while the straight waveguide that were included for characterization appear in red. (b) S-bend region: we observe sharp vertical sidewalls as well as smooth waveguide curvature. (c) Evanescent coupling region viewed from the top showing straight and smooth waveguide sidewalls. (d) Raw collected power from the two output arms a and b for both TE and TM polarization. (e) Measured (dots) and simulated (lines) splitting ratio as a function of coupling length L at a wavelength of 1550 nm. In the simulation, an offset of 166 µm was added to the coupling length L in order to reproduce the experimental results (see text for details).

of 1 % between the two waveguide width. Indeed, when averaging over all the observed structures on the chip, the first waveguide was measured to be on average 1512 nm wide while the other was 1528 nm wide. The standard deviation is 3 nm, of the order of the spatial resolution of the SEM. This shows the good pattern reproducibility of our fabrication process. Similarly, the gap between waveguides was measured to be 1461 nm with a standard deviation of 8 nm.

We then put the device on the optical test bench to measure the TE and TM splitting ratio and their dependence on the coupling length L. To do so, we used the following setup : we sent a telecom tunable laser (Tunics) at a wavelength $\lambda = 1550$ nm through a linear polarizer with transmission axis making an angle θ with respect to the vertical axis (x-axis in Fig. 8.2) then into the waveguide using a NA = 0.95 microscope objective (Zeiss AchroPlan). Light exiting the chip was collected with an identical objective. The power of the output beam was recorded using a Coherent FieldMaxII power-meter. The chip was set at a stable temperature using a Peltier cell coupled to a thermistor, like in the experimental setups described in Chapter 4. Note that, due to the 250 µm spacing between arms a and b, the short working distance of our output microscope objective does not allow measuring simultaneously the power exiting from waveguides a and b. As a consequence, we needed to measure P_a and P_b one at a time, realigning the microscope objective on the target waveguide between each measurement. We repeated the measurement for all the devices of different coupling lengths that are present on the chip.

The measured output power from the two output arms a and b for TE and TM at 1550 nm as a function of coupling length and the resulting splitting ratio are shown in Fig. 8.7 (d-e). We see that the experimental values for the splitting ratio reported in Fig. 8.7 (e) are in good agreement with simulations, represented as solid lines. We observe that the simulated and experimental values for the coupling length disagree by an offset of 166 µm. In other words, we had to add 166 µm to the nominal value of L to make the simulation in Fig. 8.7 (e) match the experimental data. This difference between the simulations and the measurements can be due to a possible residual evanescent coupling in the transition zone between the directional coupler and the S-bends. We also observe that the fabricated devices cannot reach the theoretical maximum splitting ratio. This is due to the fact that the initial simulations based on which the coupling length was chosen did not take into account the shallow etching profile of the waveguides, which shifted the value of the calculated optimal coupling length. By taking into account the simulations, we obtain the simulated curves in Fig. 8.7 (e) which reproduce the measurement very faithfully.

Chapter 9

Experimental demonstration

Contents

9.1 Chip layout 131

9.2 Classical characterization: propagation losses, phase-matching, splitting ratio 132

9.3 Photon-pair generation and on-chip polarization splitting . . . 136

9.4 Hong-Ou-Mandel interference at the chip output 136

This chapter is dedicated to the experimental characterization of the device including a photon-pair generation region and a polarization splitting region on a single chip. We first describe the chip layout before presenting the result of the classical characterization in terms of splitting ratio and phase-matching. Then we demonstrate that this device allows for the generation and spatial separation of photon-pairs directly on chip. Finally, we report on the measurement of Hong-Ou-Mandel effect directly at the chip output, showing that we can achieve on-chip polarization splitting without significantly affecting the spectral indistinguishability of the photon pairs.

9.1 Chip layout

In this new generation of device, we implement Design 2 for the polarization splitter corresponding to to $p = 2$ in Eq. (8.19) in order to get the highest possible splitting ratio. We fabricated the sample using FBMS e-beam lithography and dry ICP etching using the recipe described in Fig. 4.8. The nominal waveguide parameters are $w = 1.29\,\mu\text{m}, g = 1.51\,\mu\text{m}$. Using the same cleanroom process as in the previous chapter (descibed in Section 4.3), we fabricated a chip with 13 structures of increasing coupling length from wafer `K7AD118`. From the simulation reported in Fig. 8.4 (a) we predict an optimal coupling length of 1085 µm at a wavelength of 1550 nm. Thanks to the experimental characterization performed on the test sample, we recall that we need to subtract a 166 µm offset to the value of the coupling length. As a consequence, we fabricated devices with coupling lengths ranging from $L = 750\,\mu\text{m}$ to 1110 µm in steps of 30 µm. We inserted a test straight waveguide of width $W = 5\,\mu\text{m}$ between every three structures to characterize the generation region in terms of losses and phase-matching wavelength.

The layout of the e-beam lithography pattern is shown in Fig. 9.1. The spacing between the output ports has been reduced from 250 µm to 127 µm in order reduce the device

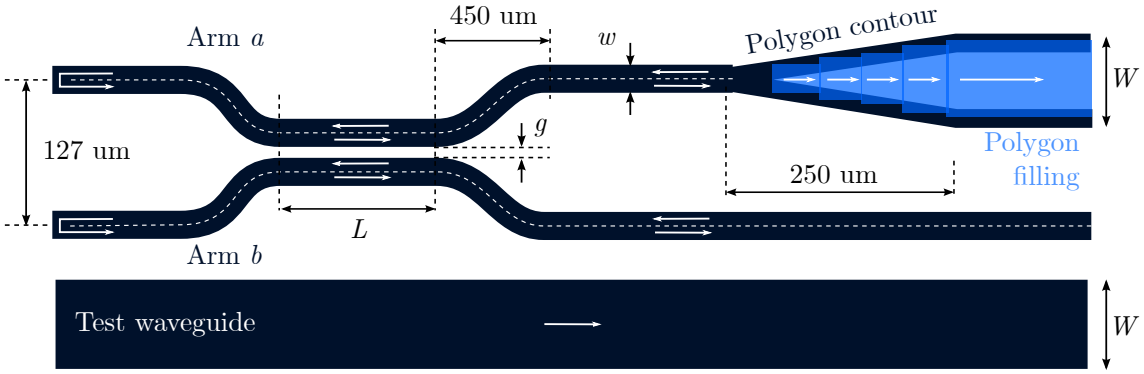

Figure 9.1: Final device layout showing the lithography pattern that was used to draw the structure. The FBMS writing direction is indicated with white arrows. See text for details.

footprint and fit more structures per unit area of the sample. The value of 127 µm is also another standard pitch for commercial fiber arrays that could be used to collect light from the waveguides. In addition to this, using a tighter pitch, we were able to collect light from both output port from a single microscope objective (NA = 0.65), which was not possible using a 250 µm spacing. This was a requirement for the measurement of HOM effect at the chip output, which can only be done if the photons from both output ports are collected simultaneously. In addition, this change in the waveguide spacing also increases the radius of curvature of the S-bends to a value of 832 µm, which minimizes the losses caused by the curvature of the waveguides.

The taper connecting the polarization mode splitter to the generation region was drawn with FBMS electron-beam lithography using the polygon patterning technique shown schematically in Fig. 9.1. Indeed, since, in FBMS mode, it is not possible to directly draw polygons but only paths of fixed width, the taper has to be drawn in two steps : first the contour then the filling. The filling is made of multiple FBMS paths of increasing width. Note that to avoid any gaps between the lithography paths at the two ends of the taper, we also draw the narrower waveguides of the polarization splitting region in two halves. Indeed, by doing so we merge the contour of the taper and generation region with the waveguides of the splitting region into a single continuous path. SEM images of the fabricated sample are shown in Fig. 9.2.

9.2 Classical characterization: propagation losses, phase-matching, splitting ratio

Once the sample was fabricated, we characterized the test straight waveguide by estimating the propagation losses with the Fabry-Perot technique and the phase-matching wavelength via a SHG spectrum. The experimental setups are identical to those described in Chapter 4. The results are shown in Fig. 9.3. We obtain a value of $0.9\,\mathrm{cm}^{-1}$ and $1.5\,\mathrm{cm}^{-1}$ for fundamental TE and TM mode losses respectively. The SHG spectrum plotted as a red solid line in Fig. 9.3 was obtained with a linearly polarized pump beam at an angle of 45 deg with respect to the vertical z-axis (see Fig. 9.2). Instead of the expected sharp Type II and Type 0 resonance separated by about 10 nm, we observe a group of tightly spaced peaks with very low amplitude. By setting the pump polarization to 0 deg with respect to the z-axis (blue solid line), we managed to identify the central and the

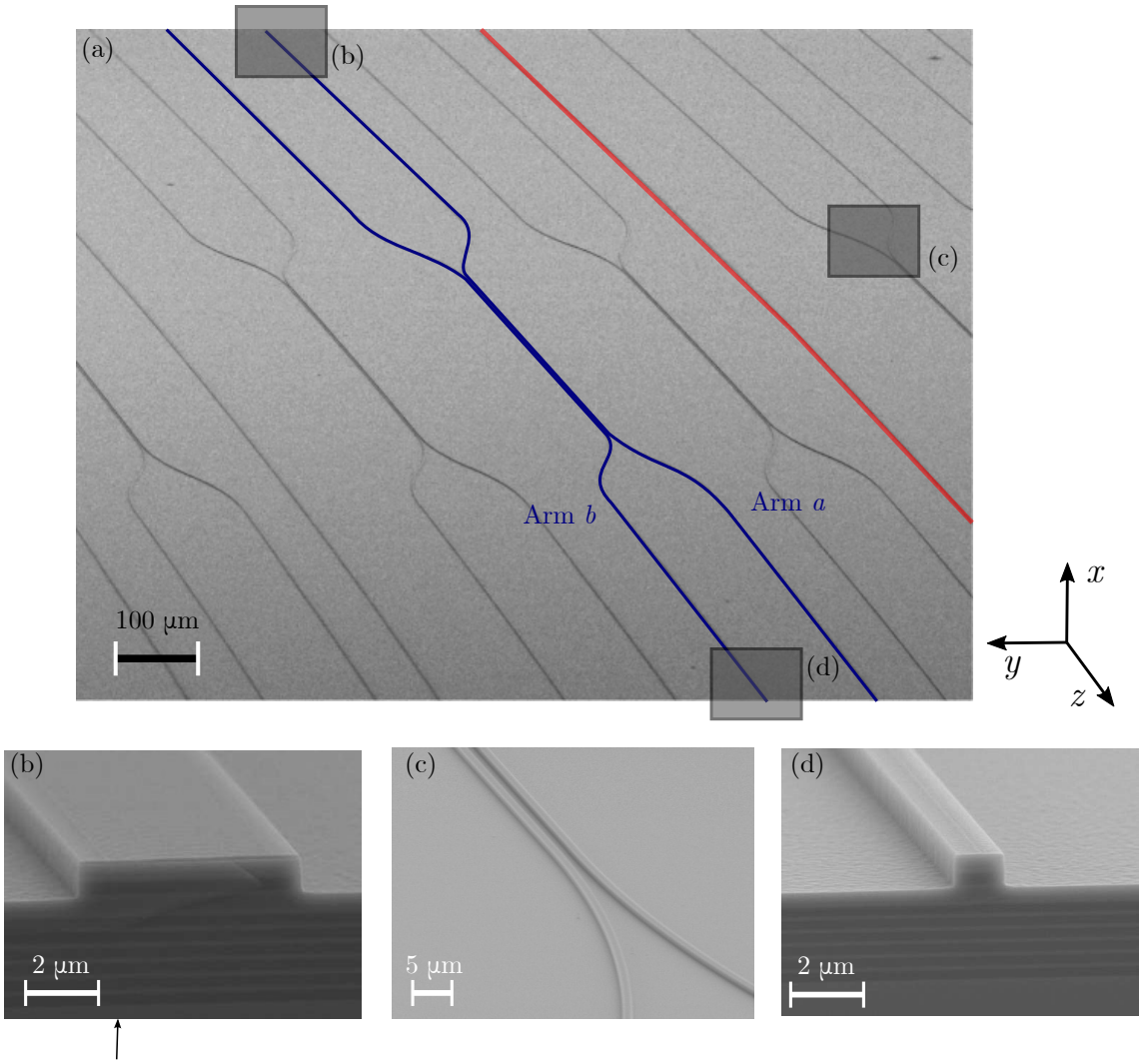

Figure 9.2: (a) False-color SEM image of the fabricated chip. The source and polarization splitter are highlighted in blue while the red line indicates a test straight waveguide. (b) Facet of the input waveguide of width $W = 5\,\mu\text{m}$. (c) S-bend and evanescent coupling region. (d) Facet of the output waveguide of width $w = 1.29\,\mu\text{m}$.

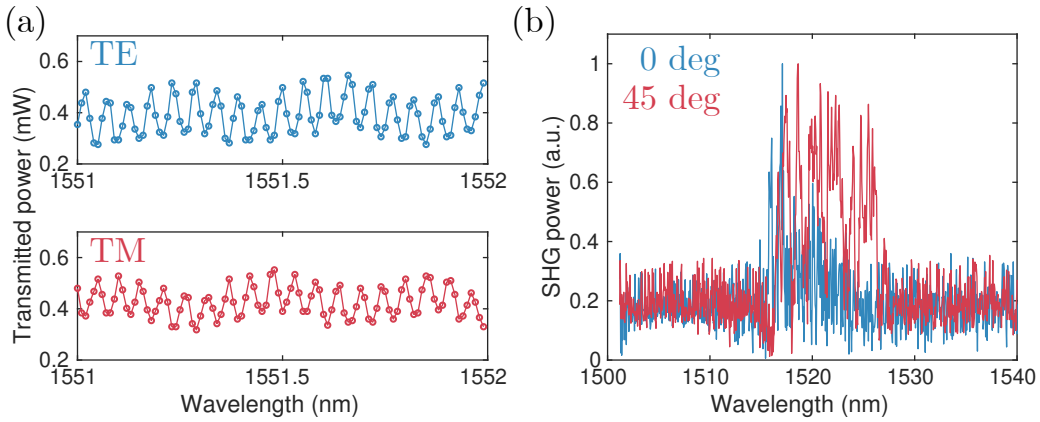

Figure 9.3: (a) TE and TM transmission and (b) SHG spectrum for a linearly polarized pump beam at 45 deg (red curve) or 0 deg (blue curve) with respect to the z-axis measured on the test straight waveguide of width $W = 5\,\mu\text{m}$.

right peak as the Type II resonances while the left peak appears to be Type 0. As a result, we extract a Type II phase-matching wavelength of 1525 nm.

The next step has been to measure the splitting ratio as a function of wavelength for all the devices having different coupling lengths L. This is done by sending a telecom laser beam into the generation region and recording the transmitted power at the two output ports like for the measurement of the test sample presented in Section 8.4. In this case the output signal is collected from both ports at the same time using a single NA=0.65 microscope objective. By scanning the input wavelength for the two input polarization, TE or TM, we were able to experimentally reconstruct the splitting ratios $s_{\text{TE}}, s_{\text{TM}}$ as a function of wavelength. We repeated this experiment for all the devices with different coupling lengths L to identify the one having the best performance. In Fig. 9.4 (a), we show the result of this measurement for the 5 devices that yielded the best splitting ratios in the spectral range of interest, namely around the measured phase-matching wavelength 1525 nm. We see that, in all cases, s_{TE} and s_{TM} reach their maximum approximately around the same wavelength. By changing L, we observe that this optimal wavelength can be blue or red-shifted, providing us with a useful tuning parameter to adjust the splitting ratio to the phase-matching of the source. As a consequence, we chose to use a device with a coupling length $L = 1080\,\mu\text{m}$ for which the TE and TM splitting ratios are optimal around 1525 nm. In addition, we see that the splitting ratio remains above 90 % over a spectral range of about 50 nm. This makes our polarization splitter compatible with the measured 60 nm FWHM spectral width of the two-photon emission of our source obtained in Section 6.2. The broadband polarization splitting of our device guarantees that most of the emitted photons will be efficiently separated on the chip. The raw data for the splitting ratio measurement in this device is shown in Fig. 9.4 (c-b). We observe that the transmission of the device is slightly lower for TE than for TM polarization (yellow and red curves in Fig. 9.4 (c)) which is consistent with the fact that the measured propagation losses were higher for TE than for TM mode (Fig. 9.3 (a)). We notice, however, that the measured transmission of the whole device is lower than that of a straight 5 µm-wide test waveguide. These losses can be attributed to the presence of S-bends and to the narrow waveguide width in the polarization splitting region (see Table 4.2).

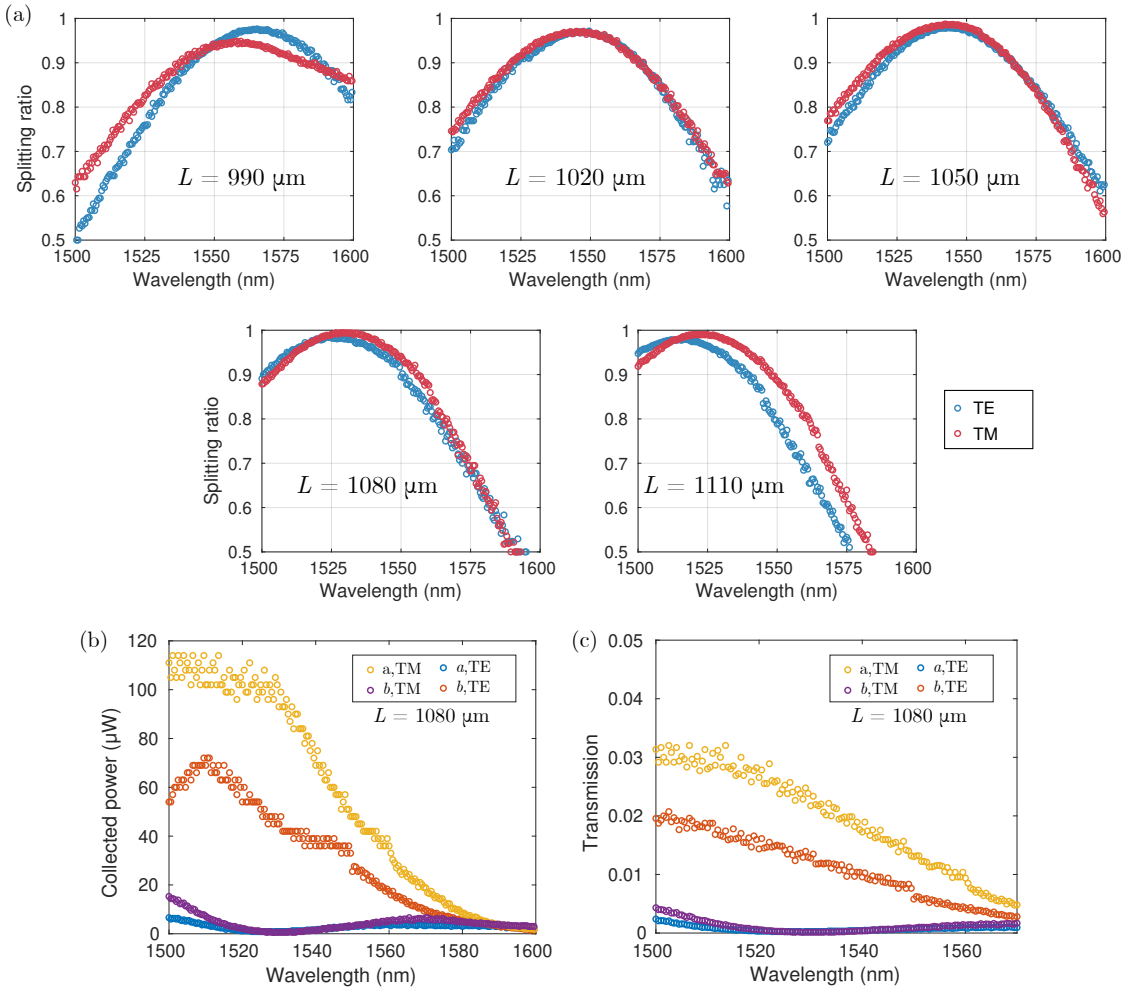

Figure 9.4: (a) Measured TE and TM splitting ratios as a function of wavelength for 5 samples with different coupling length L. (b) Collected power and (c) normalized transmission from arms a and b for TE and TM polarizations in a device with $L = 1080\,\mu\text{m}$.

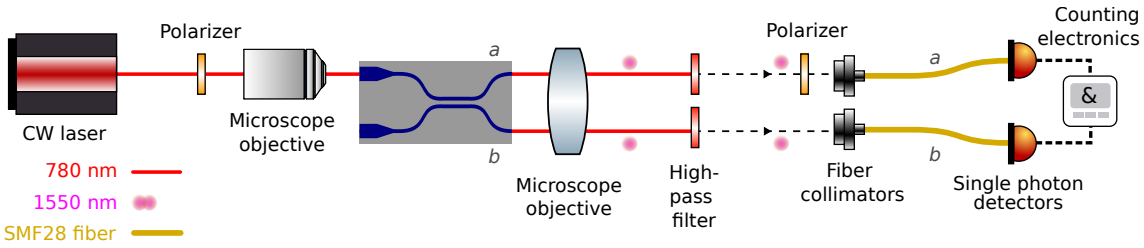

Figure 9.5: Experimental setup for the measurement of time-correlations between the on-chip generated and separated photons.

9.3 Photon-pair generation and on-chip polarization splitting

After identifying the device with the best polarization splitting profile we characterized the on-chip photon-pair generation and separation. This is done by using the setup sketched in Fig. 9.5. We pump the generation region of the sample using a NIR CW laser whose wavelength has been tuned to the measured phase-matching wavelength, in our case $\lambda_p = 762.33\,\text{nm}$, and which is coupled into the waveguide by a NA=0.95 Zeiss Achroplan microscope objective. The generated photons were collected at the output ports of the polarization splitter using a NA=0.65 objective. As can be seen from the picture in Fig. 9.6, the two output optical paths were directed towards separate fiber collimators after filtering out the pump using high pass filters. Then the photons were sent to the SNSPDs for coincidence detection. We scanned the input pump power and recorded the number of coincidence counts and CAR as shown in Fig. 9.7 (a-b). We observe that the coincidences have a nearly linear dependence on the input pump power while the CAR is inversely proportional to the pump power, as in the case of a straight waveguide (see Section 6.1).

To check the quality of the polarization splitting, we measured the number of coincidence counts after inserting a polarizer at the output of one of the arms of the device. We record the number of coincidences as a function of the polarizer transmission axis angle and repeat the measurement with the polarizer in the opposite arm. The result of these two measurements is displayed in Fig. 9.7 (c). We observe that the number of coincidences goes to zero when the polarizer transmission axis on arm a is set to 90 deg with respect to the z-axis (blue curve). Conversely, when the polarizer is in arm b, the coincidences are minimal for an angle of 0 deg with respect to the z-axis (red curve). This clearly shows that the photons collected from arm a and arm b are respectively TM and TE polarized, as expected. We note that the maximum number of counts is larger for the blue curve than for the red curve, which can be explained by the fact that TM losses are lower than TE losses, as shown in Fig. 9.4 (c).

9.4 Hong-Ou-Mandel interference at the chip output

9.4.1 HOM coincidence probability for a frequency-dependent polarization splitter

After showing that photon pairs can be generated and separated on-chip using the integrated polarization splitter, we probed their quantum state through Hong-Ou-Mandel interference.

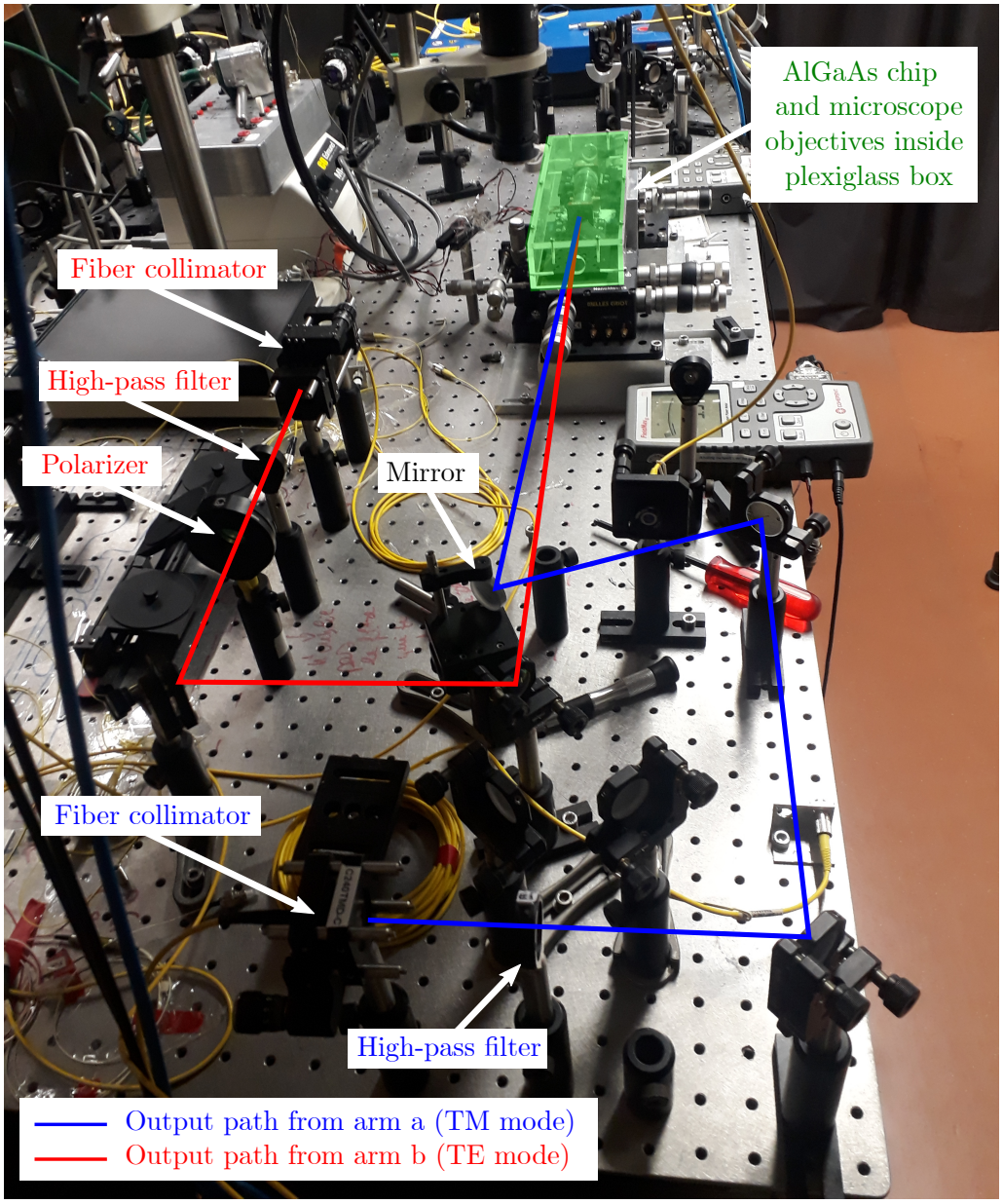

Figure 9.6: Photograph of the experimental setup showing the collection path for light exiting the chip from arm a or b (solid blue and red lines). In this image, the polarizer used for the measurement described in Fig. 9.5 is located in path b.

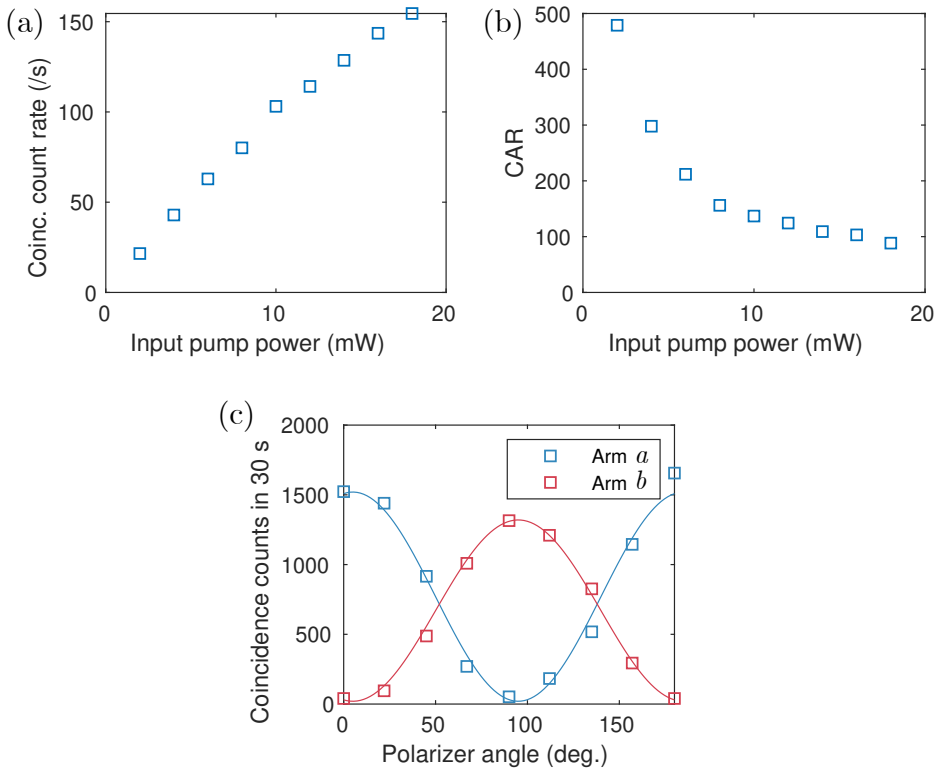

Figure 9.7: (a) Coincidence counts and (b) CAR as a function of input pump power measured at the output ports of the chip without any polarizer. (c) Coincidence counts as a function of polarizer transmission axis angle for each output arms of the device. The experimental data is fitted with sine square and cosine square functions.

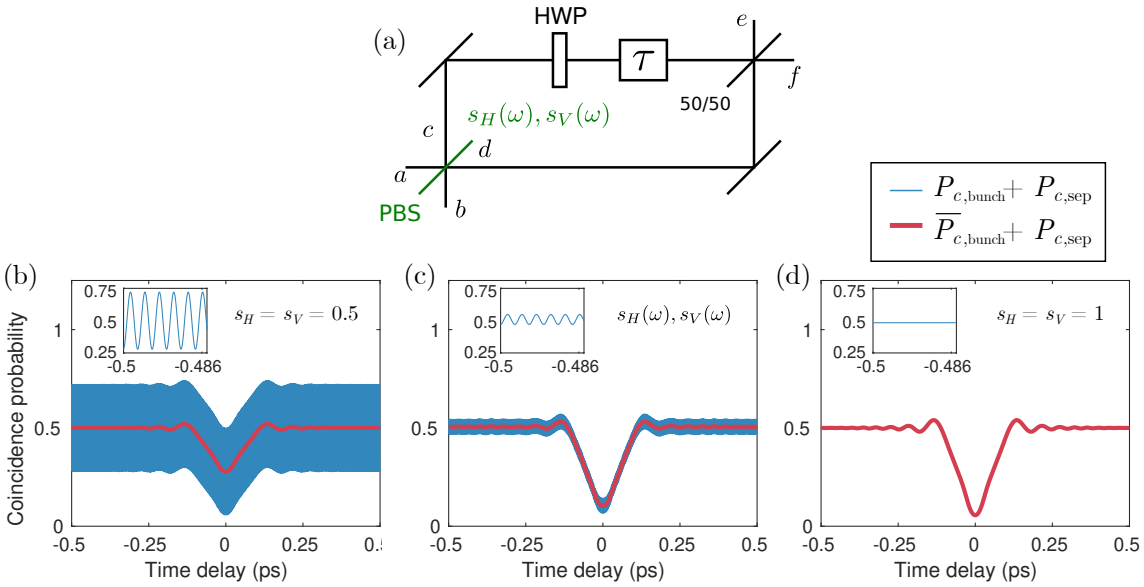

Figure 9.8: (a) Model for Hong-Ou-Mandel interference with a frequency-dependent polarizing beam splitter. HWP: Half-wave plate, PBS: Polarizing beam splitter. (b-d) Simulated HOM coincidence probability P_c showing different contributions from the terms $P_{c,\text{sep}}$ and $P_{c,\text{bunch}}$ for different values of the PBS splitting ratio: (b) $s_H = s_V = 0.5$, (c) $s_H(\omega), s_V(\omega)$ given by the experimental values of the device of coupling length $L = 1080\,\mu\text{m}$ (d) $s_H = s_V = 1$. The inset displays the value of P_c over a 14 fs window at $\tau = -0.5\,\text{ps}$ showing the oscillations originating from the term $P_{c,\text{bunch}}$.

To predict the HOM interferogram in this configuration, we needed to use a more elaborate model than the one described in section Section 6.2 in order to take into account the frequency dependence of the device's splitting ratio. The model that we used is depicted in Fig. 9.8 (a). The photon pairs emitted by the source are incident on a frequency-dependent polarizing beam splitter, which models the polarization splitting region of our device. We assume that the two photons are initially in the same arm of the PBS, say arm a. Then, after they exit the PBS, a delay is applied to arm c and the polarization in this arm is rotated with a half-wave plate such that the two photons end up with identical polarization. As in a usual HOM interferometer, the photons are recombined on a 50/50 beam splitter. The goal here is to calculate the coincidence probability between the output arms e, f of the 50/50 beam splitter. We start from the generated SPDC state:

$$|\Psi\rangle = \iint \mathrm{d}\omega_1 \mathrm{d}\omega_2 \mathcal{C}(\omega_1, \omega_2) \, |\omega_1, H, a\rangle \, |\omega_2, V, a\rangle \,, \tag{9.1}$$

where $|\omega, H, a\rangle = \hat{a}_H(\omega) \, |\text{vac}\rangle \,, |\omega, V, a\rangle = \hat{a}_V(\omega) \, |\text{vac}\rangle$ and the JSA is assumed to be normalized $\iint d\omega_1 d\omega_2 |\mathcal{C}(\omega_1, \omega_2)|^2 = 1$. The action of the frequency-dependent PBS is represented by a unitary transformation acting separately on the H and V subspaces:

$$\hat{a}_H(\omega) = \sqrt{s_H(\omega)}\hat{c}_H(\omega) + \sqrt{1 - s_H(\omega)}\hat{d}_H(\omega), \tag{9.2}$$
$$\hat{b}_H(\omega) = \sqrt{1 - s_H(\omega)}\hat{c}_H(\omega) - \sqrt{s_H(\omega)}\hat{d}_H(\omega), \tag{9.3}$$
$$\hat{a}_V(\omega) = \sqrt{1 - s_V(\omega)}\hat{c}_V(\omega) + \sqrt{s_V(\omega)}\hat{d}_V(\omega), \tag{9.4}$$
$$\hat{b}_V(\omega) = \sqrt{s_V(\omega)}\hat{c}_V(\omega) - \sqrt{1 - s_V(\omega)}\hat{d}_V(\omega), \tag{9.5}$$

where the coefficients $s_H(\omega), s_V(\omega)$ are the TE and TM splitting ratios of the polarization

splitter. After the PBS, the quantum state becomes:

$$|\Psi\rangle = \iint \mathrm{d}\omega_1 \mathrm{d}\omega_2 \mathcal{C}(\omega_1,\omega_2) \left[|\omega_1, H\rangle \left(\sqrt{s_H(\omega_1)}\,|c\rangle + \sqrt{1-s_H(\omega_1)}\,|d\rangle\right)\right] \left[|\omega_2, V\rangle \left(\sqrt{1-s_V(\omega_2)}\,|c\rangle + \sqrt{s_V(\omega_2)}\,|d\rangle\right)\right], \tag{9.6}$$

where we separated the spatial part of the kets for clarity.

The state can be divided into two parts, one describing the case where the two photons are separated into distinct paths $|\Psi\rangle_{\text{sep}}$ and another corresponding to the two photons ending up into the same spatial mode $|\Psi\rangle_{\text{bunch}}$. Using these notations, the state can be rewritten : $|\Psi\rangle = |\Psi\rangle_{\text{sep}} + |\Psi\rangle_{\text{bunch}}$ where the two independent contribution are:

$$|\Psi\rangle_{\text{sep}} = \iint \mathrm{d}\omega_1 \mathrm{d}\omega_2 \mathcal{C}(\omega_1,\omega_2)\,|\omega_1, H\rangle\,|\omega_2, V\rangle \left(\sqrt{s_H(\omega_1)}\sqrt{s_V(\omega_2)}\,|c\rangle\,|d\rangle + \sqrt{1-s_H(\omega_1)}\sqrt{1-s_V(\omega_2)}\,|d\rangle\,|c\rangle\right), \tag{9.7}$$

$$|\Psi\rangle_{\text{bunch}} = \iint \mathrm{d}\omega_1 \mathrm{d}\omega_2 \mathcal{C}(\omega_1,\omega_2)\,|\omega_1, H\rangle\,|\omega_2, V\rangle \left(\sqrt{s_H(\omega_1)}\sqrt{1-s_V(\omega_2)}\,|c\rangle\,|c\rangle + \sqrt{1-s_H(\omega_1)}\sqrt{s_V(\omega_2)}\,|d\rangle\,|d\rangle\right). \tag{9.8}$$

After being transformed by the delay line and HWP, the state reads:

$$|\Psi\rangle_{\text{sep}} = \iint \mathrm{d}\omega_1 \mathrm{d}\omega_2 \mathcal{C}(\omega_1,\omega_2)\,|\omega_1, V, c\rangle\,|\omega_2, V, d\rangle\,\sqrt{s_H(\omega_1)}\sqrt{s_V(\omega_2)}e^{-i\omega_1\tau} + \iint \mathrm{d}\omega_1 \mathrm{d}\omega_2 \mathcal{C}(\omega_1,\omega_2)\,|\omega_1, H, d\rangle\,|\omega_2, H, c\rangle\,\sqrt{1-s_H(\omega_1)}\sqrt{1-s_V(\omega_2)}e^{-i\omega_2\tau}, \tag{9.9}$$

$$|\Psi\rangle_{\text{bunch}} = \iint \mathrm{d}\omega_1 \mathrm{d}\omega_2 \mathcal{C}(\omega_1,\omega_2)\,|\omega_1, V, c\rangle\,|\omega_2, H, c\rangle\,\sqrt{s_H(\omega_1)}\sqrt{1-s_V(\omega_2)}e^{-i(\omega_1+\omega_2)\tau} + \iint \mathrm{d}\omega_1 \mathrm{d}\omega_2 \mathcal{C}(\omega_1,\omega_2)\,|\omega_1, H, d\rangle\,|\omega_2, V, d\rangle\,\sqrt{1-s_H(\omega_1)}\sqrt{s_V(\omega_2)}. \tag{9.10}$$

Then the two photons enter the 50/50 beam splitter whose action can be modeled by the usual unitary transform: $|c\rangle = (|e\rangle + |f\rangle)/\sqrt{2}$, $|d\rangle = (|e\rangle - |f\rangle)/\sqrt{2}$. We post-select the states where both photons exit through different output ports and obtain the following expression:

$$\begin{aligned} |\Psi'\rangle_{\text{sep}} = \frac{1}{2}\iint \mathrm{d}\omega_1 \mathrm{d}\omega_2 \mathcal{C}(\omega_1,\omega_2)\sqrt{s_H(\omega_1)}\sqrt{s_V(\omega_2)}e^{-i\omega_1\tau} \\ |\omega_1, V\rangle\,|\omega_2, V\rangle\,(-|e\rangle\,|f\rangle + |f\rangle\,|e\rangle) \\ +\frac{1}{2}\iint \mathrm{d}\omega_1 \mathrm{d}\omega_2 \mathcal{C}(\omega_1,\omega_2)\sqrt{1-s_H(\omega_1)}\sqrt{1-s_V(\omega_2)}e^{-i\omega_2\tau} \\ |\omega_1, H\rangle\,|\omega_2, H\rangle\,(|e\rangle\,|f\rangle - |f\rangle\,|e\rangle), \end{aligned} \tag{9.11}$$

$$\begin{aligned} |\Psi'\rangle_{\text{bunch}} = \frac{1}{2}\iint \mathrm{d}\omega_1 \mathrm{d}\omega_2 \mathcal{C}(\omega_1,\omega_2)\sqrt{s_H(\omega_1)}\sqrt{1-s_V(\omega_2)}e^{-i(\omega_1+\omega_2)\tau} \\ |\omega_1, V\rangle\,|\omega_2, H\rangle\,((|e\rangle\,|f\rangle + |f\rangle\,|e\rangle) \\ -\frac{1}{2}\iint \mathrm{d}\omega_1 \mathrm{d}\omega_2 \mathcal{C}(\omega_1,\omega_2)\sqrt{1-s_H(\omega_1)}\sqrt{s_V(\omega_2)} \\ |\omega_1, H\rangle\,|\omega_2, V\rangle\,(|e\rangle\,|f\rangle + |f\rangle\,|e\rangle) \end{aligned} \tag{9.12}$$

We group the different terms and get the final mathematical form of the quantum state:

$$\begin{aligned}
\left|\Psi'\right\rangle_{\text{sep}} = \frac{1}{2}\iint \mathrm{d}\omega_1\mathrm{d}\omega_2 \Big(&\mathcal{C}(\omega_1,\omega_2)\sqrt{s_H(\omega_1)}\sqrt{s_V(\omega_2)}e^{-i\omega_1\tau} \\
&-\mathcal{C}(\omega_2,\omega_1)\sqrt{s_H(\omega_2)}\sqrt{s_V(\omega_1)}e^{-i\omega_2\tau}\Big)\left|\omega_1,V,e\right\rangle\left|\omega_2,V,f\right\rangle \\
+\frac{1}{2}\iint \mathrm{d}\omega_1\mathrm{d}\omega_2 \Big(&\mathcal{C}(\omega_1,\omega_2)\sqrt{1-s_H(\omega_1)}\sqrt{1-s_V(\omega_2)}e^{-i\omega_1\tau} \\
&-\mathcal{C}(\omega_2,\omega_1)\sqrt{1-s_H(\omega_2)}\sqrt{1-s_V(\omega_1)}e^{-i\omega_2\tau}\Big)\left|\omega_1,H,e\right\rangle\left|\omega_2,H,f\right\rangle,
\end{aligned} \tag{9.13}$$

$$\begin{aligned}
\left|\Psi'\right\rangle_{\text{bunch}} = \frac{1}{2}\iint \mathrm{d}\omega_1\mathrm{d}\omega_2 \Big(&\mathcal{C}(\omega_1,\omega_2)\sqrt{s_H(\omega_1)}\sqrt{1-s_V(\omega_2)}e^{-i(\omega_1+\omega_2)\tau} \\
&-\mathcal{C}(\omega_2,\omega_1)\sqrt{1-s_H(\omega_2)}\sqrt{s_V(\omega_1)}\Big)\left|\omega_1,V,e\right\rangle\left|\omega_2,H,f\right\rangle \\
+\frac{1}{2}\iint \mathrm{d}\omega_1\mathrm{d}\omega_2 \Big(&\mathcal{C}(\omega_1,\omega_2)\sqrt{s_H(\omega_1)}\sqrt{1-s_V(\omega_2)}e^{-i(\omega_1+\omega_2)\tau} \\
&-\mathcal{C}(\omega_2,\omega_1)\sqrt{1-s_H(\omega_2)}\sqrt{s_V(\omega_1)}\Big)\left|\omega_1,H,e\right\rangle\left|\omega_2,V,f\right\rangle.
\end{aligned} \tag{9.14}$$

As we can see from Eqs. (9.13) and (9.14), the coincidence probability will be the sum of four terms corresponding to the four possible polarization states : VV, HH, VH, HV, in other words: $P_c = P_{c,\text{sep}} + P_{c,\text{bunch}} = P_{VV} + P_{HH} + P_{VH} + P_{HV}$. The four terms can be calculated individually using the suitable projection operators as described in Section 6.2 (Eqs. (6.15) and (6.16)):

$$P_{\mu\nu} = \langle\Psi|\left(\int \mathrm{d}\omega \left|\omega,\mu,e\right\rangle\left\langle\omega,\mu,e\right|\right)\left(\int \mathrm{d}\omega' \left|\omega',\nu,f\right\rangle\left\langle\omega',\nu,f\right|\right)|\Psi\rangle, \tag{9.15}$$

with $\mu,\nu = H,V$. We obtain the following coincidence probabilities:

$$\begin{aligned}
P_{c,\text{sep}} &= P_{VV} + P_{HH} \\
&= \frac{1}{4}\iint \mathrm{d}\omega_1\mathrm{d}\omega_2 |\mathcal{C}(\omega_1,\omega_2)\sqrt{s_H(\omega_1)}\sqrt{s_V(\omega_2)}e^{-i(\omega_1-\omega_2)\tau} \\
&\qquad -\mathcal{C}(\omega_2,\omega_1)\sqrt{s_H(\omega_2)}\sqrt{s_V(\omega_1)}|^2 \\
&\quad +\frac{1}{4}\iint \mathrm{d}\omega_1\mathrm{d}\omega_2 |\mathcal{C}(\omega_1,\omega_2)\sqrt{1-s_H(\omega_1)}\sqrt{1-s_V(\omega_2)}e^{-i(\omega_1-\omega_2)\tau} \\
&\qquad -\mathcal{C}(\omega_2,\omega_1)\sqrt{1-s_H(\omega_2)}\sqrt{1-s_V(\omega_1)}|^2,
\end{aligned} \tag{9.16}$$

$$\begin{aligned}
P_{c,\text{bunch}} &= P_{VH} + P_{HV} \\
&= 2\frac{1}{4}\iint \mathrm{d}\omega_1\mathrm{d}\omega_2 |\mathcal{C}(\omega_1,\omega_2)\sqrt{s_H(\omega_1)}\sqrt{1-s_V(\omega_2)}e^{-i(\omega_1+\omega_2)\tau} \\
&\qquad -\mathcal{C}(\omega_2,\omega_1)\sqrt{1-s_H(\omega_2)}\sqrt{s_V(\omega_1)}|^2.
\end{aligned} \tag{9.17}$$

The first term $P_{c,\text{sep}}$ defines the envelope of the HOM interferogram while the the second term $P_{c,\text{bunch}}$ is a rapidly oscillating term resulting from Franson-type interference between the two paths of the interferometer [151]. The total HOM coincidence probability is the sum of these two probabilities: $P_c = P_{c,\text{bunch}} + P_{c,\text{sep}}$. In Fig. 9.8 (b-d), we display the simulated coincidence probability for different values of the splitting ratio. The two special cases for which $s_H = s_V = 0.5$ and $s_H = s_V = 1$ are displayed in Fig. 9.8 (b) and (d) respectively. The simulated HOM interferogram that is obtained by using the experimentally measured value of $s_H(\omega), s_V(\omega)$ of our device is shown in Fig. 9.8 (c). We observe that in all three cases the general shape of the interferogram follows a typical HOM

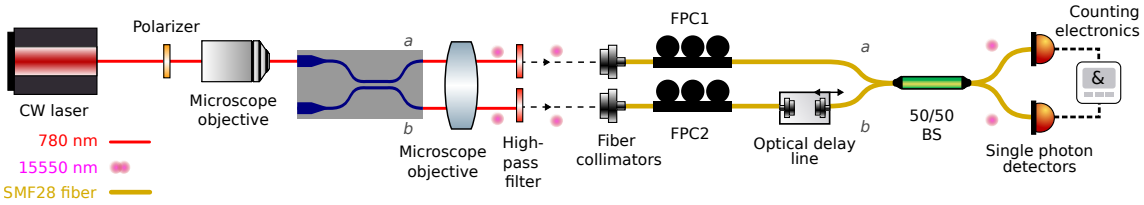

Figure 9.9: Experimental setup for the measurement of Hong-Ou-Mandel interference of the on-chip generated and separated photons. The collection microscope objective (NA=0.65) is not shown here.

dip. However, we notice that there is an oscillating background, as shown in the inset, coming from the rapid oscillations of $P_{c,\text{bunch}}$. The period of these oscillations is around 3 fs, which cannot be resolved by our free-space delay line. Hence when measuring the experimental HOM coincidence probability $P_{c,\text{exp}}$, these oscillations reduce to a constant background given by the average value of the oscillating term over a temporal window of 30 fs defined by the resolution of our free-space delay line: $P_{c,\text{exp}} = \bar{P}_{c,\text{bunch}} + P_{c,\text{sep}}$. The simulated value for $P_{c,\text{exp}}$ is shown in Fig. 9.8 (b-d) as a solid red line. We see that if $s_H = s_V = 0.5$ then the PBS reduces to a simple 50/50 beam splitter and the HOM dip visibility cannot exceed the classical threshold of 50 %. In the case of a perfectly polarizing PBS for which $s_H = s_V = 1$ we have $P_{c,\text{bunch}} = 0$ and we obtain the maximum possible visibility, here 89 % which is then only limited by the birefringence of the source, as explained in Section 6.2. For the intermediate case of our device with $L = 1080\,\mu\text{m}$, where $s_H(\omega), s_V(\omega)$ follow the experimentally measured profile displayed in Fig. 9.4, we see that the HOM visibility is slightly lower and equal to 80 %. This decrease can be attributed to the imperfect polarization splitting which gives a non-zero contribution to $P_{c,\text{bunch}}$.

9.4.2 Experimental setup and results

The experimental setup that was used to perform HOM interference at the output of the device is depicted in Fig. 9.9. We used the same NA=0.95 and NA=0.65 microscope objectives as in the previous section to couple the pump into the generation region and to collect the photons from the chip respectively. After pump filtering and fiber collimation, we applied a delay on arm b using the same free-space delay line as the one described in section Section 6.2 before recombining the two photons on a fiber 50/50 beam splitter. The standard HOM alignment procedure has also been applied to adjust the two FPCs, ensuring that the polarization of the two photon is identical at the beam splitter.

We first measured the HOM interferogram directly at the chip output, in the exact configuration depicted in Fig. 9.9. The result is displayed in Fig. 9.10 (a). We see that the experimental data points in blue are in excellent agreement with the prediction from our model, shown above in Fig. 9.8 (c), which is represented here as a red solid line. As explained in Section 6.2.3 the pump wavelength (here 773.17 nm) is the free parameter of the model and has been adjusted to yield the best agreement with the experimental results. We obtain a net visibility of $V = 80\,\%$ which, as expected, is lower than the maximum achievable 89 % that was predicted in Fig. 9.8 (d) for perfect polarization splitting. This discrepancy can be attributed to the imperfect splitting ratio of the device over the whole spectral bandwidth. Indeed, when the splitting ratio deviates from 100 %, the amplitude of the term $|\Psi\rangle_{\text{bunch}}$ becomes more important, resulting in accidental counts that deteriorate the visibility of the HOM dip.

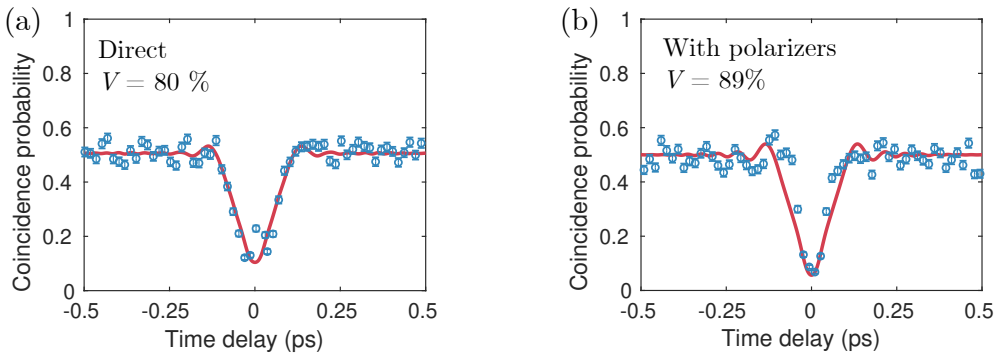

Figure 9.10: Measured HOM interferogram (blue points) and simulated HOM coincidence probability (red line) (a) in the absence of polarizers (b) with a 0 deg polarizer in arm A and a 90 deg polarizer in arm B. Background counts have been subtracted and error bars are calculated assuming Poissonian statistics.

To corroborate this supposition, we repeated the HOM measurement by adding in optical paths a and b, respectively, a linear polarizer with transmission axis at an angle of 0 deg and 90 deg with respect to the vertical axis z. The result is shown in Fig. 9.10 (b) along with a simulation where we assumed perfect polarization splitting $s_H(\omega) = s_V(\omega) = 1$ to model the effect of the two polarizers. We obtain a higher visibility of $V = 89\,\%$ confirming that, if the polarization splitter was ideal, with a splitting ratio of 1 over the whole state bandwidth, then we could reach the maximum achievable visibility, which is then only limited by the source birefringence.

A further improvement of the visibility can be achieved by spectrally filtering the state at the chip output, as we already demonstrated in Section 6.2. For example, in Ref. [69] the authors use a 1.2 nm filter and achieve 93.5 % visibility from an on-chip ppLn SPDC source with integrated polarization splitter and electro-optic delay line. Under the same spectral filtering, simulations show that our device could reach an even higher HOM visibility of 95.6 % confirming that the performance of our chip matches state-of-the-art ppLN devices. Another possible improvement to our device would be to refine the design of the polarization splitting region by using adiabatic couplers which, in $LiNbO_3$ waveguides without an on-chip photon pair source, have been shown to exhibit a very flat spectral profile with splitting ratios above 98 % for more than 100 nm [172].

Part V

Flexible entanglement-distribution network with an AlGaAs chip for secure communications

Chapter 10

Entanglement-based quantum key distribution

Contents

10.1 State of the art and motivation 147
10.2 Basic principle of the BBM92 protocol 150
10.3 Security analysis: general considerations 151
10.4 Asymptotic regime 152
10.5 Finite-key regime 153

In this chapter we give an introduction to entanglement-based quantum key distribution. We start by presenting the different experimental implementations with an emphasis on multi-user networks. Then we describe the BBM92 protocol and its security analysis both in the asymptotic and finite-key regimes.

10.1 State of the art and motivation

Quantum communications is one of the field of quantum information which have seen the greatest advances in the last three decades. The paradigmatic application is quantum key distribution (QKD) which enables the generation of cryptographic keys whose security relies on the basic principles of quantum physics. Several families of QKD protocols have been developed over the years. In **"prepare-and-measure"** protocols, a party A encodes a series of random bits in the state of a quantum system that is sent over to another party B who measures the state of the system and recovers the bit string that was generated by A. This series of bits shared by the two parties will be the secret key that can be used later on for classical cryptographic purposes. In this kind of protocol, the no-cloning theorem and uncertainty principle of quantum mechanics guarantee the security of the key and entanglement is not required. "Prepare-and-measure" protocols can be implemented using different degrees of freedom of light. In discrete variable QKD (DV-QKD), which is currently the most widely used class of protocols, the key bits are encoded in discrete degrees of freedom of photons such as polarization [28, 173] or time-bin [99], as already stated in the introduction of this thesis. Current state of the art implementations of DV-QKD use attenuated laser pulses as sources of single photons which enables distribution of secret keys with high rates and over long distances [99, 174, 175]. Continuous-variable QKD (CV-QKD) has been proposed as an alternative approach that only uses off-the-shelf telecom components which are widely employed in the industry. In this kind of protocol,

the bits are encoded in the quadratures of a many-photon field which can then be measured by homodyne detection [176]. Even though up to now the rates and achieved distances remain lower than in DV-QKD, the whole transmission process only involves commercially available standard fiber telecom components such as lasers, electro-optic modulators and photodetectors [94]. This approach has the advantage of not using single-photon detectors, whose response time can become ultimately a limitation to the achievable key rates in DV-QKD.

The second broad class of QKD protocols is **entanglement-based QKD**. The main difference with respect to "prepare and measure" protocols is that they rely on a source of entangled photons which is not controlled by any of the two communicating parties. A typical scenario is a source emitting pairs of entangled photons that are distributed to the two users A and B which then measure a projection of the state of their photon. An eavesdropper trying to intercept the photons to gain information on the key will destroy the quantum correlations between the photons. As a consequence, a simple measurement of an entanglement witness by the two parties can reveal the presence of an eavesdropper. The two main entanglement-based QKD protocols are the so-called E91 [26] and BBM92 [27] protocols, which were proposed and demonstrated in the 1990's and early 2000's [29, 30, 31]. Since then, entanglement-based QKD has been going beyond the proof-of-principle and being implemented in increasingly realistic environments. Polarization and time-bin entanglement are particularly well-suited to this kind of protocols thanks to their efficient generation using nonlinear optical processes and easy manipulation using standard optical components. As a consequence entanglement distribution and entanglement-based QKD based on these degrees of freedom have been successfully performed across long-distance fiber links [177, 178], ground-to-ground free-space links [179], submarine cables [180], satellite-to-ground links [3] and between in-flight drones [181]. These results were obtained using bulk nonlinear crystals as sources of entangled photon pairs. However, very recently, these kind of experiment were also achieved using integrated sources such as semiconductor quantum dots [86], ppLN waveguides [72, 73] or AlGaAs nonlinear waveguides [85].

Since the quantum correlations between the photons, which can be checked by the users, ultimately guarantee the security of the key, an eavesdropper could have full control over the source without hindering the success of the protocol. Indeed, even if the source was controlled by a malicious party, it could not prepare the photon pairs in an entangled state while still being able to predict the measurement outcomes of the users, as stated in Bell's theorem . Owing to the fact that the source is totally independent of the users and the emitted state is not correlated with the basis choice of any of the two parties, it has been shown that the security of entanglement-based QKD can be proved even with an uncharacterized source [182]. This is why entanglement-based QKD is often referred to as "basis-independent". This basis-independence is one of the features which makes entanglement-based QKD the main candidate for the realization of device-independent QKD (DI-QKD). This much sough-after goal of the quantum communication community consists in demonstrating a QKD protocol that is absolutely secure against any kind of attack assuming untrusted measurement devices and source. Device-independence represents the highest possible security level for a QKD protocol. Several device-independent QKD security proofs have been developed however, up to very recently, the experimental implementation of these proposals in the remained out of reach due to the need for either advanced quantum hardware or extremely low noise rates [183, 184, 185]. However, thanks to recent theoretical and experimental advances, DI-QKD has been achieved in proof-of-principle experiments based on trapped ions [186] or entangled photon pairs [187].

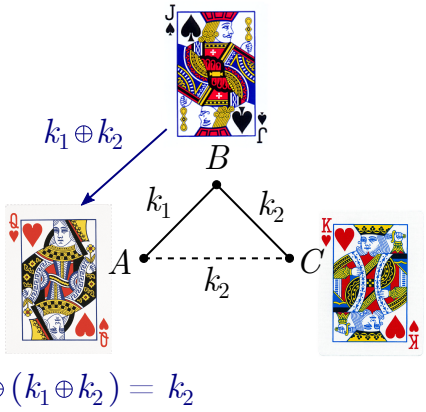

Figure 10.1: Schematic of a three-users trusted-node quantum key distribution network. Nodes A, B and B, C initially share a key k_1 and k_2 respectively. The key k_2 is transferred from B to A through a classical channel (blue arrow) after applying a bitwise XOR operation $k_1 \oplus k_2$. Then A can decode the string using its key and recover $k_2 = k_1 \oplus (k_1 \oplus k_2)$. In this scheme, B needs to be a trusted relay.

Another strength of entanglement-based QKD which stems from the basis-independence, is that it enables the implementation of trusted-node free multi-user quantum key distribution networks. Indeed, by randomly distributing the emitted photons-pairs between all possible pairs of users in a multi-node network, all parties can distill a secret key without the need for extra relay node. In contrast, in most "prepare-and-measure" QKD networks, when more than two parties need to share a secret key, they have to exchange bits of information through a trusted relay node [188, 189, 190]. Consider, for instance, the situation depicted in Fig. 10.1. In this three-node configuration A and B share a secret key k_1 and B and C share another key k_2. Then A and C do not share a key. To solve this issue, the intermediate node B can simply perform a XOR operation between the two keys and send the resulting string $k_1 \oplus k_2$ to node A. The latter can invert the CNOT operation using its own key and recover k_2. In the final configuration, A and C finally share a secret key k_2. The main security issue to this scheme is that it requires at least one trusted node. Indeed, if B were an eavesdropper, it could learn the keys k_1 and k_2 shared by the three users without being detected and therefore needs to be a trusted user. In addition, in "prepare-and-measure" protocols, the photon source needs to be operated by one of the users, which should also be trusted. Recently, an approach to realize a trusted-node free QKD network using entangled photon pairs has been demonstrated experimentally both in laboratory experiments [145, 72, 85, 191] and in field tests across optical fiber cables [97, 73]. In this scheme, the entangled photons generated by a broadband $\chi^{(2)}$ source are divided into wavelength channels that are passively routed to the different users of the network, as will be explained in detail in Chapter 12.

The AlGaAs platform is a promising system for the development of scalable chip-based entanglement-based quantum key distribution networks. Indeed, as shown in Chapter 6, nonlinear AlGaAs waveguides emit photon pairs over a broad bandwidth, of about 60 nm, which opens the possibility to build a whole multi-user network based on wavelength-multiplexed quantum links using only a single source. Thanks to its high pair generation rate and CAR, intrinsic polarization entanglement and compatibility with electrical injection, the AlGaAs photon-pair source is an ideal candidate for robust integration in QKD network architectures. In this work, we combine our source with industry-grade flexible-

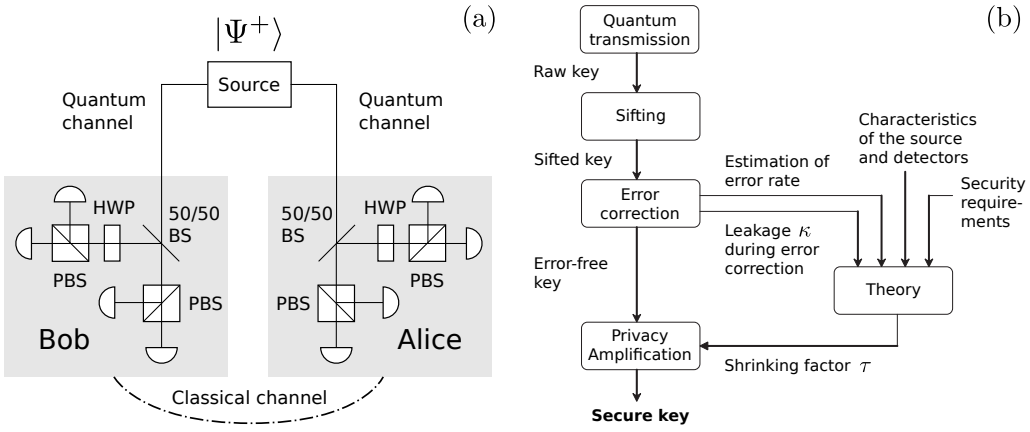

Figure 10.2: (a) Ideal polarization-based BBM92 setup. Half circles represent single photon detectors. HWP : Half wave plate. 50/50 BS : 50/50 beam splitter. PBS : Polarizing beam splitter. (b) Flowchart for a generic QKD Scheme (adapted from [192]).

grid wavelength division multiplexing techniques to implement a reconfigurable multi-user QKD network based on the BBM92 protocol [85]. This approach has been developed independently at Oak Ridge National Laboratory by the team of J.M Lukens [72, 73] using ppLN waveguides.

10.2 Basic principle of the BBM92 protocol

The basic principle of the BBM92 protocol is sketched in Fig. 10.2 (a). The two parties Alice and Bob (A and B) are assumed to share a maximally-entangled bipartite quantum state (Bell state). In all that follows, we consider the case of entanglement in the polarization degree of freedom and we focus on the Ψ^+ Bell state which can be written as :

$$\left|\Psi^+\right\rangle = \frac{1}{\sqrt{2}}\left(\left|HV\right\rangle_{AB} + \left|VH\right\rangle_{AB}\right). \tag{10.1}$$

As shown in Fig. 10.2 (a), each party receives one photon of the pair through a private quantum channel and projects its polarization state using a half wave plates and polarizing beam splitters either in the principal basis $\mathbb{X} = \{|H\rangle, |V\rangle\}$ or in the diagonal basis : $\mathbb{Z} = \{|D\rangle, |A\rangle\}$ where $|D\rangle = (|H\rangle + |V\rangle)/\sqrt{2}$ and $|A\rangle = (|H\rangle - |V\rangle)/\sqrt{2}$. When measuring $|H\rangle$ ($|V\rangle$) or $|D\rangle$ ($|A\rangle$) the user respectively records a 0 or 1 value for the received bit. The basis choice is random and can be implemented by a passive 50/50 beam-splitter. Since photons in a Ψ^+ state are cross-polarized, one of the parties has to perform a bit flip operation on his key such that the generated keys are identical. The bit string that is obtained by the two parties after the distribution protocol is called the raw key. However half the time, A and B choose different measurement basis and the obtained bits are uncorrelated. After the communication, the parties discloses their basis choices through a public classical channel and they discard all the bits that were obtained from unmatched bases, thus loosing one half of the raw key. This process is called basis reconciliation or sifting. The bit string that is obtained after sifting is called the sifted key.

In the ideal BBM92 scenario (perfect source, channels and detectors), all bits are transmitted to Alice and Bob without any errors. Moreover, Eve, a malicious party trying to gain information on the key using local measurements, will destroy the quantum correlations that exist between the polarization of the two photons. Alice and Bob can therefore

detect the presence of the eavesdropper by performing a verification of the Clauser-Horn-Shimony-Holt (CHSH) inequality.

10.3 Security analysis: general considerations

In practice, deviations from the ideal protocol arising from the imperfections of the setup introduce, on the one hand, errors in the bit strings and, on the other hand, side channels that can be exploited to collect information on the generated key [3]. Nevertheless, the security of the key can be guaranteed by applying suitable post-processing steps. Those steps are summarized in the diagram of Fig. 10.2 (b).

The goal of QKD is to distribute a key that is secure in the sense that is has to be

- Correct, which means that Alice and Bob share identical bit strings,
- Secret, meaning that the amount of information that has leaked to a potential eavesdropper (Eve) is negligible.

In order to obtain a correct key, Alice and Bob first perform a classical error-correction procedure [193]. In this step, they consume a certain portion of the bit string to correct for errors and estimate the error rate. To do so, they disclose partial information on the key over a public channel, which can be monitored by Eve. To guarantee the secrecy of the error-free key, Alice and Bob need to suppress Eve's knowledge of the key by carrying out a privacy amplification protocol. This knowledge has two sources :

- Information leakage from error correction,
- Side channels attacks.

Privacy amplification usually involves computing a hash of the error-free key that will further reduce the final key size.

Thus, if Alice and Bob generate a sifted key of length n, then the final secure key is a bit string of length :

$$n_{key} = n - \kappa - \tau \tag{10.2}$$

where κ and τ are the number of discarded bits in the error correcting and privacy amplification stages respectively. The secure key rate can be obtained as :

$$R_{\text{key}} = R_{\text{raw}} \frac{1}{2}(1 - \kappa/n - \tau/n). \tag{10.3}$$

where R_{raw} is the raw key generation rate in bit/s and the factor 1/2 accounts for the sifting procedure.

Security proofs dictate the amount of privacy amplification needed to obtain a secure key after error correction and the length of this final key in different scenarios depending on the type of side-channel attacks and the model used for the sources and the detectors. The ultimate goal of QKD is to implement a completely device-independent protocol that would guarantee unconditional security of the distributed key. Important theoretical and experimental results in this directions have been achieved recently, as stated in the previous section, however, in practical situations, weaker security requirement are enough to prevent most realistic attacks. A hierarchy in the type of attacks has been established based on the security requirements needed in order to block them [192]. The weakest type of attack is individual attacks where Eve is allowed to entangle a probe with one transmitted qubit at a time, then to store these probes in a quantum memory and wait for the public basis

reconciliation (sifting) to measure all the probes and reconstruct the key. In collective attacks, Eve has access to a quantum computer and can make a global measurement of all the probes. Finally, the most general type of attack is coherent attacks where Eve has full control over source, channels and detectors in the limits allowed by quantum mechanics. Note that even the simplest kind of attacks requires quantum memories, which are currently out of reach for today's quantum technologies

In the asymptotic regime, when the length of the key is infinite, security proofs have been derived against individual attacks [194] and against coherent attacks for ideal source and detectors [195], ideal source with uncharacterized detectors [196] and uncharacterized source with ideal detectors [182]. Finally, in Ref. [197] the authors derive a more general proof for security against coherent attacks in the presence of imperfect source and detectors. Extensions of these proofs to the case of finite keys are presented in Refs. [198, 3].

10.4 Asymptotic regime

Error correction : Shannon's channel coding theorem, a central result in information theory, states that in the limit of infinitely long keys, the maximum error-free achievable transmission rate cannot exceed the channel capacity $\mathcal{C}$, which quantifies the maximum mutual information that can flow from Alice to Bob [193]. This upper bound is often referred to as the Shannon limit. The quantum channel that is used by two parties in QKD protocols can be modeled as a binary symmetric channel with error rate e and channel capacity $\mathcal{C} = 1 - H_2(e)$ where $H_2(e) = -e\log_2(e) - (1-e)\log_2(1-e)$ is the binary entropy function [193]. Hence, at the Shannon limit, the smallest achievable data loss caused by error-correction is :

$$\lim_{n\to\infty} \frac{\kappa}{n} = -H_2(e). \tag{10.4}$$

In the context of QKD, e is referred to as the quantum bit error rate (QBER) and is defined as the fraction of erroneous bits in the raw key. Up to now, no known error-correction code can saturate the Shannon bound. To quantify the deviation from the Shannon limit of a particular code, we introduce an empirical function $f(e) \geq 1$ that is defined as

$$\lim_{n\to\infty} \frac{\kappa}{n} = -f(e)H_2(e) \tag{10.5}$$

For a given code, $f(e)$ does not necessarily have an analytical expression but the algorithm can be tested on actual data for different error rates e to obtain tabulated values of $f(e)$. One widely used error correcting code in QKD is the so-called Cascade code [199].

Privacy amplification : BBM92 being a source-independent protocol, we follow Ref. [200] and apply the Koashi-Preskill proof for an uncharacterized source with Cascade error correction protocol. The privacy amplification shrinking factor is given by

$$\lim_{n\to\infty} \frac{\tau}{n} = -H_2(e) \tag{10.6}$$

Secure key rate : The asymptotic key rate can be obtained by taking the limit $n \to \infty$ of Eq. (10.3). With the help of Eq. (10.5) and Eq. (10.6) we can write the generated secure key rate as :

$$R_{\text{key}} \geq R_{\text{raw}} \frac{1}{2} \left(1 - f(e)H_2(e) - H_2(e)\right), \tag{10.7}$$

The inequality comes from the fact that $f(e) \geq 1$ and that it is possible, in principle, to obtain better key rates by constructing an error correcting code operating closer to the Shannon limit. The Shannon limit $f(e) = 1$ provides in itself the upper bound to R_{key} and

sets the maximal tolerated error rate. Indeed, in this limit $R_{\text{key}} = R_{\text{raw}}(1/2)\,(1 - 2H_2(e))$ and the key rate becomes negative for $e \geq 11\%$. Note that this asymptotic rate is the same for all the security proofs listed in the previous section.

10.5 Finite-key regime

The security proofs that we invoked are only valid in the asymptotic regime, a situation which is not always fulfilled in practical situations. Finite-size keys impose more conservative bounds on the secure key rate. The framework developed in Refs. [198, 3] provides bounds to the achievable key rate for a given level of security defined as the probabilities ϵ_{corr} and ϵ_{sec} for the distributed key to be correct and secret respectively.

In this procedure, the parties generate a raw key of length n containing $n_{\mathbb{Z}}$ ($n_{\mathbb{X}}$) bits obtained by measuring the photon polarization in the $\mathbb{Z}$ ($\mathbb{X}$) basis. Then they estimate $e_{\mathbb{Z}}$ and $e_{\mathbb{X}}$ the error rates in in the $\mathbb{Z}$ and $\mathbb{X}$ bases. From these estimates, they perform error correction and privacy amplification following the protocol described in Ref. [198] and obtain keys in both bases separately with lengths given by :

$$n_{\text{key},\mathbb{Z}} = n_{\mathbb{Z}} - n_{\mathbb{Z}} H_2\left[e_{\mathbb{X}} + \sqrt{\frac{(n_{\mathbb{Z}}+1)\ln(1/\epsilon_{\text{sec}})}{2n_{\mathbb{X}}(n_{\mathbb{X}}+n_{\mathbb{Z}})}}\right] - f(e_{\mathbb{Z}})n_{\mathbb{Z}}H_2(e_{\mathbb{Z}}) - \log_2\left(\frac{2}{\epsilon_{\text{corr}}\epsilon_{\text{sec}}^2}\right) \tag{10.8}$$

$$n_{\text{key},\mathbb{X}} = n_{\mathbb{X}} - n_{\mathbb{X}} H_2\left[e_{\mathbb{Z}} + \sqrt{\frac{(n_{\mathbb{X}}+1)\ln(1/\epsilon_{\text{sec}})}{2n_{\mathbb{Z}}(n_{\mathbb{X}}+n_{\mathbb{Z}})}}\right] - f(e_{\mathbb{X}})n_{\mathbb{X}}H_2(e_{\mathbb{X}}) - \log_2\left(\frac{2}{\epsilon_{\text{corr}}\epsilon_{\text{sec}}^2}\right) \tag{10.9}$$

The length of the total key is given by $n_{\text{key}} = n_{\text{key},\mathbb{Z}} + n_{\text{key},\mathbb{X}}$. Just as in the asymptotic regime, the secure key generation rate can be obtained using Eq. (10.3) with error correction leakage and privacy amplification shrinking factors :

$$\kappa = -f(e_{\mathbb{Z}})n_{\mathbb{Z}}H_2(e_{\mathbb{Z}}) - f(e_{\mathbb{X}})n_{\mathbb{X}}H_2(e_{\mathbb{X}}) - 2\log_2(1/\epsilon_{\text{corr}}) \tag{10.10}$$

$$\tau = -n_{\mathbb{Z}}H_2\left[e_{\mathbb{X}} + \sqrt{\frac{(n_{\mathbb{Z}}+1)\ln(1/\epsilon_{\text{sec}})}{2n_{\mathbb{X}}(n_{\mathbb{X}}+n_{\mathbb{Z}})}}\right] - n_{\mathbb{X}}H_2\left[e_{\mathbb{Z}} + \sqrt{\frac{(n_{\mathbb{X}}+1)\ln(1/\epsilon_{\text{sec}})}{2n_{\mathbb{Z}}(n_{\mathbb{X}}+n_{\mathbb{Z}})}}\right] - 2\log_2(2/\epsilon_{\text{sec}^2}) \tag{10.11}$$

In the limit of infinite key length, we recover Eq. (10.5) and Eq. (10.6) by noticing that we can make the security parameters $\epsilon_{\text{corr}}, \epsilon_{\text{sec}}$ arbitrarily close to unity while keeping asymptotically $\log_2(2/\epsilon_{\text{sec}^2})/n \to 0$ and $\log_2(1/\epsilon_{\text{corr}})/n \to 0$.

This treatment is adapted to practical use cases where the data transmission time is limited and keys are distributed in blocks of finite lengths. The secure key rate that can be extracted from Eqs. (10.10) and (10.11) provides the figure of merit for a realistic implementation of QKD. In the present work, we will use this finite-key treatment to estimate the secure key rate that is achieved by our source.

Chapter 11

Generation of broadband polarization entanglement with an AlGaAs source

Contents

11.1 Experimental setup and calibration of the polarization analysis module 155

11.2 Demultiplexing schemes 157

11.3 Characterization of the broadband polarization-entangled state 161

In this chapter, we demonstrate the potential of our AlGaAs source for the implementation of wavelength-multiplexed entanglement-based QKD networks by characterizing the broadband polarization-entanglement of the generated quantum state. We start by describing the experimental setup before giving an thorough description of the different frequency demultiplexing schemes that have been used in the experiments. Then we present our measurements of the Bell correlation curves and fidelity to a maximally entangled state for pairs of conjugate frequency channels spanning the whole biphoton bandwidth.

11.1 Experimental setup and calibration of the polarization analysis module

11.1.1 Experimental setup

The setup that was used to characterize the quantum state of our AlGaAs source consists of three stages : entanglement generation with an AlGaAs chip, frequency demultiplexing/multiplexing (demux/mux) of the generated signal and polarization analysis of the detected photon-pairs.

Generation stage: The sample is pumped with a tunable CW diode laser (TOPTICA TM Photonics DL pro 780) which is coupled into the waveguide through a microscope objective (NA = 0.95, 63×). Light emerging from the opposite end is collected with a second identical microscope objective and sent to a fiber coupler, after filtering out the pump wavelength with a high pass filter. A thermistor and a Peltier cooler, connected to a PID controller, monitor and keep the waveguide temperature constant. We maintain the sample at 19.3 °C to set the degeneracy wavelength of the photon pairs to 1556.55 nm, corresponding to the center of the ITU 100 GHz channel number 26.

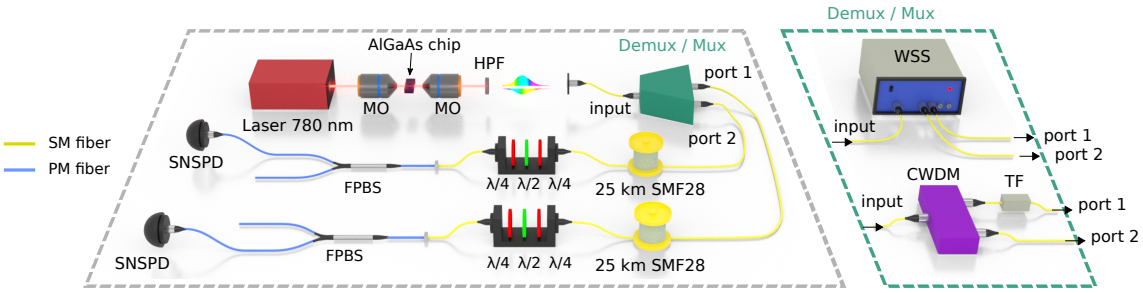

Figure 11.1: Experimental setup. MO: Microscope Objective. HPF: High Pass Filter. WSS: Wavelength Selective Switch. CWDM: Coarse Wavelength Division Multiplexing unit. TF: Tunable Filter. FPBS: Fibered Polarizing Beam Splitter. SNSPD: Superconducting Nanowire Single Photon Detector. SM: Single Mode fiber. PM: Polarization Maintaining fiber. The two 25 km SMF28 fiber spools are not present in the measurements described in this chapter but will be used later on in the long-distance QKD experiments of the next chapter.

Demux/mux stage: At the demultiplexing (demux) stage photons are separated into different fibers according to their frequency. This operation can be done either using fixed frequency channels of passive wavelength division multiplexing (WDM) components [78, 97] or programmable filters called wavelength selective switches (WSS) where the width and central frequency of each channel can be specified by the user. In our work, we combine the two demultiplexing strategies depending on the spectral region of interest: in the telecom C-Band (1530 nm to 1565 nm) we use a WSS and in the L-Band (1565 nm to 1625 nm) a coarse wavelength division multiplexing unit (CWDM) with 13 nm wide channels followed by a tunable filter (TF). The demux/mux in the C+L band could also be performed with a single WSS operating over the whole frequency band. This kind of component became commercially available only recently, after we performed our experiments. We also benchmarked a thin-film based dense wavelength division multiplexing unit (DWDM) for our QKD experiments but did not use it for our final results due to lower performance.

At the frequency multiplexing stage (mux) several frequency channels are combined into single optical fibers. In an entanglement-distribution network, this can be used to send photons generated in different frequency channels to a single user, as will be shown later. In our setup, the CWDM + TF configuration was not used for mux, only for demux. The WSS has the advantage to implement both demux and mux without extra losses, as opposed to passive WDM where one need to cascade optical add-drop filter at the mux stages thus increasing the insertion loss of the setup. Another strength of the WSS is the ability to reconfigure the frequency channels thus providing unprecedented flexibility with respect to fixed-grid WDM components.

Polarization analysis: After the demux/mux stage, the photons, which have been separated into two output ports based on their frequency, are sent towards two polarization analysis stations. The latter include a fibered polarization rotator (OZ Optics) made of a set of free-space indexed $\lambda/4, \lambda/2, \lambda/4$ waveplates, a fibered polarizing beam splitter (FPBS, Thorlabs) and a superconducting nanowire single photon detector (SNSPD, Quantum Opus). The waveplates and FPBS are used to project the polarization of the measured photons onto the states of two bases $\mathbb{X}$ and $\mathbb{Z}$ as required in the BBM92 protocol.

11.1.2 Calibration of the polarization analysis modules

The birefringence of the single mode (SM) fibers is an important issue when using all-fibered optical components for polarization management. Indeed, light at the output of the demux/mux stage will travel through SM fibers before hitting the FPBS, where orthogonal polarization components will be separated. Along the way, due to the birefringence of the fibers, the polarization of the photons will rotate in an uncontrolled way. The transformation induced by the fiber being unitary, it preserves the orthogonality of the photon polarization, and hence the entanglement. However, in this case, it is not possible to know the basis into which the projection is performed with the FPBS at the polarization analysis stage. This is not the case when using free-space optics based detection schemes as in Ref. [97].

This effect is usually canceled by inserting a fibered polarization controller, equivalent to $\lambda/4, \lambda/2, \lambda/4$ waveplates, into the fiber path. However our setup already includes a set of such waveplates for projecting the polarization onto the axis of the FPBS. Therefore, we used our free-space waveplates module both for performing a rotation on the polarization state of input light, as it was originally meant to, and for birefringence compensation.

To do so, we designed a calibration procedure that we performed before each measurement run. Given an input polarization state E_i, the action of the birefringence of the fiber can be modeled as a unitary matrix K and the action of the waveplates projecting the polarization onto the FPBS, as a second unitary matrix $U(\theta)$. We calibrate the waveplates such that $U(\theta)$ cancels action of birefringence K and performs a rotation of the input polarization state. Mathematically : $U(\theta) = K^{-1}R(\theta)$ where $R(\theta)$ is a rotation matrix of angle θ with respect to the optical axes of the FPBS.

The calibration procedure is as follows. Suppose the incoming light is in the polarization state described by the Jones vector $E_i = (1,\ 0)$ (horizontally polarized light). If all of this incoming light exits from output port 1 of the FPBS then we know the polarization state has undergone a transformation $KU(\theta = 0) = R(\theta = 0)$. Similarly, for linearly polarized light with arbitrary angle with respect to the laboratory frame $E_i = (\cos\theta,\ \sin\theta)$, if all light exits from output port 1 of the FPBS, we know we have realized the operation $KU(\theta) = R(\theta)$ with the waveplates. Therefore, to calibrate the waveplates such that they effectively realize all the rotations we need in our experiments, we send input telecom laser with known linear polarization state $E_i = (\cos\theta,\ \sin\theta)$ into the distribution stage and set the waveplates angles such that all light exits from the same FPBS arm. We write down the waveplate angles for each value of θ and use them for each measurements to perform the desired rotations on the polarization of entangled photons.

11.2 Demultiplexing schemes

11.2.1 Wavelength selective switch (WSS)

In this work, we have been using different optical components for the frequency-demultiplexing of the generated photons. The device that was used in most of our experiments is a WSS (Finisar Waveshaper 4000s) based on liquid crystal technology. It features one common port and 4 output ports. The device can fully control the amplitude and phase of an input signal and has the possibility to route specific wavelength ranges into different output ports thus acting at the same time as a pulse shaper and as a programmable optical switch. Light entering through the input port is diffracted with a grating and the different wavelengths are directed towards pixels on a liquid crystal array. The amplitude, phase and attenuation of the diffracted light can be controlled by

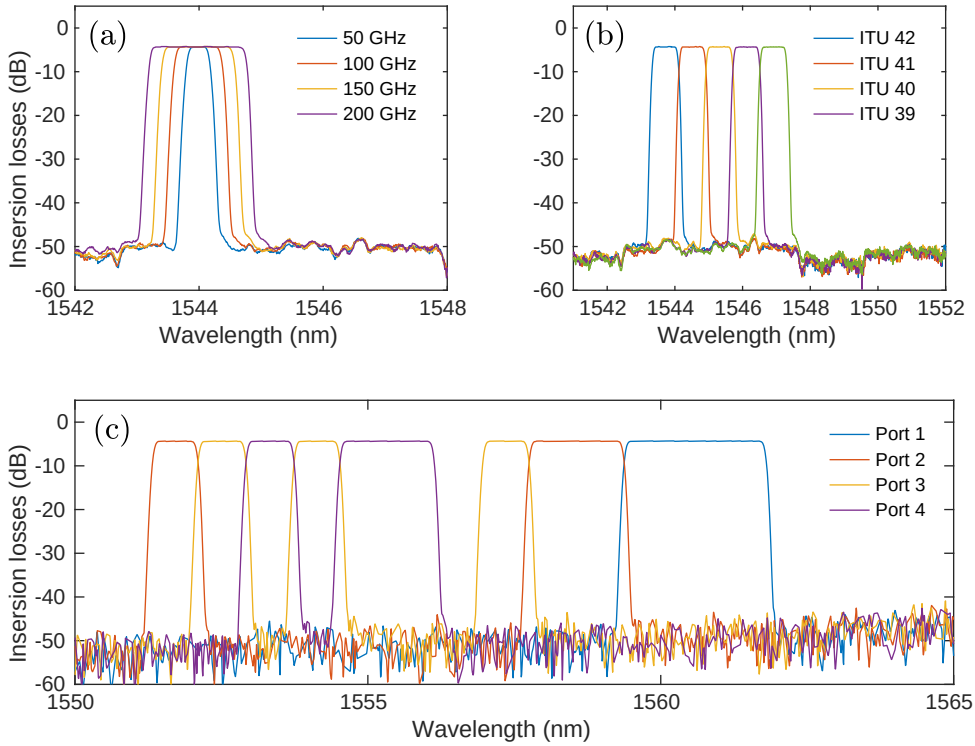

Figure 11.2: : Characterization of the WSS. (a-b) Transmitted spectrum into port 1 in a rectangular filter configuration with (a) variable bandwidth centered at 1544 nm and (b) variable central wavelength spanning ITU 100 GHz channels 39-42. (c) Example of multi-port optical switching. The input spectrum is divided into 100 GHz channels which are distributed between the four output ports.

applying a suitable voltage to the liquid crystal pixels. Light is then recombined into the output fiber ports according to the pattern programmed by the user.

Our WSS operates in the C-Band and features wavelength and polarization-independent insertion losses of 4.8 dB. In most of our experiments, we programmed rectangular lineshape of variable width, central frequency and attenuation. To characterize the transmission profile, we send the broadband spectrum of an erbium-doped fiber amplifier (EDFA) into the common port of the WSS and record the transmitted power with an optical spectrum analyzer (OSA). Fig. 11.2 shows different rectangular profiles with (a) variable bandwidth and (b) variable central wavelength. In this data all wavelength are directed to port 1 and the other 3 ports are unused. We observe a true flat-top profile with sharp edge roll-off, well suited for demux/mux applications. In Fig. 11.2 (c), we demonstrate the optical switching capability of the WSS. We carve 10 frequency channels of 100 GHz out of the EDFA spectrum and distribute them among the 4 output ports to emulate a 4-user network. We see that the WSS implements both demux, as it can separate different wavelength components, and mux, because it can recombine those wavelength components into different output ports.

We checked the polarization-insensitivity of the insertion losses by sending a linearly polarized telecom laser into a $\lambda/4, \lambda/2, \lambda/4$ fibered polarization rotation module then into the common port of the WSS that was set to a "transmit all wavelength to Port 1"

configuration. We recorded the output power from Port 1 as a function of the angles of the $\lambda/2$ and $\lambda/4$ waveplates. We observe a variation of the insertion losses of less than 0.5 % with respect to the waveplate angles, thus verifying the ability of the WSS to perform polarization-entanglement distribution.

11.2.2 CWDM and tunable filter

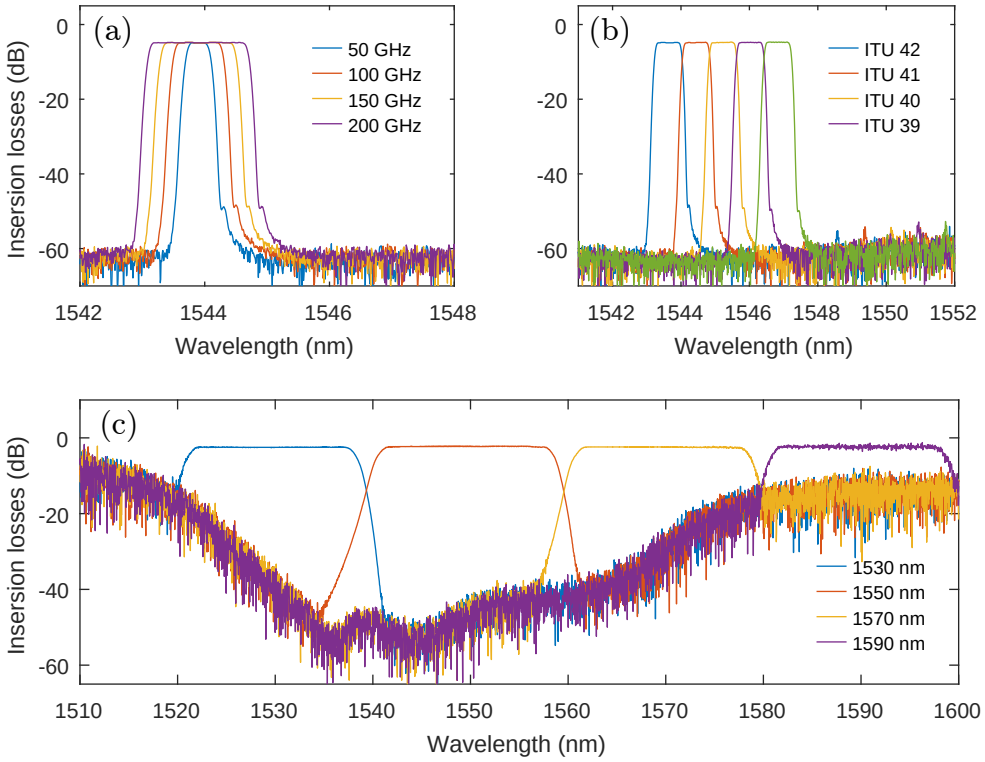

Figure 11.3: : Characterization of the TF and CWDM. Transmission profile of the TF with (a) variable bandwidth centered at 1544 nm and (b) variable central wavelength spanning ITU 100 GHz channels 39-42. (f) CWDM: Transmission profile for the four ports covering the C+L bands. The legend indicates the central wavelength of each output port

One of the shortcomings of our WSS is that its operating spectral range is limited to the C-Band while our broadband AlGaAs entangled photon source emits in the C+L band. As explained in Section 11.1, a new generation of WSS covering the C+L band is now commercially available. Nevertheless, to characterize the quantum state emitted by our source in the L-Band, we used a combination of a CWDM module followed by a C+L band TF. The CWDM module is a fibered passive WDM filter with broad frequency channels based on internal free-space optics. It can be used either in a demux or in a mux configuration, but not both at the same time like the WSS. It has 2 common ports (add, drop) 8 output (drop) and 8 input (add) ports. We used it solely for demux by sending the input signal through the "add" common port and collecting the demultiplexed signal from the "drop" ports. The CWDM module features very broad (17 nm) wide channels with insertion losses of 2.6 dB. We are interested in energy-matched channels, meaning their central wavelength are symmetric with respect to the degeneracy frequency of our

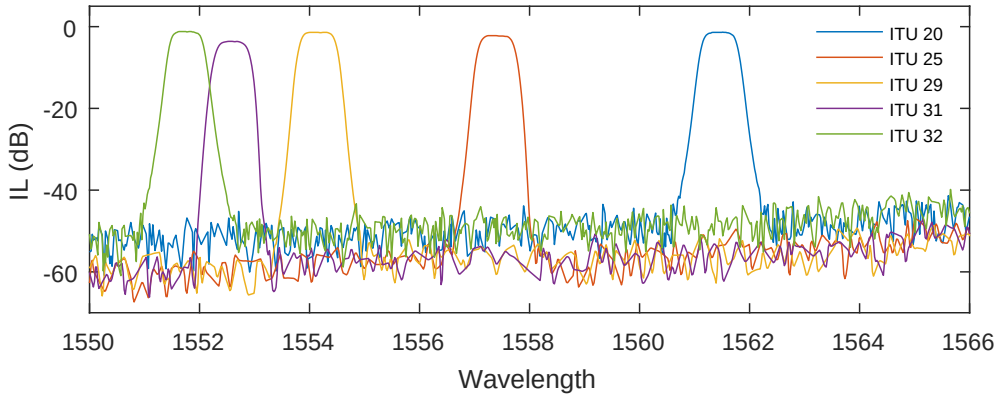

Figure 11.4: Characterization of the thin-film based DWDM. Transmitted spectrum from a selection of output ports corresponding to 100 GHz ITU channels 20, 25, 29, 31 and 32.

biphoton state (ITU CH26, 1556.55 nm). The channels pairs that meet this conditions are channels of central wavelength 1530 nm/1570 nm, 1510 nm/1590 nm and 1490 nm/1610 nm. However, those channels are too broad to be used for quantum state characterization. Indeed, in most of our measurements, we measure the properties of our state within a much smaller window (100 GHz, approximately 0.8 nm).

Consequently, we carve narrow 100 GHz rectangular windows out of these broad channels by inserting the TF in one of the output port of the CWDM, as sketched in Fig. 11.1. Thanks to the frequency anti-correlation of the quantum state, all photons within the transmission window of the tunable filter will have their energy-conjugate twin exiting from the opposite port of the CWDM. This alleviates the need for using two filters, one at each output port of the CWDM. A second filter could simply give a better signal to noise ratio since it would avoid coincidence between the filtered photons and broadband uncorrelated noise. To sum up, using the CWDM + TF arrangement, we managed to route energy-matched 100 GHz frequency channels within the C+L band into two separate fibers.

Like for the WSS, we characterize this configuration by injecting the output of an EDFA and measuring the transmitted power spectrum. The results are shown in Fig. 11.3. In (a) and (b), we illustrate the performance of our C+L-band filter by showing the tunability of the central frequency and bandwidth as well as the flat-top rectangular lineshape. In Fig. 11.3 (f) we plot the transmission profile of the 4 CWDM channels within the EDFA emission range. The line colors correspond to the different output ports of the module. Again we observe a flat-top transmission profile. We see that the filter rejection seems to decrease from −60 dB to −20 dB when going to the outer channels. This is simply due to the fact that the EDFA emission is very weak in these regions, approaching the noise baseline of the OSA, and therefore the input over output power ratio is close to unity.

11.2.3 Thin-film based DWDM

Finally, we also characterize a third demultiplexing module, namely a thin-film based fixed grid 100 GHz dense wavelength-division multiplexing filter (DWDM), such as the one used in the work of Refs. [145, 97]. The device (Opneti Communications) presents one input port and 32 output ports corresponding to ITU 100 GHz channels 10 (1569.59 nm) to 41 (1544.53 nm). One of the main drawback of the device is its highly dispersed channel insertion losses ranging from 0.64 dB for channel 20 to 3.02 dB for channel 31. The trans-

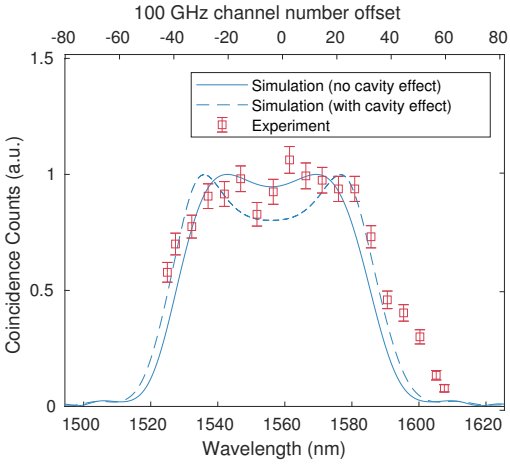

Figure 11.5: Squares: Coincidence counts after the 50/50 coupler and TF as a function of filter central wavelength (lower x-axis) and detuning to biphoton degeneracy wavelength (1556.55 nm) in units of 100 GHz channels (upper x-axis). Error bars were calculated assuming poissonian statistics. Solid line: Theoretical prediction without cavity effects. Dashed line: Theoretical prediction with cavity effects (see main text for details).

mitted spectrum from output ports corresponding to 100 GHz ITU channels 20, 25, 29, 31 and 32 is plotted in Fig. 11.4. We see that, like the other demux devices, the transmission profile has a flat-top rectangular shape.

11.3 Characterization of the broadband polarization-entangled state

11.3.1 Biphoton bandwidth from direct coincidence counts

The experimental setup described in the previous section is used for characterizing the quantum state emitted by our AlGaAs chip. The first step is to measure the biphoton emission bandwidth from direct coincidence counting. To this end, we use a 50/50 fibered coupler to separate the generated photons into two optical fibers. We plug the tunable filter to one of the output arms of the coupler and set the bandwidth of the filter to 0.8 nm (approximately 100 GHz). We record the coincidence counts between the two arms while sweeping the central wavelength of the filter over its whole operating range, from 1525 nm to 1610 nm. As we already mentioned, thanks to energy anti-correlation, photons filtered by the TF will only trigger coincidences with their energy-matched counterpart, thus avoiding the need for adding a second filter at the output of the 50/50 coupler. The result of the measurement is shown in Fig. 11.5. We observe that the counts follow a bell-shaped curve that is maximum around the biphoton degeneracy (1556.55 nm), as expected. We measure a full width at half maximum of 60 nm spanning a total of 76 ITU 100 GHz channels.

We compare this experimental data to the prediction of the model described in Section 5.4. The quantum state after the 50/50 coupler and TF is given by Eq. (5.40):

$$\begin{aligned}\left|\Psi'\right\rangle = \int_0^\infty \mathrm{d}\Omega f(\Omega) \left[\Phi(\Omega) \left|\omega_d + \Omega, H\right\rangle_A \left|\omega_d - \Omega, V\right\rangle_B \right. \\ \left. + \Phi(-\Omega) \left|\omega_d + \Omega, V\right\rangle_A \left|\omega_d - \Omega, H\right\rangle_B\right],\end{aligned} \tag{11.1}$$

with $f(\Omega)$ the rectangular lineshape of a filter centered on a fixed frequency Ω_0 (see Eq. (5.41)) and A, B denote the two output fiber path of the 50/50 coupler. To obtain the coincidence probability, we use the coincidence operators defined in Eqs. (6.15) and (6.16):

$$\hat{p}_A = \int \mathrm{d}\omega \hat{a}^\dagger(\omega) \left|\mathrm{vac}\right\rangle \left\langle\mathrm{vac}\right| \hat{a}(\omega) \tag{11.2}$$

$$\hat{p}_B = \int \mathrm{d}\omega \hat{b}^\dagger(\omega) \left|\mathrm{vac}\right\rangle \left\langle\mathrm{vac}\right| \hat{b}(\omega) \tag{11.3}$$

where $\hat{a}(\omega)$, $\hat{b}(\omega)$ are the operators associated to the annihilation of a photon of frequency ω in port A, B respectively. The coincidence probability is given by:

$$P_c = \left\langle \Psi' \right| \hat{p}_A \otimes \hat{p}_B \left| \Psi' \right\rangle . \tag{11.4}$$

This probability is proportional to the number of normalized coincidences. By evaluating Eq. (11.4) for different values of the filter central frequency Ω_0, we obtain the dependence of the number of coincidence counts as a function of wavelength. As explained in Section 5.3.2, we can include the effect of the cavity formed by the two facets of the waveguide into the expression of the JSA $\Phi(\Omega)$ that enters in the coincidence probability. In Fig. 11.5 we plot the simulated normalized coincidence counts with (dashed line) and without cavity effects (solid line). We observe that the measured points are in good agreement with the predictions of the model without cavity. When including cavity effects, we see that some data points in the plateau around the biphoton degeneracy deviate from the model. However the bandwidth of the spectrum, which is the key feature for our measurements, is well-reproduced by both theories.

11.3.2 Measurement of Bell correlation curves

A first entanglement characterization of the generated state is done by measuring the Bell correlation curves in both $\mathbb{Z}$ and $\mathbb{X}$ bases as a function of frequency. We first separate signal (high energy) and idler (low energy) photons from 100 GHz conjugate channel pairs whose central frequencies are symmetric with respect to the biphoton degeneracy (1556.55 nm). In the C-Band, we do so using a WSS and in the L-Band, a CWDM + TF combination, as explained above. Then we record coincidence counts when projecting the polarization of the signal photon onto an axis of angle $\theta_1 \in [0°, 180°]$ with respect to the horizontal axis of the laboratory frame and the polarization of the idler photon on a fixed axis, either $H\,(0°)$ for the $\mathbb{Z}$ basis or $D\,(45°)$ for the $\mathbb{X}$ basis. The projection of the polarization state is done using the waveplates and fibered polarizing beam splitter, as explained in Section 11.1 and Section 11.1.2.

In Fig. 11.6, we display the correlation curves and corresponding raw visibilities obtained between 100 GHz conjugate channel pairs spanning the C+L band. The visibility of the two-photon interference fringes is an indicator of the quality of entanglement. It is computed from the maximum and minimum values of the raw counts as

$$V = \frac{\max - \min}{\max + \min}. \tag{11.5}$$

Solid lines in Fig. 11.6 are a least-square fit to the expression [119] :

$$C = a \sin^2(\theta_1 - \theta_2) + b \tag{11.6}$$

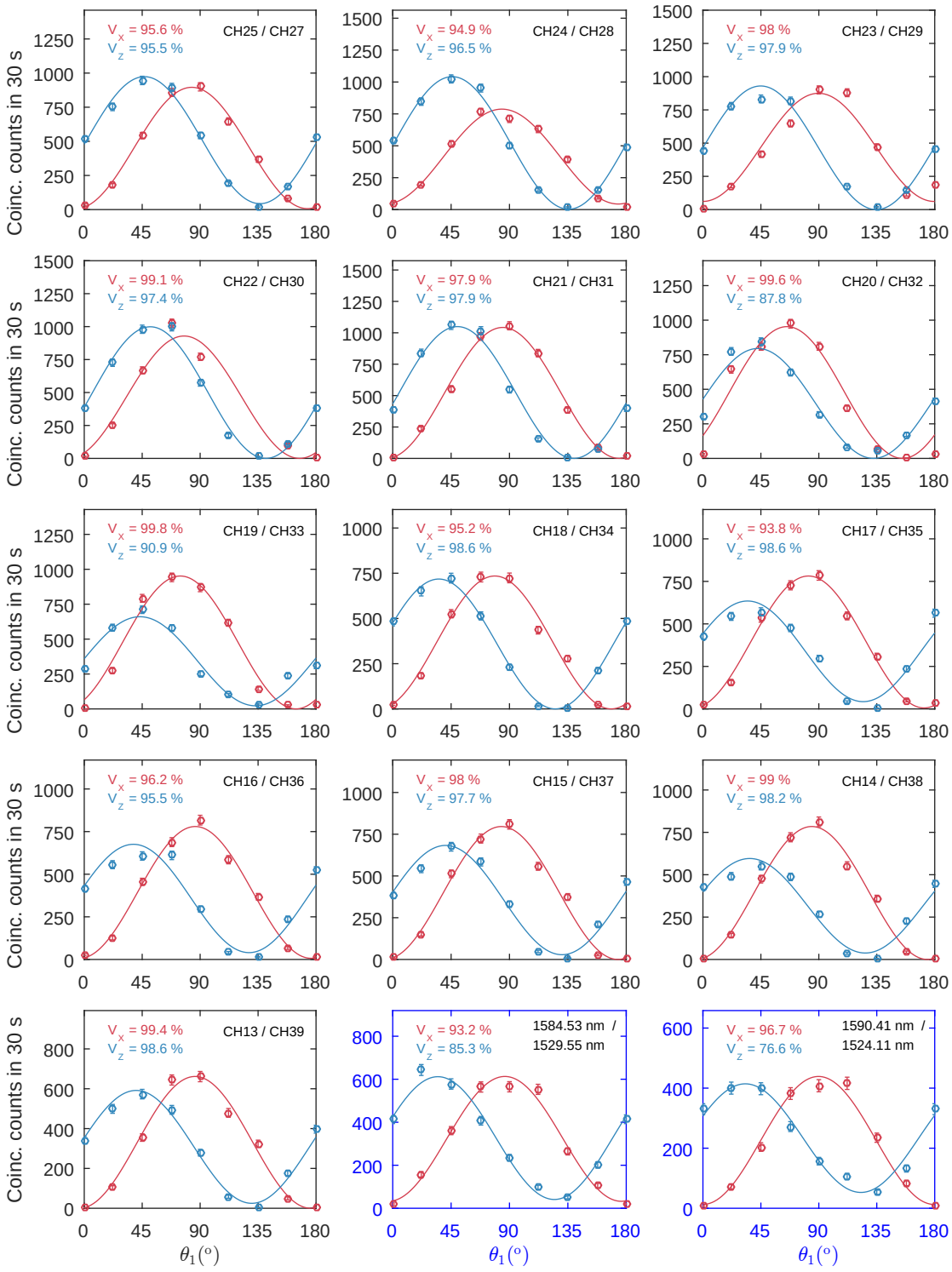

Figure 11.6: Raw Bell correlation curves for 100 GHz conjugate channel pairs with corresponding raw visibilities. Plots with black axes color are measured with a WSS for ITU channel pairs 25/27 to 13/39. Plots with blue axes color are measured with a CWDM + TF for channels pairs centered around 1584.53 nm/1529.55 nm and 1590.41 nm/1524.11 nm.

where the free parameters are θ_2, the projection angle of the idler photon, a the amplitude and b the baseline of the correlation curves. We observe that, even though we carefully canceled out the birefringence of the fibers using the polarization rotators, as detailed in Section 11.1.2, the value of θ_2 for measurements in the $\mathbb{Z}$ basis varies slightly over the different runs. This can be attributed to an additional frequency-dependent phase shift caused by this residual birefringence. We emphasize that this is not detrimental to the measured visibilities and hence to the entanglement quality of the generated quantum state.

11.3.3 Experimental estimation of a lower bound to F

These first two experiments are not sufficient to measure the effective bandwidth over which the generated photons are entangled. To do so, we estimate the lower bound to the fidelity F to a Ψ^+ Bell state, over the whole emission range of our AlGaAs source. To calculate the fidelity as a function of channel central frequency, we derive the reduced density matrix in polarization space after filtering the generated photons into channels of bandwidth $\Delta = 100\,\mathrm{GHz}$ using the same mathematical procedure as in Section 5.4. After applying the filtering operation and tracing out the frequency degree of freedom, we obtain the following density matrix:

$$\begin{aligned}\rho = \alpha \left|HV\right\rangle_{ABAB}\left\langle HV\right| + \mathcal{D}\left|HV\right\rangle_{ABAB}\left\langle VH\right| \\ + \mathcal{D}^*\left|VH\right\rangle_{ABAB}\left\langle HV\right| + \beta\left|VH\right\rangle_{ABAB}\left\langle VH\right|,\end{aligned} \tag{11.7}$$

where the 4 non-zero matrix elements are:

$$\alpha = \frac{1}{\mathcal{N}}\int_0^\infty \mathrm{d}\Omega f(\Omega)|\Phi(\Omega)|^2, \tag{11.8}$$

$$\beta = \frac{1}{\mathcal{N}}\int_0^\infty \mathrm{d}\Omega f(\Omega)|\Phi(-\Omega)|^2, \tag{11.9}$$

$$\mathcal{D} = \frac{1}{\mathcal{N}}\int_0^\infty \mathrm{d}\Omega f(\Omega)\Phi(\Omega)\Phi^*(-\Omega), \tag{11.10}$$

and the filter lineshape is given by:

$$f(\Omega) = \begin{cases} 1, & \text{for } \Omega \in [\Omega_0 - \Delta/2, \Omega_0 + \Delta/2], \\ 0, & \text{elsewhere.}\end{cases} \tag{11.11}$$

with Ω_0 the central frequency of the filter. The normalization constant is set to $\mathcal{N} = \int_0^\infty \mathrm{d}\Omega f(\Omega)\left[|\Phi(\Omega)|^2 + |\Phi(-\Omega)|^2\right]$ such that $\mathrm{Tr}\,\rho = 1$. Finally, the fidelity to a Ψ^+ Bell state can be evaluated from the definition given in Eq. (3.5).

A lower bound to F is accessible experimentally by measuring the populations (diagonal elements) of the polarization density matrix in both $\mathbb{X}$ and $\mathbb{Z}$ bases. As explained earlier, we start by separating the photon pairs into energy-matched 100 GHz frequency channels pairs spanning the biphoton bandwidth, either using the WSS in the C-Band or the CWDM and TF in the L-Band, and send the filtered photons to the two polarization analysis station (waveplates, FPBS, detectors) as shown in Fig. 11.1. Then, by recording the number of coincidence counts between the two detectors in 8 different configurations : $C_{HH}, C_{HV}, C_{VH}, C_{VV}, C_{DD}, C_{DA}, C_{AD}, C_{AA}$ we can access the populations of the density matrix in both bases. For $(\alpha, \beta) \in \mathcal{B} \times \mathcal{B}$, with $\mathcal{B} \in \{\mathbb{X}, \mathbb{Z}\}$, the diagonal matrix element $\rho_{\alpha\beta}$ corresponding to the first (second) photon in α (β) polarization state is calculated as $\rho_{\alpha\beta} = C_{\alpha\beta}/(\sum_{\mathcal{B}\times\mathcal{B}} C_{\alpha'\beta'})$. Note that the normalization factor has to be calculated

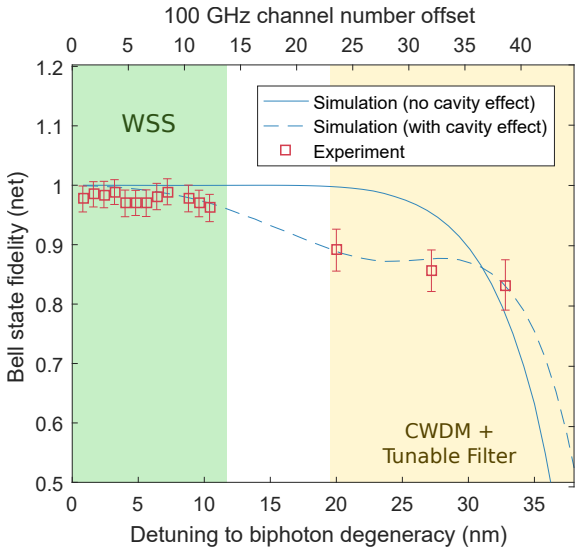

Figure 11.7: Squares: Lower bound to the fidelity to a Ψ^+ Bell state as a function of the detuning to biphoton degeneracy wavelength in nm (lower x-axis) and in units of 100 GHz channels (upper x-axis). Error bars were calculated by taking into account poissonian statistics of signal counts and subtracted noise counts. Solid line: Theoretical prediction without cavity effects. Dashed line: Theoretical prediction with cavity effects (see main text for details).

independently for the two bases. The lower bound to F is then obtained through the relation [201, 202]:

$$F \geq \frac{1}{2}\left(\rho_{HV} + \rho_{VH} - \rho_{HH} - \rho_{VV} + \rho_{DD} + \rho_{AA} - \rho_{DA} - \rho_{AD}\right). \tag{11.12}$$

The experimental results, along with the fidelity of the numerically simulated quantum state emitted by the AlGaAs chip, are shown in Fig. 11.7. The observed lower bound of the fidelity is above 95 % over a 26 nm spectral range corresponding to the first 13 pairs of 100 GHz ITU channels around degeneracy, and stays above 85 % for up to 38 channels pairs around degeneracy spanning a total 60 nm wavelength range. Since the channels of the CWDM are not centered around the biphoton degeneracy wavelength, measurements in the L-Band are limited to the conjugate channels that fall within the transmission window of the CWDM ports. For this reason only 3 data points have been acquired beyond 11 nm of detuning in Fig. 11.7. We can see from Fig. 11.7 that the experimental points are well reproduced by a model including cavity effects. As explained in Section 5.4, these effects result in a faster decrease of the fidelity with detuning arising from the asymmetry introduced in the JSA by the cavity functions (defined in Section 5.3.2) in the presence of birefringence and chromatic dispersion.

Chapter 12

Flexible multi-user entanglement-based quantum key distribution network

Contents

12.1 QKD performance before the distribution stage 167
12.2 Long-distance entanglement-based QKD 169
12.3 Comparison between WSS and passive thin-film DWDM for polarization entanglement distribution 174
12.4 A reconfigurable fully-connected multi-user entanglement-distribution network 175
12.5 Elastic quantum network with flexible bandwidth allocation . 178
12.6 Towards new topologies 178

In this chapter, we use the broadband polarization-entangled state emitted by the AlGaAs source to implement a multi-user entanglement-based QKD network. We start by measuring the figures of merit of the BBM92 protocol before and after the long-distance link that separates the source from the users and compare the achievable performance for two different demultiplexing devices: a WSS or a thin-film DWDM. Then we present our implementation of a reconfigurable wavelength-multiplexed fully-connected QKD network. We finally illustrate the flexibility of our scheme by adapting the bandwidth allocation between the users to specific network constraints such as unbalanced link distances.

12.1 QKD performance before the distribution stage

After demonstrating the emission of polarization-entangled photon over a broad frequency range, we want to evaluate the intrinsic QKD performance of our scheme. Using the same setup as described in Section 11.1, we measure the figures of merit of the BBM92 protocol right after the demultiplexing stage : the asymptotic secret key rate R_{key} and the QBER e. We perform the measurement for 13 different choices of signal and idler 100 GHz channel pairs. Note that this spectral range is limited by the upper cutoff wavelength (1565 nm) of the WSS corresponding to the boundary of the C-Band, and not by the spectral bandwidth of the generated biphoton state.

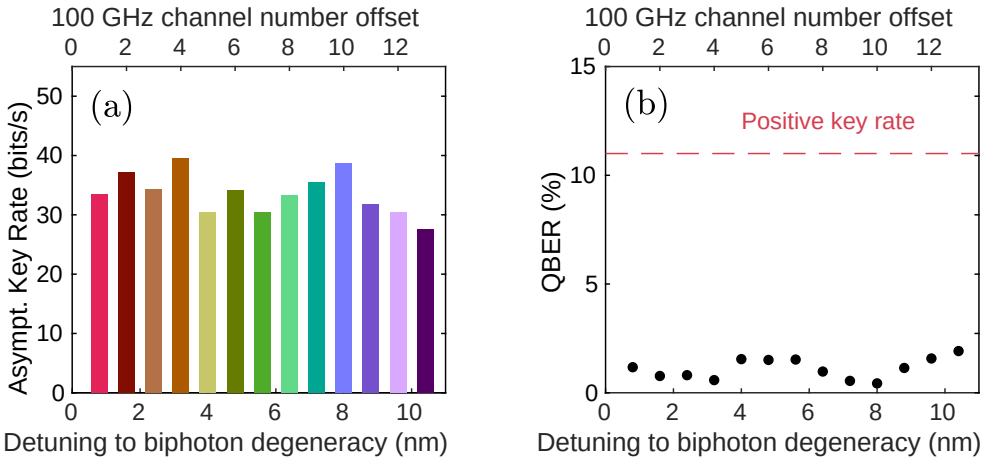

Figure 12.1: QKD performance before the distribution stage for the 13 ITU 100 GHz channel pairs forming the intersection between the biphoton spectrum and the WSS operating range. (a) Asymptotic key rate and (b) QBER as a function of the detuning to biphoton degeneracy in nm (lower x-axis) and in units of 100 GHz channels (upper x-axis). The 11 % error threshold for a positive key rate is given for an error correcting code operating at the Shannon limit.

We first express R_{key} and e in terms of the recorded coincidence counts [203]. The raw coincidence counts in each basis ($\mathbb{X}$ and $\mathbb{Z}$) read:

$$C_{\mathbb{X}}^{(\text{raw})} = C_{HH} + C_{HV} + C_{VH} + C_{VV}, \tag{12.1}$$

$$C_{\mathbb{Z}}^{(\text{raw})} = C_{DD} + C_{DA} + C_{AD} + C_{AA}. \tag{12.2}$$

The QBER can be readily obtained by taking the ratio of accidental counts against the total number of recorded raw coincidence counts:

$$e = \frac{C_{HH} + C_{VV} + C_{DA} + C_{AD}}{C_{\mathbb{X}}^{(\text{raw})} + C_{\mathbb{Z}}^{(\text{raw})}}. \tag{12.3}$$

Next, we compute the raw key rate as the arithmetic mean between the raw count rate in the $\mathbb{X}$ and in the $\mathbb{Z}$ basis:

$$R_{\text{raw}} = \frac{1}{2}\frac{C_{\mathbb{X}}^{(\text{raw})} + C_{\mathbb{Z}}^{(\text{raw})}}{\tau}, \tag{12.4}$$

with τ the integration time. Finally, the asymptotic key rate is obtained from Eq. (10.7).

The measured R_{key} and QBER are plotted in Fig. 12.1 (a). We see that both quantities are stable over the 13 ITU 100 GHz channels spanning a 10.4 nm wavelength range. The QBER stays below 2 %, well under the positive key rate threshold of 11 % defined in Section 10.4. This stability can be attributed to the flatness of the source spectrum in this spectral region as shown in Fig. 11.5 and to the wavelength-independent insertion losses of the WSS. The entanglement quality of the emitted quantum state, combined with the high conversion efficiency of AlGaAs, yields high asymptotic key rates of 28 to 39 bits/s per channel, over a very broad spectral range. In Fig. 12.2, we display an example of the raw data from which R_{key} and e were estimated (channel pair ITU 23/ITU 29). We observe that the level of background noise counts is very low, which is consistent with the moderate value of the QBER that was reported in our measurements. In the configurations where

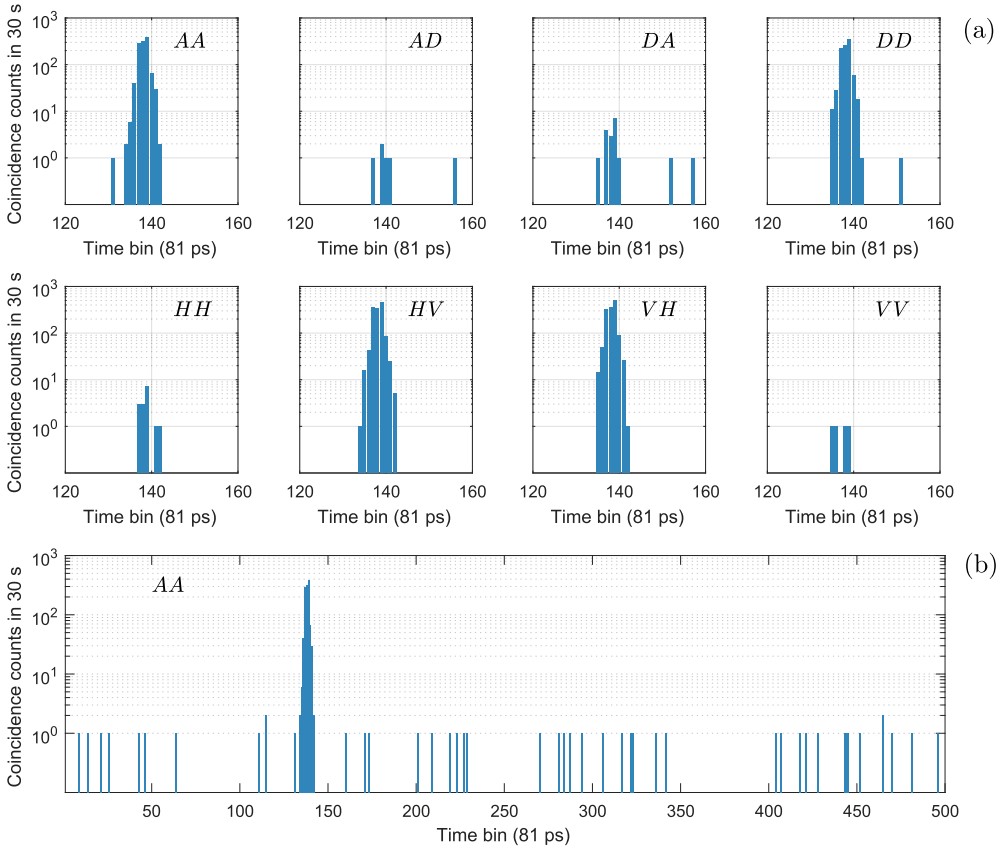

Figure 12.2: (a) Measured time-correlation histograms for the 8 projective measurements performed to obtain R_{key} and e for 100 GHz ITU channels 23 (1558.98 nm) and 29 (1554.13 nm). (b) Extended time-correlation histogram in the AA configuration showing the low level of recorded background counts.

the number of counts is maximum (AA, DD, HV, VH) we achieve a CAR of the order of 4×10^3.

12.2 Long-distance entanglement-based QKD

12.2.1 Theoretical modeling of long distance links

Mathematical model

Principle: Building on the intrinsic performance of our chip, we aim at distributing the entangled photons across long-distance fiber links. The latter induce optical losses that decrease the key rate. In this section, we present the theoretical model that is used to calculate the expected key rate and QBER as a function of link distance.

Following Refs. [200, 204] we adapt to our CW pumping scheme a model describing a parametric photon-pair pumped by a pulsed laser. The original model provides expression for the probability per pump pulse of measuring a coincidence count. Instead, we rewrite this quantity as a probability per detection window.

We are using free-running single photon detectors in a "start-stop" configuration. In all our coincidence measurements, at the data post-processing stage, we define the number of coincidences as the number of recorded counts within the m central bins of the measured

time-correlation histogram. By doing this, we define a temporal window $\tau_c = m \times \Delta\tau$ where $\Delta\tau$ is the the minimal temporal bin width allowed by the timing resolution of the counting electronics. The post-selection of the events within τ_c is equivalent to this physical picture : when one of the detector records an event, triggering a "start" signal, we open a temporal window of τ_c and record a coincidence count if the "stop" signal at the other detector happens with a time delay shorter than τ_c, and a noise count instead. Therefore instead of considering the probability that a coincidence is recorded given a pump pulse is emitted, as in the original model, we compute the probability of measuring a coincidence count within a window τ_c, given a "start" signal has been recorded.

Quantitatively, our quTau TDC has a resolution of $\Delta\tau = 81\,\text{ps}$ and the coincidence peak in the time-correlation histogram typically spreads over $m = 6$ bins. We recall that this spread is due to the detector timing jitter. As a result, we use a coincidence window of $\tau_c = 486\,\text{ps}$ in our experiments. We emphasize the fact that there is a trade-off between coincidence window size and recorded noise. Indeed, the larger τ_c, the higher the probability of a false coincidence coming from the uncorrelated noise of the source and the environment. The increasing of τ_c is therefore detrimental to the QBER and can significantly affect the long-distance performance of QKD.

Coincidence rate: We denote by

$$p(k, \lambda) = \lambda^k e^{-\lambda}/k! \tag{12.5}$$

the probability of the outcome k for a random variable following a Poisson distribution of parameter λ. Due to the poissonian statistics of light generated by parametric entangled photon source, the probability to generate a photon pair in a time τ_c is given by a Poisson distribution of parameter $\lambda = \mu\tau_c$ where μ is the internal pair generation rate (PGR) of the photon-pair source in pairs/s. The probability p_0 of generating zero pair (vacuum state) within a window τ_c is

$$p_0 = p(k = 0, \mu\tau_c) = e^{-\mu\tau_c}. \tag{12.6}$$

Assuming negligible multi-pair emission, the probability p_1 to generate one photon pair within τ_c is simply

$$p_1 = 1 - p_0 = 1 - e^{-\mu\tau_c}. \tag{12.7}$$

We now define the yields Y_0 and Y_1 as the conditional probability of measuring a coincidence count within τ_c given zero or one pair has been emitted respectively :

$$Y_0 = Y_{0A} Y_{0B}, \tag{12.8}$$

$$Y_1 = [1 - (1 - Y_{0A})(1 - \eta_A)^{n_{\text{det}}}][1 - (1 - Y_{0B})(1 - \eta_B)^{n_{\text{det}}}], \tag{12.9}$$

where Y_{0A} (Y_{0B}) is the probability of a measuring a detection event triggered by a dark count within τ_c at Alice (Bob) and n_{det} the number of detectors at each user's measurement station. In the case of BBM92 with passive basis choice, as sketched in Fig. 10.2, we have $n_{\text{det}} = 4$. Again, due to the poissonian statistics of the single photon detection process and given d_A (d_B) the dark count rate of Alice's (Bob's) detectors, we have

$$Y_{0A} = 1 - p(k = 0, d_A\tau_c) = 1 - e^{-d_A\tau_c}, \tag{12.10}$$

$$Y_{0B} = 1 - p(k = 0, d_B\tau_c) = 1 - e^{-d_B\tau_c}. \tag{12.11}$$

η_A (η_B) is the total efficiency of Alice's (Bob's) channel which includes link losses and detector efficiency and can also be seen as the probability of detecting a photon that has

been emitted by the source. The first (second) bracketed term in Eq. (12.9) represents the probability of measuring a detection event at Alice (Bob), either triggered by a photon pair or by a dark count. It is given by one minus the probability of the opposite outcome, namely no dark count detected and no photon detected. The total probability of measuring a coincidence event within τ_c is finally given by

$$Q = p_0 Y_0 + p_1 Y_1 \tag{12.12}$$

and we can obtain the coincidence rate in events/s as

$$R_c = (1/\tau_c)Q. \tag{12.13}$$

Finally, when modeling the coincidence rate as a function of link losses, one can write :

$$\eta_i = \eta_{\text{setup}} 10^{-\alpha},\ i = A, B \tag{12.14}$$

with η_{setup} the setup efficiency that includes collection and detection efficiency, α the losses of the optical link. To convert the total losses in dB into equivalent fiber link distance, we took as a reference the $0.22\,\text{dB}\,\text{km}^{-1}$ losses of a standard SMF28 fiber.

QBER : Now that an expression for the coincidence rate has been established, we apply the same formalism to derive the QBER. We start by defining the probability of error e_0 (e_1) given zero (one) pair has been emitted and a coincidence count has been recorded. We recall that an error means that Alice and Bob both measure a simultaneous click but not on the same detector, thus obtaining opposite key bit values. We have

$$e_0 = \frac{1}{2}, \tag{12.15}$$

$$e_1 = e_0 + \frac{(e_0 - b)\eta_A \eta_B}{Y_1}. \tag{12.16}$$

The first line is straightforward : when the detectors click in the absence of a pair (coincidence between two dark counts) there is an equal probability that this click occurs at the same detectors at Alice and Bob, meaning that half the time they will record the same bit value and half the time they will record different bit values (error). Similarly, in the second line, the first term is the dark counts contribution and the second term models the systematic polarization measurement errors. The parameter b is the fraction of photon pairs which are accidentally detected as errors. When $b = 0$, the only source of error are the dark counts. The overall QBER e is finally defined as

$$e = \frac{1}{Q}\left(e_0 Y_0 p_0 + e_1 Y_1 p_1\right). \tag{12.17}$$

Asymptotic key rate : Finally, the asymptotic key rate as a function of the link losses (or equivalent fiber link distance) can be evaluated by feeding Eq. (12.13), Eq. (12.14) and Eq. (12.17) into the expression Eq. (10.7) for the secure key rate derived in the security proof.

Estimation of the model parameters μ, b, η_A, η_B :

The model described above relies on four parameters : the internal PGR μ, the polarization measurement error b and the channel efficiencies of both users η_A, η_B. To measure them experimentally we send the photon-pairs generated by our source into the WSS and route the photons belonging to the two conjugate 100 GHz ITU channels 23 and 29 to the

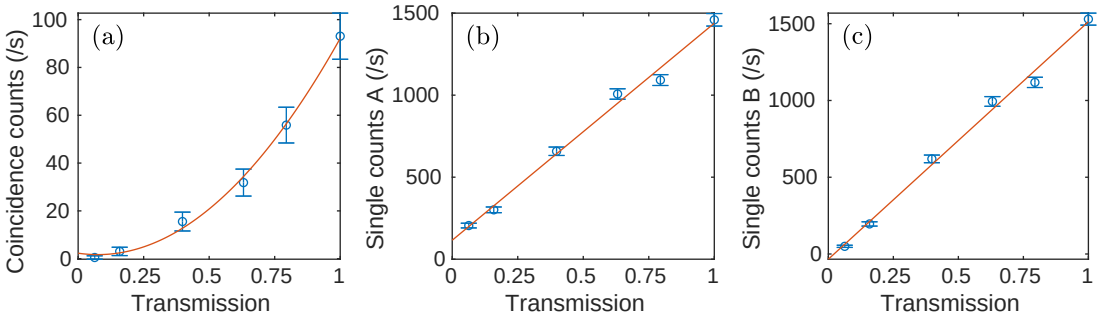

Figure 12.3: (a) Coincidence and (b-c) single counts from conjugate ITU channels 23 and 29 as a function of transmission $T = 10^{-\alpha}$. The attenuation is controlled by the WSS. Error bars are calculated assuming poissonian statistics.

two output ports. We apply a variable attenuation to those channels using the built-in attenuation control of the WSS and send the output directly to the SNSPDs to record direct coincidence counts between those two channels without polarization selection. From the measured coincidences and single counts versus attenuation, we can recover μ, η_A and η_B by fitting the data to the model of equations Eq. (12.6), Eq. (12.7), Eq. (12.8), Eq. (12.10), Eq. (12.12), Eq. (12.14) and Eq. (12.13).

The results are shown in Fig. 12.3. We observe the expected quadratic and linear dependence on link transmission $T = 10^{-\alpha}$ of coincidence counts and single counts respectively. From the least square fit to our model, we retrieve the values of $\mu = 1.65 \times 10^4\,\mathrm{s}^{-1}$ and $\eta_{\mathrm{setup}} = 0.08$.

The parameter b can be approximated from the 8 projective measurements used for the estimation of the lower bound to the fidelity (Section 11.3.3). It is defined as the ratio between error counts over total counts :

$$b = \frac{C_{HH} + C_{VV} + C_{DA} + C_{AD}}{C_{\mathbb{X}}^{(\mathrm{raw})} + C_{\mathbb{Z}}^{(\mathrm{raw})}}. \tag{12.18}$$

We see that this is the same expression as the estimated QBER shown in Eq. (12.3). Indeed, according to our simulations (Fig. 11.7) in this spectral region, the theoretical fidelity is very close to 1 and the discrepancy with the experimental data can be solely attributed to setup imperfection, and not to the mixedness of the generated state. This is why b, a parameter that only depends on the setup and not on the source characteristics, is equal the QBER around degeneracy. We find the experimental value of $b = 0.014$. We stress that b could not be estimated with Eq. (12.18) from data recorded far from degeneracy as, in this region, the reduction in the fidelity does not exclusively come from measurement errors but also from the increasing mixedness of the quantum state.

12.2.2 Long-distance QKD performance of the source

We compare our model to the experimental long-distance performance of our system by estimating R_{key} and e after adding 25 km SMF28 fiber spools between the demux/mux stage and the users' measurement station. The experimental setup is identical to the one that has been described in Section 11.1 with the addition of the two fiber spools. This measurement is performed in two configurations: symmetric (both users separated from the source by 25 km of fiber) and asymmetric (one user at 0 km and the other at

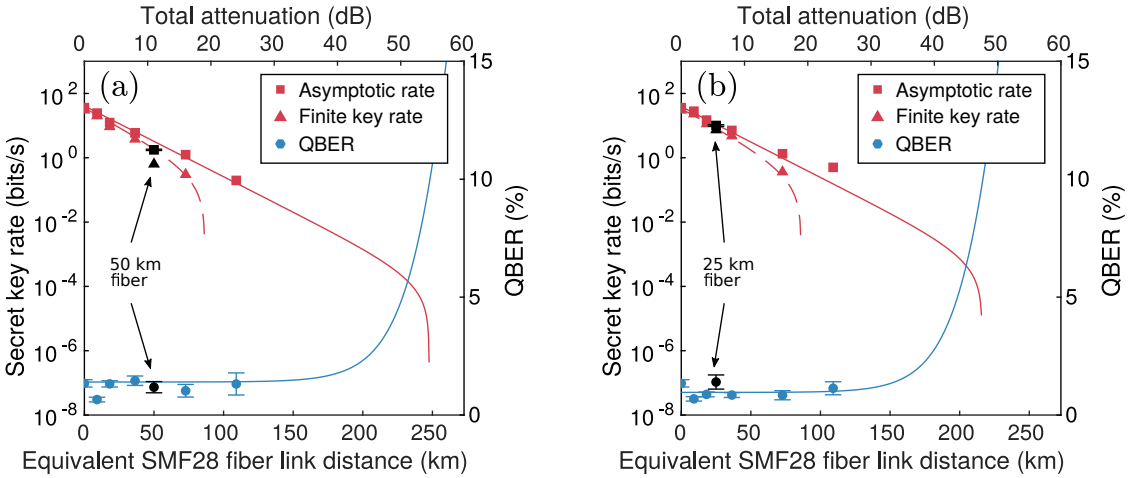

Figure 12.4: Asymptotic and finite size key rates and QBER for a (a) symmetric and an (b) asymmetric two-user link supported by 100 GHz ITU channels 23 (1558.98 nm) and 29 (1554.13 nm) as a function of SMF28 fiber distance (lower x-axis) and attenuation (upper x-axis). Symbols represent experimental data and continuous lines theoretical predictions for a BBM92 scheme. Finite key rates are estimated assuming 10 min block size.

25 km) in order to compare the performances and provide the optimized solution for secure communication. All measurement runs are performed by selecting entangled photons from 100 GHz ITU channels 23 (1558.98 nm) and 29 (1554.13 nm) which are considered representative of all the available channels. The results are shown as black symbols on Fig. 12.4 (a) and (b) for the symmetric and asymmetric configurations respectively.

We point out that we used different timing electronics for the asymmetric link. Indeed, when one photon travels through 25 km of fiber and its twin through 0 km their arrival times are separated by a delay of the order of 250 µs. This delay is much larger than the buffer of our TDC, consisting of 50 000 bins of 81 ps totalizing a 4 µs buffer size. Therefore, we replaced the TDC by a time-tagger (Swabian Instruments) that can store the timestamps of all recorded events and compute the coincidence rate after an arbitrary time delay.

To estimate the maximum distance of a repeater-less link we performed the same measurement by replacing the fiber spools by variable channel attenuation programmed on the WSS. The attenuation can then be converted into equivalent length of SMF28 fibers assuming a standard value of 0.22 dB km^{-1} for the SMF28 fiber optical losses. Results for a symmetric and asymmetric link are shown in Fig. 12.4 (a) and (b) respectively as color symbols. In order to highlight the relevance of these results for real-world implementations, we perform a finite key security analysis of our scheme as described in Section Section 10.5. We compare the experimental value of the asymptotic key rate to theoretical predictions (continuous lines) for a BBM92 scheme with passive basis selection following the model described in the previous section.

We see that the measurements performed with variable attenuation closely follow our theoretical predictions (solid and dashed lines) while measurements with fiber spools (black symbols) deviate slightly from our model. Since the QBER does not increase significantly in fiber-based experiments (black filled circles), this small discrepancy can be entirely attributed to the insertion losses induced by the presence of extra fiber connectors between the WSS and the fiber spools and not to the potential thermal and mechanical instability

Technology	Distance (km)	R_{raw} (/s)	R_{key} (asympt.) (/s)	QBER (%)
WSS	0	80.4	34.2	0.8
DWDM	0	441.4	151.5	2.1
WSS	50	4.4	1.8	1.1
DWDM	50	13.8	2.0	5.5

Table 12.1: BBM92 QKD performance of the WSS and the DWDM.

of our fiber link.

Based on this data, we can compare experimentally the long-distance performance of the BBM92 protocol in symmetric and asymmetric configurations. We observe that, in both scenarios, the key rate including finite size effects stays positive for distances of up to 75 km. However, we also observe that, at very long distances, the asymptotic key rate for a symmetric link stays positive up to 250 km, while in an asymmetric link, it drops at around 215 km. Indeed, in the latter configuration, a strong attenuation in the link between the source and the distant user induces a strong increase of the QBER as the signal approaches the noise background. On the contrary, in the symmetric case, the losses are distributed between the two users and this critical situation is reached at higher levels of attenuation. In the finite key security regime in which we are operating, the key rates become negative before the difference between symmetric and asymmetric links comes into play. This result has practical implications in the context of deployed QKD schemes; indeed this proves that a scenario involving an entangled pair source connected to one local user and one distant user will not be detrimental to the BBM92 protocol efficiency.

Furthermore, the performance of our device being practically insensitive to wavelength in the C-band, as shown in Fig. 12.1, the measured performances for the two particular channels (23 and 29) can be extrapolated to the 12 other available 100 GHz channel pairs. This means that each channel pair can support a long-distance fiber link, making our scheme compatible with large-scale fibered QKD networks.

12.3 Comparison between WSS and passive thin-film DWDM for polarization entanglement distribution

In our preliminary experiments, we decided to benchmark WSS and DWDM for polarization-entanglement distribution. The DWDM, having lower average insertion losses, seemed to be a good candidate for long-distance QKD. We choose the conjugate channels having the lowest insertion losses, in our case ITU 20 (0.64 dB) and ITU 32 (0.91 dB), and measure a very high raw key rate while maintaining a low QBER of 2.1 %, as shown in Table 12.1. We observe that before the distribution stage, the DWDM outperforms the WSS. However, when adding two 25 km fiber spools, the QBER drops sharply to 5.5 %, which consequently lowers the key rate down to similar levels as for the WSS. We note that the order of magnitude of the QBER at long distance with a DWDM is consistent with the results of Ref. [97] where the authors used an identical device.

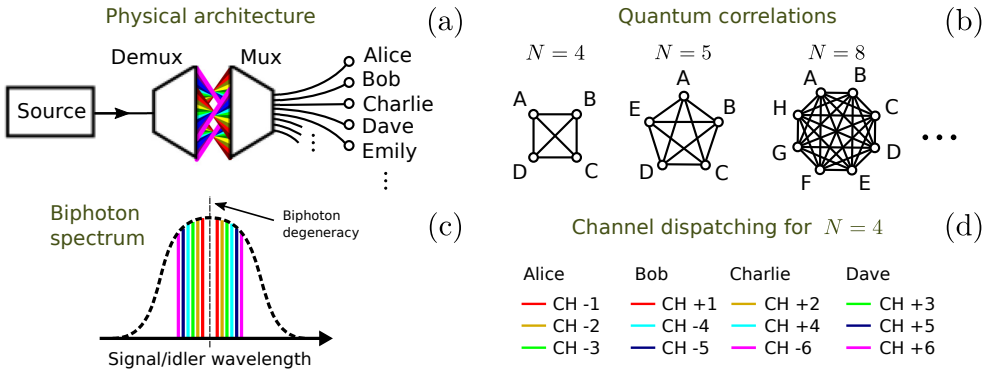

Figure 12.5: Principle of fully-connected frequency-multiplexed entanglement networks. (a) Schematic physical architecture of the network. The source constitutes the central server nodes where the entanglement is generated. After a demux/mux stage where different frequency channels are attributed to each user, the entangled photons are distributed to the user nodes. (b) Resulting quantum correlation topology. Vertices represent user nodes and edges symbolize a shared entangled state. (c) Schematic of the source spectrum with the frequency channel grid used to build a $N = 4$ fully-connected network (not to scale). (d) Detailed channel dispatching between the $N = 4$ users. Channel numbers refer to their relative offset with respect to biphoton degeneracy.

12.4 A reconfigurable fully-connected multi-user entanglement-distribution network

12.4.1 Principle

After demonstrating the capability of the AlGaAs source to distribute secure keys over a broad bandwidth and across long distances, we use our setup to build a multi-user entanglement distribution network.

We focus on a particular class of networks where each of the N users shares an entangled state with the remaining $N-1$ users [145, 97, 72, 73]. We refer to these as fully-connected networks, by analogy with graph theory: indeed, they can be represented by a complete graph where each vertex corresponds to one user node and the edges symbolize a shared entangled state between two users. Graph representations for fully-connected entanglement networks of size $N = 4, 5, 8$ are shown in Fig. 12.5 (b). Fully-connected entanglement networks can be implemented with one central server node which hosts the entangled photon source with demux/mux, and N user nodes consisting of a polarization analyzing device and single photon detectors to carry out the BBM92 protocol as schematically depicted in Fig. 12.5 (a).

The number of edges in a complete graph of size N is $N(N-1)/2$. Hence to get a complete entanglement network, one needs to establish $N(N-1)/2$ two-user links supported by $N(N-1)/2$ distinct conjugate channel pairs. To do so, we demultiplex the generated photons into

$$N_{\text{channels}} = N(N-1) \tag{12.19}$$

frequency channels, as shown in Fig. 12.5 (c). Then we recombine those channels into single optical fibers, one for each user. This is done via the WSS which implements both operations. Each user then receives photons from $N-1$ channels, one for each connected node. Photons from the $N-1$ conjugate channels are similarly distributed to the other users. As a result, each node effectively shares a Bell pair with every other node in the

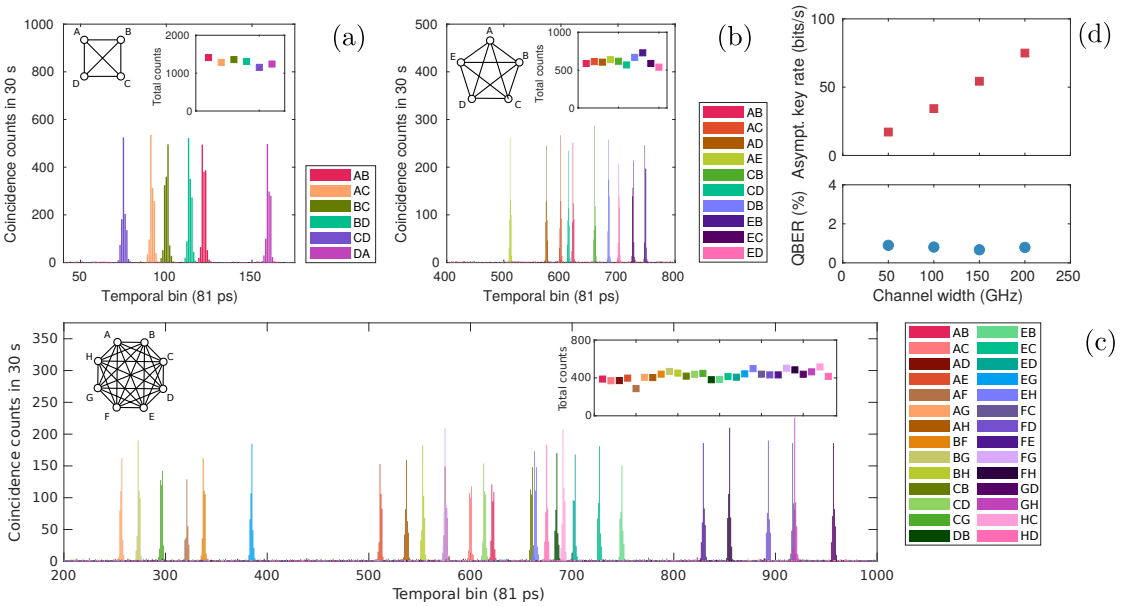

Figure 12.6: Reconfigurable multi-user entanglement network. (a-c): Time-correlation histograms for all two-user links in a fully connected network of size (a) $N = 4$ with 200 GHz channels, (b) $N = 5$ with 100 GHz channels and (c) $N = 8$ with 50 GHz channels. (d): Measured asymptotic key rate and QBER for ITU channels 23 (1558.98 nm) and 29 (1554.13 nm) as a function of channel width.

network. To illustrate this mechanism, we detail the channel dispatching for the $N = 4$ case in Fig. 12.5 (d). Here, for instance, Alice and Bob share an entangled state over channels CH$\pm$1, Alice and Charlie over channels CH$\pm$2 and so on. As stated above in Section 10.1, the main advantage of this network architecture is that it requires no trusted nodes.

12.4.2 Experimental implementation

We now demonstrate the operation of a scalable multi-user network architecture by taking advantage of the broad entanglement bandwidth of our source and of the flexible frequency management enabled by the WSS.

The number of required frequency channels scales quadratically with N. In this context, we see that the broadband entanglement of the biphoton state emitted by the AlGaAs chip is a crucial feature. In addition, the use of a WSS at the demux/mux stage enables a reconfigurable multi-user network where the central frequency and the bandwidth of each channel can be adjusted. In our setup we can increase the number of users in the network by simply reducing the bandwidth allocated to each channel. Using all the available wavelength overlap between the biphoton state and the WSS operating range, our reconfigurable complete-graph network can accommodate from 4 users, with 200 GHz channels pairs, to 8 users, with 50 GHz channel pairs.

We sequentially characterize the $N(N-1)/2$ two-user links for different network sizes: $N = 4, N = 5$ and $N = 8$. Due to the lack of additional single photon detectors, we did not run real-time QKD sessions for N users in parallel. Instead, we measure the time-correlation histograms for all $N(N-1)/2$ two-user links in the three different configurations. The obtained coincidence histograms are shown in Fig. 12.6 (a-c). The total number of counts contained in each coincidence peak is reported in the insets. We observe that the number of recorded coincidence counts is stable across all links with a relative

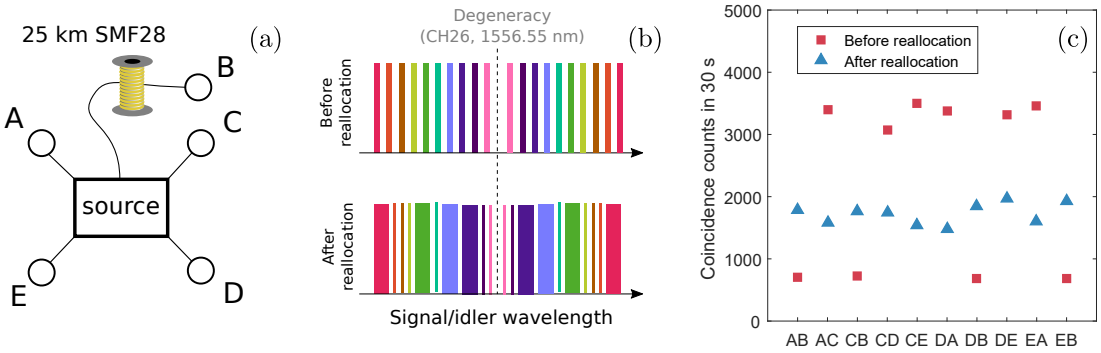

Figure 12.7: Illustration of flexible bandwidth allocation. (a) Sketch of the experiment. In a fully connected network with $N = 5$ users, user B is separated from the source by a 25 km long SMF28 fiber spool. (b) Schematic of the bandwidth distribution between all two-user links before and after applying the bandwidth reallocation algorithm. After reallocation, the four links (red, dark green, light blue and dark blue) that connect user B to the rest of the network are allowed a broader bandwidth. (c) Coincidence counts for each two-user link before (squares) and after (triangles) bandwidth reallocation.

standard deviation of 7 %, 9 % and 11 % for $N = 4, 5, 8$ respectively. As already discussed in Section 12.1, this is a consequence of the broadband character of the source and of the wavelength-insensitive insertion losses of the WSS. In contrast, in networks based on passive thin-film WDM filters, the channel transmission can be subject to strong variations, leading to unbalanced networks where some links carry more signal than others. We consolidate this result by recalling that, as shown in Fig. 12.1, the QBER and asymptotic key rate have a very weak dependence on the frequency channel. Hence we expect the key rate to be evenly distributed among all two-user links in each configuration.

Finally, we check that the QBER is not affected when changing the channel bandwidth. This is done by estimating e and R_{key} using the protocol described in section Section 12.1 for ITU channels 23 and 29 as a function of channel bandwidth. The result is shown in Fig. 12.6 (d). We see that the QBER is essentially insensitive to the channel bandwidth and the corresponding asymptotic key rates show a linear dependence with the bandwidth, as expected. We conclude that these values for R_{key} and QBER, alongside with those of Fig. 12.1, provide an estimate for the achievable QKD performances in the various N-user graphs presented in Fig. 12.6 (a-c).

Our scheme presents several advantages in terms of scalability over passive WDM QKD schemes. Indeed, the flexibility offered by the WSS makes it possible to fully reconfigure the network without modifying the hardware. On the contrary, using passive WDM demux/mux the addition of more users to the network requires either changing the complex combination of cascaded WDM filters or non-deterministically splitting some channels by combining WDM filters and multi-port fiber splitters [97, 205], which, either way, comes at the cost of extra optical losses. In contrast, the fixed insertion losses of the WSS makes it possible to extend the network without degrading the signal, a major asset in a fully deployed network scenario.

12.5 Elastic quantum network with flexible bandwidth allocation

Finally, we exploit the flexibility of our scheme to demonstrate a quantum network where the signal of each link is optimized following a structural constraint (elastic network). This experiment represents a first step towards a fully autonomous smart network, where communication rates are automatically optimized based on bidirectional information exchange between the users and the network provider. We consider a fully-connected entanglement network where one of the user nodes is located far apart from the entangled photon source, while all the other nodes are located close to the source as schematically depicted in Fig. 12.7 (a). We implement this situation for $N = 5$ by separating node B's detector from the source by a 25 km-long SMF28 fiber spool. As we mentioned in Section 12.2.2, due to the large time delay between detection events in an unbalanced link, we used a time-tagger for coincidence counting instead of our regular TDC.

If all two-user links have the same fixed bandwidth, the key rate of the four links connecting the distant user to the rest of the network, *i.e.*, AB CB DB EB, will be lower than the others. To avoid this problem, we reallocate the state bandwidth by changing the channel widths, assigning more bandwidth to long links, and less bandwidth to short links, as schematically depicted in Fig. 12.7 (b). We use a simple algorithm and distribute the available bandwidth with a 12.5 GHz resolution corresponding to current ITU standards for channel bandwidth granularity.

In order to demonstrate that we can efficiently level the measured signal across the whole network, we measure one by one the 10 two-user coincidence counts rates. The results are shown in Fig. 12.7 (c). Red squares represent the raw coincidence counts of the 10 two-user links for fixed 100 GHz channels and blue triangles are the raw coincidence counts recorded after bandwidth reallocation. We observe that, starting from a very unbalanced initial configuration, we can bring all users to a similar level of signal. The fluctuations in the signal after reallocation is due to the finite granularity of the flexible frequency grid which prevents perfect redistribution of the signal between the users.

The same technique could be applied to other ends, such as boosting the signal across specific links according to user needs. This proof-of-principle experiment shows that QKD is fully compatible with state-of-the-art telecom network management, opening the way for flexible metropolitan-scale entanglement distribution.

12.6 Towards new topologies

We discussed the special case of the fully-connected network which, up to now, is the geometry that drew the most attention for polarization-entanglement networks [145, 97, 72]. But non fully-connected networks of N users distributed into k subnets with N/k users per subnets have also been suggested in Refs. [97, 205] as a way to increase the network capacity. This geometry consists of a central k-node fully-connected network. Each of these main nodes are connected to independent fully-connected subnets of size N/k as shown in Fig. 12.8 (c). In this particular class of topologies, the number of required frequency channels is

$$N_{\text{channels}} = k\frac{N}{k}\left(\frac{N}{k} - 1\right) + k(k-1). \tag{12.20}$$

We note that the scaling of N_{channels} with the total number of users N is improved with respect to Eq. (12.19) for the fully-connected network. For a given number N of users, the

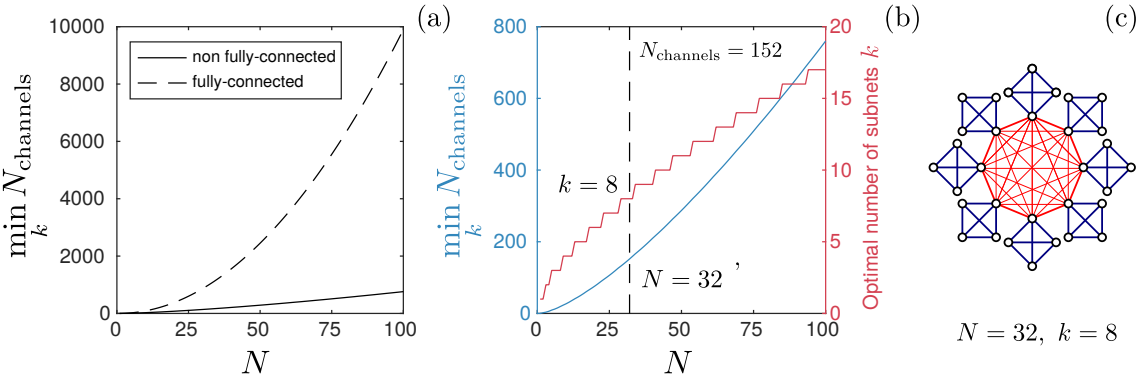

Figure 12.8: (a) Optimal number of channels for a fully-connected and non fully-connected network, given by Eq. (12.19) and Eq. (12.20). (b) Number of channels and optimal number k of subnets for a non fully-connected network as a function of the number of users N. We display optimal values for N and k assuming a source emitting over 152 50 GHz frequency channels. (c) Quantum correlation topology for a network consisting of $N = 32$ users distributed into 8 subnets. Circles and lines represent user nodes and shared entangled states respectively.

number of required channels depends on the value of k and the optimal network configuration, which involves the smallest possible number of channels, can be found by minimizing Eq. (12.20) with respect to k. The comparison of the minimum number of channels versus N for both fully and non-fully-connected networks is shown in Fig. 12.8 (a). We see that the increase in the number of channels is much faster in the case of a fully-connected network. In Fig. 12.8 (b) we plot the minimum number of channels and corresponding optimal number of subnets k against N to find the maximum network size achievable with our setup. Our source emits a state having a fidelity greater or equal to 85 % over a range of 60 nm. If we subdivide this spectral band into 50 GHz channels, we obtain a total number 152 available frequency channels. The maximum number of users we can connect using all this available resource is $N = 32$ in a network that consists of $k = 8$ subnets of 4 users. The corresponding quantum correlation topology is shown in Fig. 12.8.

The drawback to the increase in the number of users is the reduction of the degree of connectivity of the network. In non-fully-connected architectures, entanglement is only shared between a subset of the users and additional steps are needed to extend entanglement between non-connected nodes. Ref. [205] suggested that 2 users A and B within the k principal nodes can send their key to two users C and D belonging to distinct subnets after encrypting it with a XOR operation, a technique that is widely used in QKD networks based on "prepare-and-measure" protocols. Despite is simplicity, this protocol has the major drawback of introducing the need for trusted nodes in the network. A trusted-node-free protocol for propagating entanglement through the network would be entanglement swapping.

Conclusion and perspectives

Summary of this work

In this chapter, we summarize the results presented in the dissertation and give an outlook on future work. The main achievements of this doctorate have been the integration of different functionalities on monolithic AlGaAs chips, the engineering and thorough characterization of the quantum state emitted by the AlGaAs source and the utilization of this source in a quantum communication network.

We first demonstrated the design, fabrication and characterization of a device including an AlGaAs source and an electro-optic delay line on a monolithic chip. The delay line can be easily fabricated by depositing gold electrical contacts on top of a wet-etched non-linear waveguide. When applying an electric field to the structure, we demonstrated a $\pi/2$-shift voltage as low as 9 V, enabling the manipulation of the phase of generated photons directly on-chip using standard electronics.

In addition to this, we showed how we managed to monolithically integrate on a single chip an AlGaAs entangled photon pair source and a broadband polarizing mode splitter. The device consists of a ridge waveguide, into which cross-polarized photon pairs are generated, connected to a birefringent directional coupler. By carefully engineering the dispersion of the supermodes of the structure, we achieve on-chip polarization splitting of photons with a splitting ratio greater than 90 % over a bandwidth of 45 nm. To probe the spectral indistinguishability of the separated photons, we performed Hong-Ou-Mandel interference directly at the chip output. We obtained a maximum visibility of 80 % that is intrinsically limited by the inherent birefringence of the present device, showing the capability to deterministically separate the generated photon pairs on-chip without altering their quantum state.

On top of these results, we used our AlGaAs source in a multi-user quantum communication experiment. We first showed the high-quality entanglement of the polarization-entangled state generated by our source by measuring a Bell state fidelity of above 95 % over a 26 nm spectral band. By taking advantage of the broadband character of the source, we were able to demultiplex the generated photons into multiple energy-conjugate telecom channels that were distributed to up to 8 users in a fully-connected topology with fiber links of up to 50 km. We showcased the potential of our network by running an entanglement-based quantum key distribution protocol (BBM92) showing asymptotic secure key rates as high as $39\,\mathrm{bit\,s^{-1}}$. We also performed a finite-key analysis of our scheme. In addition, by using a wavelength selective switch at the demultiplexing/multiplexing stage, we showed flexible reconfiguration of the bandwidth allocation over the network. This functionality was used in a network architecture involving 5 parties to circumvent the reduction of signal in a specific two-user link due to optical losses.

Perspectives

We conclude this dissertation by giving an insight into future research perspectives. On the device side several goals are now at reach. In our work, we separately demonstrated the integration of the AlGaAs source with an electro-optic delay line and with a polarization mode splitter. Hence we could readily design and fabricate a chip that would include all three components. By going one step further, we can also think of adding an extra on-chip 50/50 splitter to this future device to realize an integrated Mach-Zender interferometer. In this configurations the photons, after being generated in a waveguide, are separated deterministically at the polarizing mode splitter and time-shifted by the electro-optic delay line then finally recombined on the 50/50 mode splitter. This chip could serve multiple purposes. An idea would be to perform a fully on-chip Hong-Ou-Mandel interference experiment, as was already shown with ppLN [69]. Moreover, it was demonstrated that one can create polarization-frequency hyper-entangled states by sending polarization-entangled photons into a balanced Mach-Zender interferometer [161]. Hence by combining our broadband source with this fully integrated interferometer, we would be able to generate directly on-chip hyperentangled photons over a wide spectral range. This type of quantum state can be a promising resource for quantum communication networks [206].

Another exciting prospect is the on-chip integration of the pump laser with the other AlGaAs photonic components using the electrical injection scheme that was previously demonstrated by our team [82]. The possible integration of III-V sources of photon pairs onto silicon photonic circuits also offers great promises. This hybrid platform would combine bright $\chi^{(2)}$ electrically pumped sources and advanced reconfigurable photonic gates. This could be a major technological breakthrough in the field of integrated quantum photonics enabling the development of low-power electrically driven photonic chips that could perform complex quantum information tasks without any external laser source. Our team, in collaboration with the Center for Nanoscience and Nanotechnologies (C2N) in Palaiseau and the Silicon technology company ST Microelectronics in Grenoble, is actively pursuing this goal.

On the quantum communication side, several other projects are underway. In this dissertation, we demonstrated a quantum communication network of up to 8 users in a fully-connected trusted-node free topology. However, due to the quadratic scaling of the number of required frequency channels with the number of users, the finite available bandwidth of the state generated by the source limits the number of nodes in the network. To solve this issue, we are planning on extending our scheme to non-fully connected network topologies which can accommodate more users at the cost of introducing trusted nodes. In close collaboration with Eleni Diamanti and Damian Markham at Sorbonne Université, we are also looking into new theoretical proposals where our network could be used for other quantum information protocols such as distributed sensing or computing.

We are also aiming at deploying our scheme over fiber communication cables spanning the Paris metropolitan area. This effort is part of a regional project supported by the DIM SIRTEQ which aims at constituting a multi-node metropolitan quantum network connecting major research centers over the Paris area. Together with the group of Eleni Diamanti, we are planning on laying the first stone of this Parisian network by running QKD protocols between our two labs, which are located several kilometers apart, first using commercially available QKD systems then our own AlGaAs source.

Finally, another ongoing project is to combine AlGaAs sources with the on-chip trapped ions platform that is being developed by the team of Luca Guidoni at Université de Paris. By coupling the photons from our source with ions in a miniature surface

trap we are planning on performing on-chip ion-photon entanglement and storage of the quantum state of the photons in a single ion. The common integration of sources of non-classical light and atomic system has never been achieved to date and would open the way to the realization of integrated quantum network nodes.

Appendix

List of publications and conferences

Journal articles

- F. Appas, F. Baboux, M. I. Amanti, A. Lemaître, F. Boitier, E. Diamanti, and S. Ducci, "Flexible entanglement-distribution network with an AlGaAs chip for secure communications", npj Quantum Information **7**, 118 (2021)
- F. Appas et al., "Monolithic integration of a photon-pair source and a broadband polarization mode splitter on an AlGaAs chip", in preparation
- N. Fabre, G. Maltese, F. Appas, S. Felicetti, A. Ketterer, A. Keller, T. Coudreau, F. Baboux, M. I. Amanti, S. Ducci, and P. Milman, "Generation of a time-frequency grid state with integrated biphoton frequency combs", Phys. Rev. A **102**, 012607 (2020)
- G. Maltese, M. I. Amanti, F. Appas, G. Sinnl, A. Lemaître, P. Milman, F. Baboux, and S. Ducci, "Generation and symmetry control of quantum frequency combs", npj Quantum Information **6**, 13 (2020)

Communications (presented in person)

- (Poster) GdR IQFA 11^{th} Colloquium, Lyon, France, July 2021
  F. Appas, F. Baboux, M. I. Amanti, A. Lemaître, F. Boitier, E. Diamanti, S. Ducci,"Flexible entanglement-distribution network with an AlGaAs chip for secure communications"
- (Oral) International Conference on Quantum Communications, Paris, France, October 2021
  F. Appas, F. Baboux, M. I. Amanti, A. Lemaître, F. Boitier, E. Diamanti, S. Ducci,"Flexible entanglement-distribution network with an AlGaAs chip for secure communications"
- (Poster) SPIE Photonics for Quantum, online, July 2021
  F. Appas, F. Baboux, M. I. Amanti, A. Lemaître, F. Boitier, E. Diamanti, S. Ducci,"Flexible entanglement-distribution network with an AlGaAs chip for secure communications"
- (Poster) French Optical Society (SFO) Annual Congress, Dijon, France, July 2021
  F. Appas, F. Baboux, M. I. Amanti, A. Lemaître, F. Boitier, E. Diamanti, S. Ducci,"Flexible entanglement-distribution network with an AlGaAs chip for secure communications"

- (Oral) PCQC QuPa Workshop at College de France, Paris, France, June 2021
  F. Appas, F. Baboux, M. I. Amanti, A. Lemaître, F. Boitier, E. Diamanti, S. Ducci,"Flexible entanglement-distribution network with an AlGaAs chip for secure communications"

- (Oral) CLEO Europe, online, June 2021
  F. Appas, F. Baboux, M. I. Amanti, A. Lemaître, F. Boitier, E. Diamanti, S. Ducci,"Flexible entanglement-distribution network with an AlGaAs chip for secure communications"

- (Poster) GdR IQFA 10^{th} Colloquium, Paris, France, 2019
  F. Appas, F. Baboux, M. I. Amanti, A. Lemaître, F. Boitier, E. Diamanti, S. Ducci,"Generation and manipulation of high-dimensional frequency states on an AlGaAs chip"

- (Poster) Les Houches Spring School, Les Houches, France, 2019
  F. Appas, F. Baboux, M. I. Amanti, A. Lemaître, F. Boitier, E. Diamanti, S. Ducci,"Generation and manipulation of high-dimensional frequency states on an AlGaAs chip"

- (Poster) SirTeQ Annual Meeting, Palaiseau, France, 2019
  F. Appas, F. Baboux, M. I. Amanti, A. Lemaître, F. Boitier, E. Diamanti, S. Ducci,"Generation and manipulation of high-dimensional frequency states on an AlGaAs chip"

- (Poster) GdR IQFA 9^{th} Colloquium, Montpellier, France, 2018
  F. Appas, F. Baboux, M. I. Amanti, A. Lemaître, F. Boitier, E. Diamanti, S. Ducci,"Generation and manipulation of high-dimensional frequency states on an AlGaAs chip"

Software credits

Numerical and analytic simulations have been done in Matlab. The simulation of the guided modes of the polarization mode splitter was performed with COMSOL and the dispersion of guided modes in single waveguides and light propagation with Lumerical (FDTD and MODE modules).

Plots have been realized in Matlab, and illustrations in Inkscape. 3D images were composed with Blender. I acknowledge Alexander Franzen for ComponentLibrary. I have used this free collection of optical components for drawing most of the optical setups of this manuscript.

Growth sheets

Layer	Cycles	Δz (nm)	x
Cap	1	20	0
Bragg mirror	2	270	80
Bragg mirror		116	25
Core	1	366 (`G5X038`) or 351 (`K7AD118`)	45
Bragg mirror	6	116	25
Bragg mirror		270	80
Substrate	1		0

Table 12.2: Growth sheet of passive structures `G5X038` and `K7AD118`.

Layer	Cycles	Δz (nm)	x
Cap	1	20	0
Bragg mirror	6	270	80
Bragg mirror		116	25
Core	1	366	45
Bragg mirror	6	116	25
Bragg mirror		270	80
Substrate	1		0

Table 12.3: Growth sheet of passive structures `EBW002`.

Layer	Cycles	Δz (nm)	x	Doping (type)	Doping (cm^{-3})
Cap	1	200	0	p	2×10^{19}
Bragg mirror	3	270	80	p	2×10^{18}
Bragg mirror		116	25	p	2×10^{18}
Bragg mirror	3	270	80	p	2×10^{17}
Bragg mirror		116	25	p	2×10^{17}
Core	1	210	45	intrinsic	
Active layer	1	8.5	11	intrinsic	
Core	1	210	45	intrinsic	
Bragg mirror	3	116	25	n	2×10^{17}
Bragg mirror		270	80	n	2×10^{17}
Bragg mirror	3	116	25	n	2×10^{18}
Bragg mirror		270	80	n	2×10^{18}
Substrate	1		0	n	2×10^{18}

Table 12.4: Growth sheet of active structure `HIY021`.

Bibliography

[1] Arute, F. *et al.* Quantum supremacy using a programmable superconducting processor. *Nature* **574**, 505–510 (2019). [Cited on page 13.]

[2] Zhong, H.-S. *et al.* Quantum computational advantage using photons. *Science* **370**, 1460 – 1463 (2020). [Cited on pages 13 and 15.]

[3] Yin, J. *et al.* Entanglement-based secure quantum cryptography over 1,120 kilometres. *Nature* **582**, 501–505 (2020). [Cited on pages 13, 148, 151, 152, and 153.]

[4] Abadie, J. *et al.* A gravitational wave observatory operating beyond the quantum shot-noise limit. *Nat. Phys.* **7**, 962–965 (2011). [Cited on pages 13 and 15.]

[5] Hensen, B. *et al.* Loophole-free bell inequality violation using electron spins separated by 1.3 kilometres. *Nature* **526**, 682–686 (2015). [Cited on pages 13 and 36.]

[6] Shalm, L. K. *et al.* Strong loophole-free test of local realism. *Phys. Rev. Lett.* **115** (2015). [Cited on page 13.]

[7] Giustina, M. *et al.* Significant-loophole-free test of bell's theorem with entangled photons. *Phys. Rev. Lett.* **115** (2015). [Cited on page 13.]

[8] Saffman, M. Quantum computing with atomic qubits and rydberg interactions: progress and challenges. *J. Phys. B: At., Mol. Opt. Phys.* **49**, 202001 (2016). [Cited on page 14.]

[9] Bruzewicz, C. D., Chiaverini, J., McConnell, R. & Sage, J. M. Trapped-ion quantum computing: Progress and challenges. *Applied Physics Reviews* **6**, 021314 (2019). [Cited on page 14.]

[10] Gross, C. & Bloch, I. Quantum simulations with ultracold atoms in optical lattices. *Science* **357**, 995–1001 (2017). [Cited on page 14.]

[11] Loss, D. & DiVincenzo, D. P. Quantum computation with quantum dots. *Phys. Rev. A* **57**, 120–126 (1998). [Cited on page 14.]

[12] Kloeffel, C. & Loss, D. Prospects for spin-based quantum computing in quantum dots. *Annual Review of Condensed Matter Physics* **4**, 51–81 (2013). [Cited on page 14.]

[13] Childress, L. & Hanson, R. Diamond NV centers for quantum computing and quantum networks. *MRS Bulletin* **38**, 134–138 (2013). [Cited on page 14.]

[14] Blais, A., Girvin, S. M. & Oliver, W. D. Quantum information processing and quantum optics with circuit quantum electrodynamics. *Nat. Phys.* **16**, 247–256 (2020). [Cited on page 14.]

[15] Kjaergaard, M. *et al.* Superconducting qubits: Current state of play. *Annual Review of Condensed Matter Physics* **11**, 369–395 (2020). [Cited on page 14.]

[16] Flamini, F., Spagnolo, N. & Sciarrino, F. Photonic quantum information processing: a review. *Rep. Prog. Phys.* **82**, 016001 (2018). [Cited on pages 14, 15, 17, and 97.]

[17] Fox, M. *Quantum optics : an introduction* (Oxford University Press, Oxford New York, 2006). [Cited on page 14.]

[18] BROWN, R. H. & TWISS, R. Q. Correlation between photons in two coherent beams of light. *Nature* **177**, 27–29 (1956). [Cited on page 14.]

[19] Kimble, H. J., Dagenais, M. & Mandel, L. Photon antibunching in resonance fluorescence. *Phys. Rev. Lett.* **39**, 691–695 (1977). [Cited on page 14.]

[20] Slusher, R. E., Hollberg, L. W., Yurke, B., Mertz, J. C. & Valley, J. F. Observation of squeezed states generated by four-wave mixing in an optical cavity. *Phys. Rev. Lett.* **55**, 2409–2412 (1985). [Cited on page 14.]

[21] Grangier, P., Roger, G. & Aspect, A. Experimental evidence for a photon anticorrelation effect on a beam splitter: A new light on single-photon interferences. *Europhysics Letters (EPL)* **1**, 173–179 (1986). [Cited on page 14.]

[22] Hong, C. K., Ou, Z. Y. & Mandel, L. Measurement of subpicosecond time intervals between two photons by interference. *Phys. Rev. Lett.* **59**, 2044–2046 (1987). [Cited on page 14.]

[23] Aspect, A., Grangier, P. & Roger, G. Experimental tests of realistic local theories via bell's theorem. *Phys. Rev. Lett.* **47**, 460–463 (1981). [Cited on pages 14 and 36.]

[24] Aspect, A., Grangier, P. & Roger, G. Experimental realization of einstein-podolsky-rosen-BohmGedankenexperiment: A new violation of bell's inequalities. *Phys. Rev. Lett.* **49**, 91–94 (1982). [Cited on pages 14, 17, and 36.]

[25] Bennett, C. H. & Brassard, G. Quantum cryptography: Public key distribution and coin tossing. In *Proceedings of IEEE International Conference on Computers, Systems, and Signal Processing*, 175 (India, 1984). [Cited on page 14.]

[26] Ekert, A. K. Quantum cryptography based on bell's theorem. *Phys. Rev. Lett.* **67**, 661–663 (1991). [Cited on pages 14 and 148.]

[27] Bennett, C. H., Brassard, G. & Mermin, N. D. Quantum cryptography without bell's theorem. *Phys. Rev. Lett.* **68**, 557–559 (1992). [Cited on pages 14, 36, and 148.]

[28] Bennett, C. H., Bessette, F., Brassard, G., Salvail, L. & Smolin, J. Experimental quantum cryptography. *Journal of Cryptology* **5**, 3–28 (1992). [Cited on pages 14 and 147.]

[29] Jennewein, T., Simon, C., Weihs, G., Weinfurter, H. & Zeilinger, A. Quantum cryptography with entangled photons. *Phys. Rev. Lett.* **84**, 4729–4732 (2000). [Cited on pages 14 and 148.]

[30] Tittel, W., Brendel, J., Zbinden, H. & Gisin, N. Quantum cryptography using entangled photons in energy-time bell states. *Phys. Rev. Lett.* **84**, 4737–4740 (2000). [Cited on pages 14 and 148.]

[31] Naik, D. S., Peterson, C. G., White, A. G., Berglund, A. J. & Kwiat, P. G. Entangled state quantum cryptography: Eavesdropping on the ekert protocol. *Phys. Rev. Lett.* **84**, 4733–4736 (2000). [Cited on pages 14 and 148.]

[32] Bouwmeester, D. *et al.* Experimental quantum teleportation. *Nature* **390**, 575–579 (1997). [Cited on pages 14 and 36.]

[33] Franson, J. D. Bell inequality for position and time. *Phys. Rev. Lett.* **62**, 2205–2208 (1989). [Cited on pages 14 and 40.]

[34] Kwiat, P. G., Steinberg, A. M. & Chiao, R. Y. High-visibility interference in a bell-inequality experiment for energy and time. *Phys. Rev. A* **47**, R2472–R2475 (1993). [Cited on pages 14, 36, and 40.]

[35] Mair, A., Vaziri, A., Weihs, G. & Zeilinger, A. Entanglement of the orbital angular momentum states of photons. *Nature* **412**, 313–316 (2001). [Cited on page 14.]

[36] Michler, P. A quantum dot single-photon turnstile device. *Science* **290**, 2282–2285 (2000). [Cited on page 14.]

[37] Kwiat, P. G. *et al.* New high-intensity source of polarization-entangled photon pairs. *Phys. Rev. Lett.* **75**, 4337–4341 (1995). [Cited on pages 14 and 17.]

[38] Lo, H.-K., Curty, M. & Tamaki, K. Secure quantum key distribution. *Nat. Photonics* **8**, 595–604 (2014). [Cited on page 15.]

[39] Pompili, M. *et al.* Realization of a multinode quantum network of remote solid-state qubits. *Science* **372**, 259–264 (2021). [Cited on page 15.]

[40] Lago-Rivera, D., Grandi, S., Rakonjac, J. V., Seri, A. & de Riedmatten, H. Telecom-heralded entanglement between multimode solid-state quantum memories. *Nature* **594**, 37–40 (2021). [Cited on page 15.]

[41] Daiss, S. *et al.* A quantum-logic gate between distant quantum-network modules. *Science* **371**, 614–617 (2021). [Cited on page 15.]

[42] O'Brien, J. L., Pryde, G. J., White, A. G., Ralph, T. C. & Branning, D. Demonstration of an all-optical quantum controlled-NOT gate. *Nature* **426**, 264–267 (2003). [Cited on page 15.]

[43] Lu, C.-Y., Browne, D. E., Yang, T. & Pan, J.-W. Demonstration of a compiled version of shor's quantum factoring algorithm using photonic qubits. *Phys. Rev. Lett.* **99** (2007). [Cited on page 15.]

[44] Lanyon, B. P. *et al.* Experimental demonstration of a compiled version of shor's algorithm with quantum entanglement. *Phys. Rev. Lett.* **99** (2007). [Cited on page 15.]

[45] Spagnolo, N. *et al.* Experimental validation of photonic boson sampling. *Nat. Photonics* **8**, 615–620 (2014). [Cited on pages 15, 16, and 18.]

[46] Crespi, A. *et al.* Integrated multimode interferometers with arbitrary designs for photonic boson sampling. *Nat. Photonics* **7**, 545–549 (2013). [Cited on pages 15 and 16.]

[47] Sparrow, C. *et al.* Simulating the vibrational quantum dynamics of molecules using photonics. *Nature* **557**, 660–667 (2018). [Cited on pages 15 and 18.]

[48] Guo, X. *et al.* Distributed quantum sensing in a continuous-variable entangled network. *Nat. Phys.* **16**, 281–284 (2019). [Cited on page 15.]

[49] Zhao, S.-R. *et al.* Field demonstration of distributed quantum sensing without post-selection. *Phys. Rev. X* **11** (2021). [Cited on page 15.]

[50] Abellán, C. *et al.* Challenging local realism with human choices. *Nature* **557**, 212–216 (2018). [Cited on page 15.]

[51] Rauch, D. *et al.* Cosmic bell test using random measurement settings from high-redshift quasars. *Phys. Rev. Lett.* **121** (2018). [Cited on page 15.]

[52] Wang, J., Sciarrino, F., Laing, A. & Thompson, M. G. Integrated photonic quantum technologies. *Nat. Photonics* **14**, 273–284 (2019). [Cited on pages 15 and 97.]

[53] Wang, Y., Jöns, K. D. & Sun, Z. Integrated photon-pair sources with nonlinear optics. *Applied Physics Reviews* **8**, 011314 (2021). [Cited on pages 15 and 82.]

[54] Qiang, X. *et al.* Large-scale silicon quantum photonics implementing arbitrary two-qubit processing. *Nat. Photonics* **12**, 534–539 (2018). [Cited on pages 16 and 18.]

[55] Bunandar, D. *et al.* Metropolitan quantum key distribution with silicon photonics. *Phys. Rev. X* **8** (2018). [Cited on pages 16 and 19.]

[56] Llewellyn, D. *et al.* Chip-to-chip quantum teleportation and multi-photon entanglement in silicon. *Nat. Phys.* **16**, 148–153 (2019). [Cited on page 16.]

[57] Pernice, W. *et al.* High-speed and high-efficiency travelling wave single-photon detectors embedded in nanophotonic circuits. *Nat. Commun.* **3** (2012). [Cited on page 16.]

[58] Taballione, C. *et al.* 8×8 reconfigurable quantum photonic processor based on silicon nitride waveguides. *Opt. Express* **27**, 26842 (2019). [Cited on page 16.]

[59] Imany, P. *et al.* 50-GHz-spaced comb of high-dimensional frequency-bin entangled photons from an on-chip silicon nitride microresonator. *Opt. Express* **26**, 1825 (2018). [Cited on pages 16, 18, 36, 42, 43, and 98.]

[60] Arrazola, J. M. *et al.* Quantum circuits with many photons on a programmable nanophotonic chip. *Nature* **591**, 54–60 (2021). [Cited on page 16.]

[61] Gyger, S. *et al.* Reconfigurable photonics with on-chip single-photon detectors. *Nat. Commun.* **12** (2021). [Cited on page 16.]

[62] Bauters, J. F. *et al.* Planar waveguides with less than 01 dB/m propagation loss fabricated with wafer bonding. *Opt. Express* **19**, 24090 (2011). [Cited on page 16.]

[63] Reimer, C. *et al.* Generation of multiphoton entangled quantum states by means of integrated frequency combs. *Science* **351**, 1176–1180 (2016). [Cited on page 16.]

[64] Carolan, J. *et al.* Universal linear optics. *Science* **349**, 711–716 (2015). [Cited on page 16.]

[65] Crespi, A. *et al.* Integrated photonic quantum gates for polarization qubits. *Nat. Commun.* **2** (2011). [Cited on pages 16 and 119.]

[66] Hoch, F. *et al.* Boson sampling in a reconfigurable continuously-coupled 3d photonic circuit (2021). `2106.08260v1`. [Cited on page 16.]

[67] Crespi, A. *et al.* Anderson localization of entangled photons in an integrated quantum walk. *Nat. Photonics* **7**, 322–328 (2013). [Cited on pages 16 and 18.]

[68] Flamini, F. *et al.* Thermally reconfigurable quantum photonic circuits at telecom wavelength by femtosecond laser micromachining. *Light: Science & Applications* **4**, e354–e354 (2015). [Cited on pages 16 and 97.]

[69] Luo, K.-H. *et al.* Nonlinear integrated quantum electro-optic circuits. *Sci. Adv.* **5**, eaat1451 (2019). [Cited on pages 16, 98, 120, 143, and 182.]

[70] Tanzilli, S. *et al.* Highly efficient photon-pair source using periodically poled lithium niobate waveguide. *Electron. Lett.* **37**, 26 (2001). [Cited on pages 16 and 81.]

[71] Jin, H. *et al.* On-chip generation and manipulation of entangled photons based on reconfigurable lithium-niobate waveguide circuits. *Phys. Rev. Lett.* **113**, 103601 (2014). [Cited on pages 16 and 98.]

[72] Lingaraju, N. B. *et al.* Adaptive bandwidth management for entanglement distribution in quantum networks. *Optica* **8**, 329 (2021). [Cited on pages 16, 148, 149, 150, 175, and 178.]

[73] Alshowkan, M. *et al.* Reconfigurable quantum local area network over deployed fiber. *PRX Quantum* **2** (2021). [Cited on pages 16, 148, 149, 150, and 175.]

[74] Mondain, F. *et al.* Chip-based squeezing at a telecom wavelength. *Photonics Res.* **7**, A36 (2019). [Cited on page 16.]

[75] Rabiei, P., Ma, J., Khan, S., Chiles, J. & Fathpour, S. Heterogeneous lithium niobate photonics on silicon substrates. *Opt. Express* **21**, 25573 (2013). [Cited on page 16.]

[76] Somaschi, N. *et al.* Near-optimal single-photon sources in the solid state. *Nat. Photonics* **10**, 340–345 (2016). [Cited on page 17.]

[77] Horn, R. *et al.* Monolithic source of photon pairs. *Phys. Rev. Lett.* **108** (2012). [Cited on pages 17 and 79.]

[78] Autebert, C. *et al.* Integrated AlGaAs source of highly indistinguishable and energy-time entangled photons. *Optica* **3**, 143 (2016). [Cited on pages 17, 41, 82, and 156.]

[79] Steiner, T. J. *et al.* Ultrabright entangled-photon-pair generation from an AlGaAs -on-insulator microring resonator. *PRX Quantum* **2** (2021). [Cited on page 17.]

[80] Wang, J. *et al.* Gallium arsenide (GaAs) quantum photonic waveguide circuits. *Opt. Commun.* **327**, 49–55 (2014). [Cited on pages 17 and 98.]

[81] Sprengers, J. P. *et al.* Waveguide superconducting single-photon detectors for integrated quantum photonic circuits. *Appl. Phys. Lett.* **99**, 181110 (2011). [Cited on page 17.]

[82] Boitier, F. *et al.* Electrically injected photon-pair source at room temperature. *Phys. Rev. Lett.* **112** (2014). [Cited on pages 17, 104, 107, and 182.]

[83] Autebert, C. *et al.* Electrically injected twin photon emitting lasers at room temperature. *Technologies* **4**, 24 (2016). [Cited on pages 17 and 104.]

[84] Agnesi, C. *et al.* Hong–ou–mandel interference between independent III–v on silicon waveguide integrated lasers. *Opt. Lett.* **44**, 271 (2019). [Cited on page 17.]

[85] Appas, F. *et al.* Flexible entanglement-distribution network with an AlGaAs chip for secure communications. *npj Quantum Inf.* **7** (2021). [Cited on pages 17, 19, 148, 149, and 150.]

[86] Basset, F. B. *et al.* Quantum key distribution with entangled photons generated on demand by a quantum dot. *Sci. Adv.* **7**, eabe6379 (2021). [Cited on pages 17 and 148.]

[87] Maltese, G. *et al.* Generation and symmetry control of quantum frequency combs. *npj Quantum Inf.* **6**, 13 (2020). [Cited on pages 17, 18, 43, 72, 73, and 93.]

[88] Fabre, N. *et al.* Generation of a time-frequency grid state with integrated biphoton frequency combs. *Phys. Rev. A* **102**, 012607 (2020). [Cited on page 17.]

[89] Istrati, D. *et al.* Sequential generation of linear cluster states from a single photon emitter. *Nat. Commun.* **11** (2020). [Cited on page 17.]

[90] Francesconi, S. *et al.* Engineering two-photon wavefunction and exchange statistics in a semiconductor chip. *Optica* **7**, 316 (2020). [Cited on pages 17 and 93.]

[91] Francesconi, S. *et al.* Anyonic two-photon statistics with a semiconductor chip. *ACS Photonics* (2021). [Cited on pages 17 and 93.]

[92] Braunstein, S. L. & van Loock, P. Quantum information with continuous variables. *Rev. Mod. Phys.* **77**, 513–577 (2005). [Cited on page 17.]

[93] Menicucci, N. C. *et al.* Universal quantum computation with continuous-variable cluster states. *Phys. Rev. Lett.* **97** (2006). [Cited on page 17.]

[94] Jouguet, P., Kunz-Jacques, S., Leverrier, A., Grangier, P. & Diamanti, E. Experimental demonstration of long-distance continuous-variable quantum key distribution. *Nat. Photonics* **7**, 378–381 (2013). [Cited on pages 17 and 148.]

[95] Orieux, A. *et al.* Direct bell states generation on a III-v semiconductor chip at room temperature. *Phys. Rev. Lett.* **110** (2013). [Cited on pages 17 and 36.]

[96] Dousse, A. *et al.* Ultrabright source of entangled photon pairs. *Nature* **466**, 217–220 (2010). [Cited on page 17.]

[97] Joshi, S. K. *et al.* A trusted node–free eight-user metropolitan quantum communication network. *Sci. Adv.* **6**, eaba0959 (2020). [Cited on pages 17, 149, 156, 157, 160, 174, 175, 177, and 178.]

[98] Takesue, H. & Noguchi, Y. Implementation of quantum state tomography for time-bin entangled photon pairs. *Opt. Express* **17**, 10976 (2009). [Cited on pages 18 and 36.]

[99] Boaron, A. *et al.* Secure quantum key distribution over 421 km of optical fiber. *Phys. Rev. Lett.* **121** (2018). [Cited on pages 18 and 147.]

[100] Brougham, T., Barnett, S. M., McCusker, K. T., Kwiat, P. G. & Gauthier, D. J. Security of high-dimensional quantum key distribution protocols using franson interferometers. *J. Phys. B: At., Mol. Opt. Phys.* **46**, 104010 (2013). [Cited on page 18.]

[101] Islam, N. T. *et al.* Scalable high-rate, high-dimensional time-bin encoding quantum key distribution. *Quantum Science and Technology* **4**, 035008 (2019). [Cited on page 18.]

[102] Silverstone, J. W. *et al.* On-chip quantum interference between silicon photon-pair sources. *Nat. Photonics* **8**, 104–108 (2013). [Cited on pages 18 and 97.]

[103] Wang, J. *et al.* Multidimensional quantum entanglement with large-scale integrated optics. *Science* **360**, 285–291 (2018). [Cited on page 18.]

[104] Wang, H. *et al.* Boson sampling with 20 input photons and a 60-mode interferometer in a 1014 -dimensional hilbert space. *Phys. Rev. Lett.* **123** (2019). [Cited on page 18.]

[105] Olislager, L. *et al.* Frequency-bin entangled photons. *Phys. Rev. A* **82** (2010). [Cited on pages 18 and 42.]

[106] Lu, H.-H., Simmerman, E. M., Lougovski, P., Weiner, A. M. & Lukens, J. M. Fully arbitrary control of frequency-bin qubits. *Phys. Rev. Lett.* **125** (2020). [Cited on pages 18 and 42.]

[107] Kues, M. *et al.* Quantum optical microcombs. *Nat. Photonics* **13**, 170–179 (2019). [Cited on pages 18 and 19.]

[108] Erhard, M., Fickler, R., Krenn, M. & Zeilinger, A. Twisted photons: new quantum perspectives in high dimensions. *Light: Science & Applications* **7**, 17146–17146 (2018). [Cited on page 18.]

[109] Mirhosseini, M. *et al.* High-dimensional quantum cryptography with twisted light. *New J. Phys.* **17**, 033033 (2015). [Cited on page 18.]

[110] Dada, A. C., Leach, J., Buller, G. S., Padgett, M. J. & Andersson, E. Experimental high-dimensional two-photon entanglement and violations of generalized bell inequalities. *Nat. Phys.* **7**, 677–680 (2011). [Cited on page 18.]

[111] Niffenegger, R. J. *et al.* Integrated multi-wavelength control of an ion qubit. *Nature* **586**, 538–542 (2020). [Cited on page 19.]

[112] Wallucks, A., Marinković, I., Hensen, B., Stockill, R. & Gröblacher, S. A quantum memory at telecom wavelengths. *Nat. Phys.* **16**, 772–777 (2020). [Cited on page 19.]

[113] Ciampini, M. A. *et al.* Path-polarization hyperentangled and cluster states of photons on a chip. *Light: Science & Applications* **5**, e16064–e16064 (2016). [Cited on page 19.]

[114] Reimer, C. *et al.* High-dimensional one-way quantum processing implemented on d-level cluster states. *Nat. Phys.* **15**, 148–153 (2018). [Cited on pages 19, 43, and 73.]

[115] Avesani, M. *et al.* Full daylight quantum-key-distribution at 1550 nm enabled by integrated silicon photonics. *npj Quantum Inf.* **7** (2021). [Cited on page 19.]

[116] Dequal, D. *et al.* Feasibility of satellite-to-ground continuous-variable quantum key distribution. *npj Quantum Inf.* **7** (2021). [Cited on page 19.]

[117] Boyd, R. *Nonlinear optics* (Academic Press, Amsterdam Boston, 2008). [Cited on pages 24, 25, and 26.]

[118] Grynberg, G., Aspect, A. & Fabre, C. *Introduction to Quantum Optics* (Cambridge University Press, 2017). [Cited on page 31.]

[119] Ou, Z.-Y. *Multi-Photon Quantum Interference* (Springer-Verlag GmbH, 2007). [Cited on pages 33, 65, and 162.]

[120] Sakurai, J. J. *Modern quantum mechanics* (Addison-Wesley, Boston, 2011). [Cited on pages 33 and 66.]

[121] Einstein, A., Podolsky, B. & Rosen, N. Can quantum-mechanical description of physical reality be considered complete? *Phys. Rev.* **47**, 777–780 (1935). [Cited on page 35.]

[122] Bell, J. S. On the einstein podolsky rosen paradox. *Physics Physique Fizika* **1**, 195–200 (1964). [Cited on pages 35 and 38.]

[123] Freedman, S. J. & Clauser, J. F. Experimental test of local hidden-variable theories. *Phys. Rev. Lett.* **28**, 938–941 (1972). [Cited on page 36.]

[124] Fickler, R. *et al.* Quantum entanglement of high angular momenta. *Science* **338**, 640–643 (2012). [Cited on page 36.]

[125] Nielsen, M. A. & Chuang, I. L. *Quantum Computation and Quantum Information: 10th Anniversary Edition* (Cambridge University Press, Cambridge, 2010). URL `https://www.cambridge.org/core/books/quantum-computation-and-quantum-information/01E10196D0A682A6AEFFEA52D53BE9AE`. [Cited on page 36.]

[126] Wootters, W. K. Entanglement of formation of an arbitrary state of two qubits. *Phys. Rev. Lett.* **80**, 2245–2248 (1998). [Cited on page 37.]

[127] Clauser, J. F., Horne, M. A., Shimony, A. & Holt, R. A. Proposed experiment to test local hidden-variable theories. *Phys. Rev. Lett.* **23**, 880–884 (1969). [Cited on page 38.]

[128] James, D. F. V., Kwiat, P. G., Munro, W. J. & White, A. G. Measurement of qubits. *Phys. Rev. A* **64** (2001). [Cited on page 40.]

[129] MacLean, J.-P. W., Donohue, J. M. & Resch, K. J. Direct characterization of ultrafast energy-time entangled photon pairs. *Phys. Rev. Lett.* **120** (2018). [Cited on page 40.]

[130] Horne, M., Shimony, A. & Zeilinger, A. Down-conversion photon pairs: A new chapter in the history of quantum mechanical entanglement. In *Proceedings of the International Conference on Fundamental Aspects of Quantum Theory — to Celebrate 30 Years of the Aharonov-Bohm-Effect, South Carolina, USA, 14 – 16 December 1989*, 356–372 (WORLD SCIENTIFIC, 1991). [Cited on pages 40 and 42.]

[131] Chen, C., Shapiro, J. H. & Wong, F. N. Experimental demonstration of conjugate-franson interferometry. *Phys. Rev. Lett.* **127** (2021). [Cited on page 42.]

[132] Bloch, M., McLaughlin, S. W., Merolla, J.-M. & Patois, F. Frequency-coded quantum key distribution. *Opt. Lett.* **32**, 301 (2007). [Cited on page 43.]

[133] Lu, H.-H. *et al.* A controlled-not gate for frequency-bin qubits. *npj Quantum Inf.* **5**, 24 (2019). [Cited on page 43.]

[134] Kues, M. *et al.* On-chip generation of high-dimensional entangled quantum states and their coherent control. *Nature* **546**, 622–626 (2017). [Cited on pages 43 and 73.]

[135] Imany, P. *et al.* High-dimensional optical quantum logic in large operational spaces. *npj Quantum Inf.* **5**, 59 (2019). [Cited on page 43.]

[136] Yariv, A. *Optical waves in crystals : propagation and control of laser radiation* (Wiley, New York, 1984). [Cited on pages 48, 53, 100, and 102.]

[137] Orieux, A. *Sources semiconductrices d'états à deux photons à température ambiante.* Theses, Université Paris-Diderot - Paris VII (2012). [Cited on pages 50 and 51.]

[138] Orieux, A., Versteegh, M. A. M., Jöns, K. D. & Ducci, S. Semiconductor devices for entangled photon pair generation: a review. *Rep. Prog. Phys.* **80**, 076001 (2017). [Cited on page 50.]

[139] Grisard, A., Lallier, E. & Gérard, B. Quasi-phase-matched gallium arsenide for versatile mid-infrared frequency conversion. *Opt. Mater. Express* **2**, 1020–1025 (2012). [Cited on page 50.]

[140] Ohashi, M. *et al.* Determination of quadratic nonlinear optical coefficient of AlxGa1-xAs system by the method of reflected second harmonics. *J. Appl. Phys.* **74**, 596–601 (1993). [Cited on page 51.]

[141] Shoji, I., Kondo, T., Kitamoto, A., Shirane, M. & Ito, R. Absolute scale of second-order nonlinear-optical coefficients. *Journal of the Optical Society of America B* **14**, 2268 (1997). [Cited on page 51.]

[142] Yeh, P. & Yariv, A. Bragg reflection waveguides. *Opt. Commun.* **19**, 427–430 (1976). [Cited on page 51.]

[143] Helmy, A. S., Bijlani, B. & Abolghasem, P. Phase matching in monolithic bragg reflection waveguides. *Opt. Lett.* **32**, 2399 (2007). [Cited on page 51.]

[144] Abolghasem, P., Han, J., Bijlani, B. J. & Helmy, A. S. Type-0 second order nonlinear interaction in monolithic waveguides of isotropic semiconductors. *Opt. Express* **18**, 12681 (2010). [Cited on page 54.]

[145] Wengerowsky, S., Joshi, S. K., Steinlechner, F., Hübel, H. & Ursin, R. An entanglement-based wavelength-multiplexed quantum communication network. *Nature* **564**, 225–228 (2018). [Cited on pages 55, 149, 160, 175, and 178.]

[146] Gehrsitz, S. *et al.* The refractive index of AlxGa1-xAs below the band gap: Accurate determination and empirical modeling. *J. Appl. Phys.* **87**, 7825–7837 (2000). [Cited on page 56.]

[147] Autebert, C. *AlGaAs photonic devices: from quantum state generation to quantum communications.* Ph.D. thesis, Université Paris 7 - Denis Diderot (2016). [Cited on page 56.]

[148] Rossi, A. D. *et al.* Measuring propagation loss in a multimode semiconductor waveguide. *J. Appl. Phys.* **97**, 073105 (2005). [Cited on page 60.]

[149] Boucher, G. *et al.* Toolbox for continuous-variable entanglement production and measurement using spontaneous parametric down-conversion. *Phys. Rev. A* **92** (2015). [Cited on page 69.]

[150] Maltese, G. *Generation and manipulation of high-dimensional photonics states with AlGaAs chips.* Ph.D. thesis, Sorbonne Paris Cité (2019). [Cited on pages 69 and 93.]

[151] Lu, Y. J., Campbell, R. L. & Ou, Z. Y. Mode-locked two-photon states. *Phys. Rev. Lett.* **91** (2003). [Cited on pages 73 and 141.]

[152] Schlager, A. *et al.* Temporally versatile polarization entanglement from bragg reflection waveguides. *Opt. Lett.* **42**, 2102 (2017). [Cited on page 74.]

[153] Javid, U. A. *et al.* Ultra-broadband entangled photons on a nanophotonic chip (2021). `2101.04877v1`. [Cited on page 82.]

[154] Wang, K. Quantum theory of two-photon wavepacket interference in a beamsplitter. *J. Phys. B: At., Mol. Opt. Phys.* **39**, R293–R324 (2006). [Cited on page 83.]

[155] Brańczyk, A. M. Hong-ou-mandel interference (2017). `1711.00080v1`. [Cited on page 83.]

[156] Liscidini, M. & Sipe, J. E. Stimulated emission tomography. *Phys. Rev. Lett.* **111** (2013). [Cited on page 90.]

[157] Eckstein, A. *et al.* High-resolution spectral characterization of two photon states via classical measurements. *Laser & Photonics Reviews* **8**, L76–L80 (2014). [Cited on page 90.]

[158] Douce, T. *et al.* Direct measurement of the biphoton wigner function through two-photon interference. *Sci. Rep.* **3** (2013). [Cited on page 91.]

[159] Jizan, I. *et al.* Phase-sensitive tomography of the joint spectral amplitude of photon pair sources. *Opt. Lett.* **41**, 4803 (2016). [Cited on page 91.]

[160] MacLean, J.-P. W., Schwarz, S. & Resch, K. J. Reconstructing ultrafast energy-time-entangled two-photon pulses. *Phys. Rev. A* **100** (2019). [Cited on page 91.]

[161] Xie, Z. *et al.* Harnessing high-dimensional hyperentanglement through a biphoton frequency comb. *Nat. Photonics* **9**, 536–542 (2015). [Cited on pages 91 and 182.]

[162] Spickermann, R., Sakamoto, S. & Dagli, N. Gaas/algaas traveling-wave electro-optic modulators. In *Optoelectronic Integrated Circuits*, vol. 3006, 272–279 (International Society for Optics and Photonics, 1997). [Cited on page 98.]

[163] qing Lu, Y., Xiao, M. & Salamo, G. J. Wide-bandwidth high-frequency electro-optic modulator based on periodically poled LiNbO3. *Appl. Phys. Lett.* **78**, 1035–1037 (2001). [Cited on page 98.]

[164] Grossard, N., Forte, H., Vilcot, J.-P., Beche, B. & Goedgebuer, J.-P. AlGaAs-GaAs polarization converter with electrooptic phase mismatch control. *IEEE Photonics Technology Letters* **13**, 830–832 (2001). [Cited on page 98.]

[165] Schwartz, M. *et al.* Fully on-chip single-photon hanbury-brown and twiss experiment on a monolithic semiconductor–superconductor platform. *Nano Lett.* **18**, 6892–6897 (2018). [Cited on page 98.]

[166] Belhassen, J. *et al.* On-chip III-v monolithic integration of heralded single photon sources and beamsplitters. *Appl. Phys. Lett.* **112**, 071105 (2018). [Cited on pages 98 and 128.]

[167] Amnon Yariv, P. Y. *Photonics* (Oxford University Press Inc, 2006). [Cited on pages 98, 101, 120, 121, 122, and 123.]

[168] Berseth, C.-A., Wuethrich, C. & Reinhart, F. K. The electro-optic coefficients of GaAs: Measurements at 1.32 and 1.52 μm and study of their dispersion between 0.9 and 10 μm. *J. Appl. Phys.* **71**, 2821–2825 (1992). [Cited on page 102.]

[169] Kiyat, I., Aydinli, A. & Dagli, N. A compact silicon-on-insulator polarization splitter. *IEEE Photonics Technology Letters* **17**, 100–102 (2005). [Cited on page 119.]

[170] Fukuda, H. *et al.* Ultrasmall polarization splitter based on silicon wire waveguides. *Opt. Express* **14**, 12401–12408 (2006). [Cited on page 119.]

[171] Wu, H., Tan, Y. & Dai, D. Ultra-broadband high-performance polarizing beam splitter on silicon. *Opt. Express* **25**, 6069 (2017). [Cited on page 119.]

[172] Chung, H.-P. *et al.* Broadband on-chip polarization mode splitters in lithium niobate integrated adiabatic couplers. *Opt. Express* **27**, 1632 (2019). [Cited on pages 119 and 143.]

[173] Peng, C.-Z. *et al.* Experimental long-distance decoy-state quantum key distribution based on polarization encoding. *Phys. Rev. Lett.* **98** (2007). [Cited on page 147.]

[174] Chen, Y.-A. *et al.* An integrated space-to-ground quantum communication network over 4,600 kilometres. *Nature* **589**, 214–219 (2021). [Cited on page 147.]

[175] Chen, J.-P. *et al.* Twin-field quantum key distribution over a 511 km optical fibre linking two distant metropolitan areas. *Nature* **15**, 570–575 (2021). [Cited on page 147.]

[176] Diamanti, E. & Leverrier, A. Distributing secret keys with quantum continuous variables: Principle, security and implementations (2015). [Cited on page 148.]

[177] Marcikic, I. *et al.* Distribution of time-bin entangled qubits over 50 km of optical fiber. *Phys. Rev. Lett.* **93** (2004). [Cited on page 148.]

[178] Inagaki, T., Matsuda, N., Tadanaga, O., Asobe, M. & Takesue, H. Entanglement distribution over 300 km of fiber. *Opt. Express* **21**, 23241 (2013). [Cited on page 148.]

[179] Ursin, R. *et al.* Entanglement-based quantum communication over 144 km. *Nat. Phys.* **3**, 481–486 (2007). [Cited on page 148.]

[180] Wengerowsky, S. *et al.* Entanglement distribution over a 96-km-long submarine optical fiber. *Proceedings of the National Academy of Sciences* **116**, 6684–6688 (2019). [Cited on page 148.]

[181] Liu, H.-Y. *et al.* Optical-relayed entanglement distribution using drones as mobile nodes. *Phys. Rev. Lett.* **126** (2021). [Cited on page 148.]

[182] Koashi, M. & Preskill, J. Secure quantum key distribution with an uncharacterized source. *Phys. Rev. Lett.* **90** (2003). [Cited on pages 148 and 152.]

[183] Lo, H.-K., Curty, M. & Qi, B. Measurement-device-independent quantum key distribution. *Phys. Rev. Lett.* **108** (2012). [Cited on page 148.]

[184] Vazirani, U. & Vidick, T. Fully device-independent quantum key distribution. *Phys. Rev. Lett.* **113** (2014). [Cited on page 148.]

[185] Schwonnek, R. *et al.* Device-independent quantum key distribution with random key basis. *Nat. Commun.* **12**, 2880 (2021). [Cited on page 148.]

[186] Nadlinger, D. P. *et al.* Device-independent quantum key distribution (2021). `2109.14600v1`. [Cited on page 148.]

[187] Liu, W.-Z. *et al.* High-speed device-independent quantum key distribution against collective attacks (2021). `2110.01480v2`. [Cited on page 148.]

[188] Peev, M. *et al.* The secoqc quantum key distribution network in vienna. *New J. Phys.* **11**, 075001 (2009). [Cited on page 149.]

[189] Stucki, D. *et al.* Long term performance of the swissquantum quantum key distribution network in a field environment. *New J. Phys.* **13** (2012). [Cited on page 149.]

[190] Chen, T.-Y. *et al.* Implementation of a 46-node quantum metropolitan area network. *npj Quantum Inf.* **7**, 134 (2021). [Cited on page 149.]

[191] Bialowons, L. *et al.* A scalable network for simultaneous pairwise quantum key distribution via entanglement-based time-bin coding. *2021* `2110.13795v1`. [Cited on page 149.]

[192] Diamanti, E. *Security and implementation of differential phase shift quantum key distribution systems.* Ph.D. thesis, Stanford University (2006). [Cited on pages 150 and 151.]

[193] Thomas M. Cover, J. A. T. *Elements of Information Theory* (Wiley John + Sons, 2006). [Cited on pages 151 and 152.]

[194] Lütkenhaus, N. Security against individual attacks for realistic quantum key distribution. *Phys. Rev. A* **61** (2000). [Cited on page 152.]

[195] Shor, P. W. & Preskill, J. Simple proof of security of the BB84 quantum key distribution protocol. *Phys. Rev. Lett.* **85**, 441–444 (2000). [Cited on page 152.]

[196] Mayers, D. Unconditional security in quantum cryptography. *Journal of the ACM* **48**, 351–406 (2001). [Cited on page 152.]

[197] Gottesman, D., Lo, H. ., Lutkenhaus, N. & Preskill, J. Security of quantum key distribution with imperfect devices. In *International Symposium onInformation Theory, 2004. ISIT 2004. Proceedings.*, 136– (2004). [Cited on page 152.]

[198] Tomamichel, M., Lim, C. C. W., Gisin, N. & Renner, R. Tight finite-key analysis for quantum cryptography. *Nat. Commun.* **3** (2012). [Cited on pages 152 and 153.]

[199] Brassard, G. & Salvail, L. Secret-key reconciliation by public discussion. In Helleseth, T. (ed.) *Advances in Cryptology — EUROCRYPT '93*, 410–423 (Springer Berlin Heidelberg, Berlin, Heidelberg, 1994). [Cited on page 152.]

[200] Ma, X., Fung, C.-H. F. & Lo, H.-K. Quantum key distribution with entangled photon sources. *Phys. Rev. A* **76** (2007). [Cited on pages 152 and 169.]

[201] Chang, X.-Y. *et al.* Experimental realization of an entanglement access network and secure multi-party computation. *Sci. Rep.* **6** (2016). [Cited on page 165.]

[202] Blinov, B. B., Moehring, D. L., Duan, L.-M. & Monroe, C. Observation of entanglement between a single trapped atom and a single photon. *Nature* **428**, 153–157 (2004). [Cited on page 165.]

[203] Zhu, E. Y. *et al.* Toward a reconfigurable quantum network enabled by a broadband entangled source. *Journal of the Optical Society of America B* **36**, B1 (2019). [Cited on page 168.]

[204] Scheidl, T. *et al.* Feasibility of 300 km quantum key distribution with entangled states. *New J. Phys.* **11**, 085002 (2009). [Cited on page 169.]

[205] Liu, X. *et al.* An entanglement-based quantum network based on symmetric dispersive optics quantum key distribution. *APL Photonics* **5**, 076104 (2020). [Cited on pages 177, 178, and 179.]

[206] Graham, T. M., Bernstein, H. J., Wei, T.-C., Junge, M. & Kwiat, P. G. Superdense teleportation using hyperentangled photons. *Nat. Commun.* **6** (2015). [Cited on page 182.]